Metallicity Gradients in Local Star-Forming Galaxies

Henry Mitchell Poetrodjojo

A thesis submitted for the degree of

Doctor of Philosophy

of The Australian National University

Australian National University

Research School of Astronomy & Astrophysics

August, 2019

Disclaimer

I hereby declare that the work in this thesis is that of the doctoral candidate, except where indicated in the text. The work was undertaken between February 2016 and August 2019 while I was a PhD student at the Australian National University, Canberra. This thesis has not been submitted in whole or in part for any other degree at this or any other university.

Henry Mitchell Poetrodjojo

28th August 2019

Acknowledgments

Although it may appear as if I completed this thesis on my own, there are countless of people who have contributed to its success.

I would first like to thank my two amazing supervisors, Brent Groves and Lisa Kewley. Without the support of Brent and Lisa, there would be no timeline within which this PhD would have been completed. I was lucky enough to have been able to present my research all over North America and Europe as well as observe in South America with the TYPHOON team (Barry Madore, Jeff Rich and Mark Seibert). By any account, my PhD experience was perfect.

My time overseas really made me appreciate the sense of community at Mt Stromlo. The support I received from fellow students and postdocs when I was a part of the GEARS3D research group remains unmatched. I grew close with many people during my 4.5 years at Mt Stromlo, especially my travel companion, Joshua D'Agostino, with whom I struggled with at Las Campanas Observatory and lived with in Pasadena.

This research was financially support by the Australian Government Research Training Program (AGRTP) Stipend Scholarship, the ANU HDR Supplementary Scholarship, and the Joan Duffield Research Award (2017-2019). I would also like to acknowledge the travel funding provided to me by ASTRO3D, the ANU Research School of Astronomy and Astrophysics, Professor Roberto Maiolino and Professor Ralf Klessen.

I first moved to Canberra almost eight years ago as an undergraduate studying the Bachelor of Philosophy, living in room A202 at Ursula Hall. Ursula Hall was my home for five years, where I met my first cat and some of my closest friends to this day. Those of you close to me know of the emotional struggles that I have experienced throughout the duration of my PhD. All of you picked me up and helped me during the toughest period of my life and my success is purely attributed to your belief in me. The ANU Jujutsu club and all of the seniors within, supported me (after throwing me into the ground) during my entire PhD. The experiences that I have had in Canberra have shaped me into who I am today and I now consider it my second home. There are too many people to thank in this short section, but I have listed a few significant people at the back of this thesis.

Finally, I would like to thank my family. To my Mum (Caroline), my Dad (Sujono) and my Sister (Sonia), I miss living at home in Melbourne with Odie and Max, but you have all supported me ever since I left for Canberra. You have looked after me in every possible way and I could not ask for a better family. Ever since I was small, you have let me pursue whatever I wanted. You encouraged me to do my best in everything I did and I hope I have made you proud. Hopefully one day, I can come back home.

Abstract

The gas-phase metallicity is one of the most fundamental properties of a galaxy. Measuring the gas-phase metallicity distribution allows us to gauge the age of the gas and hence how the galaxy has formed over time. By combining the gas-phase metallicity with galaxy evolution simulations, we can gain insight into dynamical processes which may have affected its formation process in the past.

In this thesis, we use spatially resolved spectra from the SAMI galaxy survey and TYPHOON survey to explore the gas-phase metallicity of galaxies as a function of stellar mass, environment and star-formation rate. We also investigate the systematic errors and reliability of measuring gas-phase metallicity through popular strong emission line diagnostics.

In the second chapter of this thesis, we present gas-phase metallicity and ionization parameter maps of 25 star-forming face-on spiral galaxies from the SAMI galaxy survey. We measure the metallicity gradients of each galaxy and find a weak mass dependence of the metallicity gradients ranging from -0.20 to -0.03 dex/Re. No significant trends were found in the ionization parameter distribution with the ionization parameter typically ranging between $7.0 < \log(q) < 7.8$. Ionization parameter variations of this magnitude may lead to systematic deviations of up to 0.3 dex when using the O3N2 metallicity diagnostic.

It is known that metallicity gradients are significantly flattened when undergoing merger activities. This is due to the mixing of gas through tidal forces as well as inflows of pristine gas. In the third chapter, we compare the metallicity gradients of galaxies in isolated environments to those in denser environments and find no significant trends with any of the three environment density metrics tested (fifth nearest neighbour, number of galaxies within a cylinder and the average Gaussian ellipsoid density parameter).

In the fourth chapter, we discuss the reliability of measuring gas-phase metallicity using strong emission line diagnostics and analyse the large systematic differences between them. Using 13 popular strong emission line diagnostics, we provide a method for converting metallicity gradients derived from different metallicity diagnostics, allowing for the comparison of metallicity gradients between different galaxy surveys and redshift ranges.

In the fifth chapter, we use the highly spatially-resolved TYPHOON data of M83 to explore the consequences of determining metallicity gradients from relatively low spatially-resolved data. We find that the emission of the diffuse ionized gas (DIG) significantly flattens metallicity gradients measured using the $R_{23}$and N2O2 metallicity diagnostics, has a small flattening effect on the N2Hα and O3N2 metallicity diagnostics and significantly steepens the N2S2Hα metallicity diagnostic at the kiloparsec resolution of typical multiplexing surveys.

The works within this thesis aim to inform the readers of the caveats and precautions that need to be taken when measuring the gas-phase metallicity. We hope that these articles provide an initial framework, off which improvements can be made to the way we measure and interpret the gas-phase metallicity distribution.

Contents

List of Figures

List of Tables

List of Publications

The articles listed below present research undertaken during the PhD candidature.

First Author

Poetrodjojo, H., Groves, B., Kewley, L. J., et al. 2018, *The SAMI Galaxy Survey: Spatially Resolved Metallicity and Ionization Mapping*, MNRAS, 479, 5235

Poetrodjojo, H., D'Agostino, J. J., Groves, B., Kewley, L. J., et al. 2018, *The Effects of Diffuse Ionized Gas and Spatial Resolution on Metallicity Gradients: TYPHOON Two-Dimensional Spectrophotometry of M83*, MNRAS, 487, 79

Poetrodjojo, H., Groves, B., Kewley, L. J., et al. (Accepted), *The SAMI Galaxy Survey: Reconciling Strong Emission Line Metallicity Diagnostics Using Metallicity Gradients* (Accepted by MNRAS)

Poetrodjojo, H., Groves, B., Kewley, L. J., et al. (In Preperation), *The SAMI Galaxy Survey: The Missing Environmental Dependence of Metallicity Gradients*

Co-Author

Ho, I., Seibert, M., **Poetrodjojo, H.**, et al. 2017, *The Chemical Evolution Carousel of Spiral Galaxies: Azimuthal Variations of Oxygen Abundance in NGC1365*, ApJ, 846, 39

D'Agostino, J. J., **Poetrodjojo, H.**, Ho, I., et al. 2018, *Starburst-AGN mixing: TYPHOON observations of NGC 1365, NGC 1068, and the effect of spatial resolution on the AGN fraction*, MNRAS, 479, 4907

Scott, N., van de Sande, Jesse., **Poetrodjojo, H.**, et al. 2018, *The SAMI Galaxy Survey: Data Release Two with absorption-line physics value-added products*, MNRAS, 481, 2299

CHAPTER 1

Introduction

1.1. Galaxy Formation

Galaxies are among the grandest and most spectacular structures in the observable universe. The first galaxies were formed when dark matter inhomogeneities caused clouds of primordial hydrogen and helium to collapse and form stars. Current galaxies build upon these early galaxies, and follow a similar process with sufficiently dense clouds of molecular gas undergoing gravitational collapse, forming the stars which emit the light we see today. We typically define galaxies as a gravitationally bound system of stars and gas, with galaxies coming in many different shapes and sizes. Galaxies typically range from thousands to hundreds of thousands of light-years in size.

In 1926, Hubble (1926) developed a classification system which categorised galaxies based on the appearance as either elliptical or spiral, each further divided into several sub-classes. Galaxies which lacked the defining features of either class are classified as irregular galaxies.

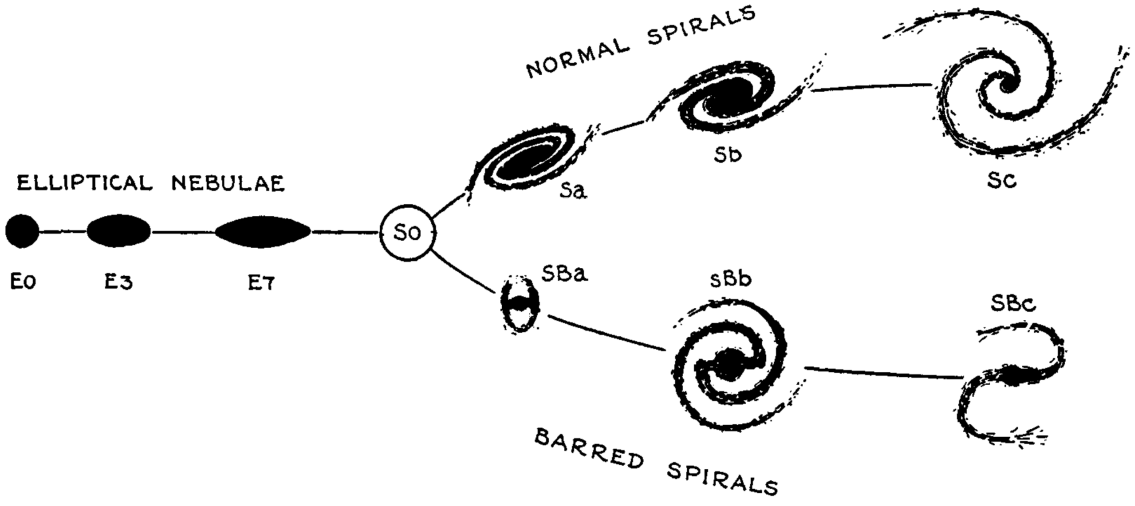

Figure 1.1 The Hubble tuning fork diagram by Hubble (1926). This galaxy morphology classification system was among the first of its time to systematically label galaxies based on their shape.

While the size of a galaxy typically depends on the length of time spent accumulating mass, the shape of a galaxy can be indicative of its formation history. It is speculated that the origin of elliptical galaxies are the remenants of major mergers (Toomre & Toomre 1972; Schweizer 1982). The organised structure of spiral galaxies is unlikely to survive the violent tidal forces induced by neighbouring galaxies during the merger process, leading to the spherical/elliptical structure.

1.1.1. Heavy Element Formation

When stars are first formed from the gravitational collapse of Hydrogen gas clouds, the heat and pressure in the core of the newborn star begins the process of stellar nucleosynthesis. Initially only Helium is produced through the fusion of Hydrogen, but as the heat and pressure builds, heavier elements such as Carbon, Oxygen and Silicon are produced through the alpha and triple-alpha process (Salpeter 1952; Hoyle 1954; Oberhummer et al. 2000). The elements produced through the alpha and triple-alpha process are collectively known as the alpha (α) elements. Supergiant stars are some of the most massive and luminous stars that exist. These supergiants are able to continue the nuclear fusing process to form dense iron cores. Due to the iron peak, a local maximum of nuclear binding energy per nucleon, typical stellar nucleosynthesis does not produce elements heavier than iron (Burbidge et al. 1957). All the heavier elements that we see naturally occurring in the universe are typically produced during supernovae, where the high-energy explosion is sufficient to continue the nuclear fusion process to elements heavier than iron.

The heavy elements produced during stellar nucleosynthesis are transferred to the surrounding gas through stellar winds and supernovae. This enriched gas is then used to form the next generation of stars, making each subsequent generation more metal-rich. This cycle of gas being recycled to form the next generation of stars gradually increases the total amount of heavy elements present in both the stars and interstellar medium (ISM). This means that the heavy element content of the gas, commonly referred to as gas-phase metallicity, provides a strong indicator of the age of the gas (Gallazzi et al. 2005). By measuring the gas-phase metallicity of the gas, we are able to place strong constraints on the formation history of the galaxy, allowing us to study how galaxies form under different environmental conditions.

1.2. Spectroscopy

The electromagnetic spectrum of light is dictated by the physical processes of emitting and absorbing light. One of the most important features of the electromagnetic spectrum are the emission and absoption lines. Electrons of an atom can be excited to a higher energy level through a number of excitation mechanisms (e.g. collisionally excited). When an electron in an excited energy state reverts back to a lower energy state, the excess energy is released in the form of light. The amount of energy released depends on the nuclear structure of the atom and the particular energy levels the electron is transitioning from and to. This means that each element and ion produces a unique emission line spectrum, commonly referred to as a spectral fingerprint.

Spectroscopy is the technique of measuring radiation intensity as a function of wavelength. In practice, this involves using a prism (refraction) or a grating (diffraction) to disperse the light along the wavelength dimension. Spectroscopy is used extensively in astronomy to analyse the spectral properties of light emitted from active galactic nuclei (AGN), stars and galaxies.

By using emission line spectroscopy, we can easily identify which elements are present in the ISM of the galaxy by simply looking for their unique emission lines. Therefore, spectroscopy provides a useful tool in measuring the gas-phase metallicity. Unfortunately, the concentration of the element in the ISM can not simply be inferred from the strength of the emission lines. The strength of emission lines can be significantly affected by the ionizing strength and radiation pressure of the ISM. To reliably use emission lines to measure gas-phase metallicity, they first must be calibrated with data of known emission line strength and metallicity.

1.2.1. Emission Line Fitting

Figure 1.2 shows the optical emission line spectrum of NGC 3998 separated into its gas and stellar emission components. Often an emission line spectrum has many superimposed components, leading to complicated emission line shapes. This makes the process of extracting the emission line fluxes difficult and sometimes requires manual fitting.

Generally, the first step in fitting an emission line spectrum is the subtraction of the underlying stellar continuum. The stellar continuum is the light produced by the stars in the galaxy and is generally removed using stellar population models (Bruzual & Charlot 2003; Vazdekis et al. 2012). The emission lines produced by the gas are first masked out, then the remaining spectrum is modelled by combining stellar population models of different ages using the Penalized Pixel-Fitting (e.g. pPXF Cappellari 2017) routine. The Penalized Pixel-Fitting method is a technique in which the complexity of a model is adjusted based on the relative strength of the spectrum to its uncertainty. For high signal to noise (S/N) spectral pixels (spaxels), we can reliably fit subtle features to the spectrum, while for low S/N spaxels, the subtle features could simply be a result of noisy data. As the S/N of a spaxel decreases, the Penalized Pixel-Fitting method will tend towards less complex fits where minute features are not as important as the overall shape of the specturm. This allows us to fit the finer details of the spectrum when we have a high S/N, but ensures we do not overfit the data when a significant amount of noise is present. Figure 1.2 shows the process of subtracting the underlying continuum.

Emission line fitting is typically done by assuming a Gaussian shape and adjusting the Gaussian parameters to fit the height, width (velocity dispersion) and wavelength offset (gas velocity). As we integrate the galaxy light along our line of sight, we may be including light from multiple gas components with different velocities and velocity dispersions. With multiple Gaussian components superimposed on each other, the difficulty of fitting each emission line is significantly increased. Figure 1.3 demonstrates the complexity of fitting overlapping emission lines with multiple Gaussian components. The top row of Figure 1.3 shows an example of a 3-component fit, with each emission line best fit with two narrow Gaussians with an underlying broad component. The origin of these independent kinematic

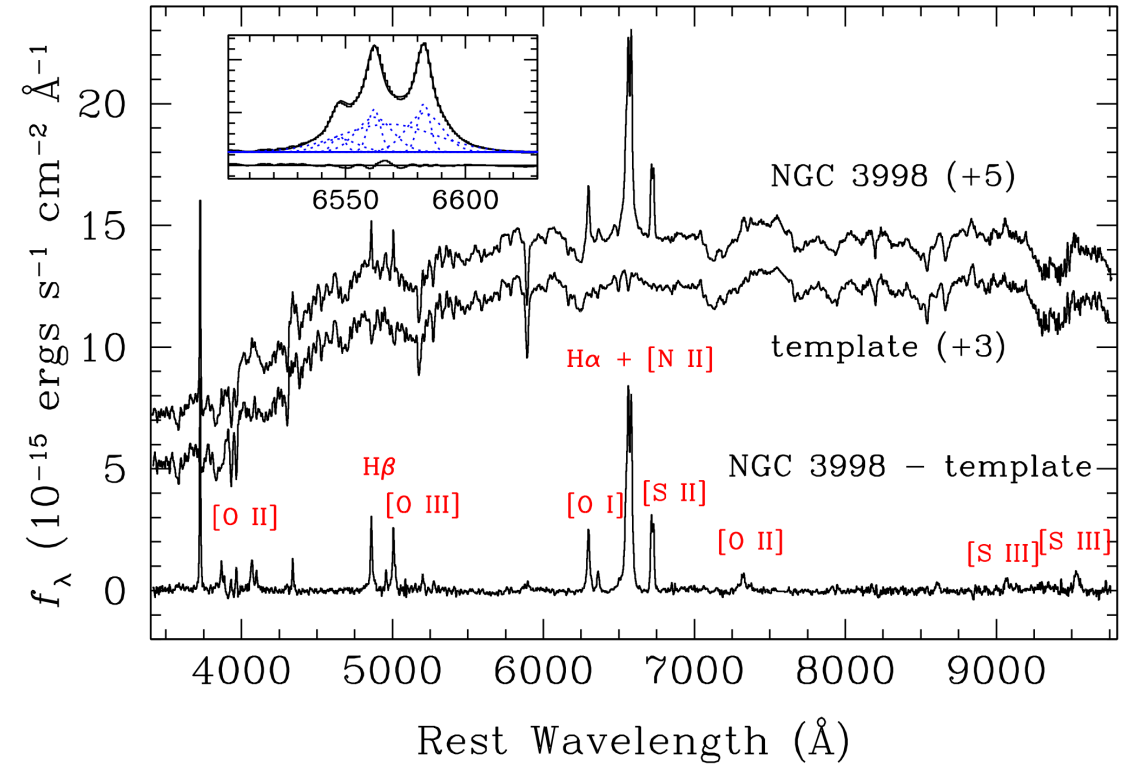

Figure 1.2 Emission line spectrum of NGC 3998 by Ho et al. (1993). In this Figure, the top spectrum shows the observed emission line spectrum from NGC 3998. The modelled stellar continuum is shown in the middle and is subtracted from the raw spectrum, leaving the gas emission line spectrum at the bottom with common strong emission lines labelled.

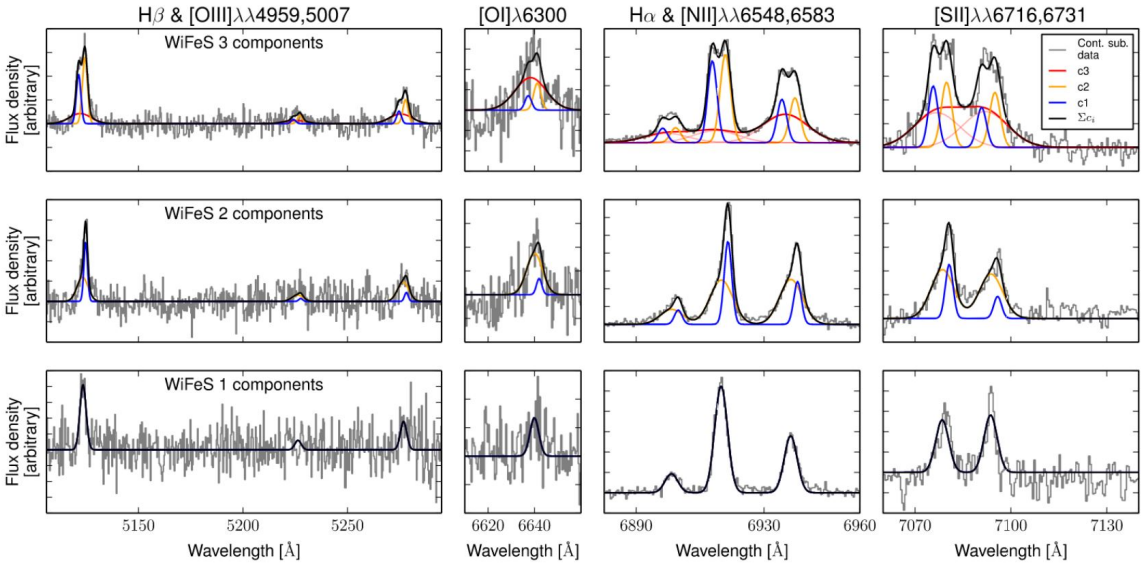

Figure 1.3 Figure from Ho et al. (2014) showing examples of spectra best fit by 1,2 and 3 Gaussian components. These spectra were obtained from galaxies with known AGN and shocks.

components is likely due to the line of sight containing emission from shocks and active galactic nuclei (AGN).

1.3. Measuring Gas-Phase Metallicity

Oxygen is the most abundant element by mass other than hydrogen or helium within the interstellar medium, and is used as a proxy for the total metal content. The total metal content is often not as important as the metal concentration, therefore the oxygen content is normalised by the total hydrogen content. The gas-phase metallicity is typically given as 12+log(O/H), given its low relative abundance to H.

1.3.1. Electron Temperature

As these strong emission lines are collisionally excited, the abundance of the emitting ion can be determined directly if the electron temperature is known. In particular, measuring the electron temperature through the [OIII]λ4363 and λ5007 emission lines provides a very reliable diagnostic for the abundance of the O^{+2} ion, and thus metallicity (Osterbrock 1989; Dopita & Sutherland 2003; Draine 2011).

This method of determining gas-phase metallicity, commonly called the direct method, is widely considered to be the most reliable method for measuring metallicity. However the weakness of the direct method lies in the relative faintness of the [OIII]λ4363 and other temperature sensitive emission lines. Metals are one of the main coolants of galaxies and thus at high metallicities, the [OIII]λ4363 emission line becomes extremely difficult to detect. Because of these weaknesses, metallicity diagnostics involving strong emission lines (SEL) have become more widely adopted for their flexibility.

1.3.2. Strong Emission Line Diagnostics

Strong emission line diagnostics are metal-sensitive emission line ratios which as the name suggests, use strong emission lines such as [OII]λ3726, λ3729, H$\beta\lambda$4861, [OIII]λ5007, H$\alpha\lambda$6563, [NII]λ6583 and [SII]λ6717, λ6731 instead of relying on the [OIII]λ4363 emission line. SEL diagnostics first need to be calibrated using theoretical photoionization models (Kewley & Dopita 2002; Kobulnicky & Kewley 2004; Dopita et al. 2016; Thomas et al. 2018), empirical calibrations based on the direct temperature method (Pilyugin 2001; Pilyugin & Grebel 2016; Pettini & Pagel 2004; Ho 2019), or a combination of both (Denicoló et al. 2002). A simple polynomial mapping of metal-sensitive emission line ratios to the gas-phase metallicity is usually done to create the metallicity calibration. In recent years, more complex methods of creating metallicity calibrations involve the use of Bayesian inference (Blanc et al. 2015; Thomas et al. 2018) or neutral network machine learning (Ho 2019; Wu & Boada 2019).

With metallicity being such a fundamental property of a galaxy, many different metallicity diagnostics have been discovered to allow for its measurement for a large subset of emission line combinations. The most common metallicity diagnostics include [NII]/Hα (N2Hα Pettini & Pagel 2004; Marino et al. 2013), ([OIII]/Hβ)/([NII]/Hα) (O3N2 Pettini & Pagel 2004; Marino et al. 2013), [NII]/[OII] (N2O2 Kewley & Dopita 2002) and ([OII]+[OIII])/Hβ (R_{23} Kobulnicky & Kewley 2004; Tremonti et al. 2004). Each metallicity diagnostic has their own advantages and disadvantages, and selecting which one to use depends entirely on the

circumstances. For example, if the variation of ionization parameter is of concern, using the N2O2 metallicity diagnostic is ideal. The N2O2 diagnostic is largely invariant with the ionization parameter, especially at metallicites above half solar (Kewley & Dopita 2002). However, the wide wavelength separation between the [OII] and [NII] emission lines, make its wide spread application difficult. Observations with very narrow spectral ranges can use a metallicity diagnostic such as N2Hα, where the wavelength separation between emission lines is small and dust extinction is negligible. However, the N2Hα suffers from a significant dependence on ionization parameter and is sensitive to contamination by the diffuse ionized gas (Zhang et al. 2017).

Figure 1.4 shows an example of a metallicity calibration using the ([OII]+[OIII])/Hβ (R_{23}) emission line ratio. R_{23}provides an excellent measure of the oxygen abundance through the direct use of oxygen emission lines. The [OII] and [OIII] emission lines capture the majority of the element which is then normalized by the hydrogen content using the Hβ emission line. The R_{23}emission line ratio presents two significant problems which prevent it from being widely used in metallicity studies. The first problem is its double valued nature, causing ambiguity in the metallicity for a range of R_{23}ratios. This degeneracy must be broken with other metal-sensitive emission line ratios, in the case of Kobulnicky & Kewley (2004), [NII]/[OII] is used to split the upper and lower metallicity branches. The second issue with the R_{23}diagnostic is the effect of the ionization parameter, shown as the different coloured lines on Figure 1.4. The ionization parameter is a measure of the ionization state of the gas and has a significant effect on line ratios where the emission lines have different ionization potentials. R_{23}, N2Hα and O3N2 are common metallicity diagnostics which are heavily affected by the ionization parameter.

One of the main issues plaguing SEL diagnostics is the significant discrepancies that exist between different diagnostics. Despite all metallicity diagnostics aiming to measure the same quantity (O/H), discrepancies of 0.6 dex exist between diagnostics calibrated through the direct temperature method and those calibrated with photoionization models (Yin et al. 2007). Figure 1.5 shows the different mass metallicity relations for 10 metallicity diagnostics and calibrations. This means that reliable comparisons of gas-phase metallicity between galaxies can only be done when the same metallicity diagnostic is used. This provides significant barriers to comparing the gas-phase metallicity distributions of low and high redshift galaxies where it becomes extremely difficult to obtain overlapping spectra with the same emission lines present in both redshift ranges.

1.3.3. Emission Line Contamination

The vast majority of SEL metallicity diagnostics rely on the assumption that emission lines are produced solely from star-forming HII regions. In an era where galaxy surveys are realistically able to observe tens of thousands of galaxies in only a few years, spatial resolution is often a trade-off to allow the observation of multiple galaxies per pointing (multi-object integral field spectroscopy). HII regions generally range from tens to hundreds of parsecs (Azimlu et al. 2011; Gutiérrez et al. 2011; Whitmore et al. 2011), while current multi-object integral field unit surveys have spatial resolutions on the scale of kiloparsecs. This means that the light from each spaxel is likely a combination of emission from HII

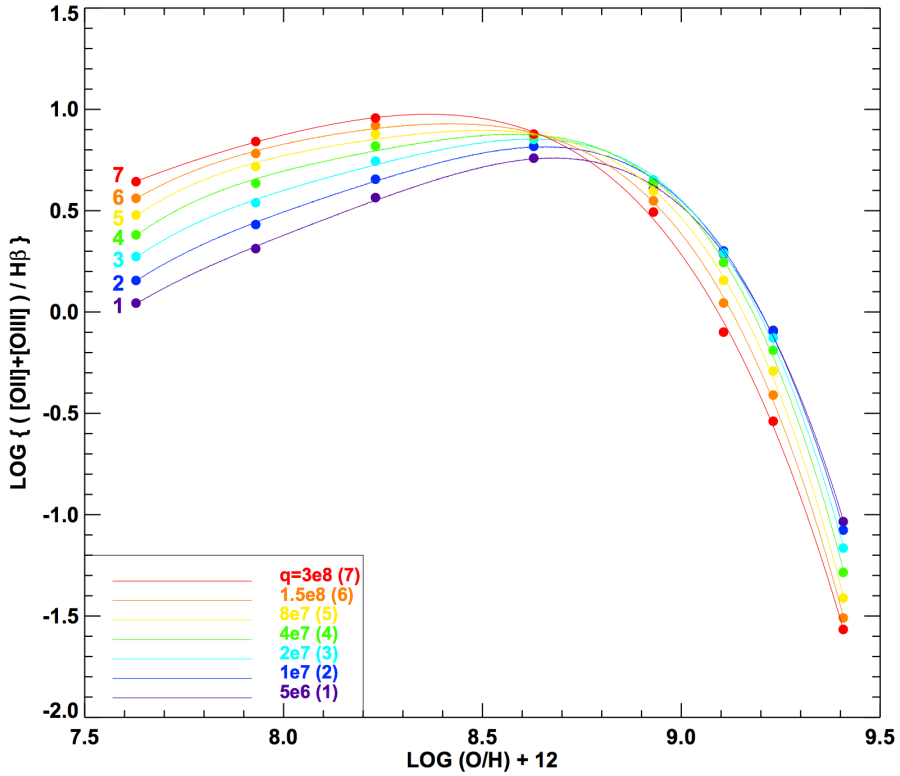

Figure 1.4 The R_{23} metallicity calibration by Kewley & Dopita (2002). The R_{23} metallicity calibration demonstrates both complexities in its double valued nature and its heavy dependence on the ionization parameter.

regions and contaminating ionization sources such as the diffuse ionized gas (DIG), active galactic nuclei (AGN) or shocks.

The contamination by the DIG is perhaps the most difficult to account for due to its presence in non-AGN galaxies as well as its prevalence throughout the entire galactic disk including above and below the galactic plane (Reynolds 1984; Hoopes et al. 1999; Rossa & Dettmar 2003). The total fraction of Hα luminosity originating from the DIG ranges between 0.3 and 0.7 (Haffner et al. 2009), demonstrating its significant contribution to the emission line spectrum. Oey et al. (2007) demonstrated that there was an anti-correlation between the DIG Hα surface brightness fraction and the overall Hα surface brightness. A mean fraction of 0.59 ± 0.19 of Hα flux originating from the DIG was found for starburst galaxies in the Survey for Ionization in Neutral Gas Galaxies (SINGG Meurer et al. 2006) sample. Figure 1.6 shows that galaxies with an overall higher Hα surface brightness tend to be less dominated by the DIG.

Although diagnostics have been recently been developed to measure the metallicity of the DIG (Kumari et al. 2019; Vale Asari et al. 2019), these still require high spatial resolution scales and a clean separation between the HII regions and the DIG.

1.3.4. Correcting for Contamination

In order to reduce the effects of foreign ionizing sources, several techniques have been developed to isolate the emission from HII regions. These techniques commonly involve using the Hα surface brightness profile or certain emission line ratios.

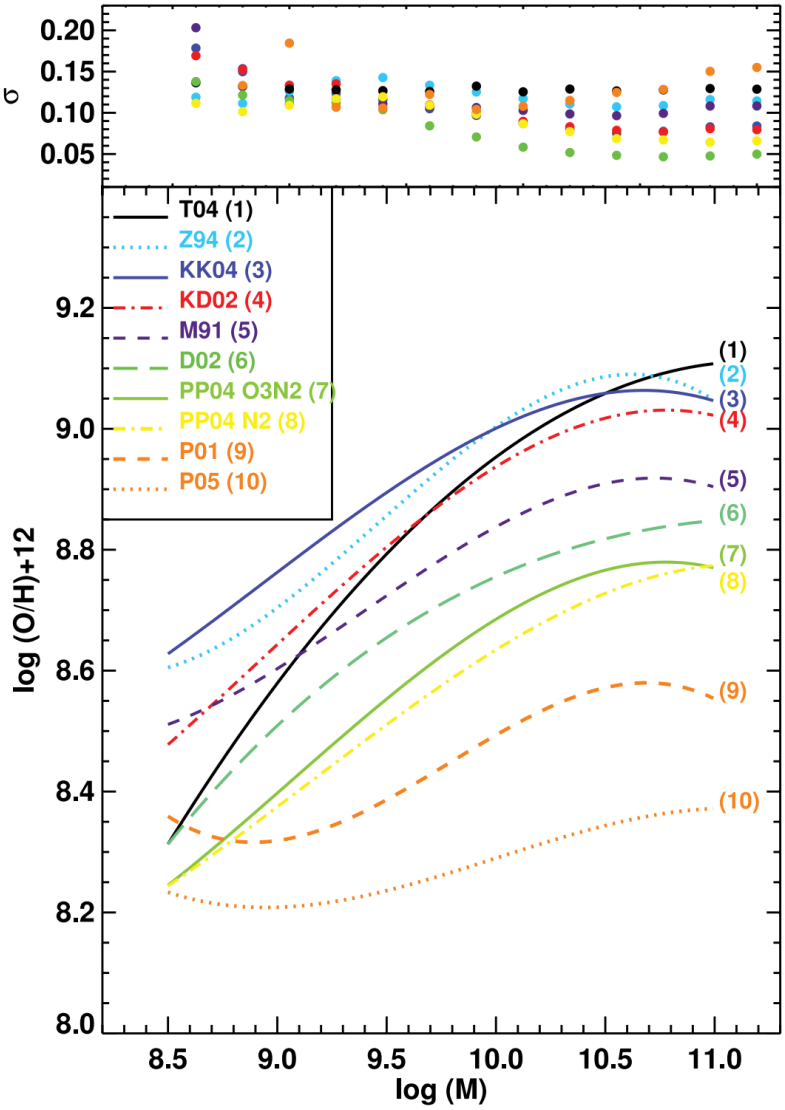

Figure 1.5 Mass-Metallicity relation using 10 different metallicity diagnostics and calibrations by Kewley & Ellison (2008). Differences in absolute scale as well as shape of the Mass-Metallicity relation show the stark differences between diagnostics.

HIIphot is an IDL based program designed to identify HII regions for highly spatially resolved data (Thilker et al. 2000). Using the Hα surface brightness profile, HIIphot first identifies local maxima which are labelled as 'seeds'. These seeds are then iteratively grown until they reach a user-specified termination condition. The Hα surface brightness radial profiles have sharp drop-offs in surface brightness at the boundaries of the HII regions. Therefore, a termination condition which can detect this drop-off, can be used to stop the iterative growing when they reach the HII region boundaries. HIIphot achieves this by monitoring the Hα surface brightness radial gradient and when this gradient steepens beyond the user-specified limit, the boundary is drawn. Figure 1.7 shows the HII regions defined by HIIphot of NGC 1365 observed by the TYPHOON survey with a spatial resolution of 169 parsecs.

The main drawback of HIIphot is its dependence on the user-specified inputs. By adjusting the seed threshold, sky-noise baseline or termination gradient, the overall size and number of detected HII regions can significantly vary. Since the user has the ability to modify these

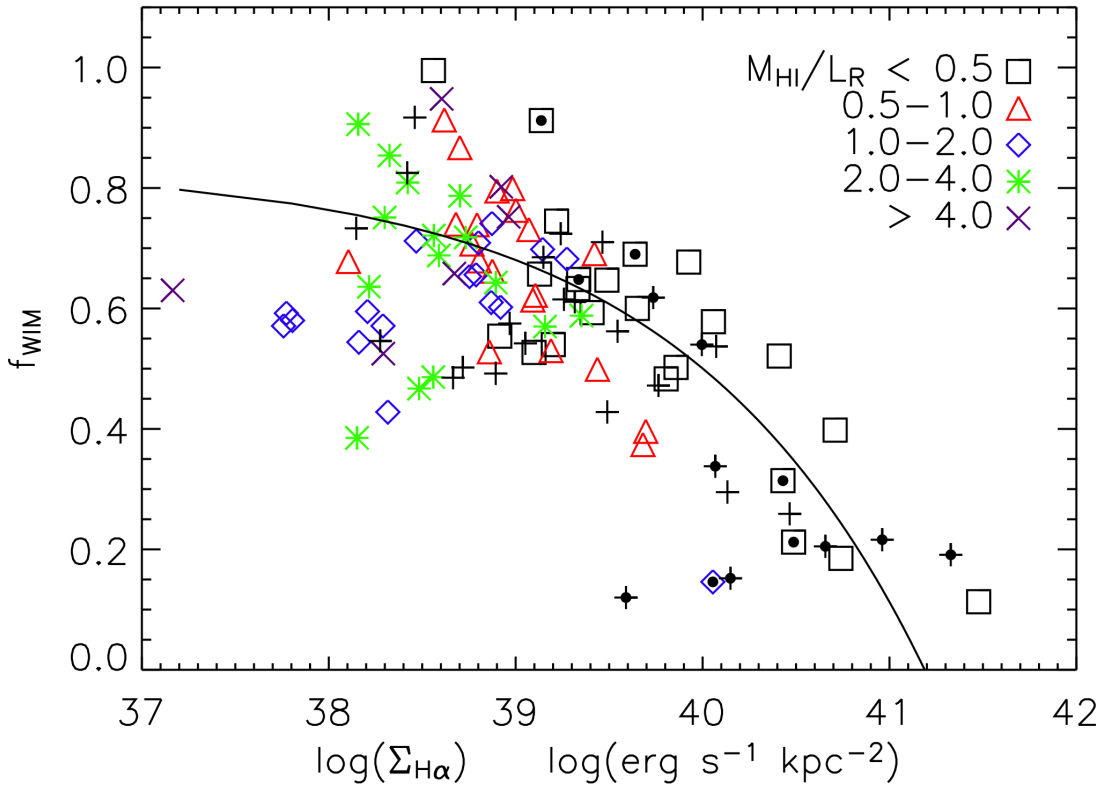

Figure 1.6 Figure from Oey et al. (2007) showing the anti-correlation between total DIG flux fraction and overall Hα surface brightness.

parameters, the HII regions defined by HIIPHOT can simply be adjusted until they satisfy what the user wants or expects the HII regions to look like. This subjectivity makes this method less than ideal, but at least provides some form of HII region isolation.

Certain emission line ratios such as [OI]/Hα, [NII]/Hα and [SII]/Hα are known to be significantly enhanced in the DIG relative to HII regions (Hoopes & Walterbos 2003; Madsen et al. 2006; Voges & Walterbos 2006; Zhang et al. 2017). Observations of the DIG in the Milky Way reveal an average [NII]/Hα=0.83 and [SII]/Hα=0.38 in the DIG, compared to [NII]/Hα=0.23 and [SII]/Hα=0.12 for HII regions (Madsen et al. 2006).

A method first developed by Blanc et al. (2009) and later expanded by Kaplan et al. (2016), allows us to predict the fraction of flux originating from the HII regions and seperate it from the DIG. The method involves determining a characteristic [SII]/Hα ratio of the HII regions and DIG by calculating the average [SII]/Hα of the brightest (based on the Hα surface brightness) 100 spaxels and dimmest 100 spaxels respectively. An assumption is then used where the [SII]/Hα of any spaxel, is a linear combination of these characteristic values. Based on this, we can determine the percentage of Hα flux originating from the HII regions and the DIG for any spaxel. Separating each spaxel into their individual contributions from HII regions and DIG, allows us to extract only the HII region portion of flux from the galaxy.

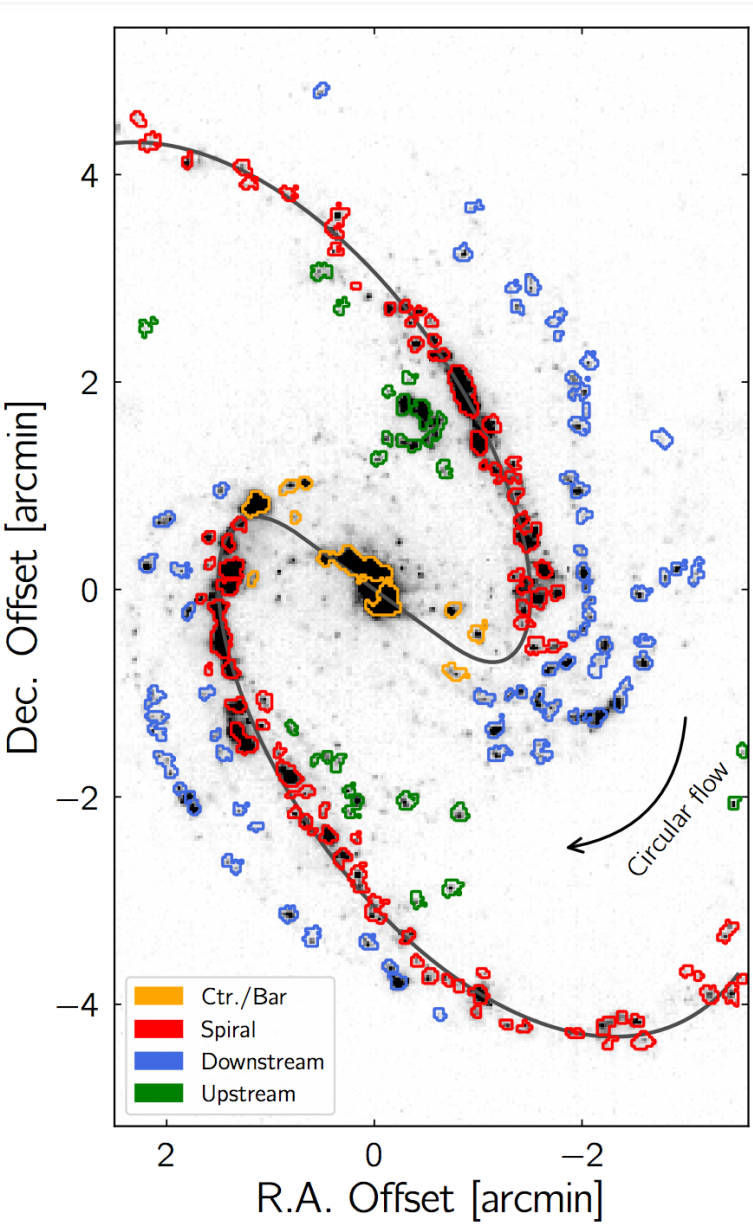

Figure 1.7 HII regions determined by HIIPHOT of NGC 1365 by Ho et al. (2017)

1.4. Metallicity Distribution in Galaxies

One of the most fundamental metallicity correlations is the mass-metallicity relation, which shows an increasing metallicity content of galaxies with greater mass. Tremonti et al. (2004) demonstrated the mass-metallicity relation using $\sim 53,400$ galaxies from the Sloan Digital Sky Survey (SDSS). Using Bayesian metallicity estimates outlined in Charlot & Longhetti (2001), Tremonti et al. (2004) found that the aperture gas-phase metallicity ranged from $8.4<12+\log(O/H)<9.1$ for galaxies between $8.5<\log(M/M_{\odot})<11.5$ as seen in Figure 1.8. We can understand this intuitively by referring back to how heavy elements are formed in the first place. For a galaxy to grow in size, it must slowly accumulate gas over a significant timeframe. The long timeframe allows the stellar nucleosynthesis cycle to repeat many times, with each cycle gradually enriching the gas. This means that massive old galaxies

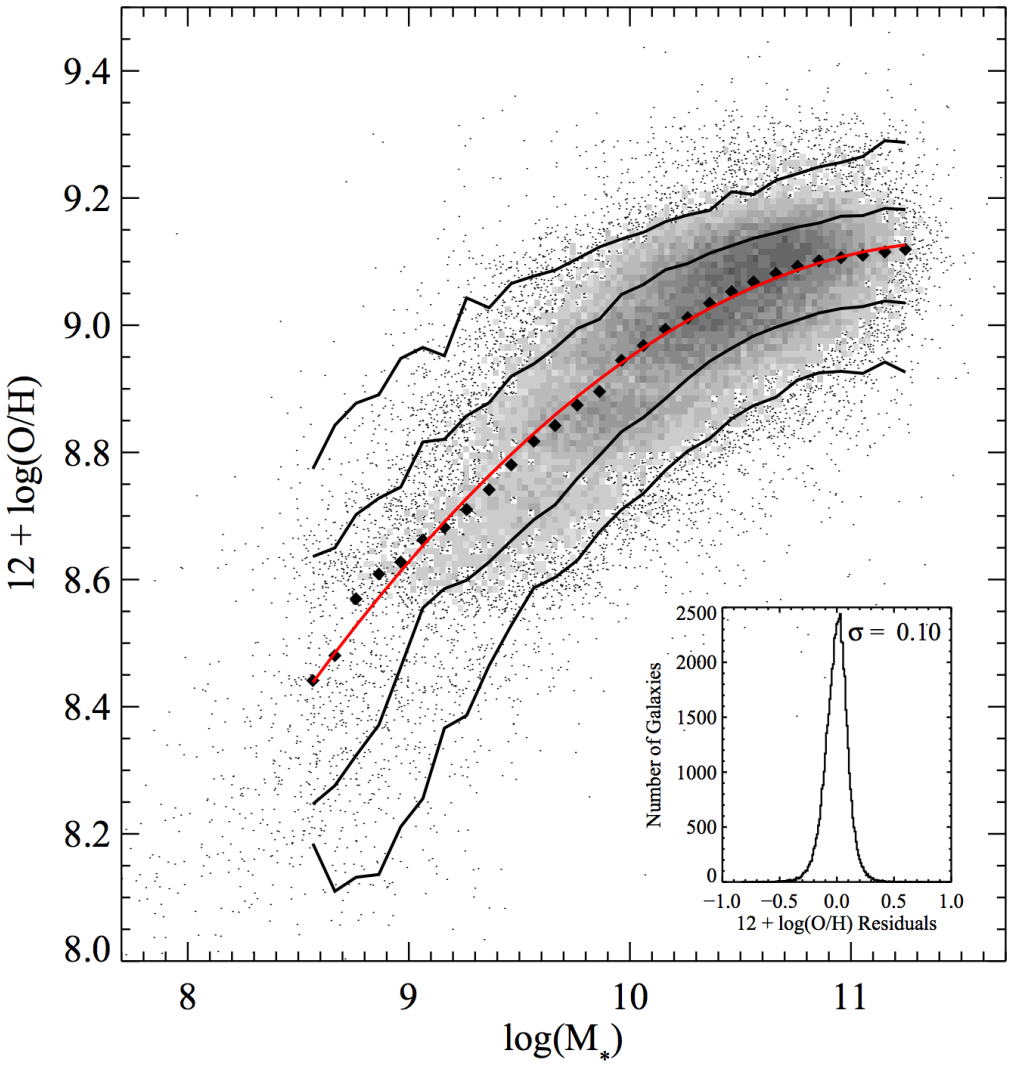

Figure 1.8 Mass-metallicity relation demonstrated by Tremonti et al. (2004) using ~ 53,400 SDSS galaxies.

tend to have higher gas-phase metallicities, leading to the mass-metallicity relation.

SDSS uses 3'' circular fibres to obtain aperture spectra of galaxies, meaning that a single spectrum is obtained per galaxy. In the past, to obtain spatially resolved spectra, multiple apertures were placed on the face of nearby galaxies to get an understanding of the spatial distribution of metallicity (e.g. Bresolin et al. 2005). In recent times, technological advances have enabled us to greatly increase the fibre density, allowing for extremely detailed views of the metallicity distribution.

In the last few years, integral field unit (IFU) spectroscopy has become the preferred method of obtaining spatially resolved spectra of galaxies. Major recent IFU galaxy surveys include the Calar Alto Legacy Integral Field Area (CALIFA) survey (Sánchez et al. 2012), the Sydney-AAO Multi-Object Integral-Field (SAMI) Galaxy Survey (Bryant et al. 2015) and the Mapping Nearby Galaxies at Apache Point Observatory (MaNGA) survey (Bundy et al. 2015). Each of these surveys utilise densely packed fibre bundles to spatially resolve the emission line spectrum of galaxies. The aim of all these surveys is to provide statistically significant samples of spatially resolved spectra.

1.4.1. Metallicity Gradients

With the introduction of IFU spectroscopy, obtaining spatially resolved spectra of galaxies has become significantly easier and measuring the gas-phase metallicity has transitioned from global and aperture metallicites to metallicity gradients. It has long been known that isolated galaxies tended to have negative metallicity gradients (Zaritsky et al. 1994; Moustakas et al. 2010; Rupke et al. 2010; Sánchez et al. 2014). However, the evolutionary history of a galaxy can have significant effects on the metallicity distribution of a galaxy. Kewley et al. (2010) showed that close pair galaxies had significantly shallowed metallicity gradients than their isolated counterparts. It is predicted that the tidal disruptions from the gravitational interactions causes pristine gas to flow and dilute the metal-rich centres, and hence flattening the metallicity gradient.

It is clear from this example that the metallicity gradient provides an insight into the evolutionary history of galaxies. Measuring not only the metallicity gradients of galaxies, but the azimuthal variations in different environments will allow us to decipher how the surrounding environment impacts the growth and evolution of galaxies. Using large IFU datasets, we can begin to isolate the individual variables which affect the formation of metallicity gradients, such as stellar mass, star-formation rate and environment. This splitting of the dataset and binning of galaxies is only possible with the thousands of spatial resolved spectra provided by IFU surveys.

Using the CALIFA survey, Sánchez-Menguiano et al. (2016b) used ~ 122 face-on spiral galaxies to analyse the spatial distribution of metallicity. Using the O3N2 metallicity diagnostic calibrated by Marino et al. (2013), they found that the metallicity gradients of galaxies appeared to be largely invariant of the stellar mass after normalizing the gradients by the effective radii (R_e). Figure 1.9 shows that between $0.5R_e$ and $1.5R_e$, the radial metallicity gradients are extremely similar between the 4 stellar mass bins.

Belfiore et al. (2017) performed a similar analysis using 550 galaxies from the MaNGA survey. Using the O3N2 metallicity diagnostic calibrated by Pettini & Pagel (2004), they found that metallicity gradients did in fact evolve with mass. Figure 1.10 shows that galaxies between $9.0 < \log(M/M_\odot) < 10.5$ had steeper metallicity gradients for galaxies with a greater stellar mass. For galaxies $\log(M/M_\odot) > 10.5$, metallicity gradients became shallower and tended towards a flat gradient. This result appears to directly contradict those found by Sánchez-Menguiano et al. (2016b). The difference between these two studies is the greater mass range of Belfiore et al. (2017). While Sánchez-Menguiano et al. (2016b) has a lower mass bin of $\log(M/M_\odot) < 10.2$, Belfiore et al. (2017) probes the metallicity gradients of galaxies with $\log(M/M_\odot) < 9.0$. Figure 1.10 shows that the correlation between metallicity gradient and stellar mass is largely driven by the low-mass end. Above $\log(M/M_\odot) > 10.2$ (mass range of Sánchez-Menguiano et al. (2016b)), very little evolution in the metallicity gradient is seen with stellar mass.

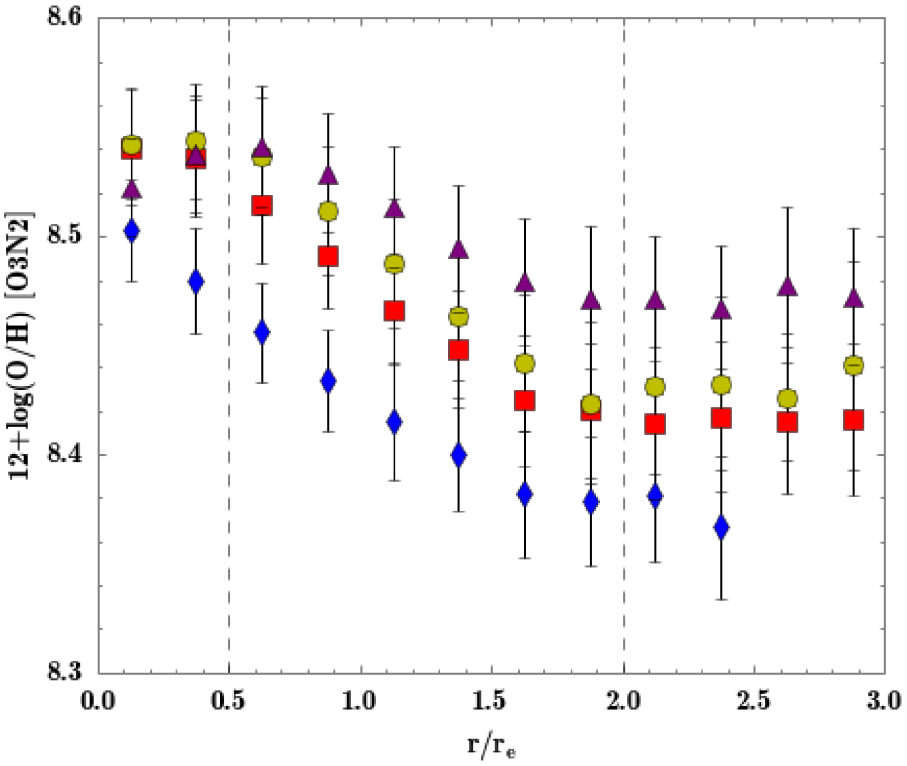

Figure 1.9 Figure from Sánchez-Menguiano et al. (2016b) showing similar metallicity gradients across a range of stellar mass ranges. $\log(M/M_\odot) \leq 10.2$, blue diamonds; $10.2 \geq \log(M/M_\odot) \leq 10.5$, red squares; $10.5 \geq \log(M/M_\odot) \leq 10.75$, yellow dots; $\log(M/M_\odot) \geq 10.75$, purple triangles.

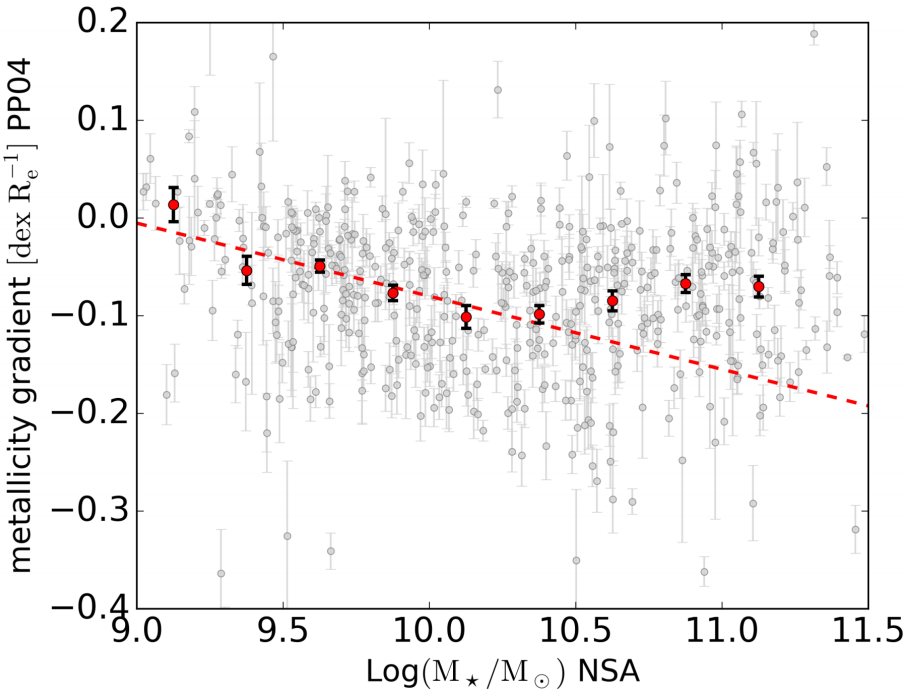

Figure 1.10 Metallicity gradients as a function of stellar mass by Belfiore et al. (2017) using the MaNGA survey. A clear trend is seen with steepening metallicity gradients with increasing mass, with the trend appearing to reverse at about $\log(M/M_\odot) > 10.5$

1.5. Thesis Overview

This thesis attempts to provide a thorough and systematic exploration into the study of galactocentric radial gas-phase metallicity gradients within galaxies. The following four chapters each represents a publication completed during the Doctor of Philosophy candidature. A brief outline of each article is as follows:

- Chapter 2 presents gas-phase metallicity and ionization parameter maps of 25 face-on star-forming galaxies from the SAMI Galaxy Survey. A key result from this article was the creation of spatial resolved maps of ionization parameter, a significant parameter in many metallicity diagnostics.
- Chapter 3 attempts to quantify the relationship between metallicity gradients and the surrounding environment. Using environmental metrics from GAMA, we attempt to link the negative metallicity gradients of isolated galaxies and flat metallicity gradients of merging galaxies in a continous manner.
- Chapter 4 extends on the work of Kewley & Ellison (2008) by investigating the discrepencies between strong emission line metallicity diagnostics. We do this by comparing the metallicity gradients of SAMI galaxies derived using different metallicity diagnostics. The conversion fits provided in this article are extremely useful for comparing metallicity gradients of low and high redshift galaxies, where obtaining common sets of emission lines is difficult.
- Chapter 5 uses high spatial resolution data from the TYPHOON survey to systematically explore the effects of diffuse ionized gas on metallicity gradients. This article focuses on the implications of measuring metallicity gradients at the kiloparsec resolution scales of modern IFU galaxy surveys.
- Chapter 6 provides a brief summary of all the major results explored in this thesis, reiterating their importance and significant impact on the measurement of metallicity gradients. We address the questions naturally raised through the discussion of novel ideas and outline the path forward for future research using larger and more advanced datasets.

CHAPTER 2

Spatially Resolved Metallicity and Ionization Mapping

This chapter presents the content of the article: The SAMI Galaxy Survey: Spatially Resolved Metallicity and Ionization Mapping. This article was published in the Monthly Notices of the Royal Astronomical Society, Volume 479, Issue 4, p.5235. The abstract of this chapter is as follows:

We present gas-phase metallicity and ionization parameter maps of 25 star-forming face-on spiral galaxies from the SAMI Galaxy Survey Data Release 1. Self-consistent metallicity and ionization parameter maps are calculated simultaneously through an iterative process to account for the interdependence of the strong emission line diagnostics involving ([OII]+[OIII])/Hβ (R_{23}) and [OIII]/[OII] (O32). The maps are created on a spaxel-by-spaxel basis because HII regions are not resolved at the SAMI spatial resolution. We combine the SAMI data with stellar mass, star formation rate (SFR), effective radius (R_e), ellipticity, and position angles (PA) from the GAMA survey to analyze their relation to the metallicity and ionization parameter. We find a weak trend of steepening metallicity gradient with galaxy stellar mass, with values ranging from -0.03 to -0.20 dex/R_e. Only two galaxies show radial gradients in ionization parameter. We find that the ionization parameter has no significant correlation with either SFR, sSFR (specific star formation rate), or metallicity. For several individual galaxies we find structure in the ionization parameter maps suggestive of spiral arm features. We find a typical ionization parameter range of $7.0 < \log(q) < 7.8$ for our galaxy sample with no significant overall structure. An ionization parameter range of this magnitude is large enough to caution the use of metallicity diagnostics which have not considered the effects of a varying ionization parameter distribution.

2.1. Introduction

The accurate measurement of gas-phase metallicity and ionization parameter in galaxies is becoming increasingly essential as we probe deeper into the universe and observe galaxies at high redshift. The gas-phase metallicity is strongly affected by processes that occur during the evolution of galaxies such as gas inflows, galaxy mergers, and galactic winds. Because

of this connection, the distribution of the metallicity in galaxies provides a strong constraint on their growth and formation and recent dynamical processes.

Simulations by Pilkington et al. (2012) show that a negative gas-phase metallicity gradient provides strong evidence for inside-out disc formation (Matteucci & Francois 1989; Boissier & Prantzos 1999). In this model, a negative metallicity gradient implies that the central metal-rich gas has been forming stars for longer than the metal poor outskirts.

Local disk galaxies typically have a negative metallicity gradient (Zaritsky et al. 1994; Moustakas et al. 2010; Rupke et al. 2010; Sánchez et al. 2014). A dependence on morphology was observed by Vila-Costas & Edmunds (1992); Zaritsky et al. (1994); Martin & Roy (1994), in that barred galaxies have shallower metallicity gradients than unbarred galaxies.

Large-scale gas inflows can disrupt metallicity gradients. Kewley et al. (2010) showed that the metallicity gradients of close pair galaxies are significantly shallower than those of isolated galaxies. Tidal disruptions from galaxy interactions drive pristine gas from the outskirts into the central regions, diluting the metal-rich centre. López-Sánchez et al. (2015) showed that one of the spiral arms belonging to NGC 1512 had a flattened metallicity gradient due to its interaction with nearby dwarf galaxy NGC 1510. Sánchez et al. (2014) also found significantly flatter metallicity gradients in galaxies that show signs of merger activity.

With advances in integral field spectroscopy (IFS), we can now spatially map the metallicity across galaxies, allowing for a deeper insight into azimuthal and radial variations within a galaxy. Several small scale surveys such as PPAK IFS Nearby Galaxies Survey (PINGS) (Rosales-Ortega et al. 2010), the VIRUS-P Investigation of the Extreme Environments of Starbursts (VIXENS) (Heiderman et al. 2011) and the VIRUS-P Exploration of Nearby Galaxies (VENGA) (Blanc et al. 2013; Kaplan et al. 2016) have been conducted. The first large survey was the Spectrographic Areal Unit for Research on Optical Nebulae (SAURON) survey (de Zeeuw et al. 2002), which initially observed 72 low redshift early-type galaxies (ETG) using IFS technology, and was later continued into the ATLAS^{3D} survey (Cappellari et al. 2011), observing 260 galaxies at $z < 0.01$.

The Calar Alto Legacy Integral Field Area Survey (CALIFA) survey (Sánchez et al. 2012) consists of 600 galaxies with $z < 0.03$. Sánchez et al. (2014) used ~306 CALIFA galaxies to analyse the oxygen abundance gradients in galaxy disks and found that all undisturbed galaxies with a disk presented similar radial metallicity gradients when normalised to the size of the disk. They showed that the existence of a characteristic metallicity gradient is independent of luminosity, mass and morphology when normalised to the size of the disk.

Similar results were obtained by Sánchez et al. (2012) using PINGS data and Ho et al. (2015); Sánchez-Menguiano et al. (2016b) who both used CALIFA data for their analysis. This contradicts the findings of Vila-Costas & Edmunds (1992); Zaritsky et al. (1994); Martin & Roy (1994) who found a clear variation in metallicity gradient between barred and unbarred galaxies. These differences could be due to earlier studies using a smaller sample size (Ho et al. 2015) or inconsistent methods of measuring metallicity gradients (Sánchez-Menguiano et al. 2016b).

While the ATLAS^{3D} and the CALIFA surveys have now managed to amass hundreds of galaxies, they do not have the multiplexing technology to easily reach thousands of galaxies.

This was made possible by the development of the hexabundle (Bland-Hawthorn et al. 2011) which led to the development of the Sydney-AAO Multi-object Integral field (SAMI) spectrograph (Croom et al. 2015). The SAMI Galaxy Survey (Bryant et al. 2015) will complete in 2018 with 3600 galaxies across a wide range of environments and stellar masses, allowing for the disentanglement of degeneracies. This will be followed by the Hector survey with an order of magnitude increase in the observed number of galaxies (Bland-Hawthorn 2015).

The Mapping Nearby Galaxies at Apache Point Observatory (MaNGA) survey (Bundy et al. 2015) is an ongoing galaxy survey aiming to achieve spatially resolved spectra of 10,000 nearby galaxies. MaNGA uses specially designed fibre bundles (Drory et al. 2015) that vary in diameter and number of fibres to allow the observation of a representative sample of local galaxies in the mass range $10^9 < M/M_\odot < 10^{12}$. Fibre bundles range from 19-127 fibres with an on-sky diameter ranging from $12'' - 32''$.

With a sample of 550 galaxies from the MaNGA survey, Belfiore et al. (2017) found a steepening of the metallicity gradients with stellar mass up to a mass of $\log(M_*/M_\odot) < 10.5$. For more massive galaxies, the metallicity gradient flattens slightly as the metallicity of the galaxy reaches a constant value.

The gas-phase metallicity is most commonly presented as the ratio between the abundance of oxygen, the most abundant heavy element by mass, and hydrogen. For star-forming galaxies, the metallicity is usually determined using the ratios of the strong emission lines. Some of the popular strong emission line diagnostics include:
([OII]λ3726, λ3729 + [OIII]λ4959, λ5007)/Hβ(R_{23}; Kobulnicky & Kewley 2004, hereafter KK04), [NII]λ6583/[OII]λ3726, λ3729 (N2O2; Kewley & Dopita 2002, hereafter KD02), ([OIII]λ5007/Hβ)/([NII]λ6583/Hα) (O3N2; Pettini & Pagel 2004, hereafter PP04), [NII]λ6583/Hα (N2HA; Pettini & Pagel 2004) and [NII]λ6583/[SII]λ6717, λ6731 (N2S2; Dopita et al. 2016, hereafter D16). Each diagnostic has its own set of advantages and disadvantages making them suitable for different situations. These diagnostics are then calibrated against data to determine metallicities. However, all these metallicity calibrations are inconsistent with each other, leading to different abundances depending on the particular diagnostic and calibration used. Kewley & Ellison (2008) attempts to consolidate the many metallicity diagnostics and calibrations by providing conversion polynomials between them. For a comprehensive review and analysis of the various metallicity diagnostics and calibrations, see Kewley & Ellison (2008); López-Sánchez et al. (2012).

Ionization parameter strongly affects many metallicity diagnostics (eg. N2HA, O3N2, R_{23}). The ionization parameter is defined as:

$$q = \frac{S_{H^0}}{n} \tag{2.1}$$

where S_{H^0} is the ionizing photon flux per unit area and n is the number density of the interstellar medium. The ionization parameter is a measure of the amount of ionizing photons passing through the interstellar medium per hydrogen atom. Dopita et al. (2014) found a strong correlation between ionization parameter and star-formation rate (SFR) and suggest that the correlation is caused by the change in geometry of the molecular and ionized gas with environment. Similar results are obtained by Kaplan et al. (2016), who found strong evidence of the existence of radial ionization parameter gradients and a correlation with SFR.

The dependence of metallicity diagnostics on ionization parameter is clearly shown in López-Sánchez et al. (2011); Ho et al. (2015). The KD02 N2O2 diagnostic is relatively independent of ionization parameter but the PP04 O3N2 diagnostic was empirically calibrated without taking into account the effect of ionization parameter. Ho et al. (2015) showed that the differences between the two diagnostics correlates strongly with the ionization parameter, highlighting the importance of correcting for ionization parameter when calculating metallicity.

In this paper we simultaneously constrain the metallicity and ionization parameter of pure star-forming SAMI galaxies through an iterative process and produce self-consistent spatially resolved metallicity and ionization parameter maps. We derive metallicity gradients and analyse the spatial distribution of the ionization parameter. We confirm the results of Sánchez et al. (2012, 2014); Ho et al. (2015); Sánchez-Menguiano et al. (2016b) by obtaining consistent metallicity gradient values. We find a weak mass-dependence of metallicity gradients using the KK04 R_{23}metallicity diagnostic, showing a similar trend to Belfiore et al. (2017). We show that the ionization parameter does not change as a function of radius with most star-forming galaxies and we investigate whether the ionization parameter correlates with fundamental galaxy properties like metallicity, SFR and specific star formation rate (sSFR). Finally we show the implications of excluding the ionization parameter from metallicity calculations.

We structure this paper in the following way. Section 2 describes the SAMI Galaxy Survey and how we select our sub-sample from the data available. We outline the methods we use for determining the metallicity and ionization parameter while taking into account the interdependence of the diagnostics in Section 3. In Sections 4 and 5, we present and briefly compare to previous work, our results of the metallicity and ionization parameter analysis respectively. We discuss the results and provide a summary and conclusion in Sections 6 and 7. Throughout the entire paper, we assume the following values for cosmological constants, $H_0 = 70$km s^{-1}Mpc^{-1}, $\Omega_M = 0.3$ and $\Omega_\Lambda = 0.7$.

2.2. Sample Selection

2.2.1. SAMI Galaxy Survey

The SAMI Galaxy Survey (Croom et al. 2012) is an ongoing integral field spectroscopic survey of $\sim$ 3600 low-redshift (z<0.12) galaxies primarily selected from the Galaxy and Mass Assembly (GAMA) survey (Driver et al. 2011), with the addition of 8 galaxy clusters to extend the sampling of environmental density (Owers et al. 2017). The survey uses the SAMI spectrograph on the 3.9 metre Anglo-Australian Telescope at Siding Spring Observatory. The final primary survey targets consist of galaxies with stellar masses between $10^7 - 10^{12} M_\odot$, redshifts between $0.004 < z < 0.095$ and magnitudes $r_{pet} < 19.4$ mag. For full details on the SAMI Galaxy Survey selection, refer to Bryant et al. (2015).

The SAMI data are released as a red and blue data cubes for each galaxy, with 50×50 0.25 (0.5×0.5) arcsec^2 spaxels covering the 14.7''diameter aperture of the SAMI hexabundle and an average seeing of 2.16''(see Green et al. 2018 for details). The blue cube covers a wavelength range between 3700 – 5700Å with a spectral resolution of R=1812 and the

red cube covers a wavelength range between 6300 – 7400Å with a spectral resolution of R=4263 (van de Sande et al. 2017). These spectral ranges cover the strong optical emission lines commonly used as diagnostics of the gas-phase metallicity and ionization parameter: [OII]λ3726, λ3729, H$\beta\lambda$4861, [OIII]λ5007, H$\alpha\lambda$6563, [NII]λ6583 and [SII]λ6717, λ6731. The red and blue datacubes are analysed using LaZy-IFU (LZIFU v0.3.2); (Ho et al. 2016). LZIFU extracts total line fluxes for the dominant emission lines by fitting and subtracting the underlying continuum and then fitting the dominant emission lines using up to three Gaussian profiles. LZIFU returns maps of the flux and flux errors for each emission line, as well as maps of the ionized gas velocity and velocity dispersion and their associated errors (see Ho et al. (2016) for a detailed explanation of the routine).

The galaxy sample for which we determine the resolved metallicity and ionization parameter is based on the 772 galaxies in Data Release 1 of the SAMI Galaxy Survey (Green et al. 2018). However, to obtain the highest S/N and largest possible maps of these parameters, we placed the following selection criteria on the galaxies (each of which is elaborated in the following subsections):

- Star-forming galaxies free of AGN and shocks using the Kewley et al. (2006) classification scheme
- Emission-line maps covering at least 70% of the hexabundle field of view in all emission lines used
- Face-on galaxies with an inclination angle less than 60 degrees based on measurements from the GAMA survey
- Each galaxy is sampled to at least 1 effective radius ($R_e < 7.4''$) based on measurement from the GAMA survey
- A S/N ratio > 3 in the [OII], Hβ, [OIII], Hα, [NII] and [SII] emission line fluxes for each spaxel

These selection criteria limit our sample to 25 star-forming, 'best-case' scenario galaxies to determine reliable metallicity and ionization parameter maps. The final sample of galaxies and their global properties as defined in the GAMA galaxy catalogue are given in Table 1. We use the R-band effective radii throughout this study. We also give the Hα derived SFR assuming a Salpeter (Salpeter 1955) initial mass function (IMF) as well as stellar mass derived from the mass-luminosity relation (Taylor et al. 2011). For a comparison between the SFR values determined with GAMA data and SAMI data, see Medling et al. (2018).

In future studies, we intend to expand this analysis to the full SAMI Galaxy Survey sample. With a larger sample, we will probe the relationships between metallicity and ionization parameter with galaxy properties in greater detail.

2.2.2. Star-Forming Galaxies

For typical blue cloud galaxies, strong emission lines arise predominantly from HII regions surrounding recently formed massive stars. However, emission lines can also arise from

gas excited by other sources of ionization, such as shocks or Active Galactic Nuclei (AGN) e.g. Groves et al. (2004). The metallicity and ionization parameter diagnostics that we rely on are calibrated assuming HII region emission, and cannot be simply applied to galaxies with significant contribution from other ionizing sources to the emission lines. In some cases it is possible to separate the star-formation dominated and other ionizing sourced line emission (eg. Davies et al. 2014, 2016), but in our case we chose to remove all galaxies that showed significant non-star-forming emission.

Medling et al. (2018) created star formation masks for the SAMI galaxy survey DR1 using the classification scheme of Kewley et al. (2006), that uses strong emission line ratios to create diagnostic curves that distinguish when non-star-forming emission is present:

$$\log \frac{[\mathrm{OIII}]}{\mathrm{H}\beta} > \frac{0.61}{\log \frac{[\mathrm{NII}]}{\mathrm{H}\alpha} - 0.05} + 1.30, \tag{2.2}$$

$$\log \frac{[\mathrm{OIII}]}{\mathrm{H}\beta} > \frac{0.72}{\log \frac{[\mathrm{SII}]}{\mathrm{H}\alpha} - 0.32} + 1.30, \tag{2.3}$$

$$\log \frac{[\mathrm{OIII}]}{\mathrm{H}\beta} > \frac{0.73}{\log \frac{[\mathrm{OI}]}{\mathrm{H}\alpha} + 0.59} + 1.33. \tag{2.4}$$

Spaxels with a S/N > 5 in the emission line fluxes that satisfy any (fail all of) these criteria were classified as non-star-forming (star-forming). In the case where S/N < 5, Medling et al. (2018) used a conservative approach to ensure that the sample remained clean.

After identifying the dominant ionization mechanism in each spaxel, Medling et al. (2018) calculated the fraction of the hexabundle field of view which is filled by the star forming spaxels. For our analysis we require that 70% of the hexabundle was star-forming to ensure that a significant portion of the field of view is filled. This reduces our DR1 SAMI galaxy sample to 91 galaxies.

Implementing this sample selection cut excludes galaxies based on several other galaxy properties. This cut clearly removes galaxies belonging to the red sequence, leaving only galaxies that lie within the blue cloud. However, we are also performing cuts based on angular size and ellipticity. Since we require at least 70% of the hexabundle to be filled with star-forming spaxels, we remove both small blue galaxies as well as highly inclined galaxies which do not sufficiently fill the field of view.

92 galaxies have star-formation fractions (fraction of Hα spaxels classified as star-forming) less than 10%. This subset is filled with red sequence galaxies that no longer undergo significant star-formation. Of the remaining 680 blue cloud galaxies, 151 (22%) galaxies have star-formation fractions greater than 70%. For 91 (13%) galaxies, the star-forming spaxels also fill 70% of the total hexabundle field-of-view. Although 60 galaxies have star-formation fractions greater than 70%, their angular size is either too small or are too inclined to fill the hexabundle field of view.

Overall this cut removes non-star-forming elliptical galaxies as well as AGN and shock-dominated galaxies, where the majority of spaxels satisfy the diagnostic curves shown in Equations 2.2, 2.3 and 2.4. Although small low surface brightness galaxies have high star formation fractions with respect to their size, their angular size is not large enough to sufficiently fill the hexabundle, making it difficult to derive radial gradients.

2.2.3. Well-resolved radial profiles

To measure reliable radial metallicity gradients, we require well-sampled radial profiles of the emission-line fluxes. In practice, this means that we select galaxies with inclinations of < 60 and effective radii R_e < 7.4'' for face-on galaxies to ensure that we sample at least 5 resolution elements across $1R_e$ and that we limit confusion along the minor axis. These selection criteria further reduce our galaxy sample to 38 galaxies.

2.2.4. High S/N Galaxies

To obtain reliable metallicity and ionization parameter measurements, we require spaxels to have a S/N> 3 in all of the emission line fluxes used in our diagnostic ratios: [OII]λ3726, λ3729, H$\beta\lambda$4861, [OIII]λ5007, H$\alpha\lambda$6563, [NII]λ6583 and [SII]λ6717, λ6731. We applied this criterion to all spaxels in our remaining galaxy sample, while still requiring a coverage of 70% of the SAMI field-of-view. This final cut, especially the limit on [OII], reduced our sample to 28 galaxies. A further 3 galaxies had such a small redshift such that the [OII] emission line was not redshifted enough to fall in the range of the detector.

Applying this final cut reduces the final sample to 25 face-on resolved star forming galaxies. Figure 2.1 compares our sample to all the galaxies in DR1 of the SAMI galaxy survey. It is clear that our sample is extremely biased with respect to the SAMI galaxy survey. The low-mass galaxies have an effective radii distribution similar to the whole DR1 sample. Since these low-mass galaxies are spread over the same area as higher-mass galaxies, they are more diffuse and hence harder to detect to a reliable S/N. The S/N requirements outlined in Medling et al. (2018) mean that low S/N spaxels are usually classified as non-star-forming, causing the lower-mass limit. The upper-limit of about $\log(M_*/M_\odot) = 10.5$ is due to the fact that the blue sequence turns over at $\log(M_*/M_\odot) \approx 10.5$ (Karim et al. 2011), with more massive galaxies belonging to the non-star-forming red sequence. We sample the middle range of effective radii due to our requirements on sampling to at least $1R_e$ and filling 70% of the hexabundle. We would not be able to sufficiently sample large angular size galaxies out to $1R_e$ and small angular size galaxies would not cover enough of the hexabundle. We have purposely selected galaxies to have high SFR, leading to the extreme bias towards high SFR galaxies compared to the DR1 sample. Since smaller galaxies tend to be the one with low SFR, by removing all the low mass galaxies, we are left only with very high star-forming galaxies.

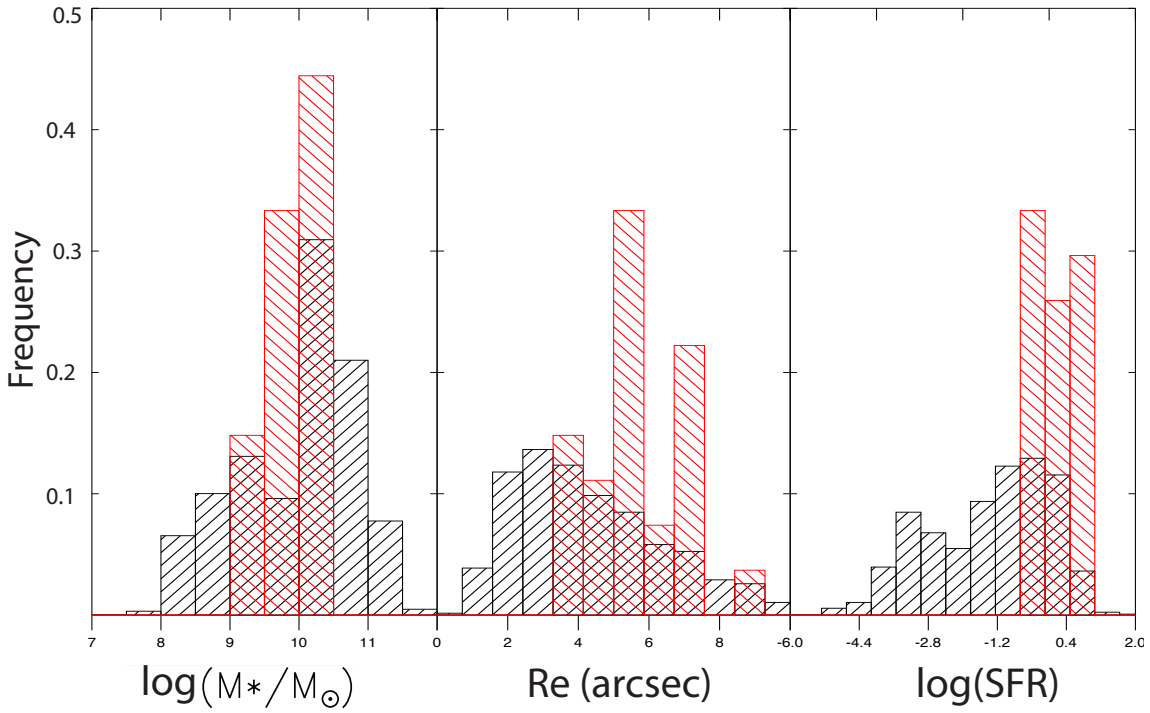

Figure 2.1 Comparison between DR1 of the SAMI Galaxy Survey (Black) and the final galaxy sample used for our analysis (Red). *Left Panel:* We have selected galaxies in the middle of the mass range ($9.0 < \log M_*/M_\odot < 10.5$) of DR1. Less massive galaxies are selected to have smaller redshifts and have comparable effective radii. This means that they are more diffuse and harder to obtain reliable S/N, leading to the lower mass limit. The upper mass limit is due to our restriction on sampling to at least 1Re. As we are observing a fairly narrow redshift range, more massive galaxies tend to have a larger apparent size, meaning we are unable to achieve the minimum 1Re we desire. *Middle Panel:* Again we sample the middle range of effective radii for the same reasons as we sample the middle range of stellar mass. The only exception is a slight spike beyond Re > 8″. This comes from GAMA-422366, which has an ellipticity of 0.354, allowing it to be sampled beyond 1Re along the minor axis despite the effective radius being larger than the SAMI field of view radius. *Right Panel:* Since we are aiming to only look at galaxies with high SFR fractions, we are only sampling the high SFR end of the DR1 SAMI Galaxy Survey.

GAMA	RA	Dec	Redshift	log(Mass)	SFR	R_e	Ellipticity	PA
	deg	deg		$M_*/M_\odot$	$M_\odot$/yr	arcsec	1-(b/a)	
008353	182.0164	0.6976	0.020	9.35	0.51	5.37	0.373	58.9
022633	178.4447	1.1934	0.070	10.28	9.93	5.08	0.297	107.3
030890	177.2579	-1.1025	0.020	9.79	0.76	7.56	0.435	27.1
053977	176.0183	-0.2109	0.048	9.94	5.02	3.79	0.202	103.7
077754	214.6477	0.1577	0.053	10.47	9.19	7.03	0.438	81.2
078667	218.0908	0.1781	0.055	10.14	-	6.85	0.225	19.7
084107	175.9984	0.4280	0.029	9.62	0.60	5.05	0.231	77.4
100192	185.9276	0.9621	0.024	9.33	0.18	5.66	0.080	127.3
106717	217.0188	1.0063	0.026	10.16	3.25	5.23	0.145	153.6
144402	179.9611	-1.3819	0.036	10.25	-	4.14	0.296	23.4
184415	176.3419	-1.5652	0.028	9.54	0.50	3.62	0.352	134.7
209181	132.1251	0.1708	0.058	10.24	3.71	4.31	0.442	120.6
209743	134.6767	0.1914	0.041	10.16	2.15	6.95	0.137	10.1
220439	181.6315	1.6166	0.019	9.52	0.72	5.64	0.237	7.1
227970	215.6045	1.1976	0.054	10.12	3.47	4.36	0.122	90.0
238395	214.2431	1.6404	0.025	9.88	2.18	4.11	0.341	157.9
273952	185.9555	1.3751	0.027	9.57	0.08	6.68	0.230	67.2
279818	139.4387	1.0554	0.027	9.55	0.58	7.24	0.476	40.0
422366	130.5955	2.4973	0.029	9.64	0.41	8.86	0.354	168.7
463288	212.4848	-1.2400	0.025	9.63	2.48	7.26	0.183	121.6
487027	222.6791	-1.7148	0.026	10.11	9.04	6.22	0.408	31.6
492414	216.5031	-1.4117	0.055	10.06	1.39	4.40	0.240	110.9
610997	182.8690	0.3786	0.020	9.32	0.21	5.48	0.043	179.6
618116	214.4055	0.3290	0.051	10.24	2.16	5.76	0.181	166.5
622744	134.8299	0.7977	0.013	9.07	1.42	5.39	0.227	52.4

Table 2.1 Selected sample of galaxies from the SAMI galaxy survey and their properties used for our analysis, obtained from the GAMA survey. SFR was not available for GAMA-78667 and GAMA-144402.

2.3. Determining Metallicity and Ionization Parameter

2.3.1. Extinction Correction

We first correct the emission lines for the attenuation by dust in the interstellar medium (ISM). The attenuation of emission lines is wavelength dependent, meaning that emission line diagnostics that use emission lines with wide wavelength differences are most heavily affected. To extinction correct the emission lines, we create maps of the observed Balmer ratio, $(\mathrm{H}\alpha/\mathrm{H}\beta)_{\mathrm{obs}}$. We solve for $E(B-V)$ by using the relation:

$$E(B-V) = \log(\frac{(\mathrm{H}\alpha/\mathrm{H}\beta)_{\mathrm{obs}}}{(\mathrm{H}\alpha/\mathrm{H}\beta)_{\mathrm{int}}})/0.4[k(\mathrm{H}\beta) - \mathrm{k}(\mathrm{H}\alpha)] \tag{2.5}$$

where $(\mathrm{H}\alpha/\mathrm{H}\beta)_{int}$ is the intrinsic ratio of 2.86 (Osterbrock 1989) assuming case B recombination. We use the Cardelli et al. (1989) extinction curve and assume a typical $R(V)$ value of 3.1 to determine k values for Hα and Hβ. We then use the calculated $E(B-V)$ to determine A(λ), the absolute extinction as a function of wavelength, at our emission line wavelengths to de-redden the emission line fluxes.

2.3.2. Aliasing caused by Differential Atmospheric Refraction

As described in Green et al. (2018), differential atmospheric refraction (DAR) can combine with limited spatial sampling as done in the SAMI survey to create aliasing effects on the spectra. The aliasing is caused by the atmostphere and is made worse by the way the SAMI instrument performs its drizzling to fill in gaps between fibres. While the overall DAR shift is accounted for, a combination of the seeing and sampling in the SAMI survey has meant the DAR has introduced aliasing into the spectra on scales comparable to the point spread function (PSF). This aliasing is most noticeable when taking the ratio of two widely separated wavelength emission lines. With an oversampled PSF, we expect variations between neighbouring spaxels to be normally distributed. However, with aliasing, we find excess noise in flux ratios with wide wavelength separations. To correct for what is in effect a variation of the PSF with wavelength, when examining the Balmer decrement, Medling et al. (2018) smoothed the line ratio map by using a 5x5 spaxel Gaussian kernel with a full-width at half maximum (FWHM) of 1.6 spaxels (0.8''). This smoothing brings the noise down to levels we would expect with an oversampled PSF. We apply this same method not only to our Balmer decrement, but also to our metallicity and ionization parameter diagnostics (R_{23}, N2O2, O32), as these all have a significant wavelength gap between emission lines.

2.3.3. R_{23} Diagnostic

One of the most popular and well calibrated strong emission line metallicity diagnostics is ([OII]λ3726, λ3729 + [OIII]λ4959, λ5007)/Hβ, also known as R_{23}, first introduced by Pagel et al. (1979). This diagnostic measures the sum of the two dominant ionization states of oxygen in HII regions, which captures the majority of the element. However, this diagnostic is sensitive to temperature and ionization, which has resulted in many R_{23}calibrations, each leading to different metallicity estimates (Pagel et al. 1979, 1980; Edmunds & Pagel 1984;

McCall et al. 1985; Dopita & Evans 1986; Torres-Peimbert et al. 1989; McGaugh 1991; Zaritsky et al. 1994; Pilyugin 2000; Charlot & Longhetti 2001; Kewley & Dopita 2002; Kobulnicky & Kewley 2004). For a comprehensive review and analysis of various metallicity calibrations see Kewley & Ellison (2008). Furthermore, due to this sensitivity to temperature, the R_{23}diagnostic can be degenerate with both a high and low-metallicity solution.

Some R_{23}metallicity diagnostics take the ionization parameter into account (McGaugh 1991; Kewley & Dopita 2002; Kobulnicky & Kewley 2004). However, the determination of the ionization parameter is similarly difficult because many ionization parameter diagnostics have a significant dependence on metallicity. By using an iterative method described in KD02, we are able to constrain metallicity and ionization parameter simultaneously (see Section 3.5).

2.3.4. O32 Diagnostic

One way of measuring the ionization parameter is to measure the relative flux of emission lines from high and low-ionization states of the same element. To determine the ionization parameter, we use the [OIII]λ5007/[OII]λ3726, λ3729 (O32) diagnostic.

KD02 and KK04 both presented theoretical calibrations for ionization parameter using the O32 diagnostic. However, the O32 diagnostic has a strong dependence on metallicity. Unlike the R_{23}diagnostic, the O32 diagnostic is unambiguous in the sense that it is not double valued except at high metallicities ($Z > 2\ Z_{\odot}$). At lower metallicities, the polynomial fits to the theoretical relationship between ionization parameter and the [OIII]/[OII] line ratio monotonically increase across the valid ionization parameter range.

2.3.5. Iteration

We determine the metallicity and ionization parameter simultaneously through an iterative process. We first use an initial metallicity estimate to constrain the R_{23}diagnostic to the upper or lower metallicity branch. The [NII]λ6583/[OII]λ3726, λ3729 (N2O2) diagnostic has very little dependence on ionization parameter (but is strongly affected by attenuation), and we use this diagnostic ratio for our initial metallicity estimate. For spaxels with N2O2< -1.2, we place the spaxel on the lower R_{23}branch and assume a metallicity of $12 + \log(O/H) = 8.2$ as the starting iteration point. For N2O2> -1.2, we use the upper R_{23}branch and assume a metallicity of $12 + \log(O/H) = 8.7$.

Once an initial metallicity estimate has been determined, we use this value in the first estimate of the ionization parameter using the O32 diagnostic. This first ionization parameter estimate is then used to improve our metallicity estimate through the R_{23}diagnostic. We continue iterating between the $R_{23}$and O32 diagnostics until the metallicity and ionization parameter converge. We consider the metallicity and ionization parameter converged if the difference between iterations in the metallicity estimate is less than 0.1 dex and the ionization parameter estimate is within 0.01 dex. We require this tolerance to be achieved for all spaxels used during analysis.

The rate at which the metallicity and ionization parameter converge is usually proportional to the S/N ratio. Spaxels with a S/N > 5 in the used emission lines generally converge in ~

3 iterations while lower S/N spaxels sometimes require 20+ iterations. We impose an upper limit of 20 iterations to remove any non-converging spaxels from the maps. Spaxels that have not converged are discarded from the metallicity and ionization parameter maps.

2.3.6. Error Propagation

The iterative method used to calculate the metallicity and ionization parameter makes it difficult to analytically propagate the error. To propagate line flux errors produced by LZIFU through to the metallicity and ionization parameter, we simulate 1000 maps for all emission lines used in the calculation. The maps are created such that the fluxes are Gaussian distributed with the LZIFU standard deviation for that emission line.

Using the simulated line maps, metallicity and ionization parameter maps are created using the iterative process described in Section 2.3.5. The non-linearity of the resulting metallicity and ionization parameter diagnostics means that the metallicity and ionization parameter distributions are not necessarily Gaussian. To represent the spread of metallicity and ionization parameter, we determine the distance from the best-fit value to the 16^{th} and 84^{th} percentiles and calculate the average. This provides us with a measure of the uncertainty of the metallicity and ionization parameter maps which are then propagated to the gradient errors.

2.4. Metallicity Distribution

We calculate metallicity and ionization parameter maps with their corresponding errors for our sample of 25 SAMI galaxies. In Figure 2.2 we show two examples of the metallicity maps using different metallicity diagnostics accompanied by their error maps. In addition to the metallicity maps, we also show the SDSS 3 colour image (gri) of the galaxy with the SAMI field of view and its effective radius. The metallicity maps for the other 23 galaxies are presented in the Appendix. The majority of galaxies in our sample have metallicities in the range 8.5 <12+log(O/H)< 9.3 in the radial ranges probed using the KK04 metallicity diagnostics. The mass-metallicity relation presented in Kewley & Ellison (2008) shows that the nuclear metallicities for SDSS galaxies range between 8.7 <12+log(O/H)< 9.05 for a mass range between $9.0 < \log M_*/M_\odot < 10.5$. This is consistent with the metallicites within our sample for the same mass range, given that the SDSS fibre samples $\sim$ 20% of the galaxies' B-band light (Kewley et al. 2005).

The gas-phase metallicity increases over time. For the inside-out model of galaxy formation, we expect isolated galaxies to have strong negative metallicity gradients (Pagel & Edmunds 1981; Edmunds & Pagel 1984; Vilchez et al. 1988; Vila-Costas & Edmunds 1992; Zaritsky et al. 1994). However, in interacting galaxies, the turbulent gas caused by the tidal forces stretches and flattens this metallicity gradient (Torrey et al. 2012). We find that in our sample, the majority of galaxies possess strong metallicity gradients (18/25), as expected for relatively isolated and undisturbed galaxies. We show these normalized metallicity gradients in Figure 2.3 and provide a table of each linear fit in Table 2.2.

For several galaxies we also find a strong positive correlation between metallicity and SFR surface density as shown in Figure 2.4. This is consistent with several recent studies using

SAMI data have shown SFR surface density gradients exist in the SAMI sample (Schaefer et al. 2017; Medling et al. 2018).

Sánchez-Menguiano et al. (2016a); Ho et al. (2017) showed that significant azimuthal variations exist in the metallicity distribution of NGC6754 and NGC1365 respectively. However, we split each galaxy into quadrants and find little evidence of significant changes in the metallicity gradient, suggesting that at the spatial resolution of SAMI, spatial smoothing is sufficient to remove any trace of azimuthal variations, leaving only the radial gradients we observe. A resolution of at least 200pc/PSF is needed to observe these azimuthal variations (Sánchez-Menguiano et al. 2016a). With a median redshift of $z = 0.028$, an average seeing of 2.16'' combined with the 0.8'' smoothing to remove DAR, our galaxy sample has median resolution elements of 1.3kpc/PSF, much coarser than the minimum requirement found in Sánchez-Menguiano et al. (2016a). While statistically significant azimuthal variations are absent, there is evidence of clumpy substructure in several metallicity maps (eg. GAMA-8353 and GAMA-106717).

2.4.1. Metallicity Gradients

While there is little azimuthal variation in the sample, there are clear radial gradients across our sample. The smoothness of these metallicity maps means that we are able to use a simple linear fit to the metallicity ($12 + \log(O/H)$) as a function of radius. Sánchez-Menguiano et al. (2018) showed that broken linear fits can also be used to describe the metallicity gradients of MUSE galaxies. Broken linear fits allow for the fitting of steepening or flattening metallicity gradients, resulting in a more robust fit for metallicity gradients which vary with radii. For this study, we use single linear fits to the galaxy metallicity gradients.

We determine the radial distance of each pixel from the centre taking into account the ellipticity and position angle of the object. We also normalise the radius by the size of its disk using its effective radius (Re) in the R band measured using GALFIT (Peng et al. 2002) by the GAMA survey Kelvin et al. (2012). This removes the size dependence that the metallicity gradient has when measured on a physical scale (Sánchez et al. 2014; Ho et al. 2015).

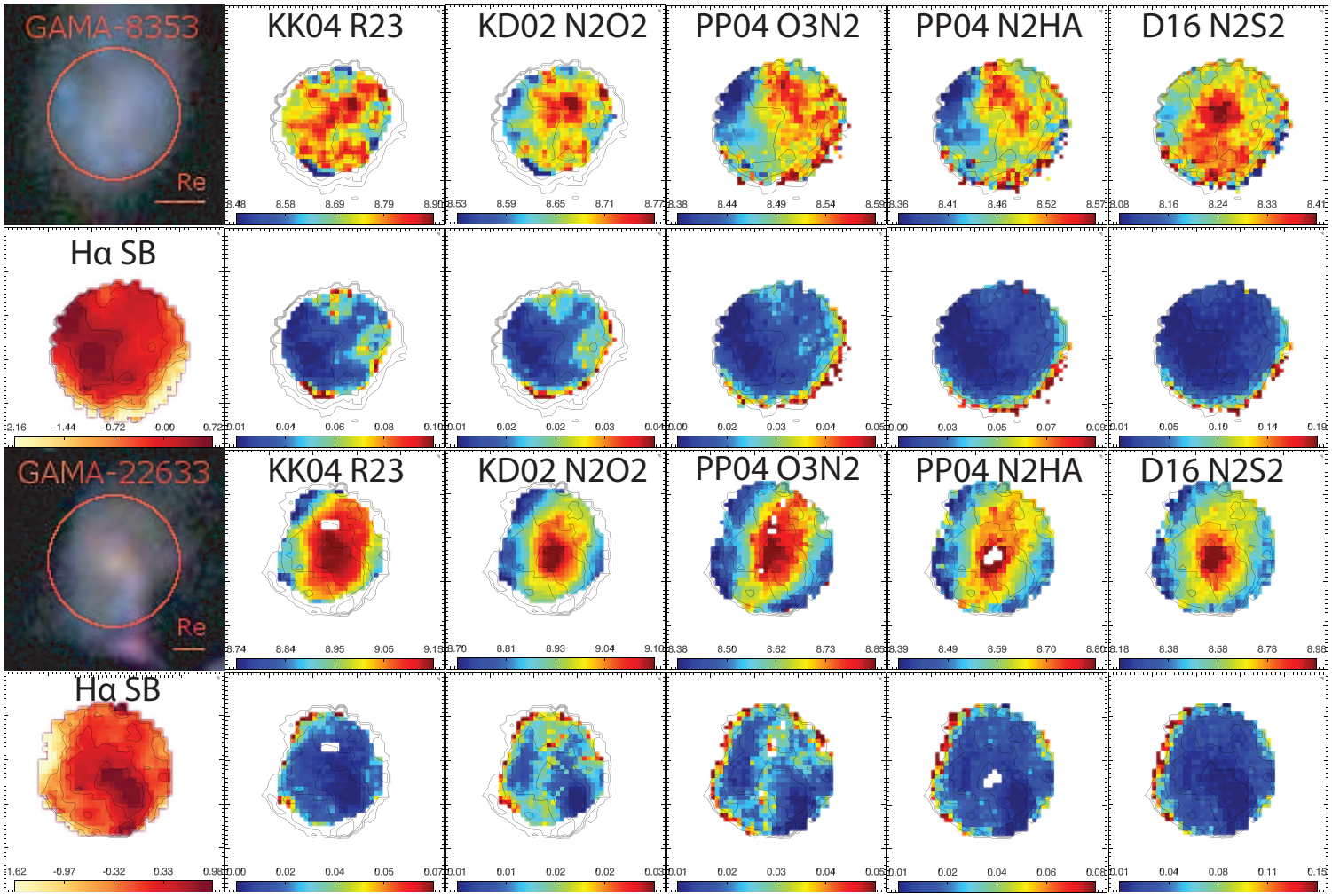

Figure 2.2 Each galaxy is presented as a 2×6 grid. The top row of each grid shows the various metallicity maps with their corresponding error maps beneath them. Note that scale bars have been varied between different maps and galaxies in order to provide the best metallicity resolution possible. *Column 1:* SDSS composite image obtained from DR10. The red circles represent the 14.7″ aperture of the SAMI hexabundle and the scale bar shows the effective radius of the galaxy obtained from GAMA R band. Below this we show the Hα emission line map. We choose the Hα emission line map because we believe it provides the best representation of the galaxy structure and morphology. We overplot the Hα contours onto each metallicity map to provide a point of reference when comparing metallicity diagnostics. *Column 2:* KK04 metallicity determined from the R_{23}line ratio. *Column 3:* KD02 metallicity determined from the N2O2 line ratio. *Column 4:* PP04 metallicity determined from the O3N2 line ratio. *Column 5:* PP04 metallicity determined from the N2HA line ratio. *Column 6:* D16 metallicity determined from the N2S2 line ratio. All metallicity maps are measured in units of 12 + log(O/H).

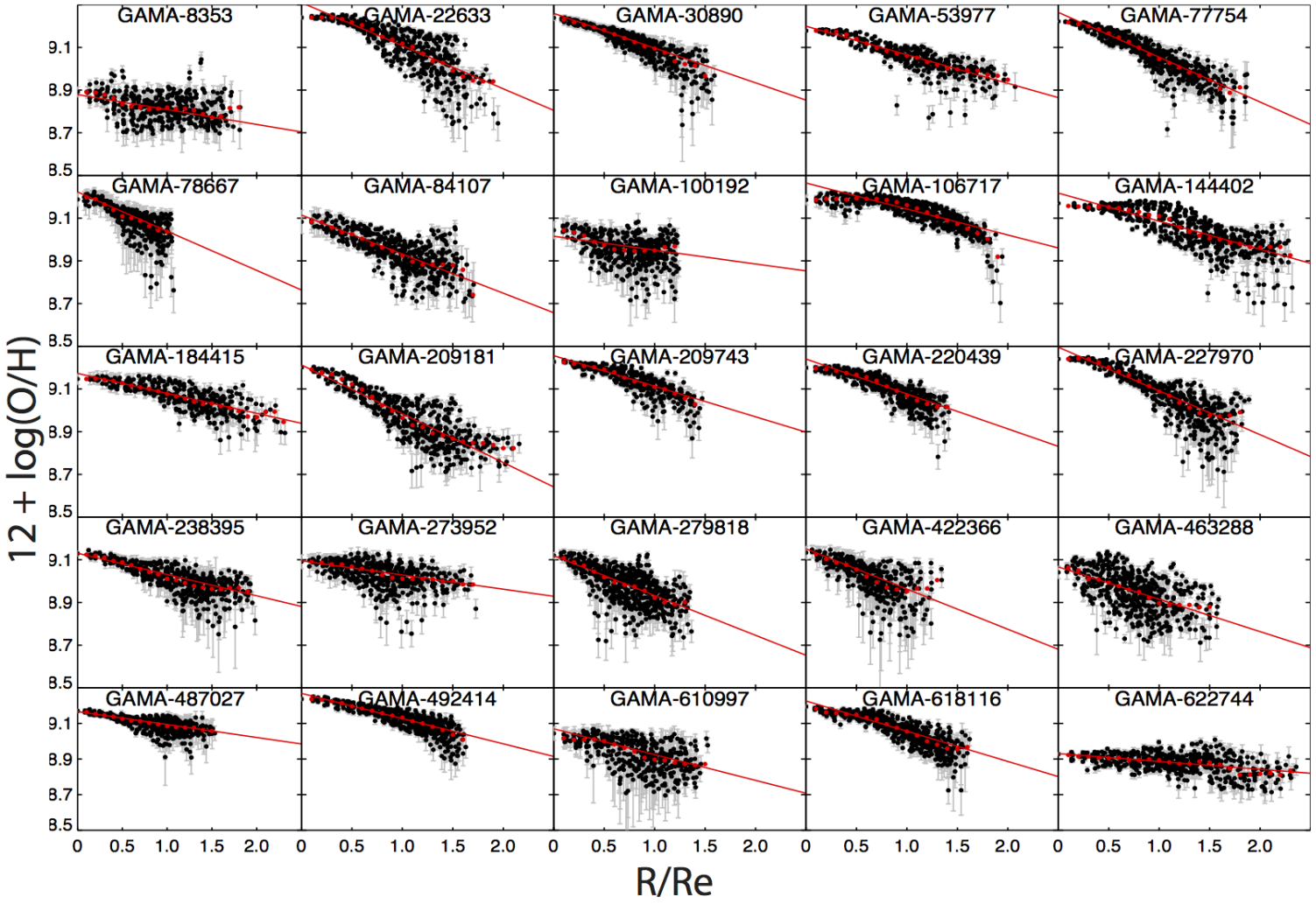

Figure 2.3 KK04 R_{23}metallicity gradients used in our analysis. We show 1σ error bars for each spaxel, determined from the method described in Section 2.3.6. The best linear fit to the metallicity gradient is given as a red line. The median metallicity in bins of 0.1 R/R_e are filled red circles. The results are summarised in Table 2.2.

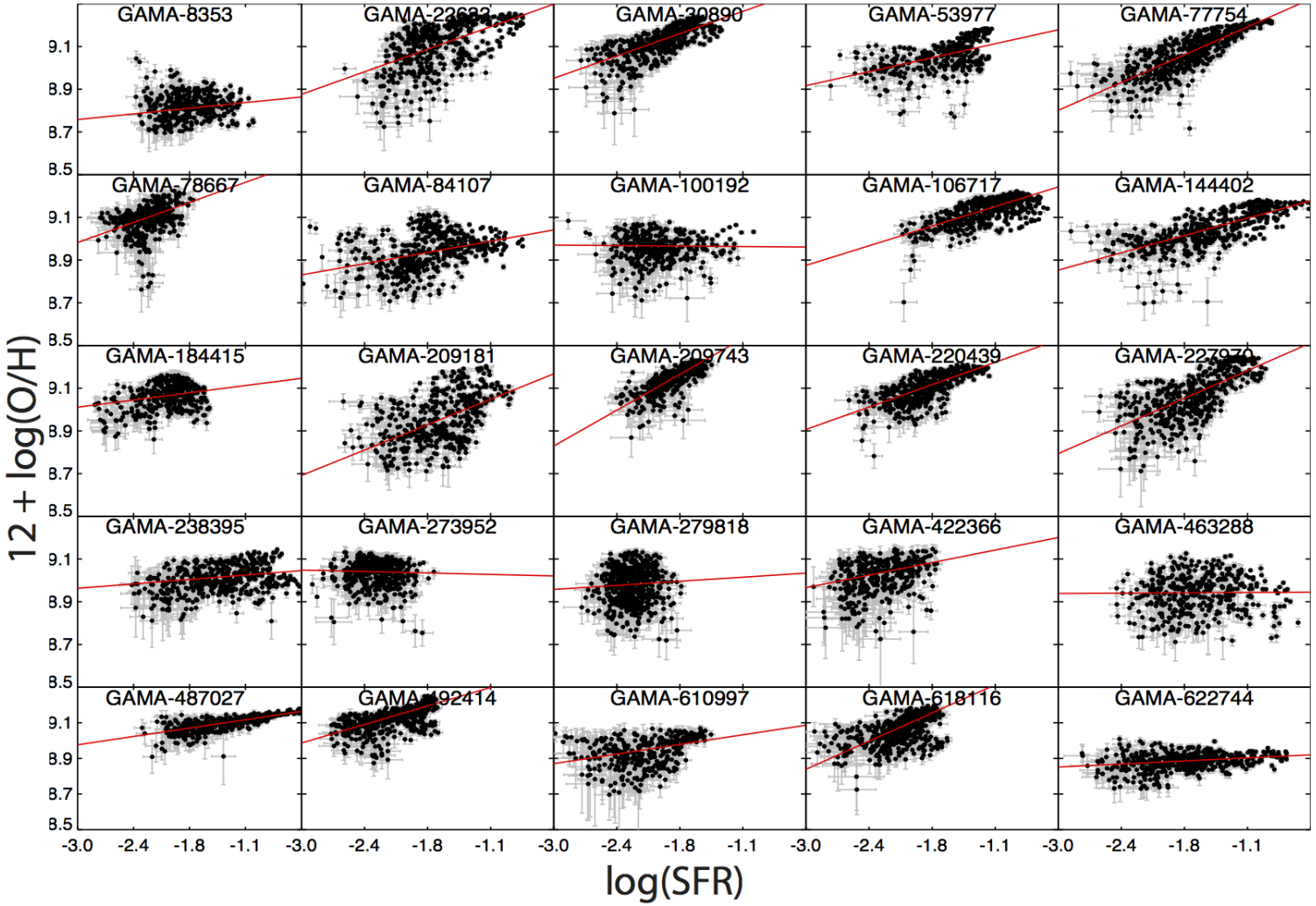

Figure 2.4 KK04 R_{23}metallicity as a function of SFR surface density. We obtain maps of SFR surface density in units of $M_{\odot}/year/kpc^2$ from Medling et al. (2018). We show the best linear fit as a red line and summarise the results in the Table 2.4.

We use the robust line fitting routine LTS_LINEFIT (Cappellari et al. 2013) to fit a linear trend to the data. We choose LTS_LINEFIT for its ability to identify and separate outliers from the input data as well as provide standard errors to the output fit parameters. To calculate the standard errors on the output fit parameters, we provide LTS_LINEFIT with the metallicity errors calculated from method described in Section 2.3.6. We show the radial metallicity gradients of our sample in Figure 2.3 along with the best linear fit and radially binned median points.

The Pearson correlation coefficient (PCC) is a measure of the presence of a linear trend. A magnitude of greater than 0.6 is usually accepted as a strong indication of a linear trend. The majority of radial metallicity gradients determined by LTS_LINEFIT show strong a strong trend (PCC magnitude > 0.6), with four galaxies presenting with very strong Pearson correlation coefficient (PCC magnitude > 0.8).

Figure 2.5 shows the normalised metallicity gradients of galaxies against their stellar masses. Within our mass range of $9.0 < \log(M_*/M_\odot) < 10.5$, the normalised metallicity gradients range from -0.20 to -0.03 dex/Re. There appears to be a slight correlation with steeper metallicity gradients occurring at higher masses. We fit the relationship with a linear trend and find a slope of -0.065 ± 0.021 dex/Re/$\log(M_*/M_\odot)$ with a PCC of -0.54. Belfiore et al. (2017) finds a similar trend with steeper metallicity gradients occurring in more massive galaxies in the mass range $9.0 < \log(M_*/M_\odot) < 10.5$.

Estimating the error on the PCC through bootstrapping analysis, we find PCC$= -0.54 \pm 0.06$ for the relationship between stellar mass and metallicity gradients. This indicates that there exists a weak negative linear trend between stellar mass and metallicity gradients for galaxies in the mass range $9.0 < \log(M_*/M_\odot) < 10.5$. This disagrees with previous studies by Sánchez et al. (2012, 2014); Ho et al. (2015); Sánchez-Menguiano et al. (2016b) who found no variation in radial metallicity gradients in their sample when normalised with either R_{25} or R_e.

2.4.2. Mass-Metallicity Relation

While the radial metallicity gradients appear to be weakly dependent on galaxy masses, across $9.0 < \log(M_*/M_\odot) < 10.5$ there still exists the global mass-metallicity relation. Figure 2.6 shows the correlation of the metallicity intercept with stellar mass for multiple metallicity diagnostics.

Kewley & Ellison (2008) provides fits to the mass-metallicity relation for a range of different metallicity diagnostics. We plot the mass-metallicity fit for several metallicity diagnostics as the dotted red line on Figure 2.6. There is a clear offset between the mass-metallicity fit and the metallicity intercepts caused by using the central interpolated metallicities rather than aperture metallicities. We fit these offsets using MPFIT (Markwardt 2009) and show the best least squares fit to the interpolated metallicities. Similar trends with the metallicity intercept were found in Sánchez et al. (2014) who also attributed it to the mass-metallicity relation.

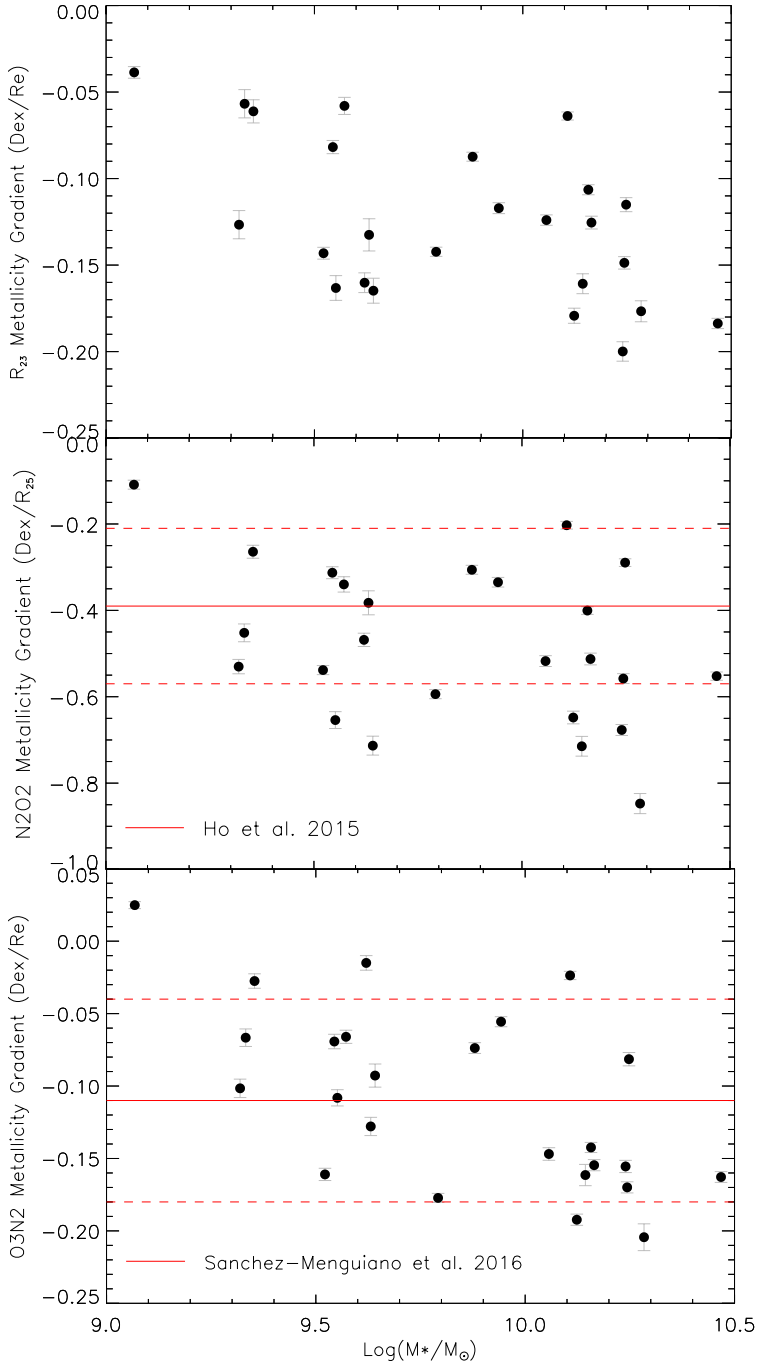

Figure 2.5 Normalised metallicity gradients as a function of mass using 3 common metallicity diagnostics. For the KD02 and PP04 metallicity diagnostics, we compare the results presented in Ho et al. (2015) and Sánchez-Menguiano et al. (2016b). The solid red line show the mean metallicity gradient with 1σ scatter shown as dotted red lines.

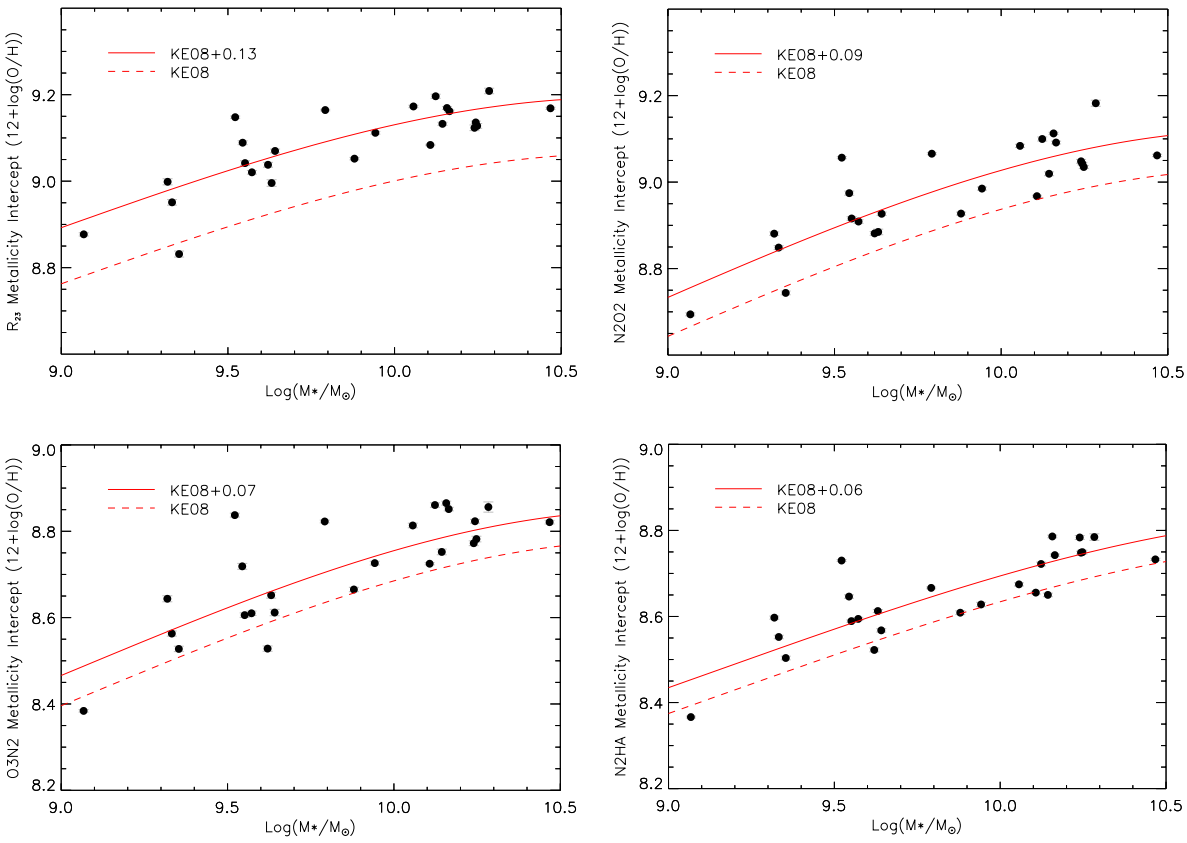

Figure 2.6 Metallicity intercepts as a function of mass for multiple metallicity diagnostics. We show the mass-metallicity relation for each diagnostic from Kewley & Ellison (2008) as the dotted red line and fit an offset shown as the solid red line.

GAMA ID	Central Metallicity 12+log(O/H)	Gradient dex/Re	RMS	PCC
008353	8.831±0.007	-0.061±0.007	0.081	-0.33
022633	9.209±0.006	-0.177±0.006	0.056	-0.71
030890	9.164±0.002	-0.142±0.003	0.034	-0.87
053977	9.112±0.003	-0.117±0.003	0.027	-0.69
077754	9.169±0.002	-0.184±0.003	0.032	-0.89
078667	9.133±0.004	-0.161±0.006	0.037	-0.70
084107	9.038±0.006	-0.160±0.006	0.047	-0.65
100192	8.951±0.007	-0.057±0.008	0.061	-0.33
106717	9.169±0.003	-0.106±0.003	0.030	-0.72
144402	9.128±0.006	-0.115±0.004	0.049	-0.68
184415	9.089±0.004	-0.082±0.004	0.033	-0.76
209181	9.123±0.007	-0.200±0.006	0.073	-0.77
209743	9.162±0.003	-0.125±0.004	0.029	-0.84
220439	9.148±0.003	-0.143±0.003	0.027	-0.79
227970	9.196±0.005	-0.179±0.004	0.065	-0.75
238395	9.052±0.003	-0.087±0.003	0.038	-0.72
273952	9.020±0.004	-0.058±0.005	0.041	-0.44
279818	9.042±0.005	-0.163±0.007	0.073	-0.30
422366	9.070±0.004	-0.165±0.007	0.067	-0.61
463288	8.996±0.008	-0.133±0.009	0.080	-0.48
487027	9.084±0.002	-0.064±0.002	0.025	-0.65
492414	9.173±0.003	-0.124±0.003	0.032	-0.84
610997	8.999±0.007	-0.127±0.008	0.082	-0.51
618116	9.136±0.003	-0.149±0.004	0.036	-0.78
622744	8.877±0.004	-0.039±0.003	0.048	-0.47

Table 2.2 List of metallicity gradients and intercepts with their 1σ uncertainties, root mean square (RMS) scatter and Pearson correlation coefficient (PCC) values.

2.5. Ionization Parameter Distribution

2.5.1. Ionization Parameter Gradients

In contrast to the metallicity maps, the ionization parameter maps (Figure 2.8) show no clear radial or azimuthal trends. Instead we see a range of different distributions ranging from weak gradients, flat maps and clumpy distributions. The majority of galaxies tend to have ionization parameters in the range $7.0 < \log(q[\mathrm{cm/s}]) < 7.8$. We measure the radial ionization parameter gradients of the galaxies using robust line fits in the same way as the metallicity gradients. The ionization parameter radial gradients are presented in Figure 2.9 and compared to stellar mass in Figure 2.7. All galaxies except three have a PCC magnitude of less than 0.4, indicating very weak significance of these linear fits. GAMA-622744 appears to be the only galaxy with a significant ionization parameter gradient (PCC magnitude = 0.73).

Kaplan et al. (2016) found significant ionization parameter gradients in their sample of 8 galaxies using VENGA data. The galaxies in their sample were chosen to have significant and highly resolved bulges. Kaplan et al. (2016) used the same O32 ionization parameter diagnostics from KK04 as we do, but use one iteration rather than a convergence condition when calculating ionization parameter. Both methods provide them with similar results. The distribution of ionization parameter in their maps follows the distribution of SFR surface density in many of their galaxies and show strong radial gradients.

2.5.2. Ionization Parameter and Galaxy Properties

While we see no significant radial or azimuthal trends in the ionization parameter for most of our sample, GAMA-8353 and GAMA-22633, show patterns in q that are suggestive of the spiral arm features seen in the associated 3-colour and Hα maps in each galaxy. Such an association could indicate that the ionization parameter is larger in areas of high star formation, a trend seen by Dopita et al. (2014) in a sample of luminous infrared galaxies (LIRGs) above a threshold ionization parameter ($\log(q[\mathrm{cm/s}]) > 7.2 - 7.4$). Dopita et al. (2014) quantified this relation as $q[\mathrm{cm/s}] \propto \mathrm{SFR}[\mathrm{M_\odot/year/kpc^2}]^{0.34\pm0.08}$. Using SFR surface density maps created by Medling et al. (2018), we find that 71% (17/24) of galaxies present a slight positive correlation between SFR surface density and ionization parameter (Figure 2.10). However the strength of these gradients is weak with only GAMA-622744 having a PCC magnitude of greater than 0.6.

We also investigate how the ionization parameter varies with metallicity (Figure 2.11). We do this by plotting the KD02 metallicity determined from the N2O2 diagnostic against the KK04 ionization parameter measurements. We use the KD02 N2O2 metallicity diagnostic instead of the KK04 R23 metallicity diagnostic to try and exclude any possible dependencies between the two parameters caused by the iterative method used to calculate the ionization parameter. Again we find that only GAMA-622744 produces a significant Pearson correlation coefficient. The correlation between metallicity and ionization parameter for GAMA-622744 is likely driven by the fact that it is the only galaxy in our sample with a significant negative ionization parameter gradient and not necessarily because of an intrinsic correlation between metallicity and ionization parameter.

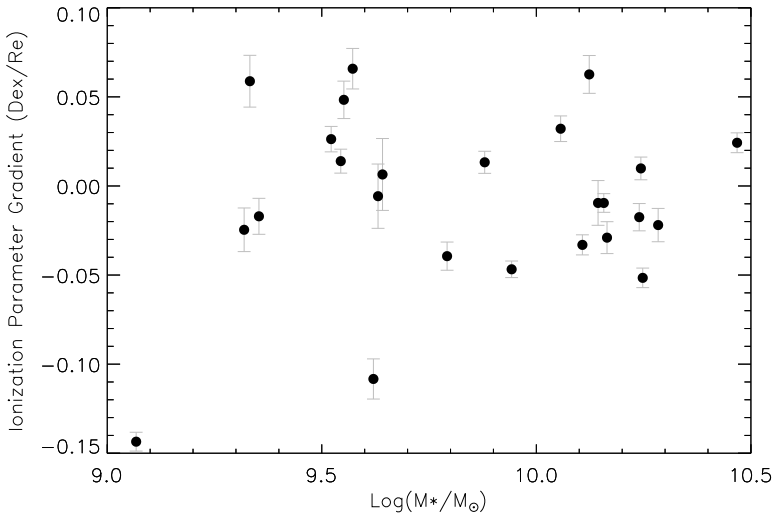

Figure 2.7 Normalized ionization parameter gradients using the KK04 O32 diagnostic as a function of stellar mass. We find no significant variation in the ionization parameter gradient as a function of galaxy mass.

Dopita et al. (2014) found a strong positive trend between the metallicity and ionization parameter, which is not seen in either this work or Kaplan et al. (2016). Dopita et al. (2006) provide a theoretical relationship between gas-phase metallicity and ionization parameter, $q[\mathrm{cm/s}] \propto \mathrm{Z[O/H]}^{-0.8}$.

2.6. Discussion

2.6.1. Metallicity Gradients

Using the KK04 R_{23}strong line emission diagnostic, we find a weak dependence in the slope of the normalised radial metallicity gradient with the stellar mass of the galaxy. This is inconsistent with the results found by several other recent studies on radial metallicity gradients in galaxies (Sánchez et al. 2012, 2014; Ho et al. 2015; Sánchez-Menguiano et al. 2016b). However, as demonstrated by Kewley & Ellison (2008), the calculated metallicities are strongly dependent upon the calibration used. Based on this, the derived metallicity gradients may also depend upon the particular diagnostic used. Belfiore et al. (2017) calculated metallicity gradients for galaxies using a diagnostic derived from the R_{23}line ratio and also found a dependence on metallicity gradients with stellar mass. Although Belfiore et al. (2017) use the same R_{23}diagnostic, they use the Maiolino et al. (2008) calibration to determine metallicites, making a direct comparison between results difficult. We find a mean metallicity gradient value of -0.12 dex/R_e with a standard deviation of 0.05 using the KK04 R_{23}metallicity diagnostic.

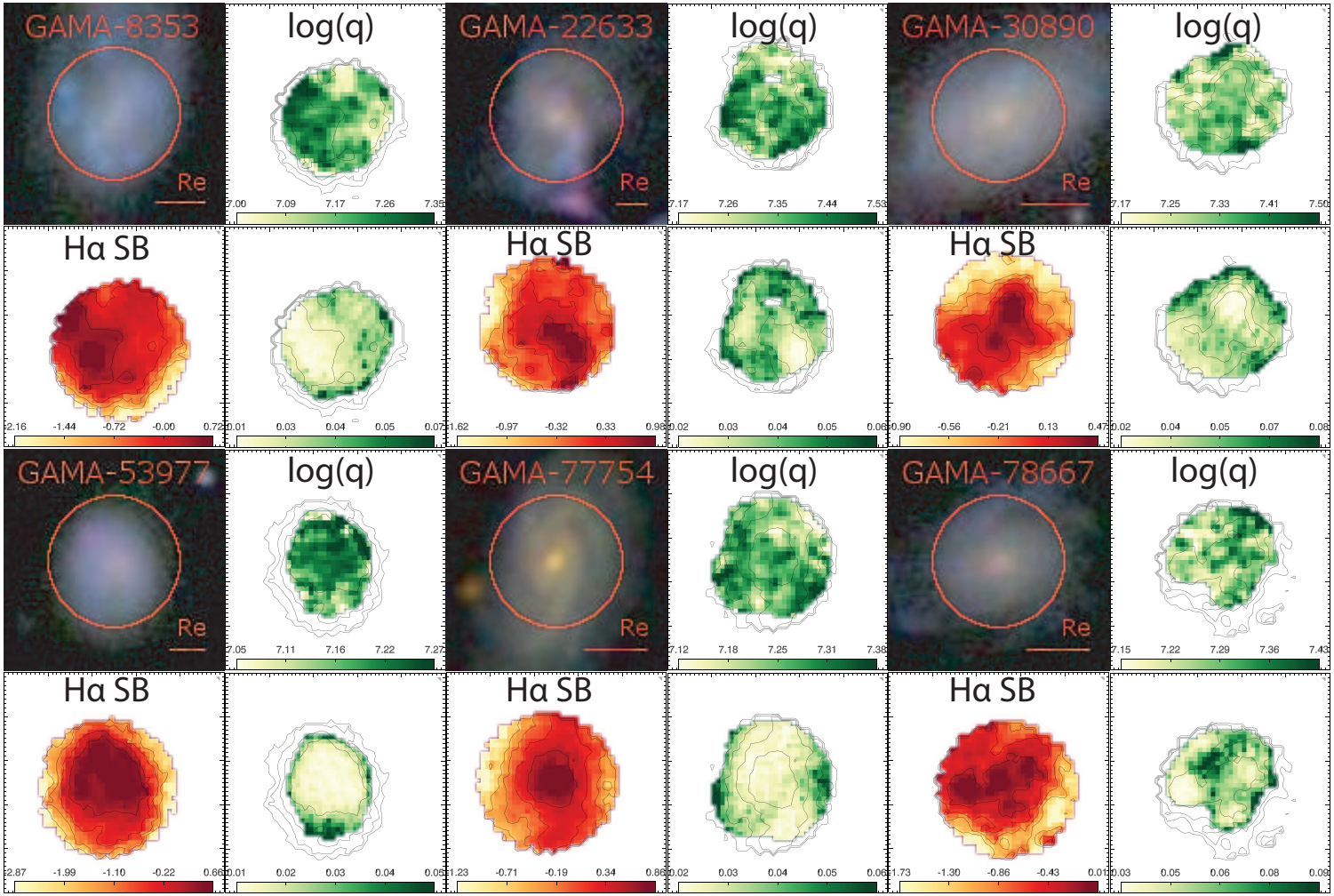

Figure 2.8 Each galaxy is presented with a 2×2 grid containing the results of our work. The top left image of each grid contains the same SDSS image as Figure 2.2. The Hα emission line map with contours below the SDSS image is also identical to Figure 2.2. To the right of each SDSS image is the ionization parameter map in units of log(cm/s) with overplotted Hα contours for comparison. Below each ionization parameter map is the associated error map as described in Section 2.3.6. Note that scale bars have been varied between different maps and galaxies in order to provide the best resolution possible

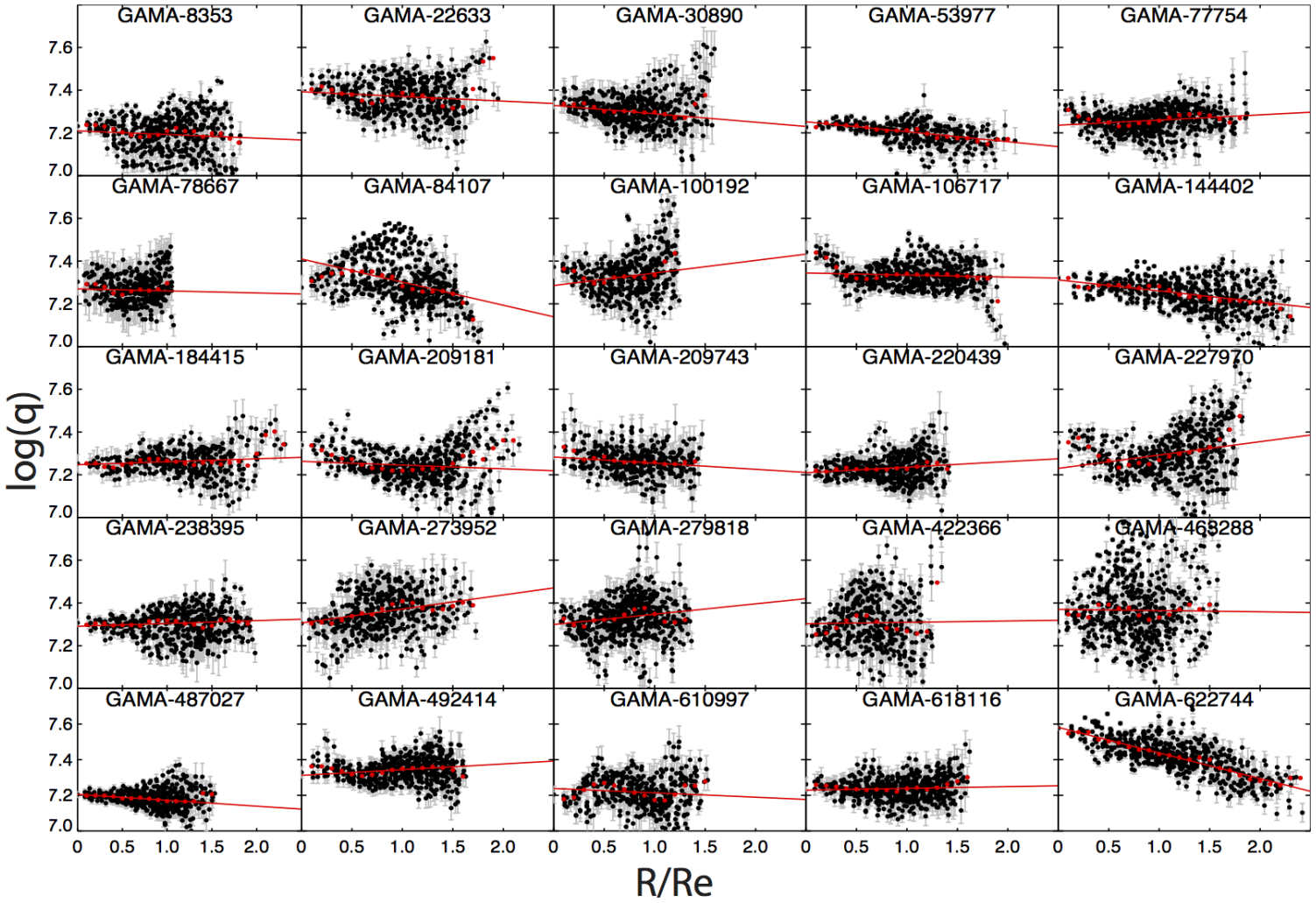

Figure 2.9 Same as Figure 2.3 for ionization parameter. The results are summarised in Table 2.3.

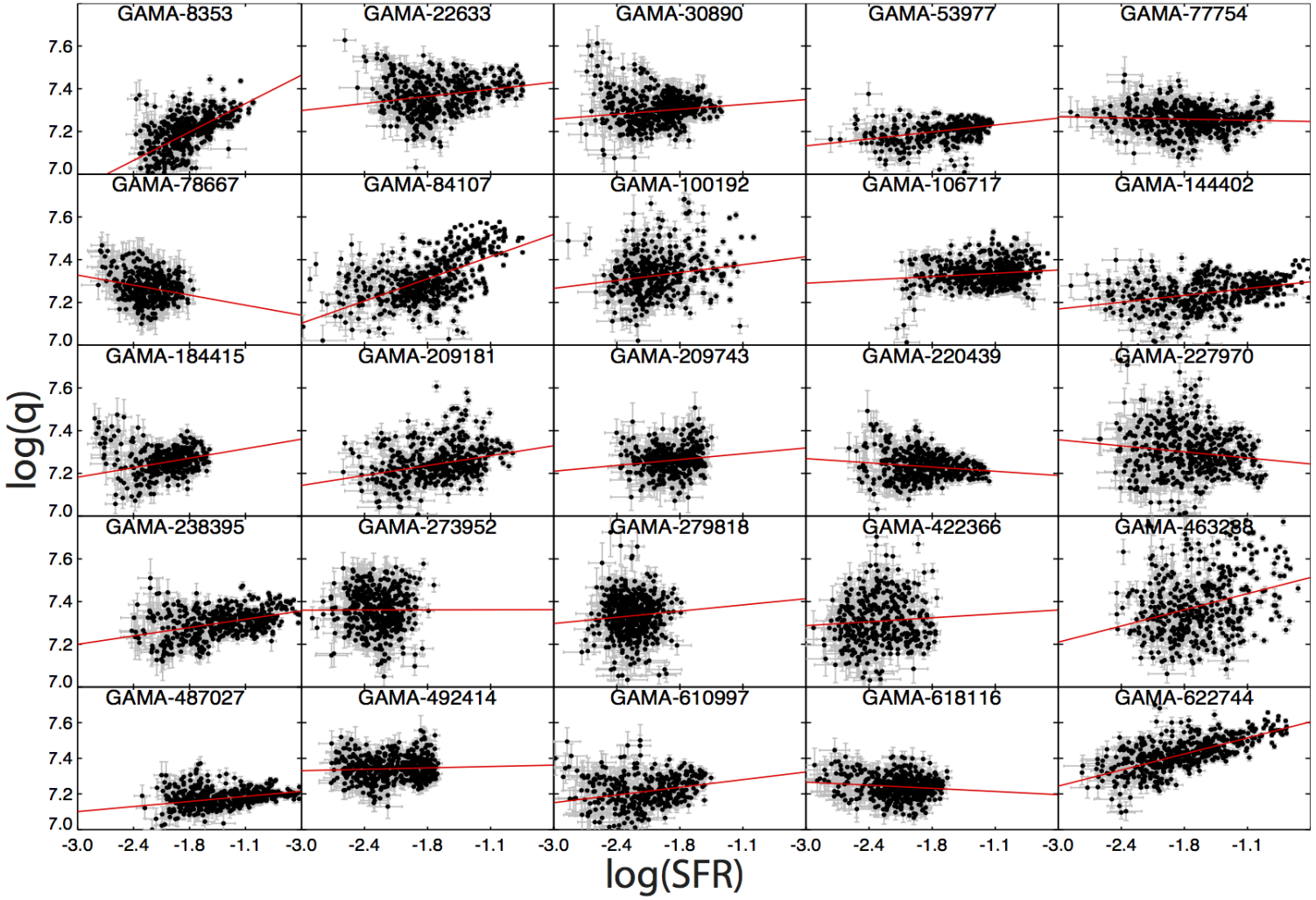

Figure 2.10 Same as Figure 2.4 for ionization parameter. We summarise the results in the Table 2.5.

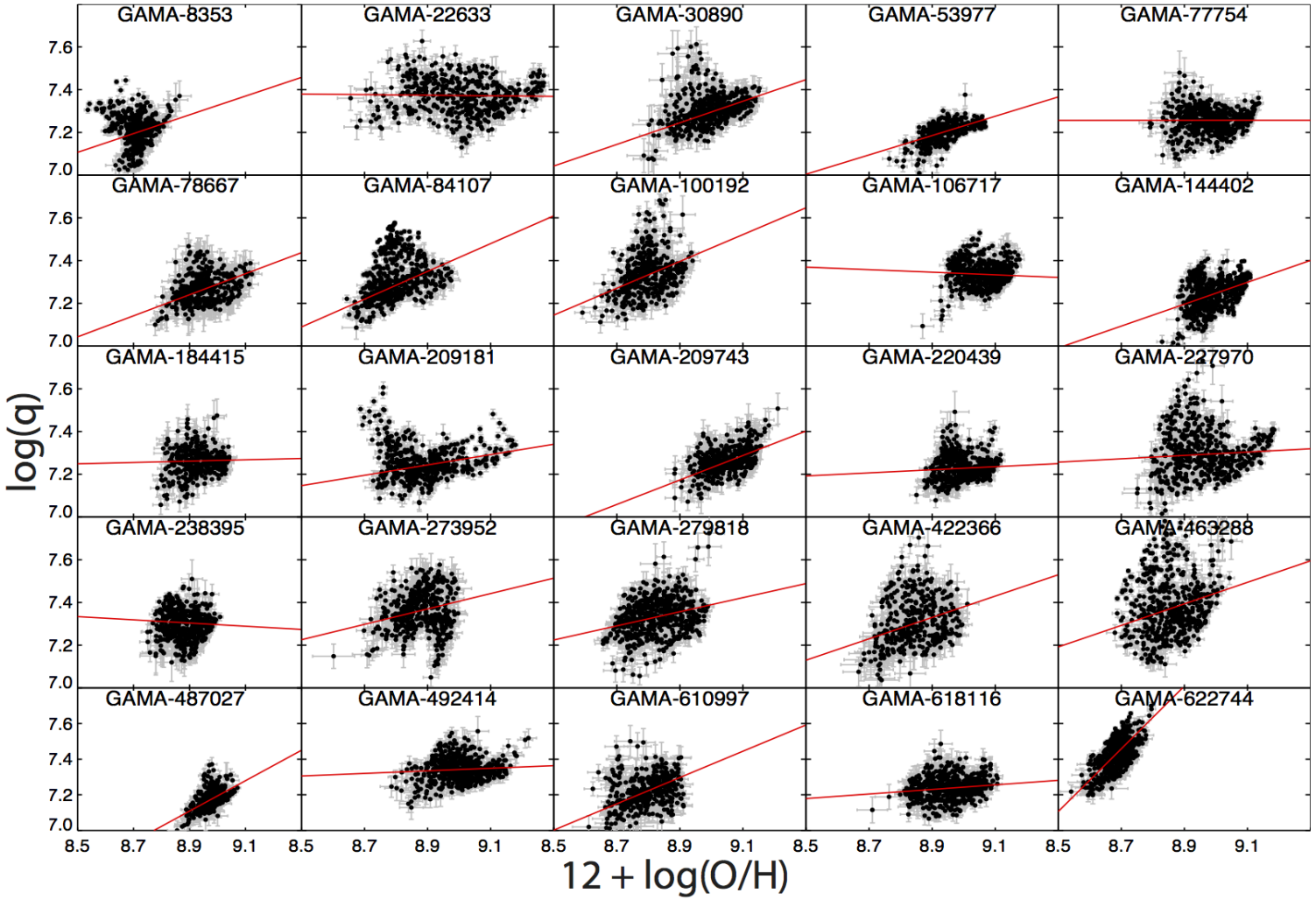

Figure 2.11 Relationship between the ionization parameter determined from the KK04 O32 diagnostic and the metallicity calculated from the KD02 N2O2 diagnostic. The best linear fit is given as a red line and we summarise the results in the Table 2.6.

Since there appears to be a dependence on metallicity gradients with stellar mass, sample selection plays an important role in the determination of mean metallicity gradients. Although Belfiore et al. (2017) uses a different metallicity calibration to the R_{23}diagnostic, we note that they seem to find a shallower, although still consistent, mean metallicity gradient (-0.08 ± 0.12 dex/R_e) than the ones determined here. The shallower mean metallicity gradient is caused by differences in sample selection. Belfiore et al. (2017) sample a wider stellar mass range, including relatively more low mass galaxies. Since metallicity gradients have a stellar mass dependence, these lower mass galaxies have shallower metallicity gradients and hence decrease the mean metallicity gradient of the sample. This effect is also demonstrated by Belfiore et al. (2017) with a shallower volume-limited mean metallicity gradient, where low mass galaxies are relatively heavier weighted.

Sánchez et al. (2012, 2014); Sánchez-Menguiano et al. (2016b) used the PP04 O3N2 diagnostic with their sample of CALIFA galaxies in order to analyse the metallicity gradients of galaxies and Sánchez-Menguiano et al. (2016b) found a mean metallicity gradient of -0.11 ± 0.07 dex/R_e. We recalculate our gradients using the PP04 O3N2 diagnostic and find a mean metallicity gradient of -0.10 ± 0.06 dex/R_e after excluding the inner ($R/R_e < 0.5$) and outer sections ($R/R_e > 2.0$) of the galaxies in the same way as Sánchez et al. (2012, 2014); Sánchez-Menguiano et al. (2016b). Our metallicity gradients are consistent with those presented in all three studies. Our results are also consistent with the PP04 O3N2 metallicity gradients presented in Belfiore et al. (2017), which found a mean metallicity gradient of -0.08 ± 0.10 dex/R_e. Belfiore et al. (2017) again presents with slightly shallower but still consistent mean metallicity gradient. Belfiore et al. (2017) also finds a mass dependence of the O3N2 metallicity gradients, meaning their wider stellar mass range may explain their slightly shallower mean metallicity gradient.

For metallicity diagnostics which display mass-dependent metallicity gradients, sample selection appears to have a strong influence on the calculated mean metallicity gradient. Therefore, care must be taken when comparing results between different studies as the stellar mass distribution of the sample may have a heavy impact on the results obtained.

Sánchez et al. (2012, 2014) and Sánchez-Menguiano et al. (2016b) excluded the inner ($R/R_e < 0.5$) and outer ($R/R_e > 2.0$) galactic radii when measuring the metallicity gradients because of the observed flattening of the metallicity gradient that occurs at these radii (Bresolin et al. 2009, 2012; Rosales-Ortega et al. 2011; Marino et al. 2012; Sánchez et al. 2012, 2014; Sánchez-Menguiano et al. 2016b). We find metallicity gradient flattening occurring at $R/R_e < 0.5$ only for GAMA-106717 using either the PP04 O3N2 or KK04 diagnostic. Only two of our galaxies (GAMA-144402 and GAMA-622744) are observed beyond $2R_e$, and neither show any clear flattening of the metallicity gradient.

Ho et al. (2015) used the KD02 metallicity diagnostic to determine the metallicity gradients of a sample of CALIFA and WiFeS galaxies. Using the R_{25} scale length to normalise the metallicity gradients, Ho et al. (2015) found no significant dependence on stellar mass. Ho et al. (2015) found a mean metallicity gradient of -0.39 ± 0.18 dex/R_{25}. We determine the metallicity gradients using the KD02 diagnostic, but the uncertainties in R_{25} for our sample were too large for a reliable comparison (based on values obtained from HyperLeda (Makarov et al. 2014)). We instead assume a crude approximation of R_{25}=3.6R_e based on fits to S0 galaxies by Williams et al. (2009). Using this approximation, we obtain a mean

GAMA ID	Central Ionization log(q)	Gradient dex/Re	RMS	PCC
008353	7.210±0.011	-0.017±0.010	0.086	-0.08
022633	7.392±0.010	-0.022±0.009	0.081	-0.12
030890	7.329±0.006	-0.039±0.008	0.059	0.00
053977	7.252±0.005	-0.047±0.005	0.038	-0.43
077754	7.236±0.005	0.024±0.006	0.051	0.18
078667	7.270±0.009	-0.010±0.013	0.060	0.08
084107	7.410±0.012	-0.108±0.011	0.091	-0.37
100192	7.286±0.012	0.059±0.015	0.084	0.24
106717	7.344±0.006	-0.010±0.005	0.048	-0.16
144402	7.312±0.008	-0.052±0.005	0.063	-0.40
184415	7.247±0.008	0.014±0.007	0.058	0.08
209181	7.263±0.009	-0.018±0.008	0.072	0.03
209743	7.284±0.007	-0.029±0.009	0.057	-0.21
220439	7.209±0.006	0.026±0.007	0.052	0.12
227970	7.230±0.012	0.063±0.011	0.095	0.25
238395	7.291±0.007	0.013±0.006	0.065	0.07
273952	7.306±0.010	0.066±0.011	0.086	0.29
279818	7.299±0.008	0.048±0.010	0.072	0.11
422366	7.303±0.014	0.006±0.020	0.109	0.01
463288	7.370±0.015	-0.006±0.018	0.135	0.03
487027	7.205±0.004	-0.033±0.006	0.043	-0.12
492414	7.312±0.007	0.032±0.007	0.059	0.09
610997	7.239±0.011	-0.025±0.012	0.087	-0.03
618116	7.229±0.006	0.010±0.006	0.055	0.09
622744	7.581±0.006	-0.144±0.005	0.062	-0.73

Table 2.3 List of ionization parameter gradients and intercepts with their 1σ uncertainties, root mean square (RMS) scatter and Pearson correlation coefficient (PCC) values.

metallicity gradient of -0.48 ± 0.18 dex/R_{25}. Although the metallicity gradients agree within the errors, it is important to keep in mind that we have only used an approximation to R_{25} and have used the R-band scale length instead of the B-band which was used in Ho et al. (2015).

2.6.2. Scatter around Metallicity Gradients

For the majority of metallicity gradients, the scatter increases noticeably at larger radii. Within $1R_e$, the standard deviation away from the metallicity gradient is approximately 0.04 dex and and increases to 0.08 dex beyond 1Re. We find that this is driven mostly by the decrease in line flux, and hence S/N, at larger radii in the SAMI data. At an integrated Hα S/N < 80 the scatter is 0.07 dex, whereas at a Hα S/N > 80 the scatter decreases to about 0.03 dex. However, a decrease in S/N does not account for all of the increase in scatter.

In five of our galaxies we notice that more than half of the spaxels within $1R_e$ have a S/N <

80, and have significantly less scatter than those spaxels at radii larger than $1R_e$. We also notice a large bias of the scatter towards lower metallicities. We find that spaxels which deviate more than 0.1dex from the metallicity gradient have an increased R_{23}line ratio. All these spaxels also lie on the upper branch of the KK04 R_{23}metallicity diagnostic. The combination of these two effects leads to a lower metallicity measurement. In addition, the KK04 R_{23}metallicity diagnostic becomes less sensitive to metallicity at higher values of R_{23}, which only enhances this deviation.

The larger R_{23}line ratio is caused by an increase in both the [OII]/Hβ and [OIII]/Hβ line ratios. The [OII]/Hβ line ratio has a larger percentage increase than the [OIII]/Hβ line ratio. This leads to an overall decrease in the [OIII]/[OII] line ratio, causing lower ionization parameter measurements for a metallicity range of 7.6 <12+log(O/H)< 9.2.

One explanation for the enhanced line ratios at large radii is diffuse ionized gas (DIG) contamination. Using data from the MaNGA survey, Zhang et al. (2017) demonstrated the effects of DIG on emission line ratios and metallicity diagnostics. They found that the [OII]/Hβ line ratio is enhanced in DIG dominated regions, while the DIG effects on the [OIII]/Hβ line ratio depends on the specific situation of the galaxy. In both cases, they also found a decrease in the [OIII]/[OII] line ratio.

2.6.3. Mass-Metallicity Relation

Figure 2.6 shows the metallicity intercepts as a function of stellar mass with the mass-metallicity fit from Kewley & Ellison (2008) shown as the dotted red line. A small positive offset of 0.13 was required to optimally fit the mass-metallicity relation to the intercept data, this is shown as the solid red line. This is to account for the fact that we are using the interpolated central metallicity which simulates an infinitesimally small central aperture. The interpolated central metallicity would be systematically higher than the global metallicity or larger aperture metallicity measurements because we are not averaging the regions of high and low metallicity. Tremonti et al. (2004) was able to simulate the effects of changing aperture metallicity measurements by showing that nearer galaxies had larger aperture metallicities than those further away of similar size. The nearer galaxies had a larger apparent size, meaning that they were restricted to sampling a smaller fraction of the galaxy.

2.6.4. Ionization Parameter Gradients

The ionization parameter maps produced by Kaplan et al. (2016) show significant radial ionization parameter gradients as well as a correlation with SFR. Correlation between ionization parameter and SFR was also observed by Dopita et al. (2014) using a sample of WiFeS galaxies.

Yuan et al. (2013); Mast et al. (2014) have shown that decreased spatial resolution leads to the flattening of observed metallicity gradients. Kaplan et al. (2016) has a median resolution of 387pc, while the full SAMI survey has resolutions on the order of kpc. Our galaxy sample has a median spatial resolution of 1.3kpc/PSF caused by the seeing limited observations with an average seeing of 2.16″ and DAR smoothing of 0.8″. Our galaxies are significantly

less massive and have a higher redshift, meaning that fine details are difficult to resolve compared to Kaplan et al. (2016). It is possible that the lack of ionization parameter gradients is due to the spatial smoothing caused by our inability to resolve the finer details due to limitations in seeing. More work using higher resolution data is needed in order to confirm if ionization parameter gradients are affected in the same way as metallicity gradients.

The SAMI spectrograph does not have the spatial resolution required to resolve HII regions at the redshift of the main galaxy survey. To obtain higher spatial resolution spectra of HII regions, a sister survey of nearby HII regions is being conducted in order to recalibrate the strong line emission diagnostics (SAMI Zoom, Sweet et al. In Prep).

The galaxies used in Kaplan et al. (2016) are also more massive ($10.2 < \log(M_*/M_\odot) < 11.6$) than the mass range of the galaxies ($9.0 < \log(M_*/M_\odot) < 10.5$) used in this study. Although we find no variation in ionization parameter gradient or intercept with mass, the difference in galaxy masses could be a factor in the absence of ionization parameter gradients.

2.6.5. Ionization Parameter and Galaxy Properties

Dopita et al. (2014) quantified the relationship between ionization parameter and $\mathrm{SFR}[\mathrm{M}_\odot/\mathrm{year}/\mathrm{kpc}^2]$ as $q[\mathrm{cm/s}] \propto \mathrm{SFR}[\mathrm{M}_\odot/\mathrm{year}/\mathrm{kpc}^2]^{0.34\pm0.08}$ when $\log(q[\mathrm{cm/s}]) \gtrsim 7.2-7.4$. From Figure 13 of Dopita et al. (2014), we observe that below $\log(\mathrm{SFR}[\mathrm{M}_\odot/\mathrm{year}/\mathrm{kpc}^2]) < -0.5$, the correlation disappears and no trends are observed. Figure 2.10 shows that all of our spaxels lie below $\log(\mathrm{SFR}[\mathrm{M}_\odot/\mathrm{year}/\mathrm{kpc}^2]) < -0.5$ with the large majority below $\log(\mathrm{SFR}[\mathrm{M}_\odot/\mathrm{year}/\mathrm{kpc}^2]) < -1.0$. We believe that this is the main reason that we do not observe the same trends as Dopita et al. (2014). The sSFR is even less correlated with ionization parameter, with PCC values consistently lower than those of SFR.

GAMA-622744 is the only galaxy that displays a significant correlation between metallicity and ionization parameter. However we believe this is not necessarily caused by an intrinsic relationship between metallicity and ionization parameter, but rather because GAMA-622744 is the only galaxy which possess a significant ionization parameter gradient. The positive correlation contradicts the theoretical relation presented in Dopita et al. (2006) ($q[\mathrm{cm/s}] \propto Z[\mathrm{O/H}]^{-0.8}$). Many of the galaxies in Dopita et al. (2014) show a positive correlation between ionization parameter and metallicity while our work lacks any significant trends.

2.6.6. Ionization Parameter effects on Metallicity Diagnostics

In Figure 2.9, we see that the typical ionization parameter range for our galaxy sample is $7.0 < \log(q[\mathrm{cm/s}]) < 7.8$. An ionization parameter range this wide is enough to significantly affect the metallicity estimates for several metallicity diagnostics (Kewley & Dopita 2002). As there are no discernible patterns in the distribution of ionization parameter, it makes it difficult to predict how the exclusion of ionization parameter will affect the metallicity distribution. We advise caution when interpreting results which have used metallicity diagnostics where ionization parameter has not been taken into account.

2.7. Summary

We have presented metallicity and ionization parameter maps of 25 high-S/N face-on star-forming galaxies in DR1 of the SAMI galaxy survey. To account for their interdependence, metallicity and ionization parameter were determined simultaneously for individual spaxels using an iterative method involving the strong emission line diagnostics outlined in Kobulnicky & Kewley (2004).

We measure metallicity gradients as a function of galactocentric radius using robust line fitting routines. We find that the majority of galaxies exhibit a negative metallicity gradient with an average metallicity gradient of -0.12±0.05 dex/R_e using the KK04 R_{23}diagnostic. Metallicity gradients show a weak negative correlation with the stellar mass of galaxies.

Using the PP04 O3N2 metallicity diagnostic we find an average metallicity gradient of -0.10±0.06 dex/Re, which agrees with the gradients determined by Sánchez et al. (2012, 2014); Sánchez-Menguiano et al. (2016b) and Belfiore et al. (2017). Due to the unreliable R_{25} measurements of the galaxies in our sample, we are unable to directly compare our metallicity gradient value to Ho et al. (2015). However, assuming $R_{25} = 3.6R_e$ based on Williams et al. (2009), we find an average N2O2 metallicity gradient of -0.48 ± 0.18, consistent with that of Ho et al. (2015).

Using the central metallicities of each galaxy based on the linear fits, we find that our galaxies are in agreement with the mass-metallicity relation polynomial presented in Kewley & Ellison (2008) after applying a positive offset of 0.13 dex. The offset is likely a result of using interpolated central metallicities rather than the aperture average value as determined for SDSS.

We show that the ionization parameter maps lack significant or coherent structure unlike the metallicity maps. We do not see significant ionization parameter gradients like those presented in Kaplan et al. (2016), however this could be due to sample selection differences or spatial resolution limitations. We do find a decrease in ionization parameter in the inter-arm regions of galaxies with resolvable spiral arms indicating a possible correlation between ionization parameter and SFR. However for our galaxy sample, we find no significant correlations between ionization parameter and SFR or sSFR.

Until a better understanding is achieved on the distribution of ionization parameter, metallicity diagnostics must be used with care. We suggest that in order to obtain reliable metallicity maps, to either use a metallicity diagnostic which explicitly provides solutions for a range of ionization parameter like the one used in this study (eg. KK04 R23), or use a metallicity diagnostic which is relatively invariant to changes in ionization parameter (eg. KD02 N2O2 or D16 N2S2).

Acknowledgements

The SAMI Galaxy Survey is based on observations made at the Anglo-Australian Telescope. The Sydney-AAO Multi-object Integral field spectrograph (SAMI) was developed jointly by the University of Sydney and the Australian Astronomical Observatory. The SAMI input catalogue is based on data taken from the Sloan Digital Sky Survey, the GAMA Survey and

the VST ATLAS Survey. The SAMI Galaxy Survey is funded by the Australian Research Council Centre of Excellence for All-sky Astrophysics (CAASTRO), through project number CE110001020, and other participating institutions. The SAMI Galaxy Survey website is http://sami-survey.org/.
Parts of this research were conducted by the Australian Research Council Centre of Excellence for All Sky Astrophysics in 3 Dimensions (ASTRO 3D), through project number CE170100013.
BG gratefully acknowledges the support of the Australian Research Council as the recipient of a Future Fellowship (FT140101202).
Support for AMM is provided by NASA through Hubble Fellowship grant #HST-HF2-51377 awarded by the Space Telescope Science Institute, which is operated by the Association of Universities for Research in Astronomy, Inc., for NASA, under contract NAS5-26555.
JvdS is funded under Bland-Hawthorn's ARC Laureate Fellowship (FL140100278).
SFS thanks CONACYT programs CB-285080 and DGAPA-PAPIIT IA101217 grants for their support to this project.
SB acknowledges the funding support from the Australian Research Council through a Future Fellowship (FT140101166).
MSO acknowledges the funding support from the Australian Research Council through a Future Fellowship (FT140100255).
NS acknowledges support of a University of Sydney Postdoctoral Research Fellowship.

2.8. Appendix: Metallicity Maps

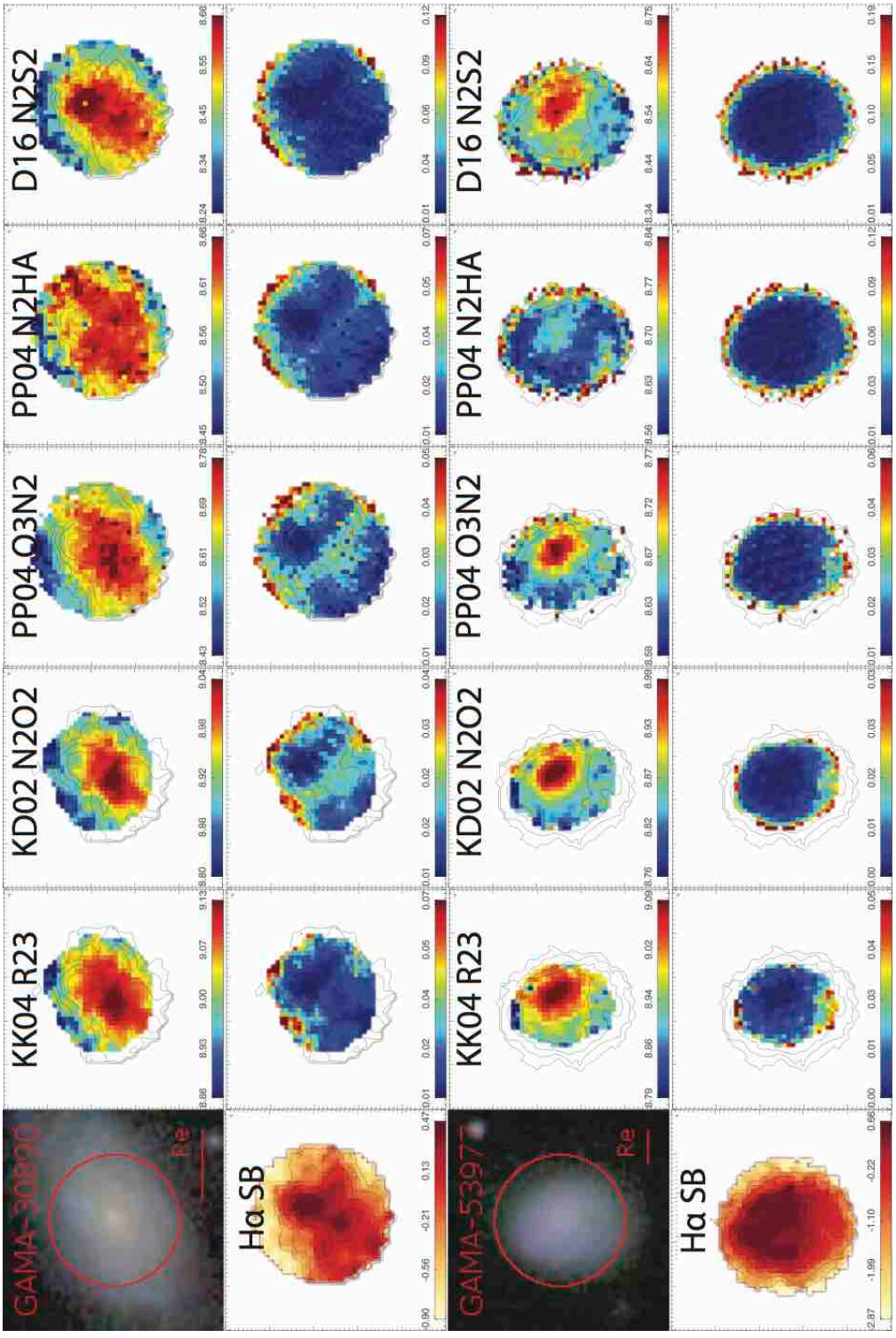

Figure 2.12 Same as Figure 2.2 for GAMA-30890 and GAMA-53977.

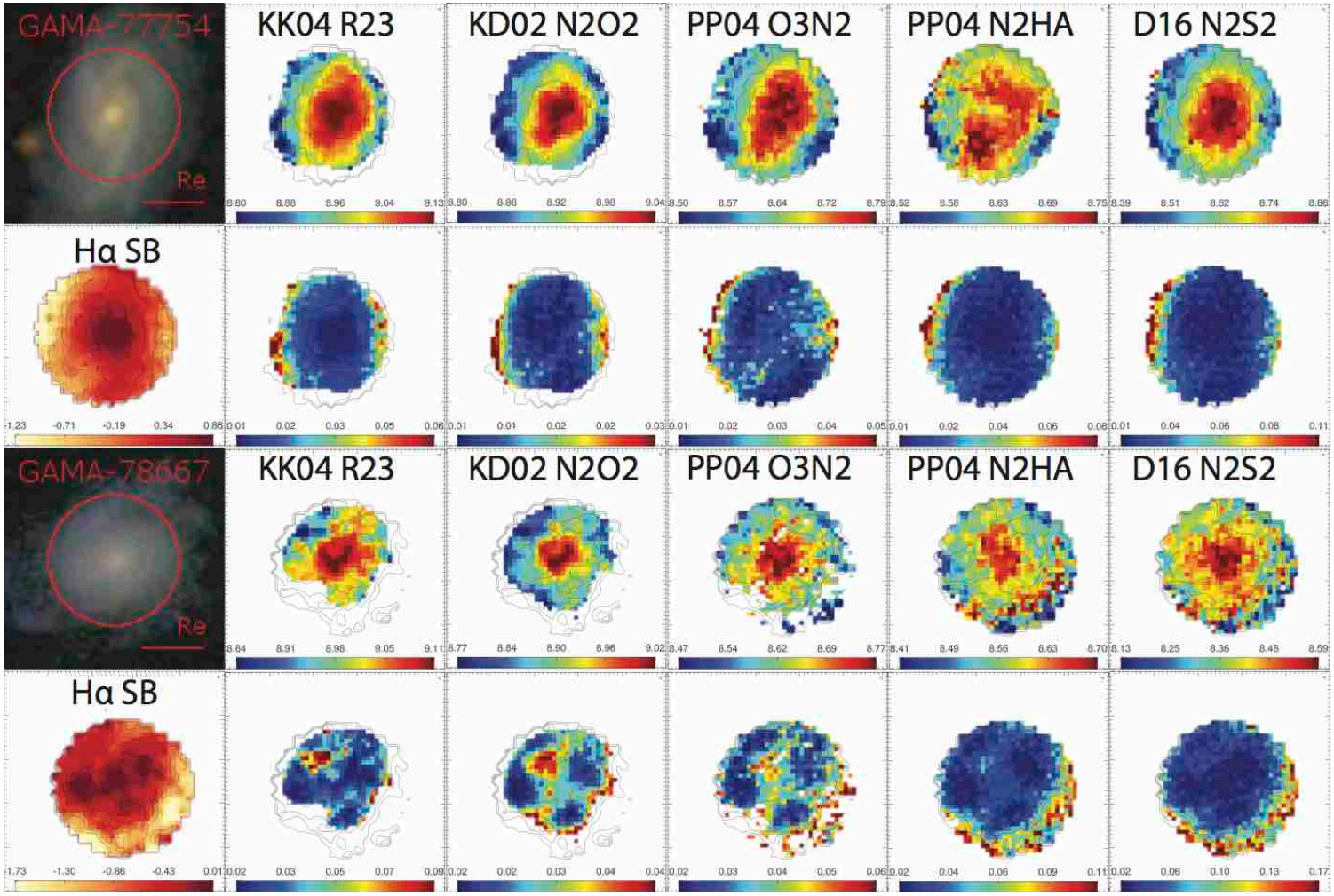

Figure 2.13 Same as Figure 2.2 for GAMA-77754 and GAMA-78667.

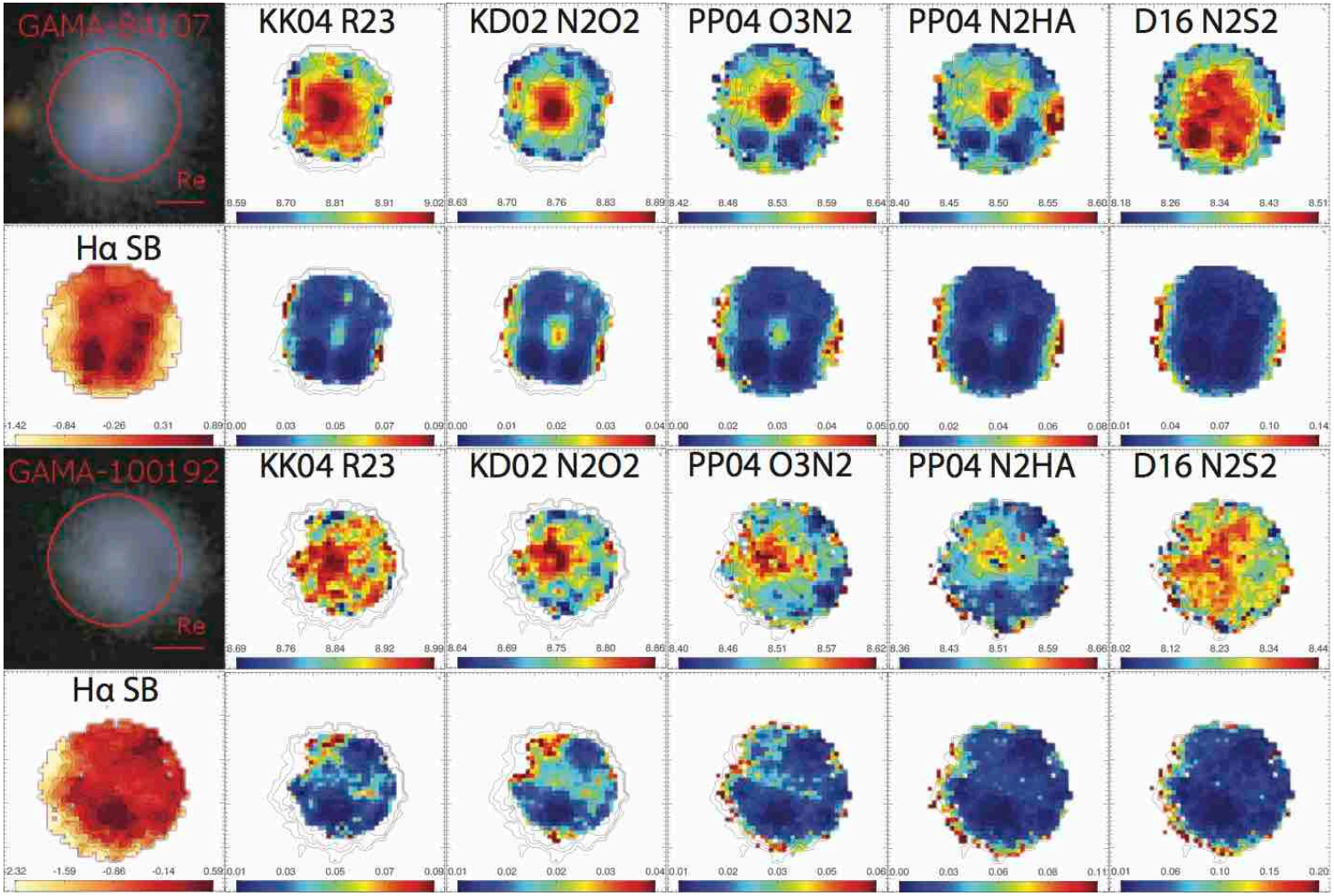

Figure 2.14 Same as Figure 2.2 for GAMA-84107 and GAMA-100192.

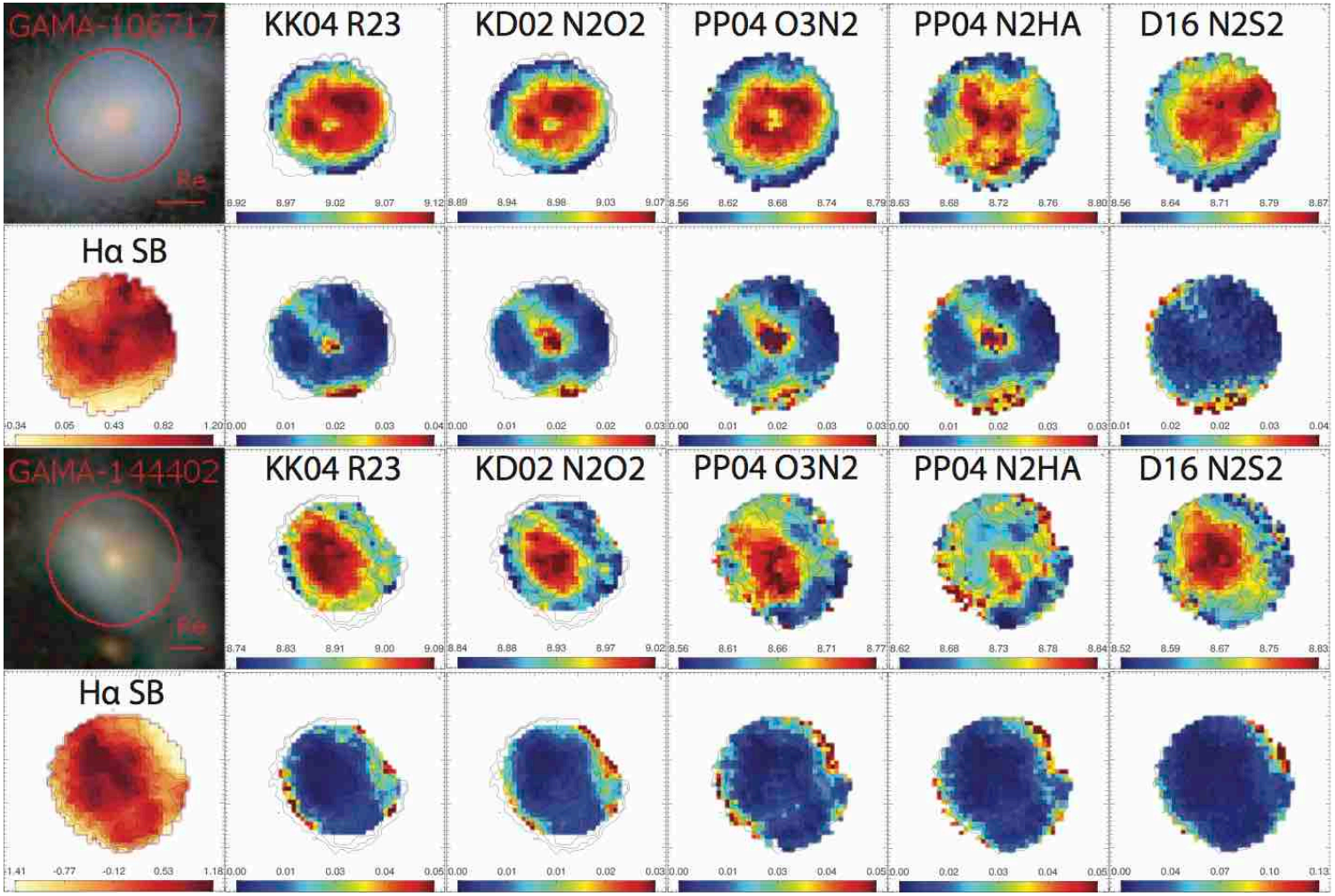

Figure 2.15 Same as Figure 2.2 for GAMA-106717 and GAMA-144402.

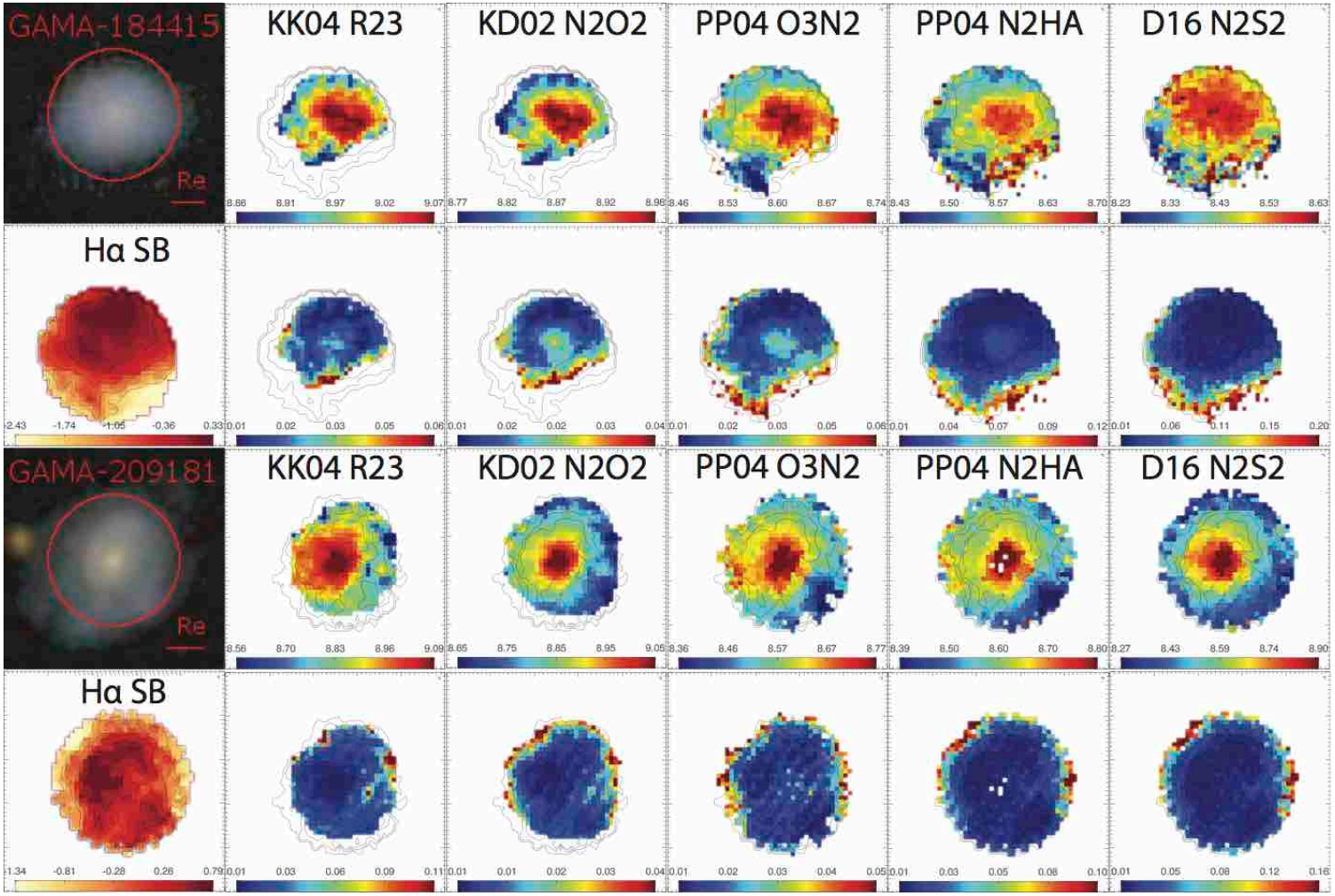

Figure 2.16 Same as Figure 2.2 for GAMA-184415 and GAMA-209181.

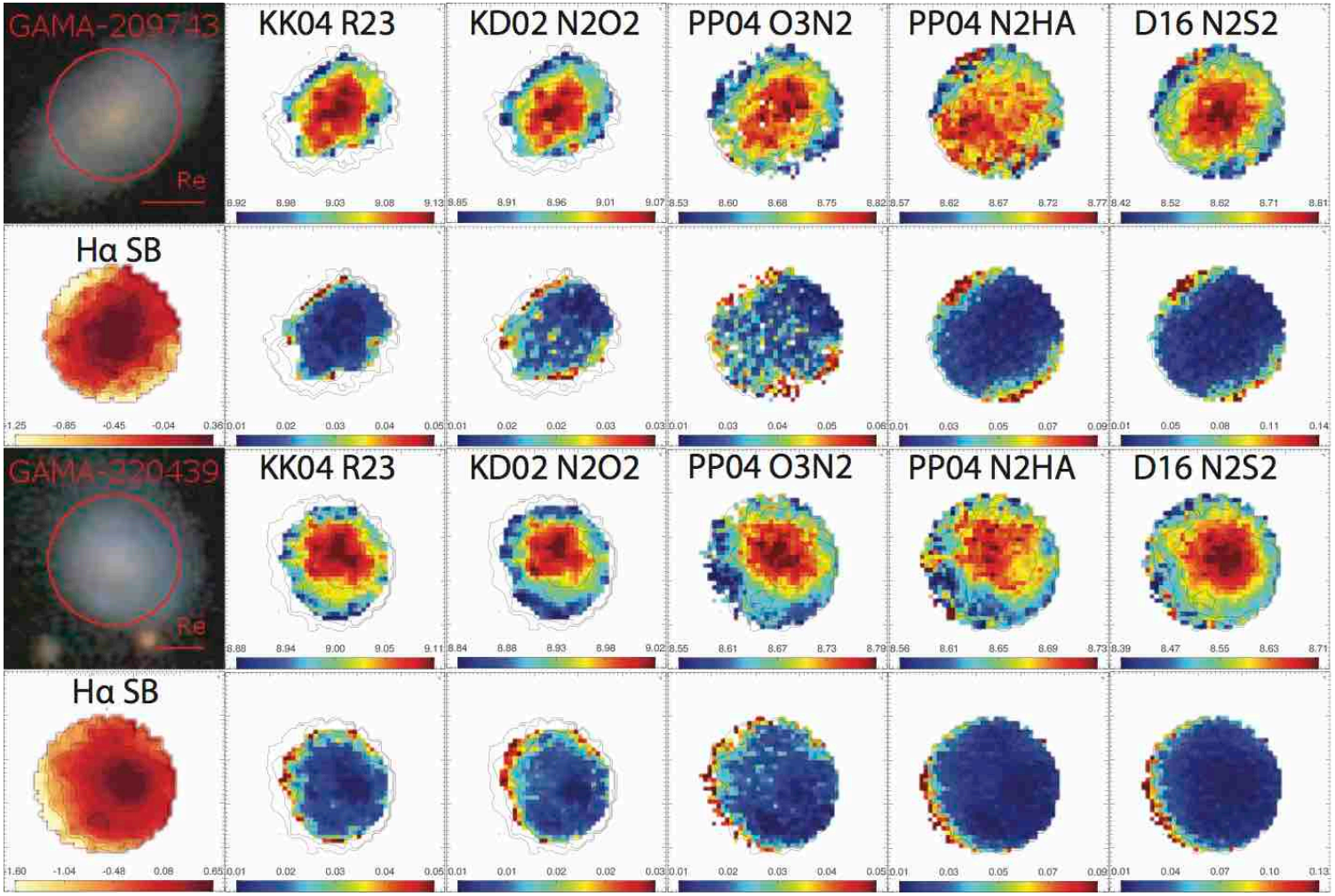

Figure 2.17 Same as Figure 2.2 for GAMA-209743 and GAMA-220439.

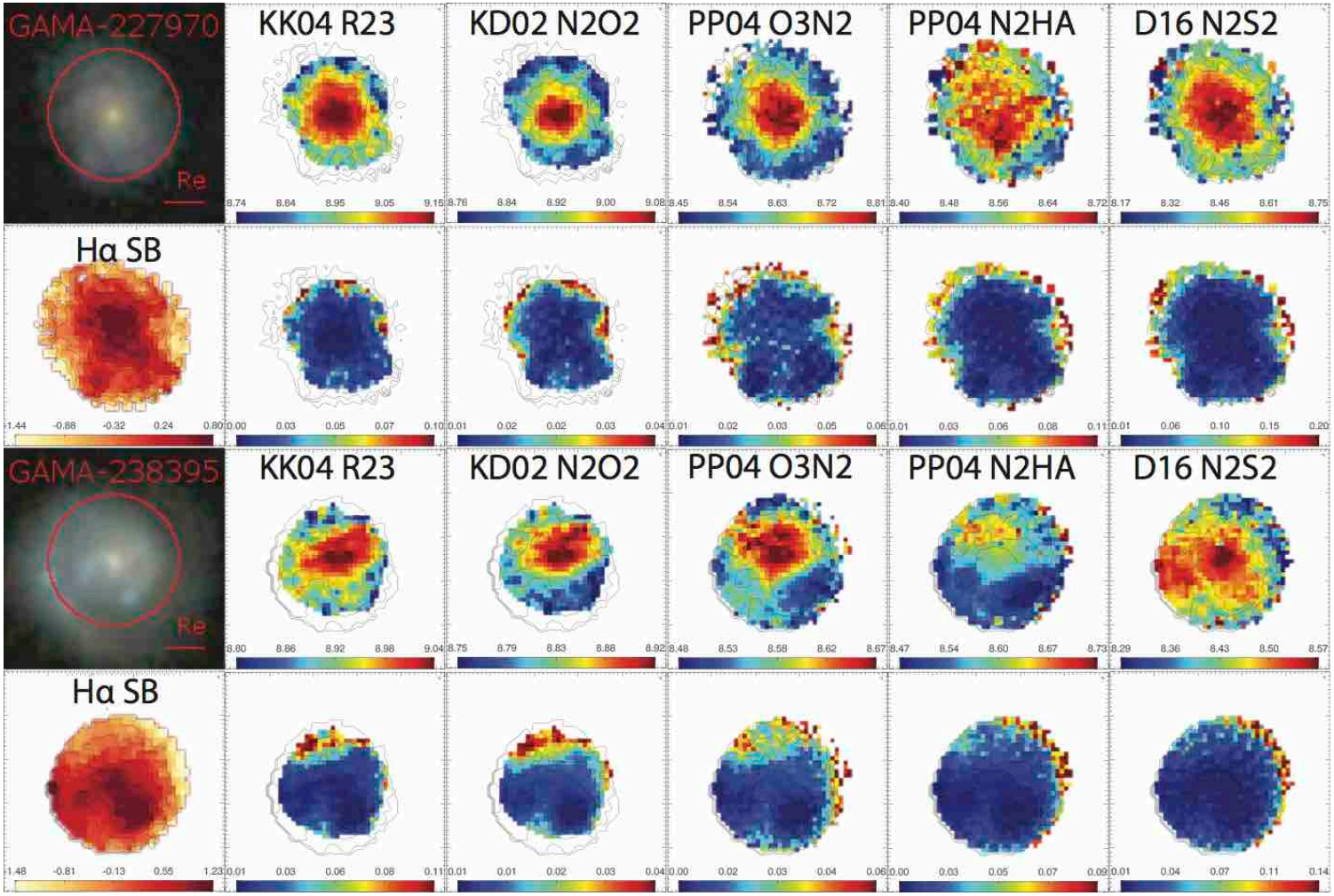

Figure 2.18 Same as Figure 2.2 for GAMA-227970 and GAMA-238395.

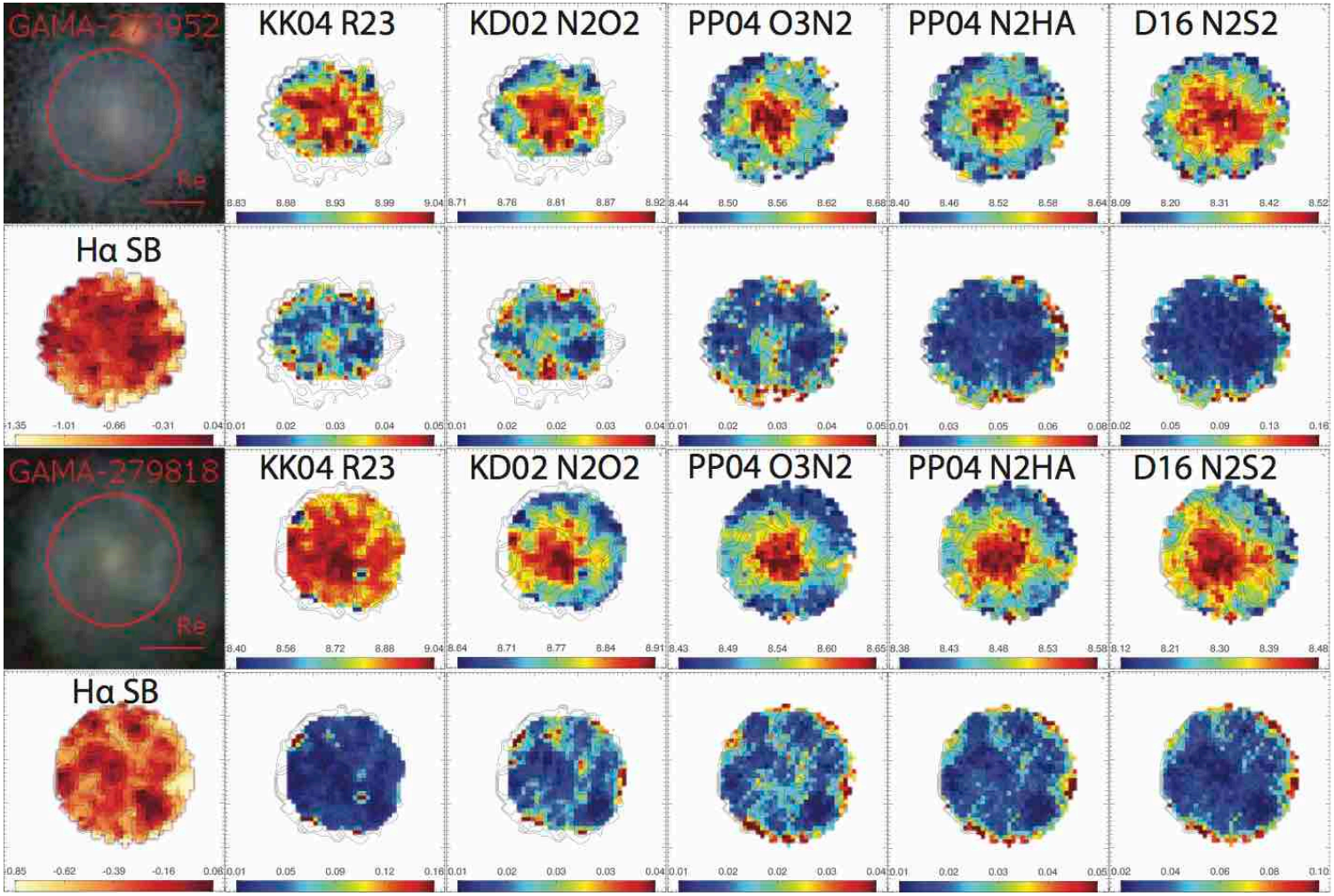

Figure 2.19 Same as Figure 2.2 for GAMA-273952 and GAMA-279818.

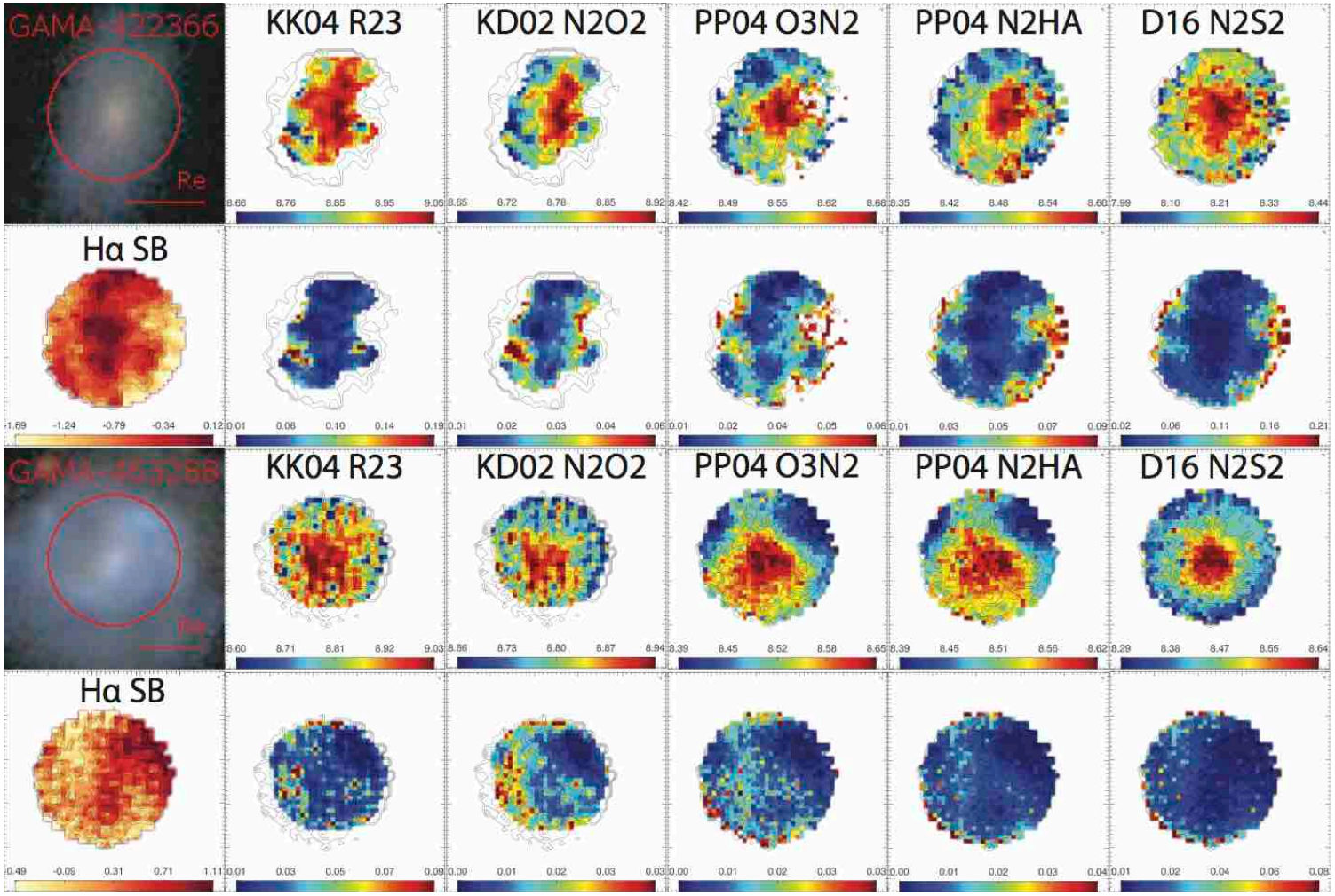

Figure 2.20 Same as Figure 2.2 for GAMA-422366 and GAMA-463288.

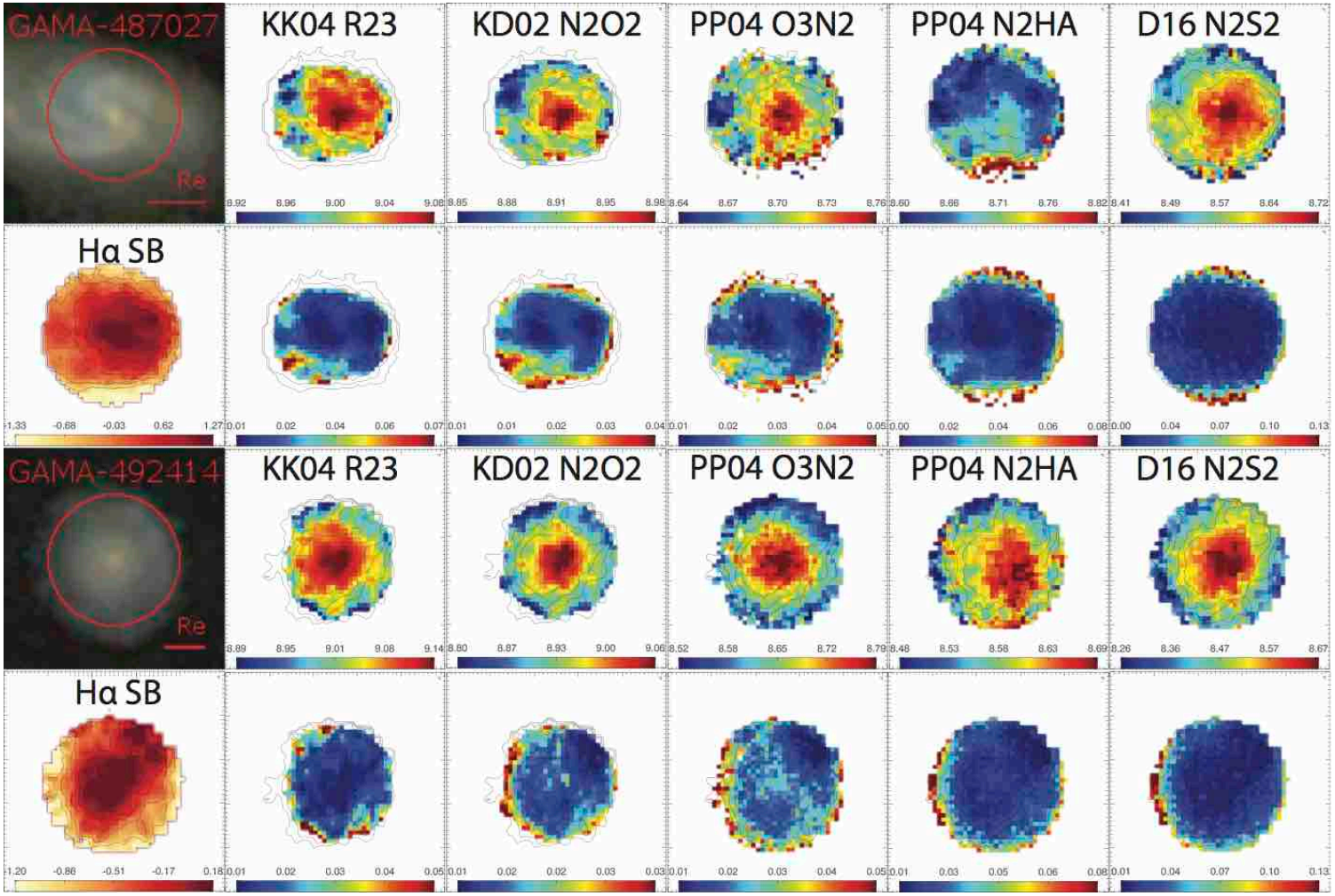

Figure 2.21 Same as Figure 2.2 for GAMA-487027 and GAMA-492414.

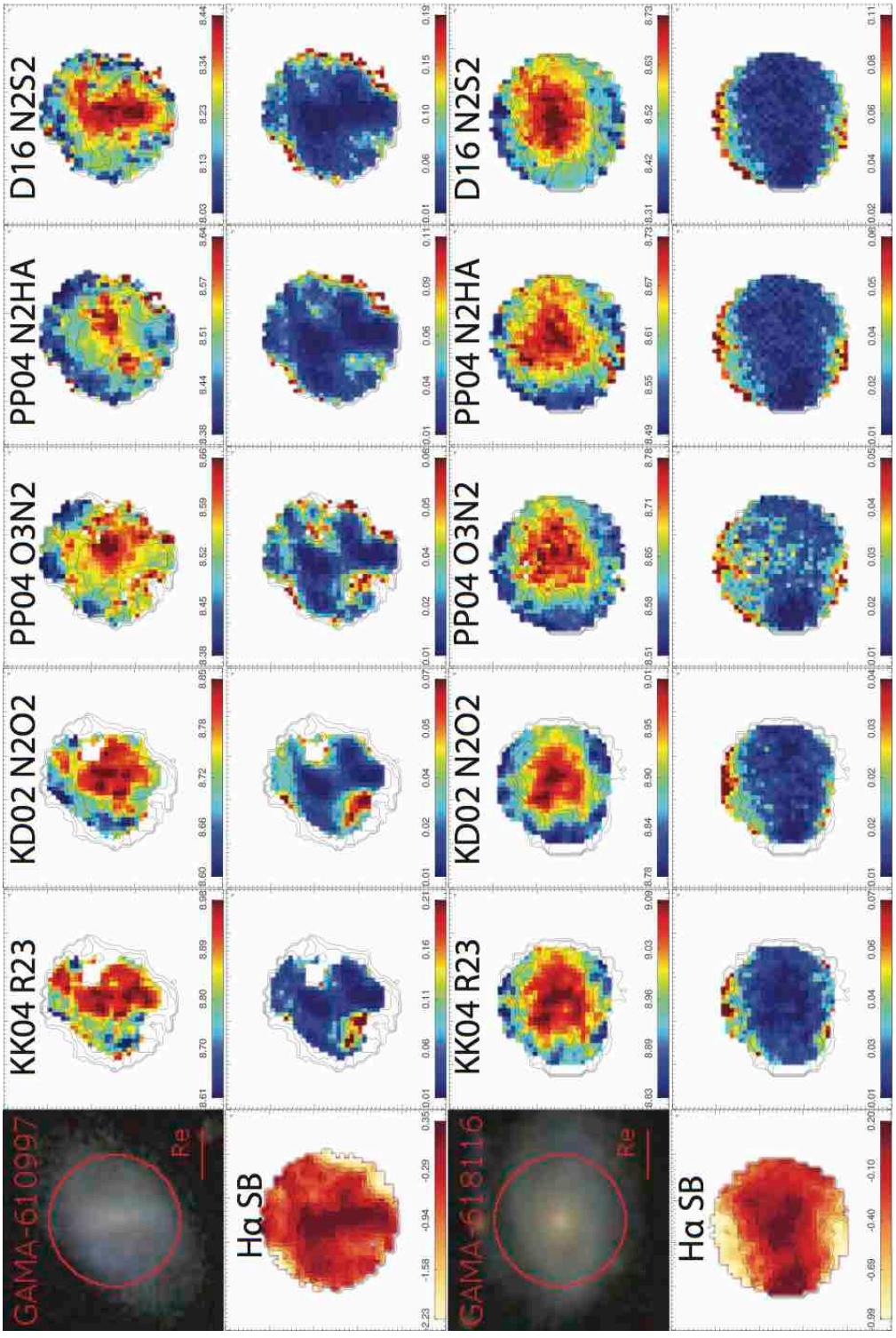

Figure 2.22 Same as Figure 2.2 for GAMA-610997 and GAMA-618116.

2.9. Appendix: Ionization Parameter Maps

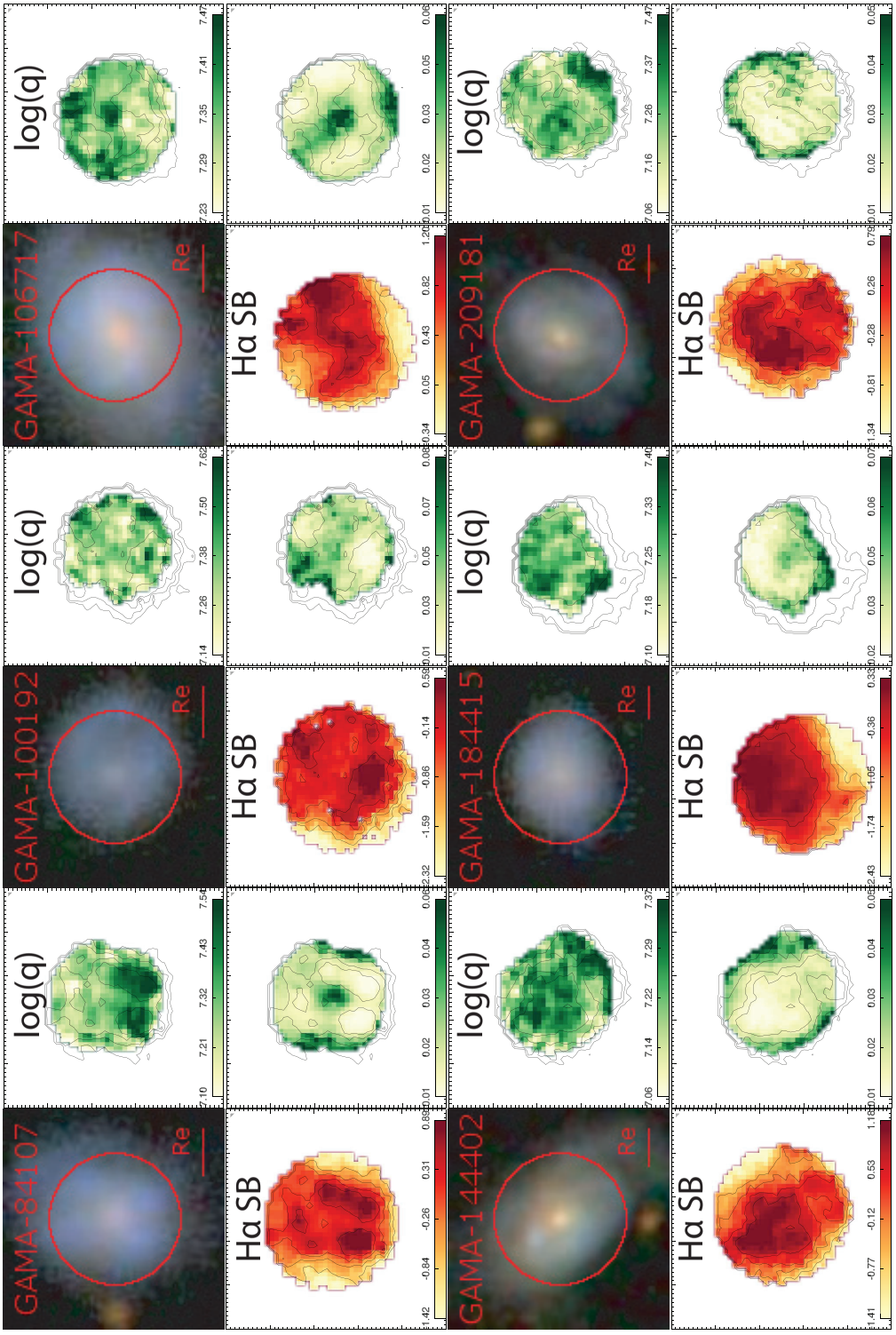

Figure 2.23 Same as Figure 2.8 for GAMA-84107, GAMA-100192, GAMA-106717, GAMA-144402, GAMA-184415 and GAMA-209181.

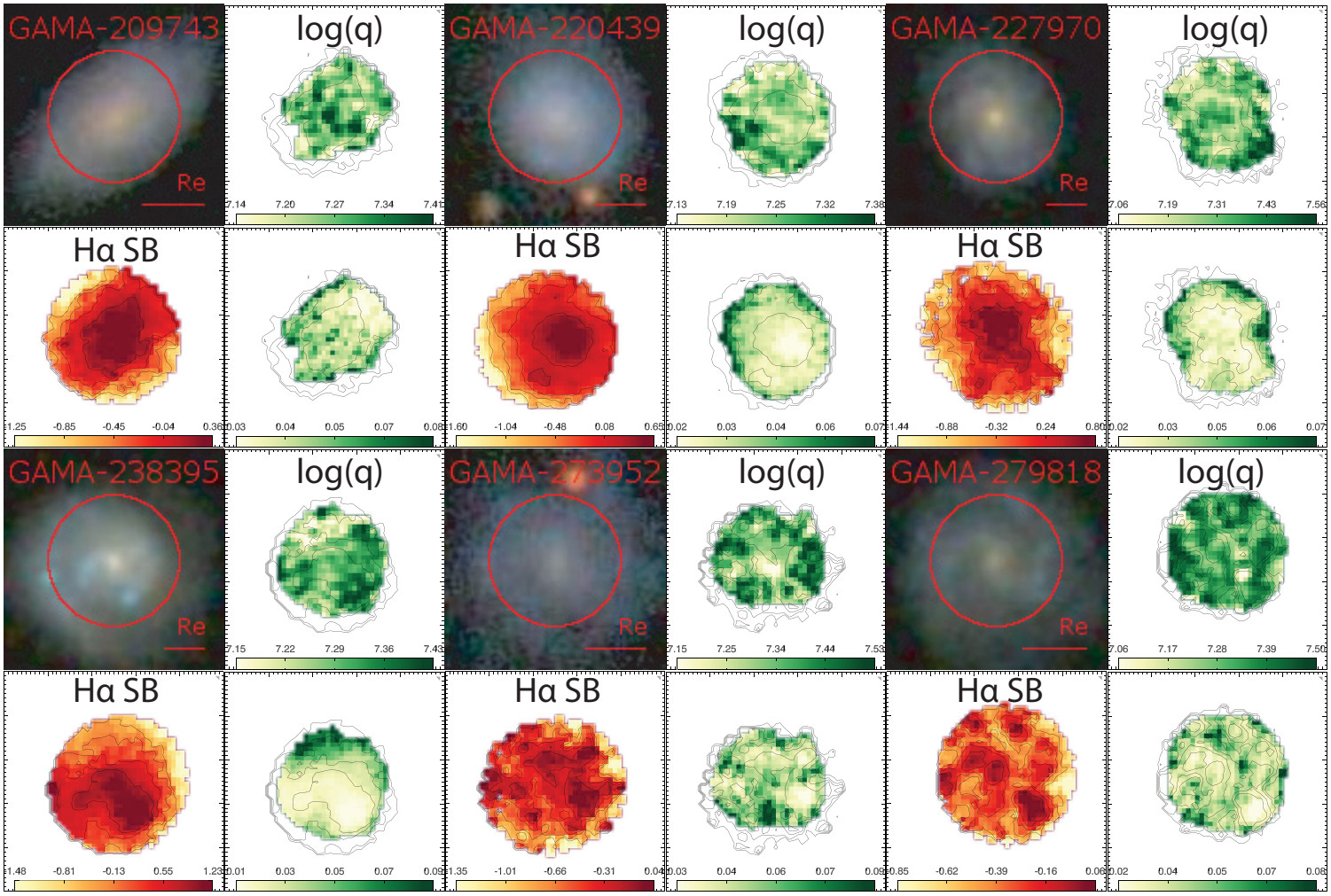

Figure 2.24 Same as Figure 2.8 for GAMA-209743, GAMA-220439, GAMA-227970, GAMA-238395, GAMA-273952 and GAMA-279818.

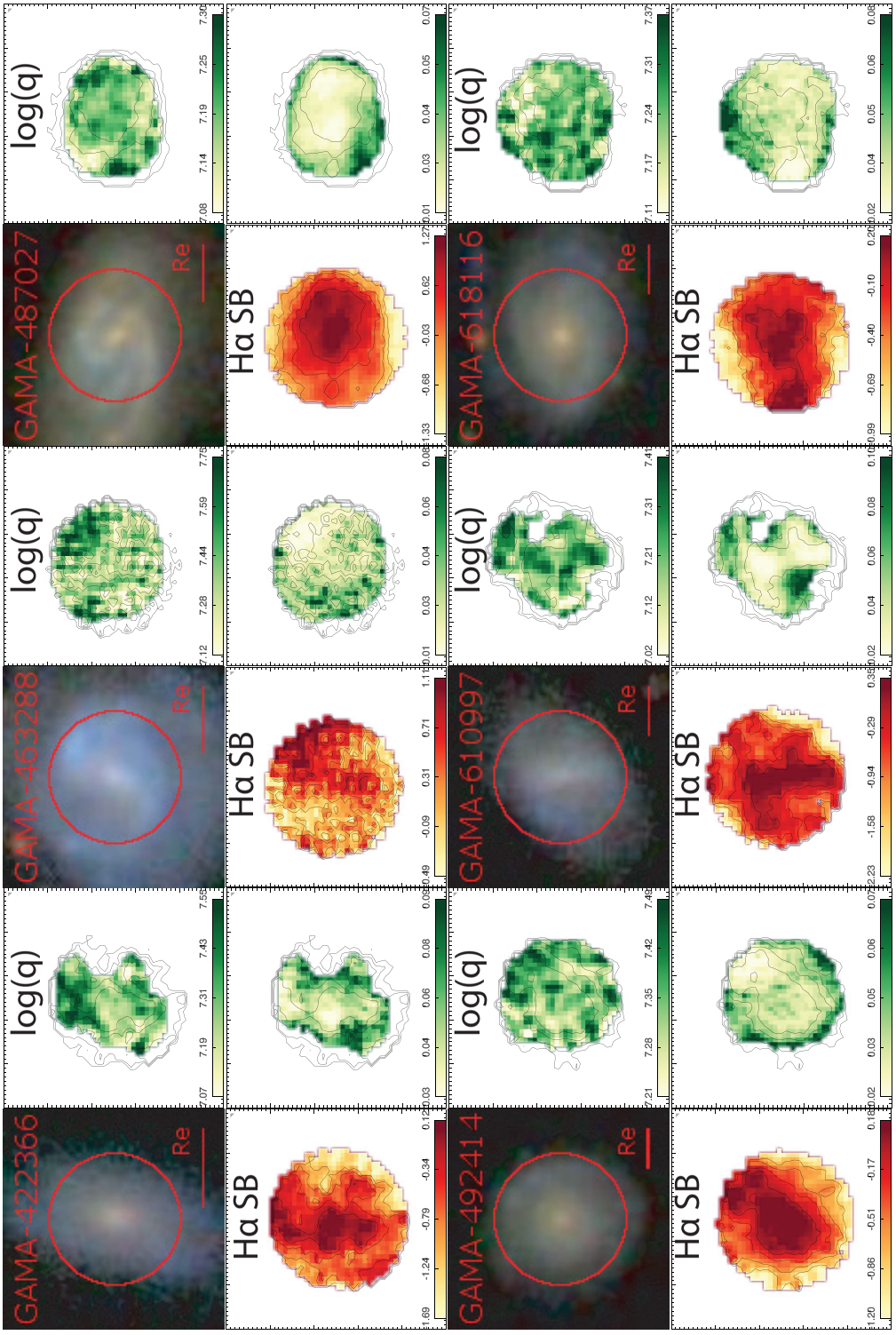

Figure 2.25 Same as Figure 2.8 for GAMA-422366, GAMA-463288, GAMA-487027, GAMA-492414, GAMA-610997 and GAMA-618116.

2.10. Appendix: Tables

GAMA ID	Intercept 12+log(O/H)	Gradient dex/log(SFR)	RMS	PCC
008353	8.837±0.017	0.037±0.010	0.060	0.22
022633	9.273±0.016	0.148±0.010	0.075	0.48
030890	9.334±0.013	0.146±0.007	0.046	0.71
053977	9.139±0.013	0.091±0.008	0.049	0.40
077754	9.310±0.008	0.182±0.005	0.045	0.81
078667	9.317±0.025	0.132±0.012	0.049	0.38
084107	9.010±0.015	0.074±0.008	0.074	0.34
100192	8.902±0.016	-0.003±0.008	0.063	0.02
106717	9.214±0.006	0.129±0.005	0.032	0.63
144402	9.149±0.007	0.113±0.004	0.046	0.71
184415	9.089±0.019	0.047±0.010	0.050	0.34
209181	9.167±0.021	0.167±0.013	0.101	0.49
209743	9.493±0.014	0.235±0.008	0.034	0.75
220439	9.296±0.011	0.147±0.006	0.037	0.65
227970	9.301±0.014	0.181±0.009	0.077	0.63
238395	8.992±0.008	0.029±0.006	0.052	0.36
273952	8.951±0.023	-0.010±0.010	0.047	-0.06
279818	8.981±0.041	0.027±0.018	0.080	0.02
422366	9.155±0.024	0.082±0.011	0.073	0.31
463288	8.890±0.017	0.002±0.010	0.085	-0.02
487027	9.114±0.002	0.066±0.002	0.023	0.74
492414	9.362±0.011	0.146±0.006	0.040	0.58
610997	9.051±0.021	0.076±0.010	0.077	0.35
618116	9.461±0.019	0.221±0.009	0.049	0.46
622744	8.879±0.006	0.024±0.004	0.042	0.28

Table 2.4 Linear fit parameters for Figure 2.4

GAMA ID	Intercept log(q)	Gradient dex/log(SFR)	RMS	PCC
008353	7.570±0.019	0.213±0.011	0.065	0.58
022633	7.457±0.016	0.053±0.010	0.076	0.15
030890	7.368±0.018	0.036±0.010	0.059	-0.02
053977	7.289±0.011	0.052±0.007	0.040	0.28
077754	7.242±0.010	-0.009±0.006	0.051	-0.08
078667	7.103±0.034	-0.075±0.015	0.062	-0.21
084107	7.602±0.018	0.166±0.010	0.084	0.53
100192	7.444±0.028	0.059±0.014	0.083	0.20
106717	7.364±0.008	0.025±0.007	0.047	0.21
144402	7.323±0.009	0.051±0.006	0.061	0.33
184415	7.396±0.023	0.071±0.012	0.054	0.02
209181	7.367±0.016	0.074±0.009	0.069	0.32
209743	7.341±0.027	0.044±0.015	0.057	0.14
220439	7.174±0.015	-0.032±0.008	0.053	-0.13
227970	7.221±0.021	-0.045±0.013	0.096	-0.12
238395	7.388±0.009	0.063±0.007	0.060	0.38
273952	7.363±0.047	0.001±0.021	0.088	-0.03
279818	7.437±0.041	0.046±0.019	0.074	-0.01
422366	7.376±0.049	0.029±0.022	0.107	0.10
463288	7.573±0.029	0.121±0.017	0.134	0.28
487027	7.238±0.006	0.046±0.005	0.043	0.23
492414	7.368±0.020	0.012±0.010	0.062	0.05
610997	7.358±0.027	0.069±0.013	0.084	0.12
618116	7.182±0.020	-0.028±0.010	0.055	-0.16
622744	7.677±0.011	0.144±0.006	0.060	0.65

Table 2.5 Linear fit parameters for Figure 2.10

GAMA ID	Intercept log(q)	Gradient dex/Z	RMS	PCC
008353	2.843±0.644	0.502±0.074	0.083	0.28
022633	7.517±0.291	-0.016±0.033	0.079	0.01
030890	2.132±0.333	0.578±0.037	0.051	0.31
053977	2.612±0.314	0.517±0.035	0.036	0.67
077754	7.250±0.298	0.001±0.033	0.052	0.02
078667	2.256±0.436	0.563±0.049	0.054	0.33
084107	0.777±0.438	0.743±0.050	0.066	0.41
100192	1.045±0.630	0.718±0.072	0.079	0.38
106717	7.953±0.381	-0.069±0.042	0.049	0.11
144402	2.011±0.495	0.586±0.055	0.065	0.42
184415	6.944±0.508	0.036±0.057	0.058	0.13
209181	4.796±0.308	0.277±0.035	0.070	0.15
209743	1.378±0.455	0.655±0.051	0.052	0.51
220439	6.491±0.389	0.082±0.044	0.051	0.15
227970	6.496±0.472	0.090±0.053	0.097	0.12
238395	8.063±0.503	-0.086±0.057	0.065	0.02
273952	3.725±0.630	0.412±0.071	0.085	0.16
279818	4.015±0.424	0.378±0.048	0.078	0.44
422366	2.275±0.684	0.571±0.078	0.102	0.33
463288	2.297±0.705	0.576±0.080	0.131	0.30
487027	-1.538±0.421	0.977±0.047	0.034	0.56
492414	6.602±0.382	0.083±0.043	0.062	0.17
610997	-0.171±0.462	0.844±0.053	0.071	0.40
618116	5.933±0.305	0.147±0.034	0.055	0.19
622744	-9.987±0.721	2.011±0.083	0.068	0.73

Table 2.6 Linear fit parameters for Figure 2.11

CHAPTER 3

The Missing Environmental Dependence of Metallicity Gradients

This chapter presents the content of the article: The SAMI Galaxy Survey: The Missing Environmental Dependence of Metallicity Gradients. This article is currently in preparation and will be submitted to the Monthly Notices of the Royal Astronomical Society. The abstract of this chapter is as follows:

It has been previously shown that the gas-phase metallicity radial gradients of merging galaxies are significantly flatter than those of isolated galaxies. However, at what point this flattening occurs in the merger process is still not clear. We explore the relationship between the gas-phase metallicity gradients of 248 galaxies from Data Release 2 of the SAMI Galaxy Survey and environmental density. We measure metallicity gradients using the Scal diagnostic and remove the stellar-mass dependence by fitting and subtracting the mass-metallicity gradient relation. The residuals are then split into three groups: steeper, flatter and consistent with the mass-metallicity gradient relation. Using three environmental density parameters from the GAMA survey, we find no evidence for variation of the metallicity gradient with density. We discuss the possible reasons for this null result and outline the steps required for future work on this topic.

3.1. Introduction

The gas-phase metallicity (hereafter metallicity) distribution of a galaxy provides a wealth of information into its star-formation history and is hence considered one of the most fundamental properties of the galaxy. Early studies of the metallicity distribution revealed that isolated galaxies typically have negative radial metallicity gradients, where the heavy element abundances in the central regions are relatively higher than the outskirts (Vila-Costas & Edmunds 1992; Zaritsky et al. 1994; Moustakas et al. 2010; Rupke et al. 2010). With advancements in integral field spectroscopy (IFS), the spatial distribution of metallicity can be mapped for thousands of galaxies relatively easily. These large datasets have confirmed that isolated galaxies posses negative metallicity gradients, however there is currently

conflicting results regarding its dependence on stellar mass. Studies completed using the Calar Alto Legacy Integral Field Area (CALIFA) survey conclude the existence of a common metallicity gradient after normalising by the size of the galactic disk (Sánchez et al. 2012, 2014; Ho et al. 2015; Sánchez-Menguiano et al. 2016b). By contrast, studies using data from the Mapping Nearby Galaxies at Apache Point Observatory (MaNGA) survey and Sydney-AAO Multi-object Integral-field spectroscopy (SAMI) Galaxy Survey have shown clear evidence of steepening negative metallicity gradients at increased stellar masses up to $\log(M/M_{\odot}) \sim 10.5$ (Belfiore et al. 2017; Poetrodjojo et al. 2018, Poetrodjojo et al. Accepted).

On the other hand, galaxies with a history of merging events show significantly shallower metallicity gradients than their isolated counterparts (Kewley et al. 2010; Rich et al. 2012; Sánchez et al. 2014). Tidal forces brought upon by the gravitational interaction between merging galaxies not only mixes gas internally, but can also drive large scale gas inflows of pristine gas, diluting the metal rich centres. The flattening of the metallicity gradient does not necessarily need to take place across the entire galaxy. López-Sánchez et al. (2015) showed that one of the spiral arms of NGC 1512 had a flattened metallicity gradient as a result of its merging interactions with NGC 1510. The significant effect that merging activity has on the metallicity gradient emphasise its importance in understand the formation history of galaxies.

The probability of a galaxy undergoing a merger event is directly related to its surrounding density. Galaxies in dense environments are more likely to interact with surrounding galaxies simply because neighbouring galaxies are closer and more numerous. A complete merger event is not the only method in which surrounding galaxies have an effect on the metallicity gradient of galaxies. Using the MaNGA survey, Schaefer et al. (2019) found evidence that satellite galaxies tend to have enhanced metallcities for more massive central galaxies, due to the direct exchange of enriched gas between galaxies. In addition, galaxies in such environments are more likely to experience tidal interactions, or even just interact with the intra-cluster or intra-group medium. We can therefore expect that galaxies in denser environments should have more disturbed metallicity gradients on average compared to those that are relatively isolated.

There are several ways of measuring the surrounding density around a galaxy. The most commonly used density metric is the fifth nearest neighbour density. The fifth nearest neighbour density is calculated by measuring the volume within which the five nearest galaxies reside. This volume is then expressed as a number density. Different density metrics typically vary the method with which they determine the enclosing volume or instead use a fixed volume to calculate the number density.

In this letter, we try to determine what impact environment has on the metallicity gradients of galaxies using the SAMI Galaxy Survey and the three environmental density parameters from the Galaxy and Mass Assembly (GAMA) survey (Driver et al. 2011).

3.2. Sample Selection

The SAMI Galaxy Survey (Bryant et al. 2015) is an IFS survey of $\sim$ 3600 low-redshift (z<0.095) galaxies observed using the 3.9 metre Anglo-Australian Telescope at Siding Springs Observatory. The majority of galaxies in the SAMI Galaxy Survey are a subset of the GAMA

survey because of the supporting data made public by the GAMA team (e.g. environmental density parameters). The SAMI Galaxy Survey observes a range of stellar masses between $10^7 - 10^{12} M_\odot$ using a 14.7'' diameter hexabundle fibre (Bland-Hawthorn et al. 2011). The blue arm of the SAMI spectrograph covers a wavelength range between 3700 – 5700Å with a spectral resolution of R=1812 while the red arm covers a wavelength range between 6300 – 7400Å with a spectral resolution of R=4263 (van de Sande et al. 2017). Within this work we use the 'sector-binned' maps from the SAMI Data Release 2, which has a sample of 1559 galaxies across a range of environments (Scott et al. 2018).

At its highest spatial resolution, the SAMI data is sampled at 0.5×0.5 arcsec^2 spaxels. To increase the signal-to-noise (S/N) of emission lines needed for the determination of the gas-phase metallicity, we instead use the sector-binned data cubes. The sector-binned data cubes takes the row stacked spectra from raw observations and bins them into five linearly-spaced elliptical annuli based on position angle and ellipticity. The cubes are then further divided into 8 equally spaced azimuthal bins to retain the azimuthal spatial resolution.

To reliably measure metallicity gradients in our galaxy sample, we apply cuts based on the inclination, effective radii, emission line S/N, and excitation mechanism of the gas (i.e. star-forming). This leads to a final sample of 248 galaxies. To allow us to sufficiently sample the minor axis, we select galaxies with inclinations of $< 60°$, this cuts our galaxy sample to 941 galaxies. We then further reduce our sample by requiring a sector at least every 0.25 R_e up to 1R_e in which we can measure the metallicity. This requires a S/N > 3 in the H$\beta\lambda$4861, [OIII]λ5007, H$\alpha\lambda$6563, [NII]λ6583 and [SII]λ6717, λ6731 emission lines for the S-calibration (Scal) metallicity diagnostics (Pilyugin & Grebel 2016), drastically reducing our galaxy sample to 257 galaxies. Finally, only star-forming spaxels may be used with this metallicity diagnostic, so we use the classification schemes from Kewley et al. (2006) to remove all non-star-forming spaxels, leaving us with a final sample of 248 galaxies. Figure 3.1 shows the stellar mass distribution of our final sample compared to the parent DR2 sample. We can see that we still maintain the same approximate distribution of the parent DR2 sample after each sample selection cut. For a more thorough analysis of each sample selection cut, refer to Poetrodjojo et al. (Accepted, Chapter 4).

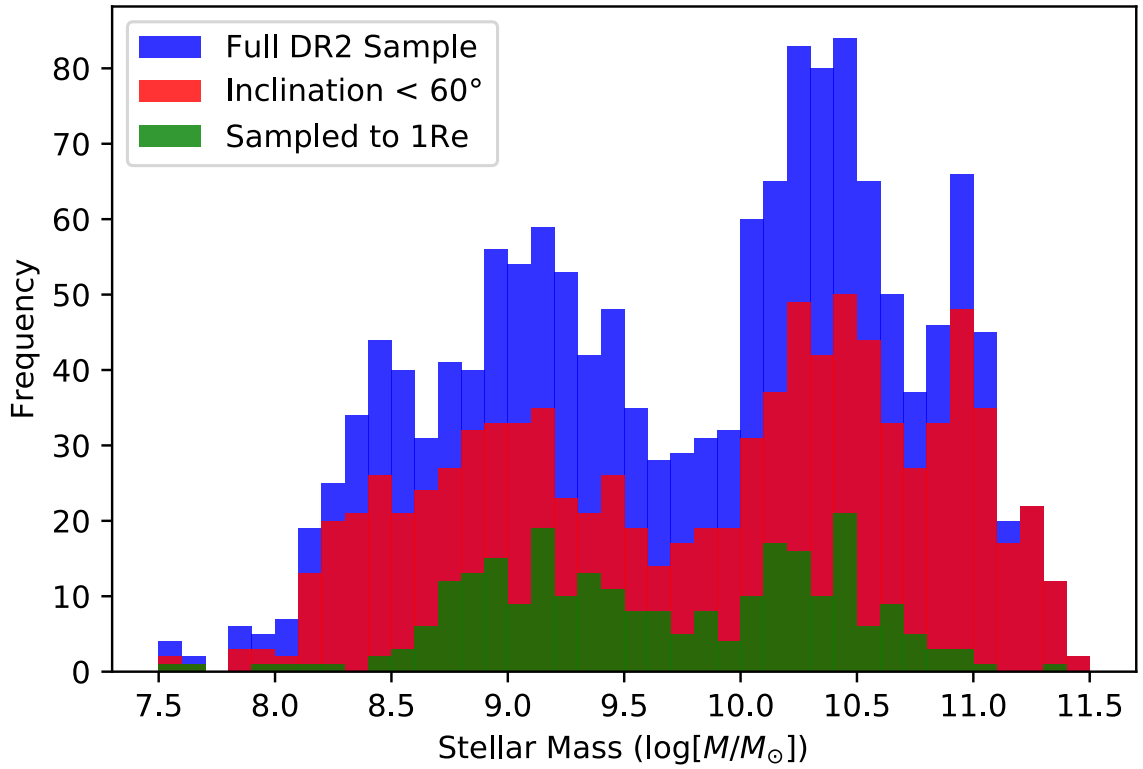

Figure 3.1 Stellar mass distribution of our galaxy sample after each sample selection cut. The final galaxy sample is almost identical in its stellar mass distribution to the parent DR2 sample. There is an obvious reduction in galaxies at the low-mass end ($\log(M/M_\odot < 8.5$) and the high-mass end ($\log(M/M_\odot > 11.0$). This is because the angular size of high-mass galaxies is relatively large due to the narrow redshift range and vice versa for low-mass galaxies. For low-mass galaxies, we are unable to achieve the minimum resolution of $0.25R_e$ and for high-mass galaxies, we are unable to sample the galaxy out to at least $1R_e$.

3.3. Metallicity Gradients and Environmental Parameters

3.3.1. Extinction Correction

Due to the attenuation caused by dust in the interstellar medium (ISM), emission lines must first be extinction corrected before being used in any emission line ratios. The reddening of the emission lines is wavelength dependent, meaning that emission line diagnostics which have wide wavelength differences are most significantly affected. To correct the emission lines, we first create maps of the observed Balmer ratio, $(H\alpha/H\beta)_{obs}$, and solve for E(B-V) by using the relation:

$$E(B-V) = \log_{10}(\frac{(H\alpha/H\beta)_{\rm obs}}{(H\alpha/H\beta)_{\rm int}})/(0.4(k(H\beta) - (k(H\alpha)))) \quad (3.1)$$

where $(H\alpha/H\beta)_{int}$ is the intrinsic ratio Balmer ratio of 2.86 assuming case B recombination (Osterbrock 1989). We then use the extinction curves by Cardelli et al. (1989), assuming R(V)=3.1, to calculate k values for Hα and Hβ. Finally, we use the calculated E(B-V) to determine A(λ), the absolute extinction as a function of wavelength, and de-redden the emission line fluxes.

3.3.2. Metallicity Diagnostics

In order to recover any trends that the metallicity gradients have with environmental density, we must first remove any known dependencies such as stellar mass. Poetrodjojo et al. (Accepted, Chapter 4) measured the mass-metallicity gradient relation for 13 metallicity diagnostics and found that the Scal diagnostic by Pilyugin & Grebel (2016) had the least scatter around the line of best fit. We therefore use the Scal diagnostic to remove as much systematic error as possible associated with the choice of metallicity diagnostic.

The Scal metallicity diagnostics is split into upper and lower metallicity branches, similar in nature to the R_{23}metallicity diagnostic. The Scal metallicity diagnostic uses the H$\beta\lambda$4861, [OIII]λ5007, [NII]λ6583 and [SII]λ6717, λ6731 emission lines calibrated using the counterpart method (Pilyugin et al. 2012). The counterpart method is a set of calibrating data points which ultimately derive their metallicity through the direct temperature method. The Scal metallicity diagnostic agrees with direct temperature metallicities to within 0.1 dex, comparable to the uncertainties of the abundances themselves.

$$\begin{aligned}(O/H)^{*}_{\mathrm{S\_lower}} &= 8.072 + 0.789 \times \log(O3S2) + 0.726 \times \log(N2H\beta) \\ &\quad + (1.069 - 0.170 \times \log(O3S2) + 0.022 \times \log(N2H\beta)) \times (S2H\beta)\end{aligned}$$

$$\begin{aligned}(O/H)^{*}_{\mathrm{S\_upper}} &= 8.424 + 0.030 \times \log(O3S2) + 0.751 \times \log(N2H\beta) \\ &\quad + (-0.349 + 0.182 \times \log(O3S2) + 0.508 \times \log(N2H\beta)) \times (S2H\beta)\end{aligned} \tag{3.2}$$

where N2Hβ = log[NII]/$H\beta$, S2Hβ = log[SII]/$H\beta$, O3S2 = log[$OIII$]/[SII] and (O/H)*=12+log(O/H). Since N2Hβ is an extremely metal-sensitive emission line ratio on its own, it is used as an initial guess to determine which branch of the Scal calibration is required:

$$\begin{aligned}&\text{Use } (O/H)^{*}_{\mathrm{Lower}} \text{ if } \log(N2H\beta) < -0.6 \\ &\qquad\qquad \text{Use } (O/H)^{*}_{\mathrm{Upper}} \text{ if } \log(N2H\beta) \geq -0.6\end{aligned} \tag{3.3}$$

3.3.3. Metallicity Gradients

To measure radial metallicity gradients, we first de-project the observed inclination using its ellipticity and position angle. We then use a linear least-squares approximation to fit a linear trend to the metallicity gradient while propagating the uncertainty in metallicity through to the linear parameters. Studies performed using high-spatial resolution data show that metallicity gradients often deviate from single linear fits (Sánchez-Menguiano et al. 2018). Especially for high stellar-mass galaxies, discernible flattening of the metallicity gradient is evident in the inner (R<0.5R_e) and outer (R>2.0R_e) edges of the galaxy. Due to the spatial resolution limitations of our data, we do not see this flattening to a great effect and hence only fit single linear fits to the metallicity gradients.The metallicity gradients are then normalized by the effective radius (R_e) to remove the disk size dependence of metallicity gradients (Sánchez et al. 2014; Ho et al. 2015; Sánchez-Menguiano et al. 2016b).

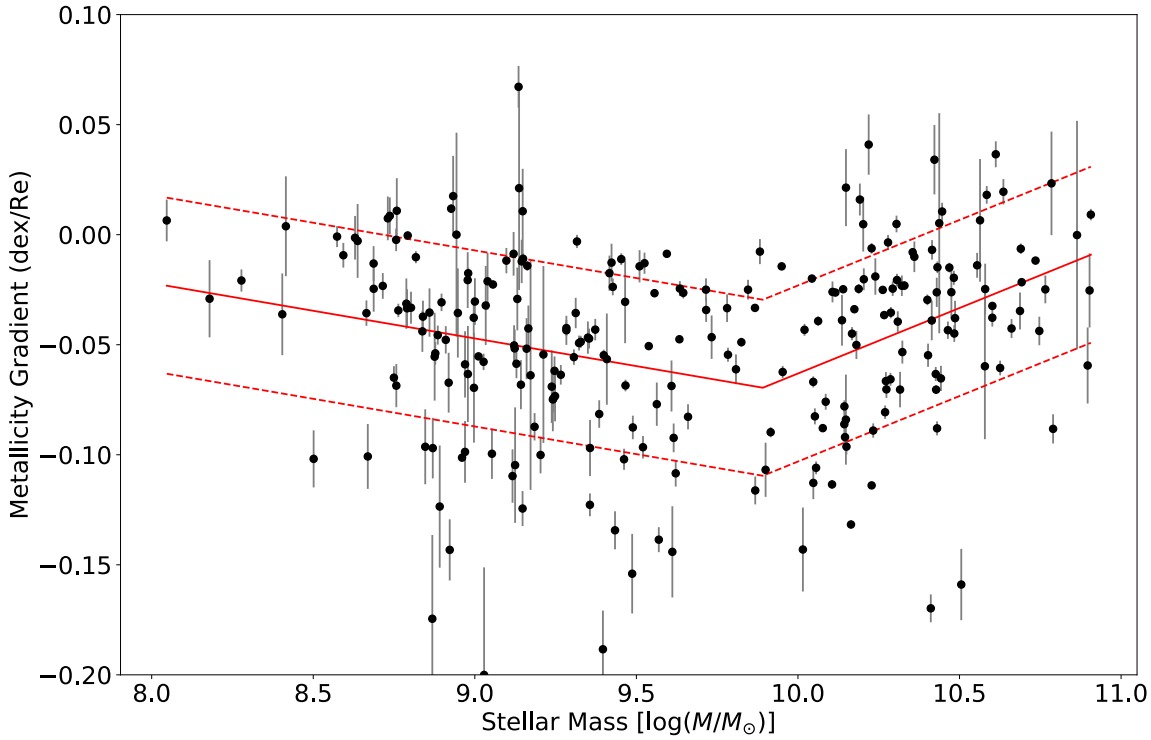

Figure 3.2 Metallicity gradients using the Scal diagnostic as a function of stellar mass. We find that a broken power law to be the best fit to the data as shown in the red solid line. The dashed lines indicate the 1σ variations from the line of best fit.

3.3.4. Environmental Density Parameters

The environmental density parameters used in this study are provided by the GAMA data release 2. We use three environmental density parameters: the fifth nearest neighbour surface density, the number of other galaxies within a co-moving cylinder and finally the density of galaxies within an adaptive Gaussian ellipsoid.

The fifth nearest neighbour surface density is calculated with the following equation:

$$\Sigma_5 = \frac{5}{\pi d_5^2} \tag{3.4}$$

where d_5 is the distance in the plane of the sky to the fifth nearest galaxy in megaparsecs. The fifth nearest neighbour must also lie within ±1000km s^{-1} of the redshift of the galaxy in question.

The number of galaxies within a co-moving cylinder is a fairly self-explanatory metric. The cylinder is centred on the galaxy with a co-moving radius of 1 megaparsec and depth of ±1000km s^{-1}.

The final environmental density parameter, the adaptive Gaussian ellipsoid, varies the volume of the density calculation based on the number of galaxies within 2 megaparsecs. The adaptive Gaussian ellipsoid is defined by:

$$\left(\frac{r_a}{3\sigma}\right)^2 + \left(\frac{r_z}{3c_z\sigma}\right)^2 \leq 1 \tag{3.5}$$

where r_a and r_z are the distances from the centre in the plane of the sky and along the

line-of-sight in co-moving megaparsecs respectively. σ = 2Mpc and $c_z = 1 + 0.2n$, where n is the number of galaxies within 2 Mpc.

For more information about each of the density parameters, see Liske et al. (2015).

3.4. Results

As previously mentioned in Section 3.1, several studies have shown that the metallicity gradient varies as a function of stellar mass. In particular, we use the same data as Poetrodjojo et al. (Accepted, Chapter 4) which found steepening metallicity gradients with increasing mass until $\log(M/M_\odot) \sim 10.0$, beyond which metallicity gradients flattened. Figure 3.2 shows the metallicity gradients as a function of stellar mass with a fitted broken power law identical to the one presented in Poetrodjojo et al. (Accepted, Chapter 4). To remove the effects of stellar mass, we instead look at the residuals (Δ O/H) after subtracting the fit to the data.

Figure 3.3 shows the histogram of metallicity gradient residuals after removing the stellar mass dependence. We fit a Gaussian to the histogram and find a mean of 0.01 with a standard deviation (σ) of 0.04 dex/R_e. We then use the standard deviation to split our galaxies into three groups. Galaxies with metallicity gradients within 1σ ($|\text{Residual}| <$ 0.04 dex/R_e) of the broken power law are consistent with the expected metallicity gradients based on Figure 3.2. Galaxies with steeper metallicity gradients than expected (Residual < -0.04) are those which we expect to be in isolated environments. Conversely, galaxies with

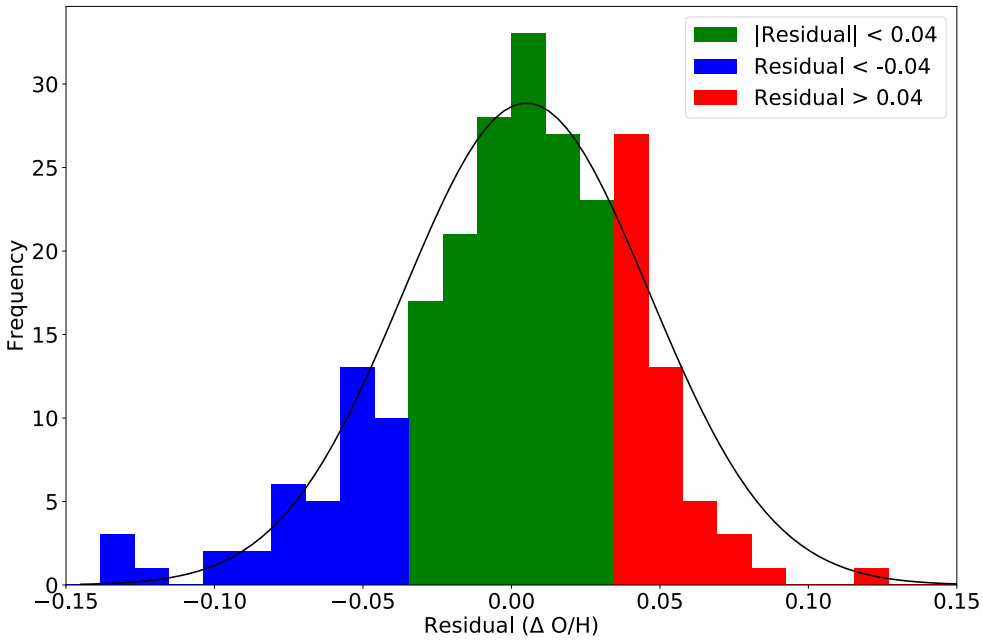

Figure 3.3 Histogram of metallicity gradient residuals after subtracting the broken power law in Figure 3.2. We fit a Gaussian profile to the residuals shown as the solid black line. We then colour code the residuals based on their deviation from the mean.

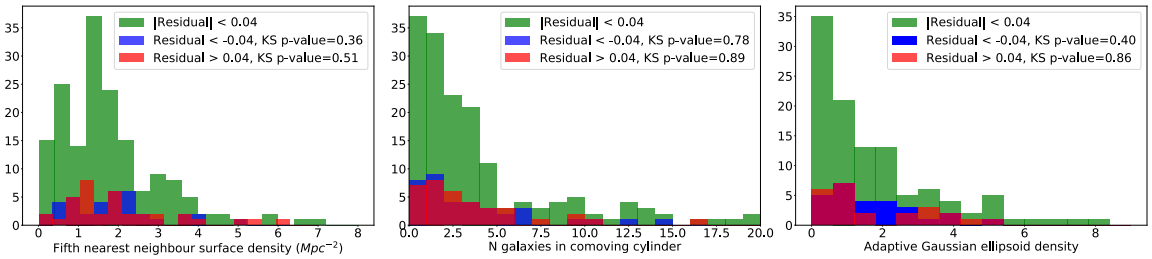

Figure 3.4 Histogram of environmental density parameters, colour-coded by their metallicity gradient deviation from the mean. The same colour scheme is used as in Figure 3.3. No obvious differences in distribution are found among any of the three environmental density parameters.

shallower than expected metallicity gradients (Residual > 0.04) are thought to be in denser environments where merger activity is more likely.

We find no significant correlation between metallicity gradients and the three environmental density parameters used. Figure 3.4 shows the histogram of each environmental density parameter split into our three metallicity gradient groups. For each environmental density parameter, a smaller value indicates a more isolated environment and a higher value indicates a denser environment. It is clear from Figure 3.4 that the vast majority of our galaxies are in relatively isolated environments.

However, there appears to be no significant difference in distribution between our outlier groups (red and blue) and the group which follows the stellar mass dependence within 1σ (green).

The Kolmogorov-Smirnov test (KS test) is a non-parametric test designed to quantify the differences between two distributions by analysing their cumulative distribution functions. We compare both of our outlier groups (red and blue) to our consistent group (green) for each environmental density parameter and show the p-values in Figure 3.4. Assuming a standard significance of p-value < 0.05, we can see that neither of the outlier distributions are significantly different to the consistent distribution.

3.5. Discussion and Summary

Figure 3.4 shows that we have been unable to link the variation around mass-metallicity gradient relation to differences in environmental density. Here we discuss the possible reasons for this missing link by looking at the limitations of spatial resolution, metallicity diagnostic and the environmental density parameters.

Several studies have shown the detrimental effects of the diffuse ionized gas on measuring metallicity gradients (Mast et al. 2014; Poetrodjojo et al. 2018). At the kiloparsec spatial resolution of the SAMI galaxy survey, contamination by the DIG is inevitable and may affect our measurement in an unpredictable way. This is further amplified since we have binned our data into sectors, making the isolation of HII regions more difficult. Using higher spatial resolution data can easily overcome this limitation and must be used when attempting to look at small variations in the metallicity gradient.

Poetrodjojo et al. (Accepted, Chapter 4) shows the variation in measured metallicity gradient depending on which metallicity diagnostic was used. In particular, the mass-metallicity

gradient relation had varying levels of scatter depending on which diagnostic was used. To minimise this effect, we have used the Scal metallicity diagnostic, which showed the least amount of intrinsic scatter around the broken linear-fit. It is possible that this scatter is much greater than the expected variation with environment. Part of this scatter is likely associated with the DIG as just previously mentioned, but may also be due to a secondary relation, which has not been accounted for. The fundamental metallicity relation is an extension of the mass-metallicity relation showing that the star-formation rate is another important parameter which affects metallicity (Mannucci et al. 2010). Star-formation rate may be a prime lead in attempting to reduce the intrinsic scatter seen in Figure 3.2.

While metallicity gradient flattening can occur without the direct interaction between galaxies (galactic fountains Bresolin et al. 2012; Kudritzki et al. 2014; Sánchez et al. 2014), we expect significant flattening to occur in major mergers where large scale gas inflows drive pristine gas between galaxies. All three environmental density parameters used in this study rely on some form of counting galaxies within a specified volume. While this does by definition measure the density, it can only tell us how likely a merger is to occur and not if one has definitively occurred. For example, a galaxy in a dense environment which has not directly interacted with a neighbouring galaxy is likely to have a steeper metallicity gradient than a pair of merging galaxies in a relatively isolated environment. This suggests that a more specialised parameter may be needed to capture the merger history of a galaxy.

Using DR2 of the SAMI galaxy survey, we have shown that the three environmental density parameters, fifth nearest neighbour density, number of galaxies within a cylindrical volume and the adaptive Gaussian ellipsoid, were not able to explain the scatter in the mass-metallicity gradient relation. We believe that the main limitation of this study was the lack of spatial resolution. Without sufficient spatial resolution, we are unable to account for the effects of DIG could be a reason for the large intrinsic scatter seen in Figure 3.2. The scatter may also be due to unexplored secondary relations of the metallicity gradient with star-formation rate.

Acknowledgements

Parts of this research were conducted by the Australian Research Council Centre of Excellence for All Sky Astrophysics in 3 Dimensions (ASTRO 3D), through project number CE170100013.
BG gratefully acknowledges the support of the Australian Research Council as the recipient of a Future Fellowship (FT140101202).

CHAPTER 4

Reconciling Strong Emission Line Metallicity Diagnostics Using Metallicity Gradients

This chapter presents the content of the article: The SAMI Galaxy Survey: Reconciling Strong Emission Line Metallicity Diagnostics Using Metallicity Gradients. This article has been accepted by the Monthly Notices of the Royal Astronomical Society. The abstract of this chapter is as follows:

We measure the gas-phase metallicity gradients of 248 galaxies selected from Data Release 2 of the SAMI Galaxy Survey. We demonstrate that there are large systematic discrepancies between the metallicity gradients derived using common strong emission line metallicity diagnostics. For galaxies within the mass range $8.5 < \log(M/M_{\odot}) < 11.0$, we find discrepancies of up to 0.11 dex/R_e between seven popular diagnostics. We find that a break in the mass-metallicity gradient relation, where the gradient shifts from negative to positive, occurs between $9.5 < \log(M/M_{\odot}) < 10.5$ for the seven chosen diagnostics. We determine which pairs of diagnostics have Spearman's rank coefficients greater than 0.6 and provide linear conversions to allow the accurate comparison of metallicity gradients derived using different strong emission line diagnostics. These conversions provide the most accurate method of converting metallicity gradients when key emission lines are unavailable. We find that diagnostics that share common sets of emission line ratios agree best, and that diagnostics calibrated through the electron temperature provide more consistent results compared to those calibrated through photoionization models. Applying our conversions to the metallicity gradient-mass relation, we are able to reduce the maximum dispersion between seven metallicity diagnostics from 0.11 dex/R_e to 0.02 dex/R_e.

4.1. Introduction

The global gas-phase metallicity (hereafter metallicity) of a galaxy correlates strongly with its stellar mass, giving rise to the well known mass-metallicity relation (Lequeux et al. 1979; Garnett & Shields 1987; Tremonti et al. 2004; Sweet et al. 2014; Sánchez et al. 2019). With advancements in integral field spectroscopy (IFS), the metallicity of a galaxy on intra-galactic

scales can now be resolved for large numbers of galaxies. Local disk galaxies typically exhibit negative metallicity gradients, where the metallicity of a galaxy decreases radially from the centre (Vila-Costas & Edmunds 1992; Zaritsky et al. 1994; Moustakas et al. 2010; Rupke et al. 2010). The existence of a common metallicity gradient among isolated galaxies, when normalized by scale length, has been found with the introduction of current generation IFS surveys such as the Calar Alto Legacy Integral Field Area (CALIFA) survey, the Sydney Australian Astronomical Observatory Multi-Object Integral Field Spectrograph (SAMI) Galaxy Survey and the Mapping Nearby Galaxies at Apache Point Observatory (MaNGA) survey (Sánchez et al. 2012, 2014; Ho et al. 2015; Sánchez-Menguiano et al. 2016b, 2018; Poetrodjojo et al. 2018). Other studies indicate that the metallicity gradient of a galaxy steepens with stellar mass up to $\log(M/M_{\odot}) \sim 10.5$, beyond which the metallicity gradients begin to flatten (Belfiore et al. 2017). In contrast, galaxies that show evidence of a major merger or merger remnants at some point during their evolution show shallower metallicity gradients than isolated galaxies (Kewley et al. 2010; Rich et al. 2012; Sánchez et al. 2014; López-Sánchez et al. 2015).

The gas-phase abundance of oxygen, i.e., the ratio between oxygen and hydrogen, O/H, is often used to measure the metallicity of a galaxy. Oxygen is the most abundant element in the Universe after hydrogen and helium, having very strong optical emission lines which are easy to detect even in very distant objects. Since these strong emission lines are collisionally excited, the abundance of the emitting ion can be determined directly if the electron temperature is known. In particular, measuring the electron temperature through the [OIII]λ4363 and λ5007 emission lines provides a theoretically very reliable diagnostic for the abundance of O^{+2}, and thus metallicity (known as the 'direct temperature method'; Alloin et al. 1979; Pagel et al. 1979). The practical weakness of the direct temperature method lies in the relative faintness of the [OIII]λ4363 and other auroral emission lines, especially at high metallicities (since the intensity of the auroral lines anticorrelates with metallicity). Because of this limitation, metallicity diagnostics involving strong emission lines have become more widely adopted for their ability to be used with low surface brightness, distant and metal-rich sources.

Strong emission line metallicity diagnostics are usually calibrated using:

- Theoretical models (e.g., Kewley & Dopita 2002; Kobulnicky & Kewley 2004; Dopita et al. 2016; Thomas et al. 2018).
- Empirical calibrations based on the direct temperature method (e.g., Alloin et al. 1979; Pagel et al. 1979; Pilyugin 2001; Pilyugin & Grebel 2016; Ho 2019).
- A combination of the above (e.g., Denicoló et al. 2002; Pettini & Pagel 2004).

Metallicity calibrations are generally a simple polynomial mapping of emission line ratios to the gas-phase metallicity, but more complex metallicity calibrations can involve the use of Bayesian inference (Blanc et al. 2015; Thomas et al. 2018) or neural network machine learning (Ho 2019; Wu & Boada 2019). Despite all metallicity diagnostics aiming to measure the same quantity (O/H), large discrepancies of up to 0.6 dex exist between diagnostics calibrated through the direct method and theoretical models (Yin et al. 2007; Kewley & Ellison 2008; López-Sánchez & Esteban 2010; López-Sánchez et al. 2012). Yin et al. (2007)

also found discrepancies of 0.2 dex between the direct method calibrations from Tremonti et al. (2004), Pilyugin (2001) and Pilyugin & Thuan (2005). These variations in metallicity means that the absolute metallicity scales of galaxies are highly uncertain and cannot be compared between different methods.

Another source of uncertainty that could lead to differences between metallicity diagnostics is the Diffuse Ionized Gas (DIG). The vast majority of strong emission line metallicity diagnostics rely on the assumption that the emission lines are produced from star-forming HII regions. However, HII regions are not the only source of emission in a galaxy. Other sources of emission include Active Galactic Nuclei (AGN), shocks, and the DIG (Kewley et al. 2006). While AGN are relatively simple to identify and separate from star-forming regions (Davies et al. 2016, 2017; D'Agostino et al. 2019a,b), the DIG is difficult to remove from the spectrum. The DIG is generally found over the entire disc of the galaxy as well as above and below the galactic plane, making it hard to isolate at low spatial resolution scales where the boundaries between HII regions and the DIG are blurred (Walterbos & Braun 1994; Ferguson et al. 1996; Hoopes et al. 1996; Greenawalt et al. 1998). Boettcher et al. (2017) was able to isolate the extra-planar DIG (eDIG) by using high spectral resolution (R=5490) and Markov Chain Monte Carlo methods. Oey et al. (2007) found a mean fraction of 0.59 ± 0.19 of Hα surface brightness originating from the DIG. At high spatial resolution scales (such as CALIFA, Physics at High Angular resolution in Nearby Galaxies (PHANGS) or TYPHOON), the isolation of the DIG from HII regions is much simpler and can be done with a variety of techniques (e.g. [SII]λ6717, λ6731/Hα or the equivalent width of Hα). At the spatial resolution scales of SAMI or MaNGA, completely removing the DIG from HII region emission is difficult. With such a large portion of emission line flux originating from the DIG, DIG contamination inevitably affects our measurements of metallicity (Zhang et al. 2017). Poetrodjojo et al. (2019) showed how the metallicity gradient of M83 was affected by the DIG for 5 different metallicity diagnostics, showing clear differences in how each diagnostic responds to the contamination of DIG emission. Using the direct temperature method, Richards et al. (2014) found that the metallicity of an offset unresolved HII complex within a dwarf galaxy, to be 0.2 dex lower than the surrounding DIG. Conversely, Sweet et al. (2014) found that for a sample of star-forming dwarf galaxies, that including emission from the surrounding DIG gave mean metallicities consistent with those measured using emission only from the HII regions with metallicity calibrations by Dopita et al. (2013). The consistent metallicities between the HII regions and the DIG are likely because the large gas reservoirs in the sampled dwarf galaxies were well mixed (Kobulnicky & Skillman 1997; Lee & Skillman 2004). However, even without the contamination of DIG, the HII regions of M83 show very different metallicity gradients depending on which metallicity diagnostic is used (Poetrodjojo et al. 2019).

Recent studies on the mass-metallicity relation attempt to remove any biases caused by the choice of gas-phase metallicity calibrator by performing their analysis with a wide range of calibrations (Barrera-Ballesteros et al. 2017; Sánchez et al. 2017, 2019). Each of these three studies find little to no evidence of any secondary dependence of the mass-metallicity relation with star-formation rate, regardless of which metallicity diagnostic or calibrator is used. Not only is the robustness of conclusions increased by utilizing many different metallicity calibrations, Barrera-Ballesteros et al. (2017), Sánchez et al. (2017) and Sánchez et al. (2019) demonstrate that although systematics plague the measurement of gas-phase

metallicity, overall trends are conserved. However, the comparison of individual objects from different samples still remains difficult without the luxury of a wide wavelength coverage.

Although Kewley & Ellison (2008) provided conversions between the current available diagnostics at the time, the conversions were calibrated using SDSS aperture spectroscopy. With the rise of spatially resolved IFS observations, we are moving away from measuring global metallicities and instead measuring metallicity *gradients*. With all the issues presented, it is inadvisable to compare metallicity gradients determined from different diagnostics. With the large amount of different instruments observing a wide range of redshifts currently available, we cannot reasonably expect there to always be overlapping wavelength coverage. In these situations, it becomes essential to develop a way to convert and compare metallicity gradients determined from different diagnostics. This is especially important in understanding how metallicity gradients evolve as a function of redshift, where it becomes extremely difficult to obtain a broad range of optical emission lines.

In this paper, we use galaxies from SAMI Data Release 2 (DR2, Scott et al. 2018) to measure metallicity gradients using 13 different metallicity diagnostics and calibrations. We then compare the measured metallicity gradients to determine which diagnostics and calibrations can be empirically converted from one another and provide the conversion fits in a table. We discuss the differences between the diagnostics which lead to their inconsistencies and compare different calibration methods.

We structure this paper in the following way. Section 2 describes the SAMI Galaxy Survey and how we select our sub-sample from the data available. We outline the methods we use for determining the gas-phase metallicity based on popular strong emission line diagnostics in Section 3. In Sections 4 and 5, we present and briefly discuss our results on the metallicity gradients and provide a method for converting between different diagnostics. Finally, we summarise our findings and outline future work that we hope will stem from these results. Throughout the entire paper, we assume the following values for cosmological constants, $H_0 = 70\text{km s}^{-1}\text{Mpc}^{-1}$, $\Omega_\text{M} = 0.3$ and $\Omega_\Lambda = 0.7$ (Hinshaw et al. 2009).

4.2. Sample Selection

4.2.1. SAMI Galaxy Survey

The SAMI Galaxy Survey (Bryant et al. 2015) is an integral field spectroscopic survey of $\sim 3,000$ low-redshift ($z < 0.095$) galaxies primarily selected from the Galaxy and Mass Assembly (GAMA) survey (Driver et al. 2011), with the addition of eight galaxy clusters to extend the sampling of environmental density (Owers et al. 2017). The Sydney Australian Astronomical Observatory Multi-Object Integral Field Spectrograph (SAMI; Croom et al. 2012) is located on the 3.9 metre Anglo-Australian Telescope at Siding Spring Observatory. The SAMI Galaxy Survey covers a wide range of galaxies with stellar masses ranging between $10^7 - 10^{12} M_\odot$, and redshifts between $0.004 < z < 0.095$.

The SAMI data are sampled at 0.25 (0.5×0.5) arcsec^2 spaxels covering the 14.7″diameter aperture of the SAMI hexabundle (Bland-Hawthorn et al. 2011; Bryant et al. 2014) with

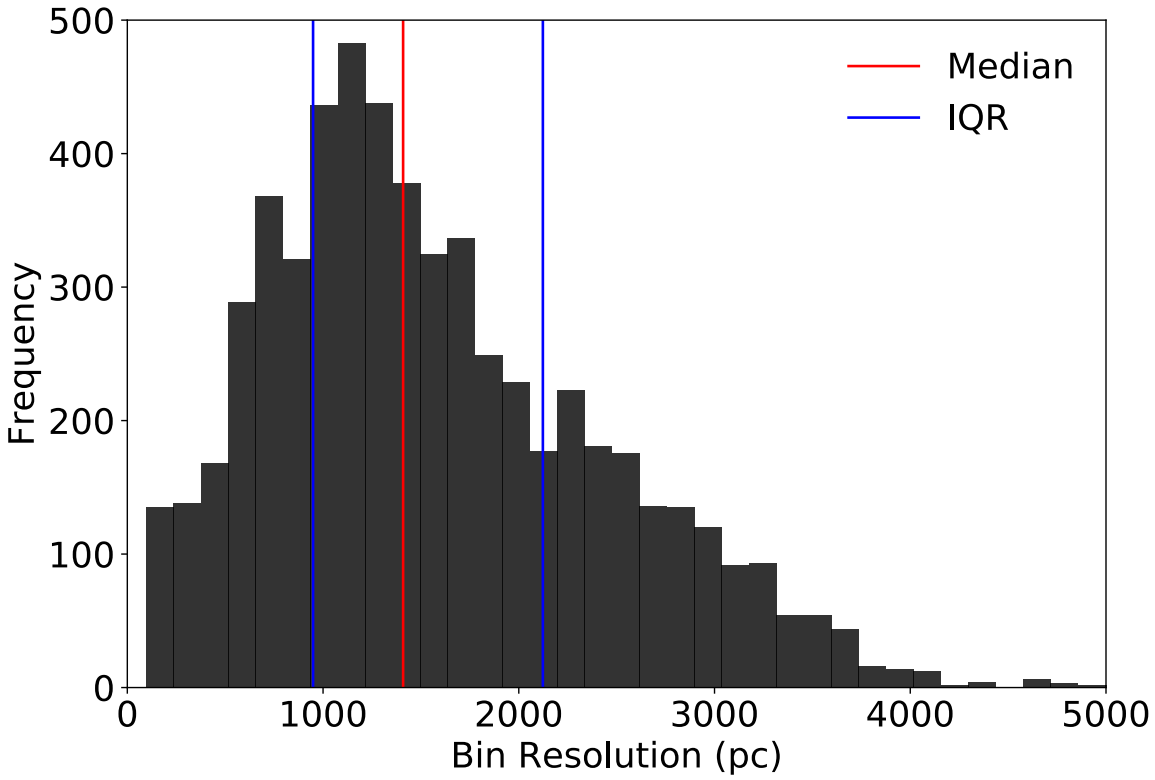

Figure 4.1 Spatial resolution distribution of the sector-binned data cubes in our final galaxy sample. The median spatial resolution of our sample is 1409pc with a 25th and 75th percentile of 735pc and 2507pc respectively.

an average seeing of 2.16'' (Green et al. 2018). Since the average seeing is much larger than the individual spaxel sizes, this leads to an oversampling of our data, resulting in a covariance between neighbouring spaxels. We take this covariance into account when implementing the various binning schemes on the SAMI data. The SAMI fibres are fed into the double-beam AAOmega spectrograph (Sharp et al. 2006). The blue cube covers a wavelength range between 3700 – 5700Å with a spectral resolution of R= 1812 and the red cube covers a wavelength range between 6300 – 7400Å with a spectral resolution of R= 4263 (van de Sande et al. 2017). The spectral range of the AAOmega spectrograph allows us to observe the important metal-sensitive emission lines: [OII]λ3726, λ3729, H$\beta\lambda$4861, [OIII]λ5007, H$\alpha\lambda$6563, [NII]λ6583 and [SII]λ6717, λ6731.

Poetrodjojo et al. (2018) found that the relatively weak detection of the [OII] emission line compared to the other metal-sensitive emission lines significantly reduced the ability to measure the metallicity using the R_{23} and N2O2 emission line diagnostic. To increase the detection of the weaker emission lines, we will use the sector-binned data cubes released in the SAMI Data Release 2 (Scott et al. 2018). The row stacked spectra (RSS) are first binned into five linearly-spaced elliptical annuli based on their position angle (PA) and ellipticity. The cubes are then further azimuthally subdivided into eight regions, resulting in sector-binned cubes. The sector-binned data cubes have the advantage over unbinned data of increasing the S/N of emission lines while maintaining both azimuthal and radial spatial resolution. Figure 4.1 shows the spatial resolution distribution of the sector-binned data cubes of our final galaxy sample. For full details on the generation of the binned datacubes, see Scott et al. (2018).

The emission line fitting was done using the SAMI line fitting routine LZIFU (Ho et al.

2016; Medling et al. 2018). We first subtract the underlying stellar continuum using PPXF (Cappellari & Emsellem 2004; Cappellari 2017) and the MIUSCAT simple stellar population models (Vazdekis et al. 2012). The dominant emission lines are then fit using up to 3 Gaussian profiles with the Levenberg-Marquardt least-squares method implemented in MPFIT (Markwardt 2009). Each emission line is constrained to have the same kinematic velocity and velocity dispersion. The flux ratios of [OIII]$\lambda\lambda$4959, 5007 and [NII]$\lambda\lambda$6548, 6583 are fixed to those given by quantum mechanics.

4.2.2. Well-resolved radial profiles

While the SAMI DR2 consists of 1559 galaxies, many are observed at high inclination angles or found to have significant non-stellar emission contaminating their spectra. To measure reliable metallicity gradients, we select galaxies with relatively face-on profiles so that the minor axis can be well sampled. We select galaxies with inclinations of < 60, which reduces our sample from 1559 galaxies to 941 galaxies. We calculate the inclination angle of the galaxy using the standard Hubble formula (Hubble 1926):

$$\cos^2(i) = \frac{(b/a)^2 - {q^2}_0}{1 - {q^2}_0} \tag{4.1}$$

where i is the inclination angle, $q_0 = 0.2$ and b/a is the ratio between the minor and major axis as measured in the r band by the Sloan Digital Sky Survey (SDSS; York et al. 2000) using GALFIT (Peng et al. 2010). To sufficiently sample the entire scale length over which we measure the metallicity gradients, we require at least one sector every $0.25R_e$ up to $1R_e$ (as measured by GALFIT), further reducing our sample to 257 galaxies. This large drop in our galaxy sample is mostly driven by requiring a S/N > 3 in all of the strong emission line fits within the spectral range of SAMI in each sector. The lower throughput in the blue arm of the spectrograph causes the S/N of the [OII] emission line to be relatively weak compared to the other optical emission lines. However, the use of sector-binned cubes increases our sample size tenfold compared to the 25 galaxies used in Poetrodjojo et al. (2018) (who used unbinned data).

4.2.3. Star-Forming Cuts

Blue cloud galaxies typically emit strong emission lines from HII regions surrounding recently formed massive stars. However, HII regions are not the only possible source of emission. Gas excited from the DIG, shocks or AGN may contribute to the overall emission line profile (e.g., Groves et al. 2004). The large majority of strong emission line metallicity diagnostics are calibrated on the assumption that all of the emission is produced from HII regions. Recent work by Kumari et al. (2019) and Vale Asari et al. (2019) allows for the measurement of gas-phase metallicity in spaxels (integrated spectra in the case of Vale Asari et al. 2019) dominated by the DIG by providing correction factors to remove its effects. At the spatial resolution of multiplexing IFS surveys, contamination by the DIG is inevitable and causes systematic biases in the measurement of metallicity gradients (Mast et al. 2014; Erroz-Ferrer et al. 2019; Poetrodjojo et al. 2019). In some cases, it is possible to separate the star-formation dominated and other ionizing sourced line emission using high spatial

resolution observations (e.g., Davies et al. 2014, 2016; D'Agostino et al. 2018; Lacerda et al. 2018), but in our case we chose to remove all sectors that showed significant non-star-forming emission.

We use the classification scheme of Kewley et al. (2006) to distinguish when non-star-forming emission is present using the following strong emission line ratio diagnostic curves:

$$\log\left(\frac{[\mathrm{OIII}]}{\mathrm{H}\beta}\right) > \frac{0.61}{\log\left(\frac{[\mathrm{NII}]}{\mathrm{H}\alpha}\right) - 0.05} + 1.30, \tag{4.2}$$

$$\log\left(\frac{[\mathrm{OIII}]}{\mathrm{H}\beta}\right) > \frac{0.72}{\log\left(\frac{[\mathrm{SII}]}{\mathrm{H}\alpha}\right) - 0.32} + 1.30, \tag{4.3}$$

$$\log\left(\frac{[\mathrm{OIII}]}{\mathrm{H}\beta}\right) > \frac{0.73}{\log\left(\frac{[\mathrm{OI}]}{\mathrm{H}\alpha}\right) + 0.59} + 1.33. \tag{4.4}$$

Sectors with a S/N > 3 in the emission line fluxes that satisfy any of (fail all of) these criteria are classified as non-star-forming (star-forming). After this cut is performed, we still require at least one sector every $0.25\mathrm{R}_e$ up to $1\mathrm{R}_e$ to reliably measure the metallicity gradient. We are left with a final sample of 248 galaxies (5,832 sectors) for which we can measure metallicity gradients using any of the metallicity diagnostics outlined in the following section. Figure 4.2 shows the stellar mass distribution of our galaxies after each sample selection cut. For galaxies $\log(M/M_\odot) < 8.5$ and $\log(M/M_\odot) > 10.5$, the ability to sufficiently sample the galaxy to $1\mathrm{R}_e$ is reduced. With low mass galaxies ($\log(M/M_\odot) < 8.5$), we are unable to sample to fine enough resolution scales (at least $0.25\mathrm{R}_e$) to reliably measure metallicity gradients. Due to the limited redshift range, the effective radii of massive galaxies ($\log(M/M_\odot) > 10.5$) are larger than the SAMI field of view and are therefore excluded from the sample.

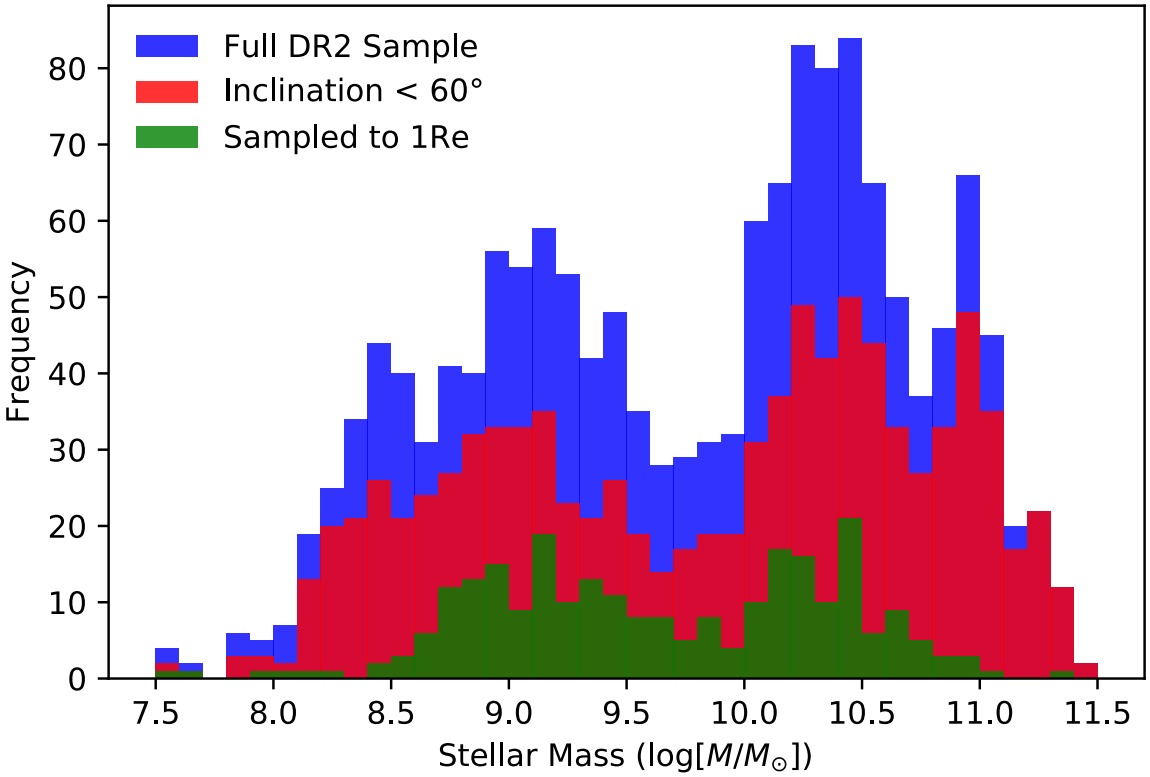

Figure 4.2 Stellar mass distribution of our galaxy sample. Between a stellar mass range of $8.5 < \log(M/M_\odot) < 10.5$ we have a similar mass distribution as the full DR2 sample.

4.3. Measuring Metallicity Gradients

4.3.1. Extinction Correction

Before being used in diagnostic ratios, emission lines must be first corrected for attenuation by dust in the interstellar medium (ISM). The attenuation of emission lines is wavelength dependent, meaning that diagnostics that use emission lines that are widely-separated in wavelength are most heavily affected, such as N2O2, R_{23} and O32. To correct the emission lines, we create maps of the observed Balmer ratio, $(H\alpha/H\beta)_{obs}$, and solve for E(B-V) by using the relation:

$$E(B-V) = \log_{10}(\frac{(H\alpha/H\beta)_{obs}}{(H\alpha/H\beta)_{int}})/(0.4(k(H\beta) - (k(H\alpha)))) \quad (4.5)$$

where $(H\alpha/H\beta)_{int}$ is the intrinsic ratio of 2.86 for case B recombination (Osterbrock 1989). We note that the intrinsic Balmer line ratio is also a function of metallicity (López-Sánchez et al. 2015). We use the Cardelli et al. (1989) extinction curve and assume a typical R(V) value of 3.1 to determine k values for Hα and Hβ. We then use the calculated E(B-V) to determine A(λ), the absolute extinction as a function of wavelength, at our emission line wavelengths to de-redden the emission line fluxes. Although emission line ratios with small wavelength separations are not significantly affected by dust extinction, we apply an extinction correction to all emission line ratios to maintain a fair comparison when using them in metallicity diagnostics.

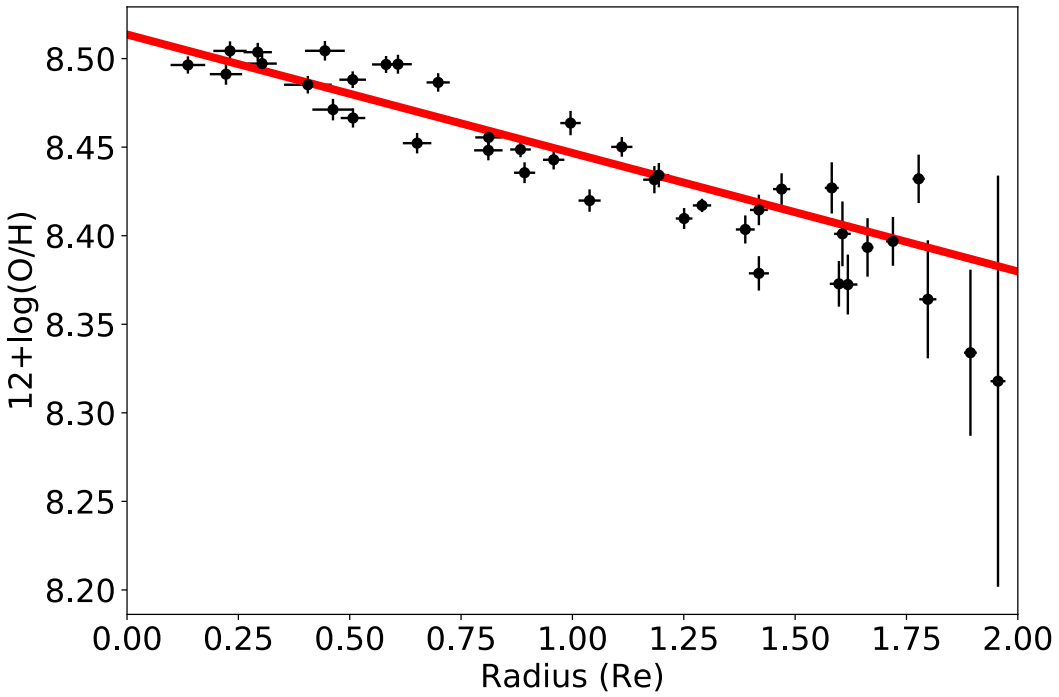

Figure 4.3 A typical negative radial metallicity gradient of GAMA-492414 using the Scal metallicity diagnostic. The red line represents the best linear fit to the sector metallicities.

4.3.2. Metallicity Diagnostics

Due to the enormous amount of metallicity diagnostics and calibrations available, it is unrealistic to analyse every single one. We therefore limit this study to popular metallicity diagnostics, which are used extensively by the gas-phase metallicity community. To cover as much parameter space as possible, we select diagnostics which use unique combinations of strong emission lines, calibrations using different photoionization codes and electron temperature methods, as well as exploring calibration mapping methods including polynomial mapping, Bayesian inference and machine learning algorithms. The equations for all diagnostics and calibrations used in this study are given in the Appendix.

$\mathbf{R_{23}}$

The ([OII]$\lambda\lambda$3726, 3729 + [OIII]$\lambda\lambda$4959, 5007)/Hβ (R_{23}) emission line ratio measures the oxygen abundance through the direct use of oxygen emission lines. Due to its popularity, many calibrations for the R_{23} diagnostic exist (Pagel et al. 1979, 1980; Edmunds & Pagel 1984; McCall et al. 1985; Dopita & Evans 1986; Torres-Peimbert et al. 1989; McGaugh 1991; Zaritsky et al. 1994; Pilyugin 2000; Charlot & Longhetti 2001; Kewley & Dopita 2002; Kobulnicky & Kewley 2004). However, one major complication with the R_{23} emission line ratio is its strong dependence on the ionization state of the gas, as quantified by the ionization parameter. We use two popular calibrations by Kobulnicky & Kewley (2004, hereafter K04R_{23}) and Curti et al. (2017, hereafter C17R_{23}). Kobulnicky & Kewley (2004) used the R_{23} emission line ratio in conjunction with the [OIII]$\lambda\lambda$4959, 5007/[OII]$\lambda\lambda$3726, 3729 (O32) emission line ratio

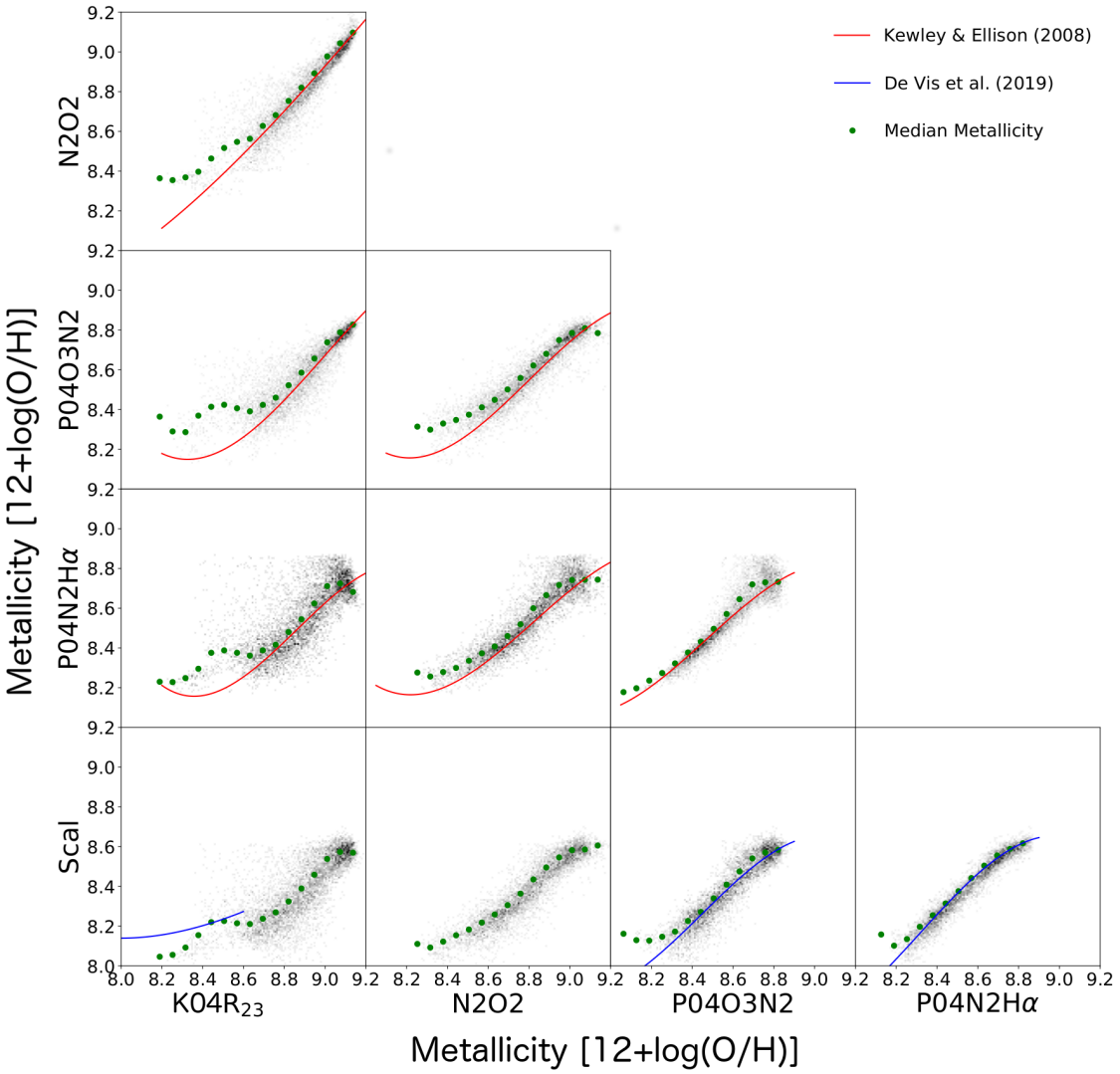

Figure 4.4 Metallicities of individual sectors calculated through different metallicity diagnostics as a function of each other. The red line represents the empirical conversions determined by Kewley & Ellison (2008) and the blue line represents the empirical conversions determined by De Vis et al. (2019). While the conversions by Kewley & Ellison (2008) and De Vis et al. (2019) follow the general trend, a noticeable scatter exists around each fit.

to simultaneously constrain the metallicity and ionization parameter through an iterative method. Curti et al. (2017) takes a more conventional approach in which the R_{23} emission line ratio is mapped to the direct temperature metallicities through a high-order polynomial. This approach is much less computationally expensive and provides an easy way to calculate the gas-phase metallicities using the oxygen emission lines.

N2O2

Unlike R_{23}, the [NII]λ6583/[OII]λ3726, λ3729 (N2O2) emission line ratio is relatively insensitive to the ionization parameter because of the similar ionizing potentials of the nitrogen and oxygen species. The biggest drawback of the N2O2 emission line ratio is the strong extinction required due to the large wavelength differences between the [NII] and [OII] emission lines. We use the calibration outlined in Kewley & Dopita (2002), where they

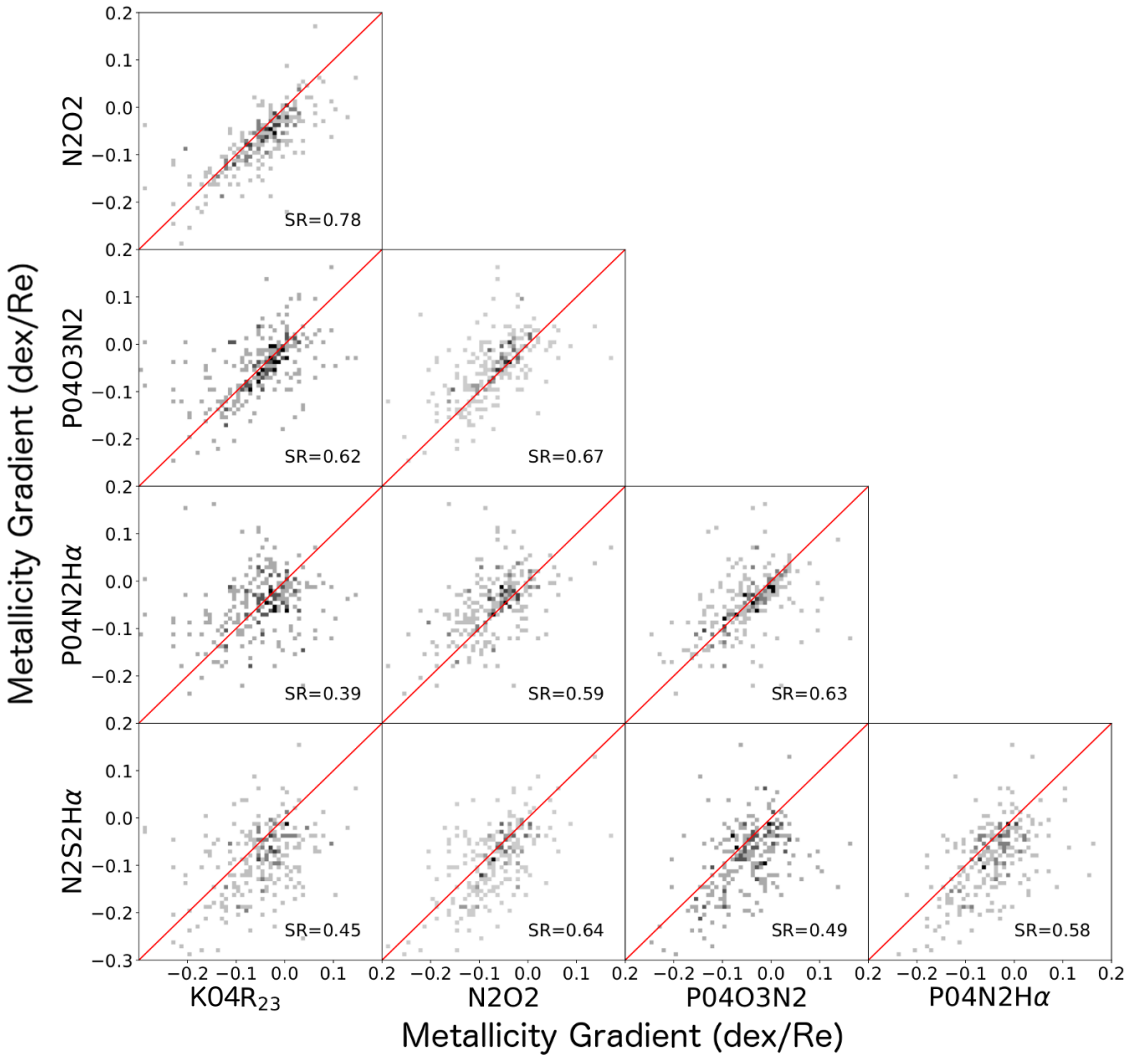

Figure 4.5 Metallicity gradient of each galaxy calculated through different metallicity diagnostics as a function of each other. The red line represents the one-to-one line indicating perfect agreement between the diagnostics. The Spearman rank coefficient of each diagnostic pair is calculated to test the level of correlation and tabulated in Table 4.1. For pairs of diagnostics with a Spearman rank greater than 0.6, there exists obvious systematic deviations away from the one-to-one line which are corrected for.

calibrate the N2O2 emission line ratio using the MAPPINGS III photoionization models (Sutherland et al. 2013) shown in Equation 4.8.

N2Hα

Perhaps one of the mostly widely used metallicity diagnostics is the [NII]λ6583/Hα (N2Hα) emission line ratio. Due to the small wavelength separation of the [NII] and Hα emission line, the N2Hα emission line ratio is popular among high-redshift studies where extinction correction may be difficult or only a small wavelength coverage is available (e.g., Storchi-Bergmann et al. 1994). We use two popular calibrations of the N2Hα emission line ratio from Pettini & Pagel (2004, hereafter P04) and Marino et al. (2013, hereafter M13). The main difference between the calibrations presented by Pettini & Pagel (2004) and Marino et al. (2013) occurs at the high metallicity end. Due to the limitations of constraining the electron temperature, Pettini & Pagel (2004) used photoionization models by Diaz et al.

(1991) and Castellanos et al. (2002a,b) to calibrate the N2Hα diagnostic at high metallicities. With advances in the sensitivity of spectrographs, Marino et al. (2013) was able to measure the electron temperature using the [NII]λ5755 emission line, leading to a more consistent calibration.

O3N2

Similar to the N2Hα diagnostic, ([OIII]λ5007/Hβ)/([NII]λ6583/Hα) (O3N2) uses emission lines that have minimal wavelength separation to remove the need for an extinction correction. O3N2 uses the same emission lines that are commonly presented on the BPT diagram (Baldwin et al. 1981), a method for separating star-forming regions from Active Galactic Nuclei (AGN) dominated regions. The calibrations by Pettini & Pagel (2004) and Marino et al. (2013) show that the gas-phase metallicity is a linear function of the O3N2 emission line ratio, allowing for efficient calculations. We use the calibrations from Pettini & Pagel (2004) and Marino et al. (2013), the same studies as our N2Hα calibrations, for our analysis.

	K04R$_{23}$													
	0.39													
P04N2Hα	(0.06)	P04N2Hα												
	0.39	**0.96**												
M13N2Hα	(0.06)	**(0.01)**	M13N2Hα											
	0.62	**0.63**	**0.63**											
P04O3N2	**(0.05)**	**(0.05)**	**(0.04)**	P04O3N2										
	0.61	**0.62**	**0.61**	**0.98**										
M13O3N2	**(0.05)**	**(0.05)**	**(0.05)**	**(0.01)**	M13O3N2									
	0.78	0.59	0.59	**0.67**	**0.68**									
N2O2	**(0.03)**	(0.05)	(0.05)	**(0.05)**	**(0.04)**	N2O2								
	0.45	0.58	0.52	0.49	0.51	**0.64**								
N2S2Hα	(0.06)	(0.05)	(0.06)	(0.06)	(0.06)	**(0.05)**	N2S2Hα							
	0.51	0.39	0.40	**0.62**	**0.60**	**0.61**	0.57							
0.15cm ONS	(0.06)	(0.07)	(0.07)	**(0.05)**	**(0.05)**	**(0.05)**	(0.05)	ONS						
	0.52	0.17	0.18	0.39	0.40	0.57	0.53	**0.79**						
ON	(0.06)	(0.07)	(0.07)	(0.06)	(0.06)	(0.06)	(0.05)	**(0.04)**	ON					
	0.44	**0.82**	**0.79**	0.53	0.52	**0.65**	**0.88**	0.57	0.44					
Scal	(0.06)	**(0.03)**	**(0.03)**	(0.06)	(0.06)	**(0.05)**	**(0.03)**	(0.06)	(0.06)	Scal				
	0.60	**0.84**	**0.85**	0.58	0.57	**0.83**	**0.65**	0.52	0.41	**0.85**				
Rcal	**(0.05)**	**(0.02)**	**(0.02)**	(0.05)	(0.05)	**(0.03)**	**(0.05)**	(0.06)	(0.06)	**(0.02)**	Rcal			
	0.52	0.37	0.30	0.55	0.56	0.59	0.44	0.34	0.22	0.38	0.46			
NeBayes	(0.06)	(0.06)	(0.07)	(0.05)	(0.06)	(0.05)	(0.06)	(0.06)	(0.07)	(0.06)	(0.06)	NeBayes		
	0.53	**0.86**	**0.85**	**0.65**	**0.65**	**0.77**	**0.68**	0.52	0.40	**0.83**	**0.90**	0.45		
MLP	(0.05)	**(0.02)**	**(0.02)**	**(0.04)**	**(0.04)**	**(0.03)**	**(0.04)**	(0.06)	(0.07)	**(0.03)**	**(0.02)**	(0.06)	MLP	
	0.37	0.39	0.42	**0.71**	**0.71**	0.40	0.26	0.39	0.21	0.30	0.32	0.38	0.39	
HII-CHI	(0.07)	(0.06)	(0.06)	**(0.04)**	**(0.04)**	(0.06)	(0.07)	(0.06)	(0.07)	(0.06)	(0.06)	(0.07)	(0.06)	HII-CHI
	0.69	0.27	0.20	0.59	**0.60**	**0.66**	0.50	0.50	0.46	0.37	0.41	0.58	0.37	0.42
C17R$_{23}$	**(0.04)**	(0.06)	(0.07)	(0.05)	**(0.05)**	**(0.05)**	(0.05)	(0.05)	(0.06)	(0.06)	(0.06)	(0.05)	(0.06)	(0.06)

Table 4.1 Spearman rank coefficients (1σ error) between all metallicity diagnostics and calibrations. Pairs of diagnostics with a Spearman rank coefficient greater than 0.6 are selected for further analysis and are highlighted in bold font. We deem diagnostic pairs with a Spearman rank coefficient less than 0.6 to have no significant correlation.

N2S2Hα

The N2S2Hα emission line diagnostic is a combination of the [NII]λ6583/Hα and [NII]λ6583/[SII]$\lambda\lambda$6717, 6731 emission line ratios. As with N2Hα and O3N2, N2S2Hα uses emission lines close in wavelength to remove the need for extinction corrections. The N2S2Hα emission line diagnostic is sensitive to the metallicity through the [NII]/Hα emission line ratio and removes the ionization parameter dependence through the [NII]/[SII] emission line ratio. This combination of emission lines is calibrated through the MAPPINGS V photoionization models by Dopita et al. (2016, hereafter D16).

ONS and ON

The emission line diagnostics introduced so far have been a combination of one or two emission line ratios. The Oxygen-Nitrogen-Sulphur (ONS) emission line diagnostic incorporates four different emission line ratios to measure gas-phase metallicity. Similar to K04R$_{23}$, the ONS calibration is split into multiple branches. The calibration is split into three classes of HII regions; cool, warm and hot. The conditions of the HII regions are determined from the [NII]/Hβ and [NII]/[SII] emission line ratios. The ONS calibration also includes an explicit excitation parameter, [OIII]/([OII]+[OIII]), allowing for changes in the ionization parameter. Pilyugin et al. (2010) also provides an additional metallicity calibration, the Oxygen-Nitrogen (ON) diagnostic, that provides comparable quantities as the ONS calibration for all HII region classes without using the [SII] emission line. Although the metallicity calibrations themselves do not use the [SII] emission line, it is still required to classify the HII region.

Rcal and Scal

Similar their previous works, Pilyugin & Grebel (2016) created two new metallicity diagnostics involving more than two emission line ratios. The R-calibrations (Rcal) and S-calibrations (Scal) were calibrated using the counterpart method (Pilyugin et al. 2012), which ultimately derives metallicity from the T$_e$ method. The emission lines used in Rcal and Scal only differ by swapping out the [OII] emission line in Rcal for the [SII] emission line in Scal. Like the K04R$_{23}$ diagnostic, the calibration is split into low and high metallicity branches based on the [NII]/Hβ emission line ratio. The Rcal and Scal diagnostics agree with directly measured abundances to within 0.1 dex, comparable to the expected uncertainties of the abundances themselves.

NebulaBayes

The use of Bayesian Inference to constrain the ionization parameter and metallicity was first introduced by Blanc et al. (2015) with the Interactive Data Language (IDL) code IZI. The advantage of using Bayesian inference to constrain the metallicity and ionization parameter is the ability to include additional emission line information to improve estimates. For example, with simple emission line ratios such as R$_{23}$ and N2O2, we are unable to include the [SII] emission line to better predict the gas-phase metallicity. With Bayesian analysis, we

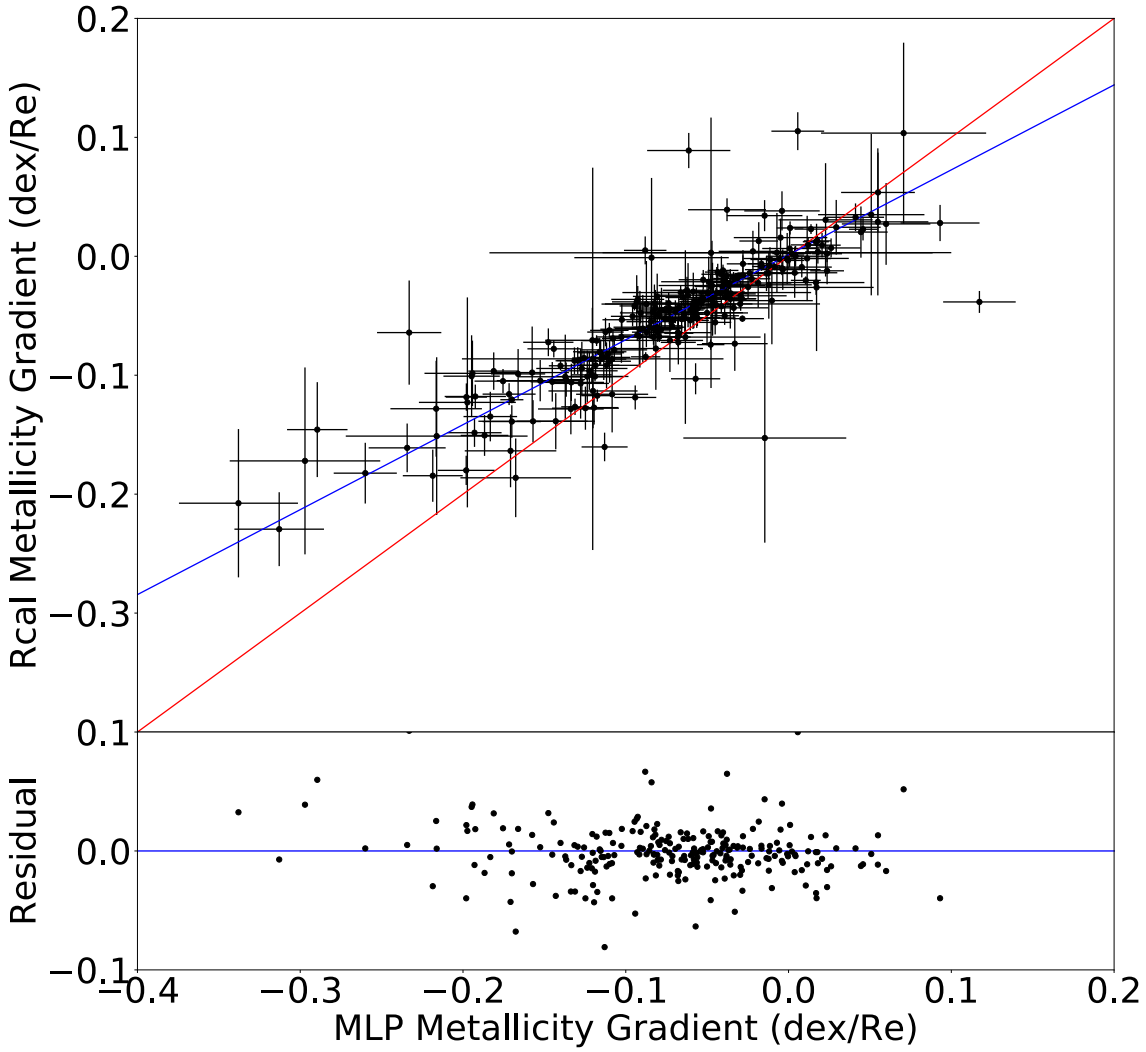

Figure 4.6 Metallicity gradient calculated using Rcal as a function of the MLP metallicity gradient. The red line represents the one-to-one relation and the blue line shows the best linear fit to the data.

are able to include the entire suite of available emission lines to determine the metallicity. For this study we use NebulaBayes (NB, Thomas et al. 2018), a Bayesian Inference code inspired by IZI with more generalised capabilities. We use the following emission lines to constrain the metallicity and ionization parameter using NB: [OII]$\lambda\lambda 3726, 3729$, H$\beta\lambda 4861$, [OIII]$\lambda 5007$, H$\alpha\lambda 6563$, [NII]$\lambda 6583$ and [SII]$\lambda\lambda 6717, 6731$.

Machine Learning

Recently, the use of Machine Learning algorithms has spiked with the ability to dedicate large portions of time to training neural networks. Two recent examples include implementations by Wu & Boada (2019) and Ho (2019). Wu & Boada (2019) use a convolutional neural network (CNN) to predict the gas-phase metallicity of SDSS galaxies using only the optical *gri* images. Ho (2019) uses a multi-layer perceptron (MLP) model to predict the gas-phase metallicity using the extinction-corrected [OII], Hβ, [OIII], [NII] and [SII] emission lines. For this study, we use OxygenMLP (MLP; Ho 2019) as our machine learning fiducial model. Unlike NB, MLP requires that all emission lines are available for use.

Photoionization Models

Pérez-Montero (2014) presents HII-CHI-mistry (hereafter, HII-CHI), a method of determining metallicity through photoionization models calculated with CLOUDY v17.00 (Ferland et al. 2017). HII-CHI-mistry v4.0 is a publicly available Python routine which aims to constrain O/H, N/O and log(U) using several of the already introduced extinction corrected optical emisison lines [OII], [NeIII]λ3868, [OIII]λ4363, Hβ, [OIII]λ5007, [NII] and [SII]. Due to the relative weakness of the [NeIII]λ3868 and [OIII]λ4363 emission lines, we do not provide these fluxes to HII-CHI, limiting its usage to the 'log U limited' photoionization grids.

4.3.3. Error Propagation

To propagate the line flux errors produced by LZIFU through to the metallicity calculations, we simulate 1000 maps for all emission lines used in the calculation. The maps are created such that the fluxes are Gaussian distributed within the LZIFU standard deviation for that emission line.

Using the simulated line maps, metallicity maps are created for each metallicity diagnostic. The non-linearity of some of the metallicity diagnostics means that the metallicity distributions are not necessarily Gaussian. To represent the spread of metallicity, we determine the distance from the true value to the 16^{th} and 84^{th} percentiles and calculate the average. This average provides us with a measure of the error of the metallicity maps, which are then propagated to the gradient errors.

4.3.4. Metallicity Gradients

When determining the radial metallicity gradients, we first correct for the observed inclination of the galaxy using its ellipticity and position angle as measured in the *r*-band by the GAMA survey (Driver et al. 2011). We then use a linear least-squares algorithm to fit a linear trend to the metallicity gradient, propagating the uncertainty in metallicity through the linear parameters. We use FITEXY (Press et al. 1992), available for use with IDL, to perform the fitting because it does not detect and remove outliers. We have specifically avoided more robust line fitting algorithms such as LTS_LINEFIT (Cappellari et al. 2013) because they automatically remove any detected outliers. Since we are investigating how the metallicity gradient varies among different metallicity diagnostics, using an algorithm that may detect a sector as an outlier in one diagnostic but not another is undesirable and introduces a potential source of uncertainty. The gradients are then normalised by the effective radius (R_e) of the galaxy to remove the size dependence of metallicity gradients (Sánchez et al. 2014; Ho et al. 2015; Sánchez-Menguiano et al. 2016b). Sánchez-Menguiano et al. (2018) found wide-spread deviations from single linear metallicity gradients and instead used multiple linear gradients to more accurately fit the radial metallicity distribution. However, for this study we adopt a single linear fit to our metallicity gradients because at the spatial resolution of the sector binned cubes, we are unable to resolve a broken linear fit to the metallicity gradient.

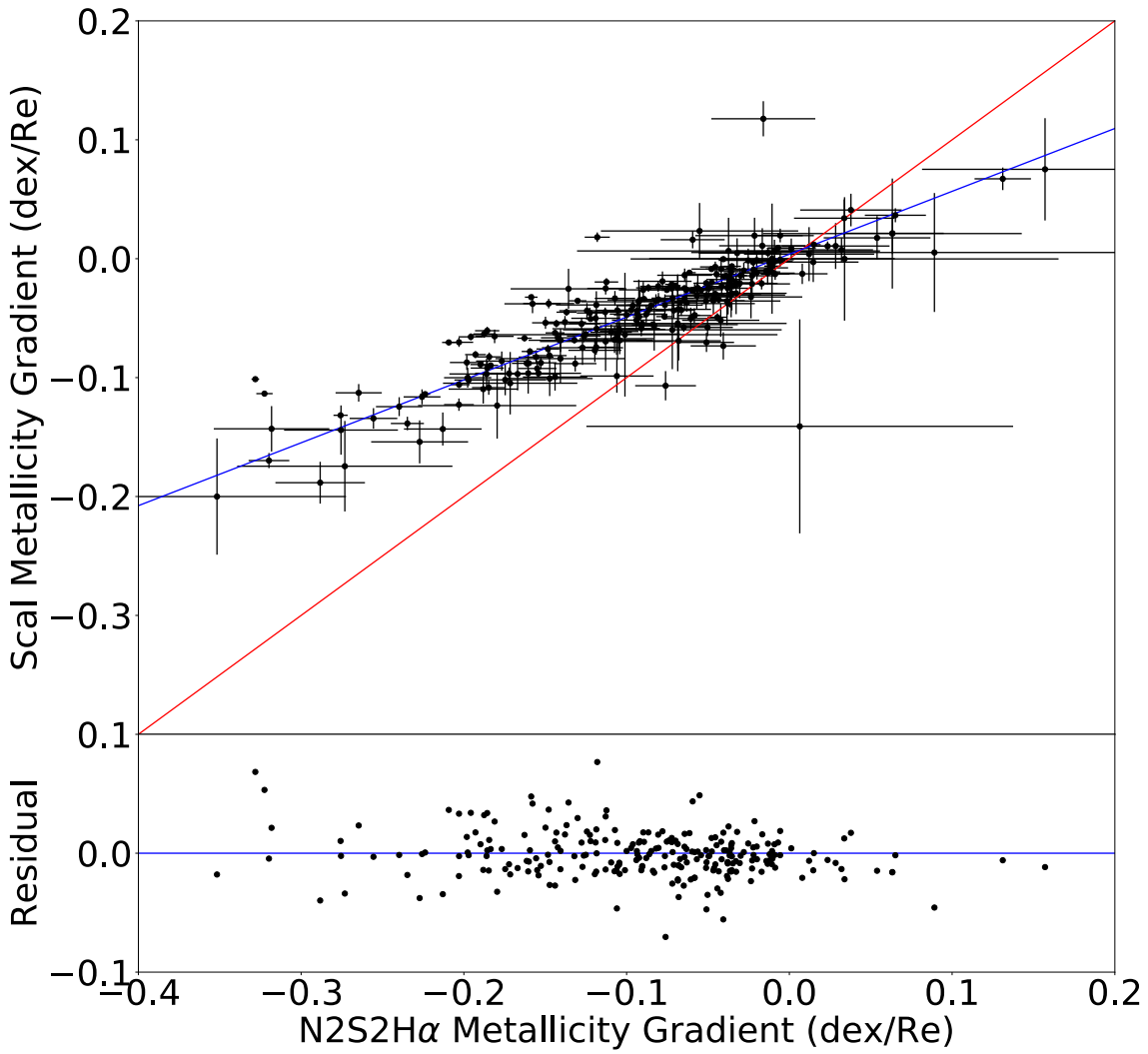

Figure 4.7 Same as Figure 4.6 but for Scal metallicity gradients as a function of N2S2Hα metallicity gradients. In this example, the difference in slope is even greater.

Several studies (Yuan et al. 2013; Mast et al. 2014; Poetrodjojo et al. 2019) have shown that there is a systematic flattening of the metallicity gradient at lower spatial resolution scales. Although the sector-binning of the SAMI data cubes is effectively reducing the spatial resolution, we find that the metallicity gradients are not affected in a significant way. This is because the flattening of metallicity gradients is most noticable at higher spatial resolutions and the effect is heavily diminished at the kiloparsec resolution scales of most SAMI galaxies. We show an example of a radial metallicity gradient in Figure 4.3. We can see that there is sufficient spatial resolution to characterise a single linear fit to the metallicity gradient, but finer resolutions scales are needed for multi-linear fits.

Base Metallicity (**x**)	Final Metallicity (**y**)	K04R$_{23}$	P04N2Hα	M13N2Hα	P04O3N2	M13O3N2	N2O2	N2S2Hα	ONS	ON	Scal	Rcal	MLP	HII-CHI	C17R$_{23}$
	m (Gradient)	-	-	-	1.49	0.73	1.04	-	-	-	-	0.50	-	-	-
K04R$_{23}$	c (Intercept)	-	-	-	0.01	0.00	-0.02	-	-	-	-	-0.02	-	-	-
(Photoionization)	rms scatter	-	-	-	0.047	0.034	0.080	-	-	-	-	0.036	-	-	-
	m (Gradient)	-	-	-	1.29	0.55	-	-	-	-	0.56	0.65	1.20	-	-
P04N2Hα	c (Intercept)	-	-	-	0.01	-0.01	-	-	-	-	-0.02	-0.02	-0.01	-	-
(Mixed)	rms scatter	-	-	-	0.034	0.026	-	-	-	-	0.024	0.029	0.030	-	-
	m (Gradient)	-	-	-	2.87	2.04	-	-	-	-	1.39	1.39	2.03	-	-
M13N2Hα	c (Intercept)	-	-	-	0.03	0.02	-	-	-	-	-0.01	-0.01	-0.02	-	-
(T_e)	rms scatter	-	-	-	0.027	0.026	-	-	-	-	0.019	0.019	0.015	-	-
	m (Gradient)	0.67	0.78	0.35	-	-	0.95	-	0.53	-	-	-	1.62	0.46	-
P04O3N2	c (Intercept)	-0.01	-0.01	-0.01	-	-	-0.02	-	-0.01	-	-	-	0.01	0.02	-
(Mixed)	rms scatter	0.047	0.034	0.027	-	-	0.065	-	0.034	-	-	-	0.041	0.036	-
	m (Gradient)	1.37	1.83	0.49	-	-	1.35	-	2.49	-	-	-	2.39	1.22	1.79
M13O3N2	c (Intercept)	0.00	0.00	-0.01	-	-	-0.01	-	0.03	-	-	-	0.01	0.03	0.02
(T_e)	rms scatter	0.034	0.026	0.026	-	-	0.032	-	0.030	-	-	-	0.027	0.031	0.033
	m (Gradient)	0.96	-	-	1.06	0.74	-	1.67	0.66	-	0.55	0.78	1.34	-	0.79
N2O2	c (Intercept)	0.02	-	-	0.02	0.01	-	0.01	0.00	-	-0.01	0.01	0.02	-	0.01
(Photoionization)	rms scatter	0.080	-	-	0.065	0.032	-	0.078	0.054	-	0.049	0.062	0.077	-	0.071
	m (Gradient)	-	-	-	-	-	0.60	-	-	-	0.53	0.42	0.58	-	-
N2S2Hα	c (Intercept)	-	-	-	-	-	-0.01	-	-	-	0.00	-0.01	-0.01	-	-
(Photoionization)	rms scatter	-	-	-	-	-	0.078	-	-	-	0.017	0.036	0.043	-	-
	m (Gradient)	-	-	-	1.89	0.40	1.51	-	-	1.03	-	-	-	-	-
ONS	c (Intercept)	-	-	-	0.02	-0.01	0.00	-	-	0.00	-	-	-	-	-
(T_e)	rms scatter	-	-	-	0.034	0.030	0.054	-	-	0.042	-	-	-	-	-
	m (Gradient)	-	-	-	-	-	-	-	0.97	-	-	-	-	-	-
ON	c (Intercept)	-	-	-	-	-	-	-	0.00	-	-	-	-	-	-
(T_e)	rms scatter	-	-	-	-	-	-	-	0.042	-	-	-	-	-	-
	m (Gradient)	-	1.80	0.72	-	-	1.83	1.89	-	-	-	1.18	1.71	-	-
Scal	c (Intercept)	-	0.01	0.01	-	-	0.01	0.00	-	-	-	0.00	0.01	-	-
(T_e)	rms scatter	-	0.024	0.019	-	-	0.049	0.017	-	-	-	0.024	0.023	-	-
	m (Gradient)	1.99	1.53	0.72	-	-	1.29	2.35	-	-	0.84	-	1.40	-	-
Rcal	c (Intercept)	0.02	0.02	0.01	-	-	0.00	0.01	-	-	0.00	-	0.00	-	-
(T_e)	rms scatter	0.036	0.029	0.019	-	-	0.062	0.036	-	-	0.024	-	0.021	-	-
	m (Gradient)	-	0.83	0.49	0.62	0.42	0.74	1.71	-	-	0.59	0.71	-	-	-
MLP	c (Intercept)	-	0.01	0.01	-0.01	0.00	-0.02	0.02	-	-	-0.01	0.00	-	-	-
(T_e)	rms scatter	-	0.030	0.015	0.041	0.027	0.077	0.043	-	-	0.023	0.021	-	-	-
	m (Gradient)	-	-	-	2.16	0.82	-	-	-	-	-	-	-	-	-
HII-CHI	c (Intercept)	-	-	-	-0.03	-0.03	-	-	-	-	-	-	-	-	-
(Photoionization)	rms scatter	-	-	-	0.036	0.031	-	-	-	-	-	-	-	-	-
	m (Gradient)	-	-	-	-	0.56	1.27	-	-	-	-	-	-	-	-
C17R$_{23}$	c (Intercept)	-	-	-	-	-0.01	-0.01	-	-	-	-	-	-	-	-
(T_e)	rms scatter	-	-	-	-	0.033	0.071	-	-	-	-	-	-	-	-

Table 4.2 Linear conversion fits to convert metallicity gradients from one metallicity diagnostic to another. The conversion relations follow the general form of y=mx+c, where x is the base metallicity which can be calculated through available emission lines, and y is the final metallicity which you wish to convert to. For completeness, we have included redundant metallicity conversions (e.g. O3N2 to N2Hα) by calculating the inverse function (shown in red), but advise against their usage as simply calculating the metallicity gradient with the simpler metallicity diagnostic will yield better results.

4.4. Results

Before we compare metallicity gradients derived from different metallicity diagnostics, we first compare our data to the fits determined by Kewley & Ellison (2008). Figure 4.4 shows the metallicities of the individual sectors from all the galaxies in our sample. The red line in Figure 4.4 shows the empirical conversions determined by Kewley & Ellison (2008) using single aperture spectra from SDSS. In the bottom row of Figure 4.4, the blue line shows the empirical conversion between Scal and three other metallicity diagnostics determined by De Vis et al. (2019) using spectra obtained from DustPedia and MUSE. We also show the median metallicities in green as a comparison. The upturn in the K04R_{23} metallicities around $12 + \log(O/H) \approx 8.5$ is caused by the dual branched nature of the K04R_{23} metallicity diagnostic. We find that although the fits by Kewley & Ellison (2008) and De Vis et al. (2019) follow the general trend in all cases, there appear to be significant deviations from the median metallicities in some cases (e.g. N2O2 vs P04N2Hα). The spread around the empirical conversions by Kewley & Ellison (2008) and De Vis et al. (2019) means that the simple solution of doing a spaxel by spaxel conversion may not produce realistic metallicity gradients.

Figure 4.5 compares the metallicity gradients derived from five different diagnostics. The red line represents the one-to-one line where we expect points to lie when the metallicity diagnostics are in agreement. It is obvious in Figure 4.5 that significant scatter exists between the diagnostics, with some diagnostics agreeing better than others. In some cases (e.g., K04R_{23} vs N2S2Hα), no trend can be discerned from the scatter, meaning that converting between these two diagnostics is unreliable. Figure 4.4 shows that the relationship between metallicity diagnostics tend to be monotonic, which also holds for the remaining diagnostics not shown in Figure 4.4. We therefore expect metallicity gradients to also be monotonic between diagnostics. The Spearmans rank coefficient provides a measure of how well the relationship between two variables can be represented by a monotonic function, with a coefficient of 1 indicating a perfect one-to-one relation. To determine which diagnostics can be reasonably compared, we calculate the Spearmans rank coefficient between the metallicity gradients of all diagnostics and list them in Table 4.1. We consider diagnostics with a Spearmans rank coefficient greater than 0.6 able to be reliably described by an empirical fit. Approximately 40%(36/91) of all possible diagnostic pairs have a Spearmans rank coefficient greater than 0.6. Using LTS_LINEFIT, we fit linear functions to pairs of diagnostics with Spearmans rank coefficients greater than 0.6. Here we switch to using LTS_LINEFIT instead of FITEXY as it is now desireable to remove outliers. The outlier detection of LTS_LINEFIT uses the Least Trimmed Squares (LTS) regression approach by Leroy & Rousseeuw (1987). The algorithm aims to find the subset of h data points which produces the smallest χ^2 amongst all possible subsets of $h > N/2$. This computational intensive algorithm provides accurate linear fits to empirical conversions between the different metallicity diagnostics.

Figures 4.6 and 4.7 show specific examples of Figure 4.5, where we fit our own linear functions to more accurately describe the relationships between diagnostics. These two examples are specifically chosen as they have Spearman ranks greater than 0.6 with gradients significantly different from unity, which clearly demonstrates the systematic uncertainties between metallicity diagnostics. Figure 4.6 shows the metallicity gradients from MLP

against the metallicity gradients from Rcal. It is clear that assuming a one-to-one relation (red line) between the diagnostics would introduce significant systematic biases. The best-fit linear curve, shown in blue, indicates that a much shallower gradient is needed when converting between these two diagnostics. We show the residuals in the lower panel of the figure, and find a standard deviation dispersion of 0.026 dex/R_e. Another example is shown in Figure 4.7 between N2S2Hα and Scal. While only small zero-point offsets are present (flat gradients remain flat gradients between the diagnostics), there is a clear difference in slope from the one-to-one relation in both examples. This highlights the danger in assuming that metallicity gradients obtained through different metallicity diagnostics are consistent. We provide all the linear conversions between significant diagnostic pairs in Table 4.2.

4.5. Discussion

4.5.1. Comparing with Previous Method

The purpose of empirically fitting metallicity gradients from different diagnostics is to allow us to freely compare metallicity gradients obtained from different methods. Prior to this study, a logical approach to this problem would be to convert individual spaxel metallicities using the conversion functions presented in either Kewley & Ellison (2008) or De Vis et al. (2019) and remeasure the metallicity gradient with the converted metallicities, we refer to this as 'spaxel-converted gradients'. To compare this solution to the one outlined in this study, we convert the P04O3N2 metallicities to P04N2Hα and N2O2 metallicities using the polynomial functions outlined in Kewley & Ellison (2008) and measure their metallicity gradients. We then compare the residuals between the spaxel-converted gradients and the metallicity gradients derived from the traditional emission lines (i.e. deriving the P04N2Hα metallicity gradients using the [NII]/Hα emission line ratio rather than converting from P04O3N2).

Figure 4.8 shows the distribution of the difference between the metallicity gradients derived from the traditional emission lines and the spaxel-converted metallicity gradients in blue, when converting from P04O3N2 to P04N2Hα metallicity gradients. Although the mode of the distribution is close to 0, there is a significant standard deviation of 0.09 dex/R_e and an obvious positive skewness. We then compare the spaxel-converted distribution with the distribution of error obtained by using our empirically converted metallicity gradients in red. The standard deviation of the errors is significantly reduced and the positive skewness disappears. The gradient conversion method produces a higher concentration of galaxies with correctly converted metallicity gradients (error of 0) with fewer significant outliers on the wings. Another example of Figure 4.8 is shown in Figure 4.9, where instead of a decrease in scatter, we correct for the systematic offset present when converting between the P04O3N2 and the N2O2 metallicity gradients. Although the scatter is comparable between the two distributions, there is a clear systematic shift when using the spaxel-converted metallicity gradients.

4.5.2. Comparing Pettini & Pagel (2004) and Marino et al. (2013) Calibrations

The N2Hα and O3N2 line ratios are amongst the most popular diagnostics used to derive metallicity because the wavelength separation of the emission lines is small enough to minimise the effect of dust reddening. The strength and wavelength proximity of the emission lines used in the N2Hα and O3N2 diagnostics make them relatively easy to observe at multiple redshifts. This convenience has resulted in many calibrations to the diagnostic (e.g. Pettini & Pagel 2004; Maiolino et al. 2008; Marino et al. 2013), each of which provide slightly different estimates of the metallicity. In this work we have chosen the N2Hα and O3N2 calibrations outlined in Pettini & Pagel (2004) and Marino et al. (2013) due to their popularity. The calibration by Pettini & Pagel (2004) has been used extensively in metallicity studies, especially at high-redshift where extinction correction can be difficult. Recently, the calibrations by Marino et al. (2013) have become the preferred calibration for N2Hα and O3N2 diagnostics due to their better reliability at high metallicites.

From Table 4.1, we can see that both calibrations of the N2Hα and O3N2 diagnostics produce extremely similar Spearmans rank coefficient, with the largest difference of 0.03 occurring between the N2Hα and Scal. Table 4.2 shows the root mean square (rms) error of each of the linear fits applied to the pair of diagnostics with Spearmans ranks greater than 0.6. For both the N2Hα and O3N2 diagnostics, the calibrations by Marino et al. (2013) agree significantly better than those by Pettini & Pagel (2004) for all the metallicity diagnostics chosen for this study. We therefore recommend that the Marino et al. (2013) calibration be used over the Pettini & Pagel (2004) calibration to allow for more reliable comparisons to other diagnostics. Users of the N2Hα and O3N2 metallicity diagnostics should also be aware of their limitations at low metallicites when being applied to high redshift objects (López-Sánchez et al. 2012).

4.5.3. Comparing Metallicity Diagnostics

Pilyugin et al. (2010) provided two empirically calibrated metallicity diagnostics, ONS and ON. From Table 4.1, we can see that the ON metallicity diagnostic can only be converted to the ONS diagnostic (Spearman rank = 0.78). This similarity is expected as Pilyugin et al. (2010) found that the ON diagnostic was comparable to the ONS diagnostic across all classes (cool, warm and hot) of HII regions. Although the ON diagnostic may be comparable to the ONS diagnostic, the addition of the [SII] emission line into the ONS diagnostic allows it be converted to O3N2 and N2O2 metallicity gradients, giving the ONS diagnostic more versatility in terms of being able to compare it to metallicity gradients from other studies.

In addition, the calibrations for the ON and ONS diagnostic are given in three separate equations for each class of HII region. To distinguish these classes, Pilyugin et al. (2010) used the [NII]/Hβ and [NII]/[SII] emission line ratios. These definitions mean that although the ON calibration does not directly use the [SII] emission line to derive the metallicity, it is still required to distinguish which HII regime the emission lines fall under. It is therefore better to use the ONS diagnostic because of its ability to be easily compared to the O3N2 and N2O2 diagnostic without the need for extra information over the ON diagnostic.

As mentioned in Section 4.1, there are generally two methods for calibrating metallicity diagnostics, the direct temperature method or through photoionization models. Scal and

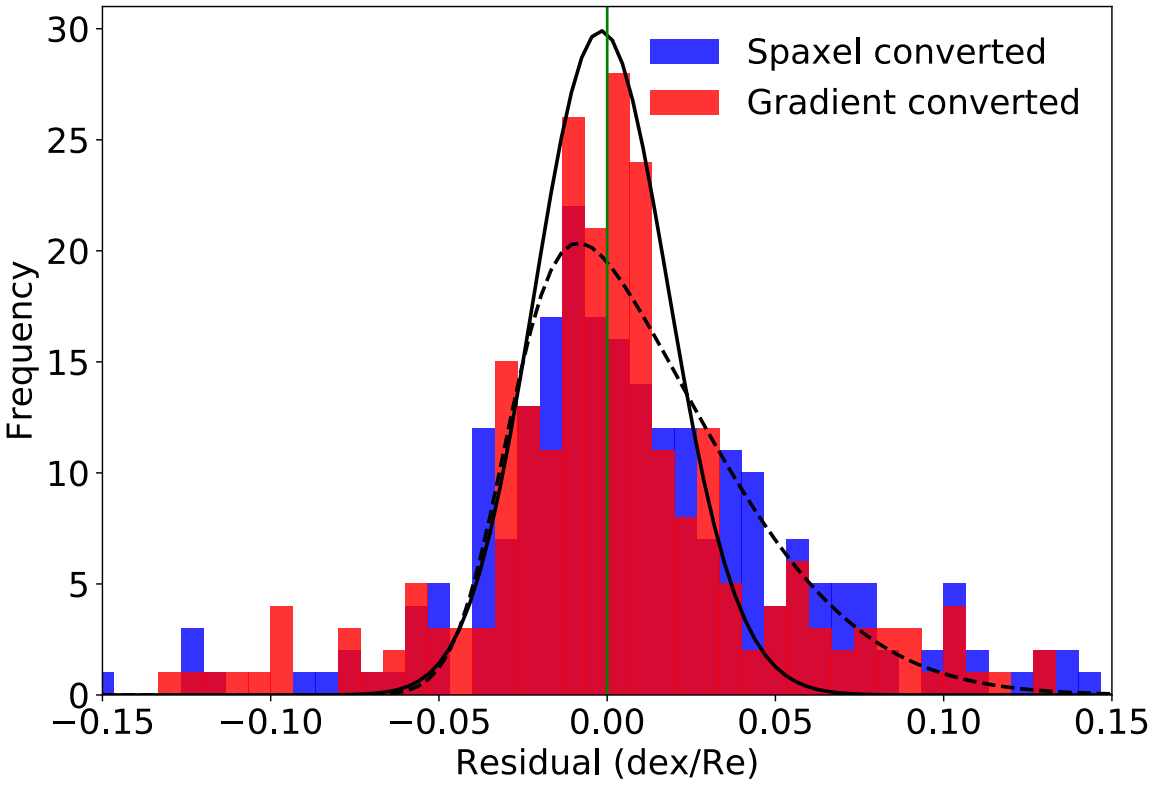

Figure 4.8 Distribution of residuals when comparing spaxel-converted (blue) and empirically converted metallicity gradients (red) to the true metallicity gradient. The fitted skewed Gaussians (solid line for red and dashed line for blue) clearly show the reduction in residual dispersion when converting P04O3N2 metallicity gradients empirically to P04N2Hα instead of spaxel-converted metallicity gradients.

Rcal are calibrated using the counterpart method outlined in Pilyugin et al. (2012). The counterpart method involves matching the observed HII region with that of a reference sample containing HII regions of known metallicity. The metallicity of the reference sample used by Pilyugin et al. (2012) is determined through the direct temperature method. Therefore, we classify the Scal and Rcal metallicity diagnostics as being calibrated through the direct temperature method.

The Scal and Rcal metallicity diagnostics differ only by replacing the [SII] emission line in the Scal diagnostic with the [OII] emission line in the Rcal diagnostic. This simple change effectively highlights that diagnostics that utilise similar emission line ratios tend to agree better than those that use different sets of emission lines. The Scal and Rcal diagnostics can be converted to the N2Hα, N2O2, N2S2Hα diagnostics, as well as to the Machine Learning algorithm and to each other. Additionally, with the [OII] emission line, the K04R_{23} calibration can be converted to the Rcal diagnostic. Similarly, The N2S2Hα diagnostic provides a lower rms error when converting to the Scal diagnostic compared to the Rcal diagnostic. Interestingly, the N2O2 diagnostic has a higher Spearmans rank with the Rcal diagnostic but a lower rms error with the Scal diagnostic. This apparent discrepancy could be due to the sensitivity of the Spearmans rank to outliers that are being removed during the linear-fitting process.

From Table 4.2, we see that the diagnostics calibrated through the direct temperature always have a lower rms error than diagnostics calibrated through photoionization models regardless of whether or not the reference diagnostic was calibrated by direct temperature

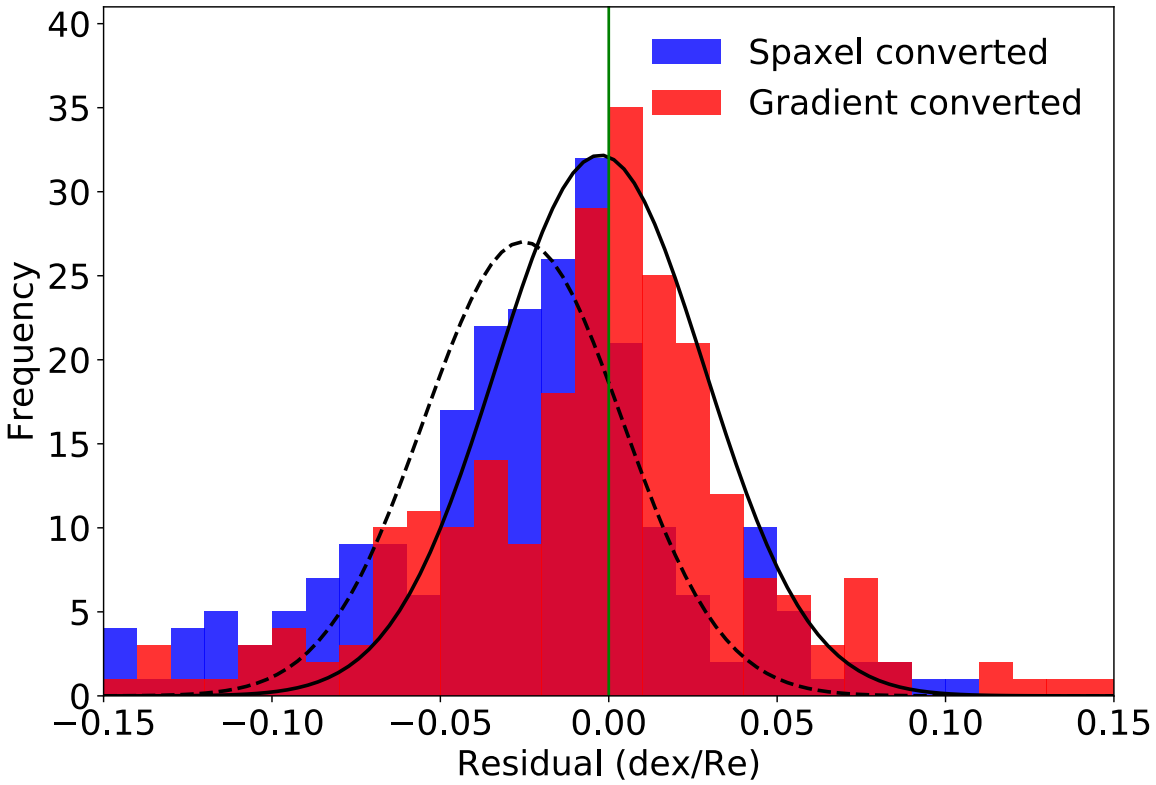

Figure 4.9 Same as Figure 4.8 but converting the P04O3N2 sector metallicites to N2O2. In this example, an offset is corrected for by converting metallicity gradients directly using the conversion relations presented here.

or through photoionization models. The exception to this is between the Scal and N2S2Hα diagnostics, which agree remarkably well.

It is unsurprising that when comparing direct temperature calibrations to other direct temperature calibrations, we obtain a lower rms error compared to diagnostics calibrated through photoionization models. This is partially due to several diagnostics sharing a considerable fraction of HII regions as calibration points. However, the diagnostics calibrated through photoionization models have a larger rms error when compared to other photoionization model calibrations relative to the direct temperature calibrations. The obvious answer to this problem is that different photoionization models with different assumptions were used to calibrate the diagnostics.

For example, the N2O2 diagnostic was calibrated through MAPPINGS III photoionization models (Sutherland et al. 2013) while the N2S2Hα diagnostics was calibrated through MAPPINGS V photoionization models (Sutherland et al. 2018). Significant changes have been made between MAPPINGS III and MAPPINGS V, that may cause the discrepancies we see here. Differences in model conditions may also contribute to the differences we see, such as pressure and electron temperature. The large number of free parameters available to theoretical models is likely the cause of the rms error seen between N2O2 and N2S2Hα.

However, different versions of MAPPINGS does not fully explain the scatter between the K04R_{23} and N2O2 diagnostic. Although these two diagnostics were calibrated by different authors (Kewley & Dopita (2002) and Kobulnicky & Kewley (2004)), they both use the same photoionization grids outlined in Kewley & Dopita (2002). This highlights that even if consistent photoionization models are used, different metallicity diagnostics produce

greater scatter compared to direct temperature methods.

4.5.4. Machine Learning vs Emission Line Ratio

We see from Table 4.1 that MLP is convertible (Spearmans rank > 0.6) for diagnostics that include the N2 ([NII]/Hα or [NII]/Hβ) emission line ratio as well as the N2O2 diagnostic. Although the N2O2 diagnostic can be converted to MLP, the rms scatter indicates that it does not perform as well as the other diagnostics that can also be converted to MLP (i.e. N2Hα, O3N2, N2S2Hα, Scal and Rcal). MLP also does significantly better with the M13 calibrations compared to the P04 calibrations. For both N2Hα and O3N2 diagnostics, MLP is amongst the worst when compared to the P04 calibration, but has the smallest rms error for the M13N2Hα calibration and is only marginally (0.01) beaten by the N2 calibrations for M13O3N2. MLP performing better for the M13 calibration rather than the P04 calibration is consistent with the testing performed by Ho (2019) when developing MLP.

Diagnostics that do not include the [NII]/Hα emssion line ratio (R_{23}, ONS and ON) do not correlate well with MLP with the exception of N2O2 in which MLP is outperformed by a number of other diagnostics. This dependence on the [NII]/Hα emssion line ratio arises due to the large variation of the ratio with metallicity, visible in the classic BPT diagram. This large variation is caused by the secondary nucleosynthetic pathway of nitrogen (see e.g. Nicholls et al. 2017).

4.5.5. Metallicity Gradient-Mass Relation

One of the most well-known galaxy correlations is the mass-metallicity relation (Tremonti et al. 2004). In the era of integral field spectroscopy and spatially resolved metallicity maps, this correlation has evolved into the metallicity gradient-mass relation. The main point of contention with the metallicity gradient-mass relation is whether or not metallicity gradients evolve as a function of mass. Some studies show the existence of a characteristic metallicity gradient once it has been normalized to the size of the disk, i.e., the metallicity gradient is the same regardless of the mass (Sánchez et al. 2012, 2014; Ho et al. 2015; Sánchez-Menguiano et al. 2016b, 2018). Others show that the metallicity gradients become steeper for higher mass galaxies up to a stellar mass of about $10^{9.5} - 10^{10.5} M_{\odot}$. Beyond a mass of $10^{10.5} M_{\odot}$, a break in the metallicity gradient-mass relation appears and the metallicity gradients become shallower with increasing mass (Belfiore et al. 2017).

Several studies have proposed and clearly shown that single linear fits do not accurately represent the metallicity as a function of radius (Vila-Costas & Edmunds 1992; Sánchez et al. 2012, 2014; Sánchez-Menguiano et al. 2016b; Belfiore et al. 2017). Using MUSE data, Sánchez-Menguiano et al. (2018) showed the presence of inner and outer flattening of the metallicity radial gradient, especially for high mass galaxies. This flattening suggests that a broken linear-fit may be a better method for characterising metallicity radial gradients. The inner and outer flattening of massive galaxies may be artificially flattening the overall metallicity radial profile when fit with single linear gradients.

Figure 4.10 shows the metallicity gradient-mass relation of seven different metallicity calibrations, each of which can be converted to the Scal metallicity diagnostic based on the

linear fits provided in this paper. We perform a broken linear regression to each of the panels. We require the broken linear-fit to be continuous, but allow the position of the break to be a free variable. We find that for each of the calibrations, a break in the metallicity gradient-mass relation occurs between $10^{9.5} - 10^{10.5} M_{\odot}$. As we are not directly forcing a break in the linear trend while fitting, this indicates a consistent trend in the metallicity gradient-mass relation when using single linear fits to metallicity gradients. Due to the relatively low spatial resolution of our data, we are unable to test how this trend changes if a broken linear-fit is used to fit metallicity gradients.

We summarise Figure 4.10 in the left panel of Figure 4.11, where we show the broken linear-fits to the metallicity gradient-mass relation of each calibration. We can see that the metallicity gradient-mass relation varies substantially depending on which metallicity calibration is used. We have chosen these diagnostics specifically as they can be converted to the Scal diagnostic based on the analysis presented in this paper. We have chosen Scal to be our fiducial metallicity diagnostic because apart from MLP and NB, it requires the availability of the majority of the strong optical emission lines alongside Rcal and ONS. Selecting a fiducial metallicity diagnostic that requires a large number of emission lines is important because the only situation where these conversions should be used is when going from a basic (in terms of how many emissions lines are required) metallicity diagnostic such as N2Hα to a more complicated one. Although the ONS diagnostic uses more emission lines, the majority of metallicity diagnostics do not agree with its calculations, meaning it would not be a useful case study. In the right panel of Figure 4.11, we convert each of the metallicity gradient-mass relations to the Scal diagnostic. By applying the metallicity calibration conversions, we reduce the maximum deviations between calibrations from 0.11 dex/R_e to 0.02 dex/R_e, a significant improvement. The reduction in maximum deviation demonstrates the effectiveness of using the metallicity calibrations conversions to convert from single emission line ratio diagnostics (N2Hα and N2O2) to multiple emission line ratio diagnostics.

Although we have been able to significantly reduce the dispersion in the metallicity gradient-mass relation between the metallicity calibrations in Figure 4.11, there is clearly a large amount of scatter around each of the lines of best fit in Figure 4.10. This implies that the conversion fits presented in Table 4.2 are most suitable for converting mean metallicity gradients of a sample of galaxies and we caution against its usage on individual galaxies.

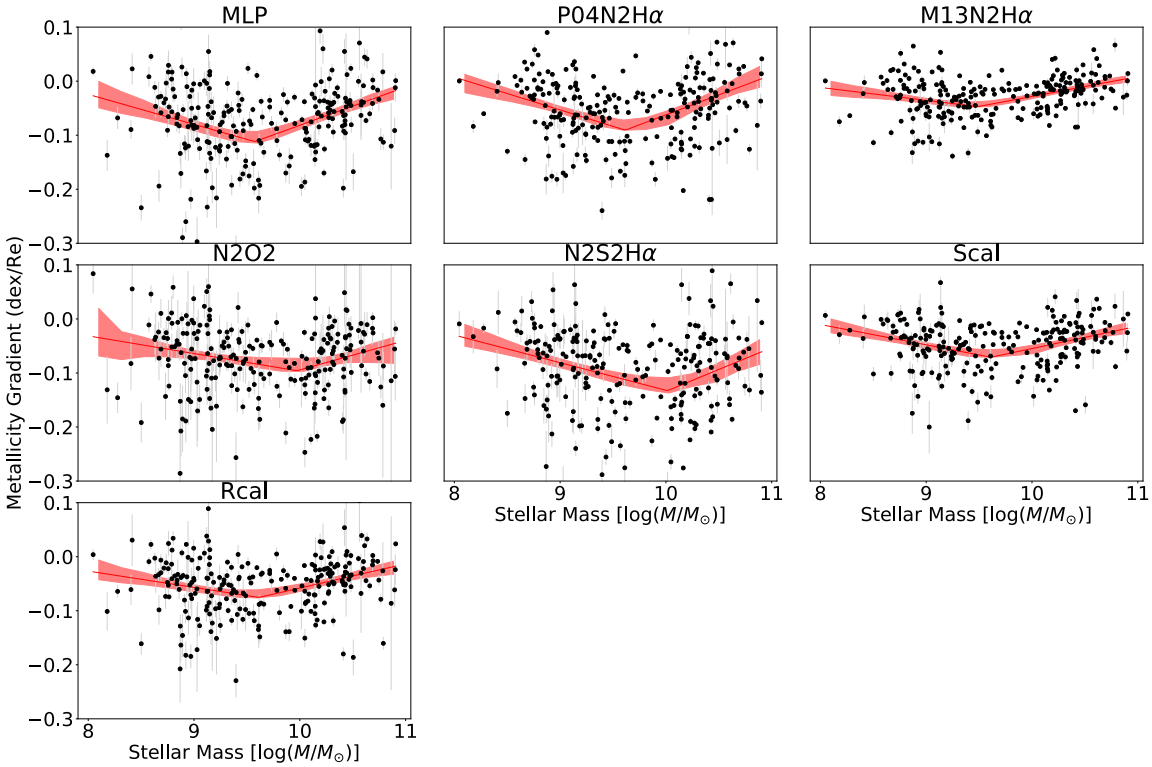

Figure 4.10 Metallicity gradient-mass relation for calibrations that can be converted to Scal. We apply a broken linear-fit to each of the panels, allowing the location of the break to vary between diagnostics. Red bands indicate the 1 σ uncertainties of the broken linear-fits. Even though we do not force a break in the linear trend, each of the panels shows a broken linear-fit where the measured gradient switches from negative to positive for galaxies with stellar masses between $10^{9.5}$ and $10^{10.5} M_{\odot}$.

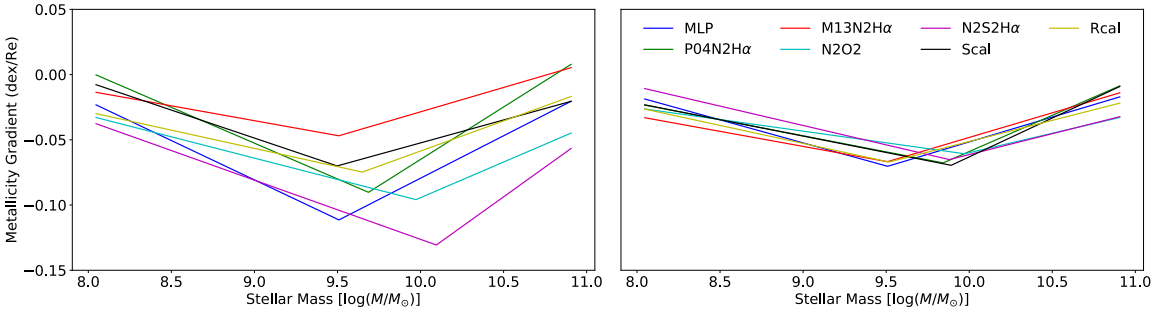

Figure 4.11 *Left:* We take each of the metallicity gradient-mass fits from Figure 4.10 and put them all on the same axis, highlighting the significant differences that we find in this relation depending on which diagnostic is used. The maximum difference between the different metallicity gradient-mass fits is 0.11 dex/R_e. *Right:* We convert each of the metallicity gradients to an Scal metallicity gradient based on the conversion factors in Table 4.2. We then re-fit the metallicity gradient-mass relation using the converted metallicity gradients. One can see that the dispersion from diagnostic to diagnostic is significantly reduced once we convert all the metallicity gradients to Scal. The maximum difference is reduced from 0.11 dex/R_e to only 0.02 dex/R_e.

4.6. Summary

Using SAMI DR2 sector-binned cubes, we create metallicity maps and measure their metallicity gradient using 13 popular emission line diagnostics and techniques. We investigate the differences in measured metallicity gradients and determine if we can accurately compare metallicity gradients obtained through different methods. For pairs of diagnostics with a Spearmans rank > 0.6, we provide empirical fits to allow for the conversion between the two diagnostics. The ability to convert between diagnostics is important for high-redshift studies where a wide range of emission lines are unavailable and there is a need to compare high-redshift metallicity gradients to local galaxies.

We find that the relationship between most of the diagnostics are accurately represented as a linear function with a non-unity slope. The non-unity slope demonstrates that one cannot expect metallicity gradients to be the same across different diagnostics, demonstrating the importance of the conversion functions we provide in this paper. We also find that the zero-point of the linear relations is close to 0, meaning that flat metallicity gradients remain as flat gradients across the diagnostics tested in this study.

We compare two common calibrations of the N2Hα and O3N2 emission line diagnostics by Pettini & Pagel (2004) and Marino et al. (2013) to determine which calibration provides more flexibility in terms of comparing to other metallicity gradients. We find that the calibrations by Marino et al. (2013) provide better agreement than the calibrations by Pettini & Pagel (2004) across all the diagnostics tested here. Better agreement is likely due to the enhanced accuracy of high-metallicity measurements used by Marino et al. (2013) for calibration, which were not available to Pettini & Pagel (2004) at the time of writing.

As expected, emission line diagnostics that share similar emission line ratios tend to agree better than those that use different sets of emission lines. For example, the Rcal diagnostic by Pilyugin & Grebel (2016) provides a lower rms error when converting to the K04R_{23} and N2O2 diagnostic compared to the Scal diagnostic, which replaces the [OII] emission line for the [SII] emission. Similarly, the Scal diagnostic provides a better agreement with the N2S2Hα diagnostic compared to the Rcal diagnostic.

The use of machine learning to measure gas-phase metallicity has only recently emerged (Ho 2019; Wu & Boada 2019). We find that OxygenMLP (Ho 2019) agrees well with diagnostics which include either the [NII]/Hα or [NII]/Hβ emission line ratios. This strongly suggests that the N2 emission line ratio is one of the strongest tracers of gas-phase metallicity.

Our analysis highlights the stark differences present between various metallicity diagnostics and the uncertainties of comparing metallicity diagnostics derived through different methods. When comparing metallicity gradients, we recommend using the same methods as the original author (where possible) in order to reduce systematic errors. If the same emission lines are not available, Table 4.2 can be used to convert metallicity gradients from one diagnostic to another. We find that directly converting the metallicity gradients empirically provides a closer estimate of the desired metallicity gradient than individually converting spaxels. These conversion relations will be useful tools for analysing the gas-phase metallicities of galaxies at high-redshift, where the availability of a wide range of emissions lines is scarce.

Acknowledgements

Parts of this research were conducted by the Australian Research Council Centre of Excellence for All Sky Astrophysics in 3 Dimensions (ASTRO 3D), through project number CE170100013.
BG gratefully acknowledges the support of the Australian Research Council as the recipient of a Future Fellowship (FT140101202).
This research has made use of the NASA/IPAC Extragalactic Database (NED), which is operated by the Jet Propulsion Laboratory, California Institute of Technology, under contract with the National Aeronautics and Space Administration.

4.7. Appendix: Metallicity Diagnostics and Calibrations

Here we provide the functional forms of all the metallicity calibrations used in this study.

4.7.1. K04R$_{23}$(Kobulnicky & Kewley 2004)

The first step involves assigning an initial metallicity guess using the [NII]λ6583/[OII]λ3726, λ3729 (N2O2) emission line ratio. If log([NII]/[OII]) < -1.2, then we place the spaxel on the lower branch and assume an initial 12 + log(O/H) = 8.2. If log([NII]/[OII]) > -1.2, then we place the spaxel on the upper branch and assume an initial 12 + log(O/H) = 8.7. The initial estimate of metallicity is then used to calculate the ionization parameter using Equation 4.6;

$$\begin{aligned}\log(q) = 32.81 - 1.153y^2 + [(\mathrm{O/H})^*](-3.396 - 0.025y + 0.1444y^2) \\ \times (4.603 - 0.3119y - 0.163y^2 + [(\mathrm{O/H})^*](-0.48 + 0.0271y + 0.02037y^2))^{-1}\end{aligned} \quad (4.6)$$

where y = log([OIII]$\lambda\lambda$4959, 5007/[OII]$\lambda\lambda$3726, 3729) and (O/H)*=12+log(O/H).

The initial estimate of ionization parameter is then used to calculate the metallicity using the ([OII]$\lambda\lambda$3726, 3729 + [OIII]$\lambda\lambda$4959, 5007)/Hβ (R$_{23}$) emission line ratio with the relevant calibration depending on which branch the spaxel was initially assigned by the N2O2 emission line ratio:

$$\begin{aligned}(\mathrm{O/H})^*_{\mathrm{lower}} = 9.40 + 4.65x - 3.17x^2 - \log(q) \times (0.272 + 0.547x - 0.513x^2) \\ (\mathrm{O/H})^*_{\mathrm{upper}} = 9.72 - 0.777x - 0.951x^2 - 0.072x^3 - 0.811x^4 \\ - \log(q) \times (0.0737 - 0.0713x - 0.141x^2 + 0.0373x^3 - 0.058x^4)\end{aligned} \quad (4.7)$$

where x = log(R$_{23}$) and (O/H)*=12+log(O/H).

The spaxel is then iterated between Equations 4.6 and 4.7 until convergence is achieved within a predetermined tolerance. Three iterations are typically needed to reach a converegence level of 0.01 dex.

4.7.2. N2O2 (Kewley & Dopita 2002)

$$(\mathrm{O/H})^* = 1106.87 - 532.154x + 96.3733x^2 - 7.81061x^3 + 0.239282x^4 \quad (4.8)$$

where x = log($N2O2$) and (O/H)*=12+log(O/H).

4.7.3. N2Hα (Pettini & Pagel 2004; Marino et al. 2013)

$$\begin{aligned}(\mathrm{O/H})^*_{P04} = 9.37 + 2.03x + 1.26x^2 + 0.32x^3, \text{where} - 2.5 < x < -0.3 \\ (\mathrm{O/H})^*_{M13} = 8.743 + 0.462x, \text{where} - 1.6 < x < -0.2\end{aligned} \quad (4.9)$$

where x = log($N2H\alpha$) and (O/H)*=12+log(O/H).

4.7.4. O3N2 (Pettini & Pagel 2004; Marino et al. 2013)

$$\begin{aligned}(\mathrm{O/H})^{*}_{P04} &= 8.73 - 0.32x, \text{where} -1.0 < x < 1.9\\ (\mathrm{O/H})^{*}_{M13} &= 8.533 - 0.214x, \text{where} -1.1 < x < 1.7\end{aligned} \tag{4.10}$$

where $x = \log(O3N2)$ and (O/H)*=12+log(O/H).

4.7.5. N2S2Hα (Dopita et al. 2016)

$$(\mathrm{O/H})^{*}_{D16} = 8.77 + x + 0.45(x + 0.3)^{5}, \text{where} -1.1 < x < 0.5 \tag{4.11}$$

where $x = \log([\mathrm{NII}]/[\mathrm{SII}]) + 0.264 \times \log(N2H\alpha)$ and (O/H)*=12+log(O/H).

4.7.6. ONS and ON (Pilyugin et al. 2010)

$$\begin{aligned}(\mathrm{O/H})^{*}_{\mathrm{ONS\_Cool}} &= 8.277 + 0.657 \times P - 0.399 \times \log(O3H\beta)\\ &\quad - 0.061 \times \log(N2O2) + 0.005 \times \log(S2O2)\end{aligned}$$

$$\begin{aligned}(\mathrm{O/H})^{*}_{\mathrm{ONS\_Warm}} &= 8.816 - 1.855 \times P + 1.517 \times \log(O3H\beta)\\ &\quad + 0.710 \times \log(N2O2) - 0.337 \times \log(S2O2)\end{aligned}$$

$$\begin{aligned}(\mathrm{O/H})^{*}_{\mathrm{ONS\_Hot}} &= 8.774 - 1.855 \times P + 1.517 \times \log(O3H\beta)\\ &\quad + 0.304 \times \log(N2O2) + 0.328 \times \log(S2O2])\end{aligned} \tag{4.12}$$

$$\begin{aligned}(\mathrm{O/H})^{*}_{\mathrm{ON\_Cool}} &= 8.606 - 0.105 \times \log(O3H\beta) - 0.410 \times \log(O2H\beta)\\ &\quad - 0.150 \times \log(N2O2)\end{aligned}$$

$$\begin{aligned}(\mathrm{O/H})^{*}_{\mathrm{ON\_Warm}} &= 8.642 + 0.077 \times \log(O3H\beta) + 0.411 \times \log(O2H\beta)\\ &\quad + 0.601 \times \log(N2O2)\end{aligned}$$

$$\begin{aligned}(\mathrm{O/H})^{*}_{\mathrm{ON\_Hot}} &= 8.013 + 0.905 \times \log(O3H\beta) + 0.602 \times \log(O2H\beta)\\ &\quad + 0.751 \times \log(N2O2)\end{aligned} \tag{4.13}$$

where P is the excitation parameter [OIII]/([OII]+[OIII]), O3Hβ = log([OIII]/$H\beta$) and S2O2 = log([SII]/[OII]).

$$\begin{aligned}&\text{Use } (\mathrm{O/H})^{*}_{\mathrm{Cool}} \text{ if } \log(N2H\beta) \geq -0.1\\ &\text{Use } (\mathrm{O/H})^{*}_{\mathrm{Warm}} \text{ if } \log(N2H\beta) < -0.1 \text{ and if } \log(N2S2) \geq -0.25\\ &\text{Use } (\mathrm{O/H})^{*}_{\mathrm{Hot}} \text{ if } \log(N2H\beta) < -0.1 \text{ and if } \log(N2S2) < -0.25\end{aligned} \tag{4.14}$$

where N2Hβ = log([NII]/$H\beta$) and N2S2 = log([NII]/[SII]).

4.7.7. Rcal and Scal (Pilyugin & Grebel 2016)

$$
\begin{aligned}
(\mathrm{O/H})^{*}_{\mathrm{R\_lower}} &= 7.932 + 0.944 \times \log(O32) + 0.695 \times \log(N2H\beta) \\
&\quad + (0.970 - 0.291 \times \log(O32) - 0.019 \times \log(N2H\beta)) \times (O2H\beta)
\end{aligned}
$$

$$
\begin{aligned}
(\mathrm{O/H})^{*}_{\mathrm{R\_upper}} &= 8.589 + 0.022 \times \log(O32) + 0.399 \times \log(N2H\beta) \\
&\quad + (-0.137 + 0.164 \times \log(O32) + 0.589 \times \log(N2H\beta)) \times (O2H\beta)
\end{aligned}
\tag{4.15}
$$

$$
\begin{aligned}
(\mathrm{O/H})^{*}_{\mathrm{S\_lower}} &= 8.072 + 0.789 \times \log(O3S2) + 0.726 \times \log(N2H\beta) \\
&\quad + (1.069 - 0.170 \times \log(O3S2) + 0.022 \times \log(N2H\beta)) \times (S2H\beta)
\end{aligned}
$$

$$
\begin{aligned}
(\mathrm{O/H})^{*}_{\mathrm{S\_upper}} &= 8.424 + 0.030 \times \log(O3S2) + 0.751 \times \log(N2H\beta) \\
&\quad + (-0.349 + 0.182 \times \log(O3S2) + 0.508 \times \log(N2H\beta)) \times (S2H\beta)
\end{aligned}
\tag{4.16}
$$

where O2Hβ = log([OII]/$H\beta$), S2Hβ = log([SII]/$H\beta$) and O3S2 = log([OIII]/[SII]).

$$\begin{aligned} &\text{Use } (\mathrm{O/H})^{*}_{\mathrm{Lower}} \text{ if } \log(N2H\beta) < -0.6 \\ &\text{Use } (\mathrm{O/H})^{*}_{\mathrm{Upper}} \text{ if } \log(N2H\beta) \geq -0.6 \end{aligned} \tag{4.17}$$

4.7.8. C17R$_{23}$(Curti et al. 2017)

$$\log \mathrm{R}_{23} = 0.527 - 1.569y - 1.652y^2 - 0.421y^3 \tag{4.18}$$

where $12 + \log(\mathrm{O/H}) = y + 8.69$

CHAPTER 5

Effects of Diffuse Ionized Gas and Spatial Resolution on Metallicity Gradients

This chapter presents the content of the article: The Effects of Diffuse Ionized Gas and Spatial Resolution on Metallicity Gradients: TYPHOON Two-Dimensional Spectrophotometry of M83. This article was published in the Monthly Notices of the Royal Astronomical Society, Volume 487, Issue 1, p.79. The abstract of this chapter is as follows:

We present a systematic study of the diffuse ionized gas (DIG) in M83 and its effects on the measurement of metallicity gradients at varying resolution scales. Using spectrophotometric data cubes of M83 obtained at the 2.5m duPont telescope at Las Campanas Observatory as part of the TYPHOON program, we separate the HII regions from the DIG using the [SII]/Hα ratio, HIIPHOT (HII finding algorithm) and the Hα surface brightness. We find that the contribution to the overall Hα luminosity is approximately equal for the HII and DIG regions. The data is then rebinned to simulate low-resolution observations at varying resolution scales from 41 pc up to 1005 pc. Metallicity gradients are measured using five different metallicity diagnostics at each resolution. We find that all metallicity diagnostics used are affected by the inclusion of DIG to varying degrees. We discuss the reasons of why the metallicity gradients are significantly affected by DIG using the HII dominance and emission line ratio radial profiles. We find that applying the [SII]/Hα cut will provide a closer estimate of the true metallicity gradient up to a resolution of 1005 pc for all metallicity diagnostics used in this study.

5.1. Introduction

The gas-phase metallicity of a galaxy is strongly affected by the processes that occur during the galaxy's evolution. Gas inflows, galaxy mergers and galactic winds are a few examples of events that alter the spatial metallicity distribution. Measuring the metallicity of a galaxy therefore leads to strong constraints on its growth and formation. Many studies have shown that isolated spiral galaxies exhibit a characteristic metallicity gradient when normalised

by the disc scale length (Sánchez et al. 2012, 2014; Ho et al. 2015; Sánchez-Menguiano et al. 2016b; Poetrodjojo et al. 2018). This implies that galaxies tend to form along the same evolutionary track if they are relatively unaffected by their environment. Conversely, interacting galaxies consistently show significantly shallower metallicity gradients than their isolated counterparts (Kewley et al. 2010; Rich et al. 2012; Sánchez et al. 2014). This flattening is caused by a combination of many processes which stem from the gravitational interactions between the galaxy pairs. Dilution of the metal-rich centre caused by inflows of pristine gas from the outskirts of a galaxy is an example of how flattening can occur in interacting galaxy pairs (Rupke et al. 2010; Kewley et al. 2010).

Advances in integral field unit (IFU) spectroscopy allow astronomers to spatially resolve detailed physical properties of individual galaxies. Using these spatially resolved emission line spectra, we are able to produce the metallicity map of a galaxy to great detail. Metallicity maps allow us to view the variations of metallicity within a galaxy and to constrain the metallicity gradients with greater certainty rather than placing limited apertures throughout a galaxy. Recently there have been several large scale IFU surveys such as the Calar Alto Legacy Integral Field Area survey (CALIFA, Sánchez et al. 2012), the Sydney-Australian-Astronomical-Observatory Multi-object Integral-Field Spectrograph survey (SAMI, Allen et al. 2015; Croom et al. 2015; Bryant et al. 2015) and the Mapping Nearby Galaxies at APO survey (MaNGA, Bundy et al. 2015). The SAMI and MaNGA surveys aim to observe ~ 3600 and ~ 10000 galaxies respectively, through the use of multiplexing technology which allows them to view multiple galaxies at once. Such studies greatly increases the number of observed galaxies, and allow statistical studies of resolved properties like metallicity gradients to be determined (Sánchez et al. 2012, 2014; Ho et al. 2015; Sánchez-Menguiano et al. 2016b; Belfiore et al. 2017; Poetrodjojo et al. 2018).

The disadvantage of these large scale IFU surveys is that, because of the wide field needed to sample multiple galaxies at once, they often have seeing-limited spatial resolutions on the order of $\sim 1-2$ kpc. Typical HII regions range from ten to hundreds of parsecs (Azimlu et al. 2011; Gutiérrez et al. 2011; Whitmore et al. 2011), much smaller than the resolution of these large IFU surveys. This means that the vast majority of resolution elements of the SAMI and MaNGA data contain a mixture of emission from HII regions and surrounding diffuse ionized gas (DIG). Most strong emission line metallicity diagnostics are generated on the assumption that the emission lines are produced purely from HII regions. The contamination by DIG causes systematic variations in metallicity, which can cause the metallicity gradient to be steepened or flattened depending on the galaxy and metallicity diagnostic used (Zhang et al. 2017).

The diffuse ionized gas, also known as the Warm Ionized Medium (WIM), has long been a region of interest in nearby galaxies. It was first identified by Reynolds (1984) in the Milky Way and was named the Reynolds layer. Further studies have uncovered it has a significant contribution to the overall luminosity of a galaxy as well as its prevalence in most star-forming galaxies (Walterbos & Braun 1994; Ferguson et al. 1996; Hoopes et al. 1996; Greenawalt et al. 1998). For a comprehensive review of the DIG, see Haffner et al. (2009).

DIG is found within the plane of the galaxy disk as well as above and below it, more specifically referred to as the extraplanar diffuse ionized gas (eDIG) (Hoopes et al. 1999; Rossa & Dettmar 2003). One of the defining features of the DIG are its enhanced emission

line ratios including [SII]/Hα, [NII]/Hα and [OI]/Hα relative to HII regions (Hoopes & Walterbos 2003; Madsen et al. 2006; Voges & Walterbos 2006), which shifts the DIG towards the LINER and AGN regions of the BPT diagram (Baldwin et al. 1981). These variations in the emission line ratios combined with its prominent contribution to the total emission line flux, means that it can significantly alter the emission line products of a galaxy such as metallicity, ionization parameter and star-formation rate calculations. In low-resolution observations such as those at high-redshift, large galaxy surveys and aperture measurements, where the DIG can not be isolated due to spatial resolution limitations, a contribution by the DIG is inevitable.

The source of ionizing photons of the DIG is still a debated topic with two likely explanations: leakage of ionizing photons from HII regions and ionization by low-mass evolved stars. The spatial correlation of HII regions and the DIG suggests leaky HII regions as a strong candidate for the source of ionizing photons. Using the Survey for Ionization in Neutral Gas Galaxies (SINGG) sample, Oey et al. (2007) found an anti-correlation between the fraction of Hα surface brightness from the DIG and the overall Hα surface brightness. A mean fraction of 0.59 ± 0.19 was found with starburst galaxies ($\Sigma(H\alpha) > 2.5 \times 10^{39}$ erg s^{-1} kpc^{-2}) containing the lowest fraction of DIG. However, leaky HII regions are unable to fully reproduce the emission line spectrum that we see in the DIG. In particular, HII region photon leakage enhances the [SII]/Hα, [NII]/Hα and [OI]/Hα emission line ratios, but is unable to produce the [OIII]/Hβ emission line enhancement (Zhang et al. 2017). It is likely that the DIG is ionized by some combination of ionizing photons produced by leaky HII regions and low-mass evolved stars.

Gradient smoothing is another disadvantage caused by the kiloparsec resolution scales of these low-spatial resolution IFU surveys. With large resolution scales of $1-2$ kpc, regions of high metallicity are mixed with regions of lower metallicity, causing the overall smoothing of the metallicity gradient. Yuan et al. (2013) demonstrated this flattening through annular binning and discussed the implications for measuring metallicity gradients at high redshift using the [NII]/Hα metallicity diagnostic (Pettini & Pagel 2004). Mast et al. (2014) used galaxies from the PPAK IFS Nearby Galaxies Survey (PINGS) and degraded the data to different spatial resolutions and showed the flattening of the metallicity gradient at coarser resolution scales, simulating the effects of observing at higher redshifts.

One way to obtain high resolution observations is to observe large nearby galaxies. The large angular size of nearby galaxies allows for an intrinsically higher seeing limited physical resolution. However, because these galaxies tend to occupy a large area of the sky, the typical IFU field of view is far too small to observe the entire galaxy.

TYPHOON/PrISM is a wide field spectrograph survey which aims to produce highly spatially resolved spectrophotometric data of nearby galaxies. Instead of using fibre bundles like large IFU surveys, TYPHOON uses a very long 18′ slit with a width of 1.65″ and steps across the face of the galaxy. By choosing nearby galaxies ($z \leq 0.005$), TYPHOON is able to achieve seeing-limited resolutions of up to 2 pc, with a median of 48 pc across their galaxy sample. At these resolution scales we are able to resolve individual HII regions without any DIG contamination. When calculating metallicity gradients, we also avoid the smoothing that occurs at coarser resolution scales.

In this paper, we use TYPHOON data to determine the true metallicity gradient of

M83/NGC5236 unaffected by DIG contamination or spatial smoothing. We then degrade the data to coarser resolution scales to show the systematic flattening of the metallicity gradient and the implications this will have on large scale IFU surveys. We discuss the effectiveness of applying DIG corrections at low resolution scales when measuring metallicity gradients.

We structure this paper as follows: in Section 2 we summarise the properties of M83 and describe the TYPHOON observations. We describe our procedures for rebinning the native resolution data cube to coarser resolutions and discuss the various metallicity diagnostics we use in Section 3. The results of our study are presented in Section 4 and we discuss the implications our results will have on the interpretation of coarse resolution data products in Section 5. Finally in Section 6 we provide a brief summary and future directions of the research involving the TYPHOON dataset.

5.2. M83

5.2.1. Observations and Properties

M83/NGC 5236 is a nearby face-on barred spiral galaxy with a galactocentric distance of 4.47 Mpc (Tully et al. 2008) with a redshift of $z = 0.001711$. M83 was observed as part of the TYPHOON program using the 2.5m du Pont telescope at the Las Campanas Observatory in Chile. For full information regarding the TYPHOON survey and instrument, see Seibert et al. (in prep). The imaging spectrograph of TYPHOON, Wide Field reimaging CCD (WFCCD), is configured to have a resolving power of approximately R≈ 850 at 7000Å and R≈ 960 at 5577Å, covering a wavelength range between 3650Åto 8150Å. This allows us to completely separate the [NII] emission lines from Hα, but does not provide enough resolving power to fit multiple Gaussian components to emission lines.

A total of 243 observations were spread during 9 nights over 2 observing runs in May 2011 (5 nights) and February 2016 (4 nights). Each slit position was integrated for 600 seconds before being moved by 1.65″(width of the TYPHOON slit) for the next integration. This process was repeated until the optical disk of M83 was covered, resulting in an image covering an area of $6.7' \times 18'$. The data is then reduced using standard long-slit data techniques and the final spectrum fit using LZIFU (Ho et al. 2016) to produce emission line flux datacubes.

In order to ensure the quality of the data over multiple nights and observing runs, we employ strict observational requirements. We only include data into the final datacube when conditions are photometric with a seeing less than the width of the slit at all times (seeing < 1.65″). This means that any emitted light is not being lost due to our narrow slit width. The long length of the slit (18′) means that we are able to utilise the upper and low portions not occupied by the galaxy for calibration purposes. This allows us to calibrate each slit individually, ensuring consistent calibration over the multiple nights which galaxies of the TYPHOON survey are typically observed.

At the proximity of M83, the 1.65″ slit gives us a native resolution of 41 pc. Its proximity and face-on profile have made it one of the most popular and widely studied galaxy to date. This resolution scale allows us to separate HII dominated regions from DIG. A table of all intrinsic properties used for this study are given in Table 5.1.

Name	M83/N5236	Reference
Right Ascension	$13^h37^m0.95^s$	Díaz et al. (2006)
Declination	−29°51′55.5″	Díaz et al. (2006)
Distance	4.47 Mpc	Tully et al. (2008)
$\log(M_*/M_\odot)$	10.55	Bresolin et al. (2016)
Effective Radius	196.7″	Lauberts & Valentijn (1989)
Position Angle	44.9°	Lauberts & Valentijn (1989)
Inclination	32.5°	Lauberts & Valentijn (1989)

Table 5.1 Fundamental properties of M83 used in this study.

In Figure 5.1 we show the BVR composite image, Hα and [SII]/Hα line ratio of M83 constructed from the TYPHOON datacube. The bright hot spots that appear along the spiral arms of the Hα image indicate the HII regions where metallicity diagnostics are valid. We also see significant Hα detection in the inter-arm regions corresponding to emission from the DIG. At the native resolution 41pc, we push down to a detection limit of 5.4×10^{-17} erg/s/cm^2/arcsec^2 with a mean noise level of 4.2×10^{-17} erg/s/cm^2/arcsec^2. As we degrade the spatial resolution, we are able to push towards lower detection limits but the boundary between the HII regions and DIG becomes blurred and can no longer be separated.

Observations of the DIG indicate that it is hotter and lower ionization than nearby HII regions, with increased [SII]/Hα and [NII]/Hα ratios. The [SII]/Hα ratio is most often used as a DIG indicator as it provides a clean separation between HII regions and DIG regions (e.g. Blanc et al. 2009). The [SII]/Hα map in Figure 5.1 clearly shows a significant increase in [SII]/Hα in the inter-arm regions.

5.2.2. Previous Research

Due to its proximity, M83 has been a popular subject of many studies over the years. Using strong emission line diagnostics by Kobulnicky et al. (1999), a shallow radial metallicity gradient was reported by Bresolin & Kennicutt (2002) by combining their own HII region observations and those obtained by Dufour et al. (1980) and Webster & Smith (1983). A break in the metallicity gradient is observed in the extended disk of M83 beyond the R_{25} isophotal radius, where the metallicity gradient becomes flat (Bresolin et al. 2009). Using the "counterpart" method, Pilyugin et al. (2012) was unable to find solid evidence for a discontinuity between the inner at outer disk of M83. They did however acknowledge that the metallicity gradient did become flatter at the transition point.

With significant deviations in the metallicities measured from different strong emission line diagnostics (Kewley & Ellison 2008), Bresolin et al. (2016) provides stellar metallicity measurements of blue supergiants within the inner disk of M83. They find that the stellar metallicity measurements are in good agreement with the T_e-based metallicities. With the exception of the ([OIII]/Hβ)/([NII]/Hα) metallicity diagnostic (Pettini & Pagel 2004), the strong emission line diagnostics produce significantly different radial profiles to those calculated by the T_e method.

The presence of extra-planar diffuse ionized gas (eDIG) in M83 was detected by Boettcher et al. (2017) using Markov Chain Monte Carlo methods to decompose the HII regions from

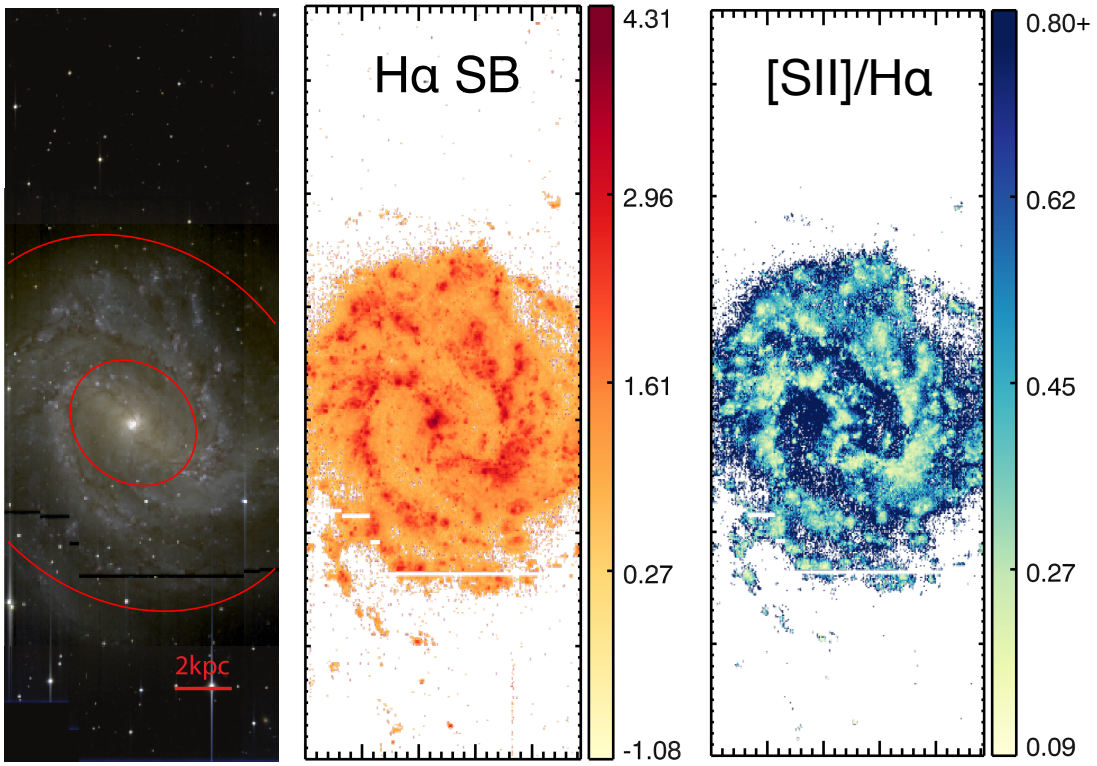

Figure 5.1 *Left*: BVR composite image of M83 created from the TYPHOON datacube. The two red ellipses correspond to 0.5 and 1.5 R_e of the galactic disk. *Middle*: Hα surface brightness map of M83 extracted by LZIFU in units of log(10^{-17} erg/s/cm^2/arcsec^2). *Right*: The [SII]/Hα emission line ratio map of M83. Diffuse ionized gas is known to have increased emission line ratios such as [SII]/Hα and [NII]/Hα . As a result, [SII]/Hα is often used as a tracer for diffuse ionized gas.

the eDIG using high spectral resolution observations from the South African Large Telescope (SALT). Due to the relatively low (R~ 850) spectral resolution of TYPHOON, we are unable to spectrally decompose the emission line fluxes into multiple components and separate the eDIG from the planar DIG. Although we are unable to separate the eDIG from the DIG that exists in the midplane, Boettcher et al. (2017) found that for M83, the DIG within the plane of the disk was several orders of magnitudes brighter than the extraplanar component. This means that any HII regions that we define in the plane of the disk will be relatively unaffected by the presence of eDIG.

5.3. Method

5.3.1. Data Binning

Figure 5.2 shows the Hα image at each binned resolution scale. An important feature of Figure 5.2 is the gradual blurring of the HII regions. At the native resolution of 41 pc, the HII regions are clearly distinguishable from the DIG regions as high surface brightness (red) spots mostly distributed along the spiral arms. At the 150 pc resolution, most of the individual HII regions are still distinguishable, but some of the more densely packed HII regions begin to merge. The resolutions of 330pc and 502 pc are typical of the highest resolution IFU galaxy surveys (eg. CALIFA). At these resolutions, HII regions become

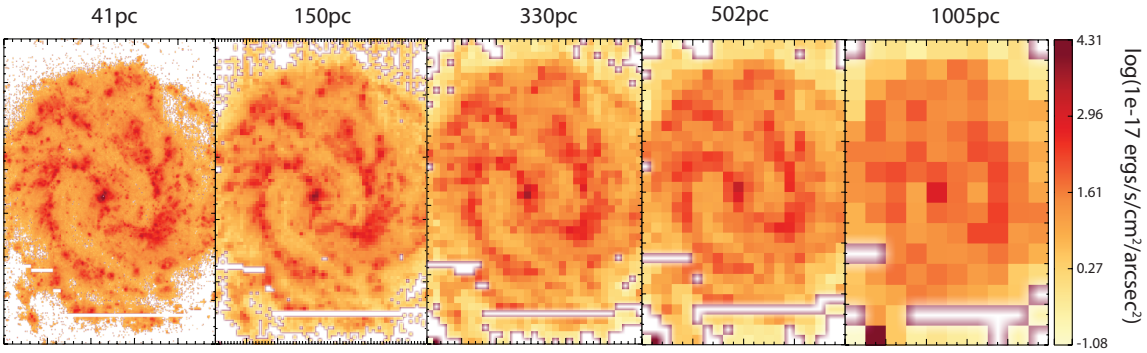

Figure 5.2 Hα map of M83 at different resolution scales. The spatial resolutions from left to right: 41 pc, 150 pc, 330 pc, 502 pc and 1005 pc. The gradual blurring of defined HII regions and the merging of the spiral arms with the inter-arm regions can be clearly seen in this figure.

completely merged with each other and the spiral arm structure becomes the new HII region boundary. At 502 pc we also see the boundary between DIG and HII regions begin to blur, suggesting increasing DIG contamination. We would expect SAMI and MaNGA on average to achieve resolutions on the scale of our final panel at 1005 pc. Large morphological features such as the strong spiral arms are no longer distinguishable at this level and clearly distinguishing between DIG and HII regions is difficult. When working with data at this resolution, DIG contamination is almost certain and thus needs to be taken into consideration.

Our goal is to find a simple mechanism to remove or minimise the effects of DIG from the determination of metallicity and other emission line derived physical parameters. To do this we must first define the boundary between DIG and HII regions. Previous studies have attempted to define DIG by using Hα surface brightness (Zhang et al. 2017), emission line ratios such as [NII]λ6583/Hα and [SII]$\lambda\lambda$6717, 6731/Hα (Blanc et al. 2009) and advanced HII region finding algorithms such as HIIPHOT (Thilker et al. 2000) and HIIEXPLORER (Sánchez et al. 2012). We apply each of these methods to demonstrate the systematics involved in HII and DIG separation on emission line derived physical parameters. We list the number of HII and DIG region spaxels for each DIG classification scheme within 1.5 R_e in Table 5.2. Before any of the emission lines are used for defining HII regions, we subtract the stellar continuum and fit the strong emission lines using LZIFU. We describe the LZIFU routine in more detail in Section 5.3.1. In the following sections we describe our application of each HII region classification method.

Separation by Hα Surface Brightness

Individual HII region sizes are typically on the order of tens to hundreds of parsecs (Azimlu et al. 2011; Gutiérrez et al. 2011; Whitmore et al. 2011) while the typical resolution of multiplexing IFU surveys tend to have a spatial resolution coarser than $\sim$ 1 kpc. This means that a clean separation between HII regions and DIG emission is difficult. While HII regions are typically orders of magnitude brighter than DIG regions, the DIG covers a larger fraction of the galactic disk. However the difference in surface brightness means that a crude separation between HII dominated spaxels and DIG dominated spaxels is possible

by looking at the surface brightness alone.

Zhang et al. (2017) used galaxies observed by the MaNGA survey to analyse the effects that the DIG has on emission line ratios in MaNGA observations and its derived properties. With a spatial resolution greater than ~ 1 kpc, they are unable to cleanly separate the HII regions from the DIG. Instead they analyse how the emission line ratios and their products change with Hα surface brightness.

For this paper, we use the method outlined in Kaplan et al. (2016) to determine the fraction of flux originating from the HII regions and the DIG. This method was first developed by Blanc et al. (2009) and expanded by adding a parameter to allow variation in the DIG surface brightness due to the star-formation distribution. Using the assumption that the brightest spaxels are dominated by HII emission and the dimmest spaxels are dominated by DIG emission, Kaplan et al. (2016) determines a characteristic [SII]/Hα emission line ratio for HII and DIG regions. The linear distance between the HII characteristic [SII]/Hα and DIG [SII]/Hα ratio determines the percentage of flux originating from each region. For example, if the HII characteristic [SII]/Hα = 0.2 and the DIG characteristic [SII]/Hα = 0.9, a spaxel with [SII]/Hα = 0.55 would have equal contribution of emission line flux from HII regions and the DIG.

The fraction (C_{HII}) of emission originating from the HII regions is then mapped to the extinction corrected Hα surface brightness (extinction correction method described in Section 5.3.2) and fit using a function of the form:

$$C_{HII} = 1.0 - \left(\frac{f_0}{f(H\alpha)}\right)^{\beta} \tag{5.1}$$

where f_0 is the threshold below which a spaxel is completely comprised of DIG and β allows for the variation in DIG surface brightness. We fit both parameters using MPFIT(Markwardt 2009) and provide all values in Appendix 5.9. We define a HII region to be a spaxel in which 90% of its emission originates from HII regions. This corresponds to a Hα surface brightness cut-off of 1.86×10^{-15} erg s^{-1} cm^{-2} arcsec^{-2} at the native resolution of 41 pc.

[SII]/Hα Emission Line Ratio

Madsen et al. (2006) found a significant increase in the [SII]/Hα and [NII]/Hα line ratio in the DIG components of the Milky Way. The HII regions had an average value of [SII]/Hα = 0.12 and [NII]/Hα = 0.23, while the DIG regions had an average value of [SII]/Hα = 0.38 and [NII]/Hα = 0.83. However the [NII]/Hα line ratio has a larger scatter than the [SII]/Hα line ratio, making it less reliable for separating the HII and DIG dominated regions.

Using the characteristic [SII]/Hα emission line ratio for HII and DIG regions determined previously, we linearly map each spaxel to determine the fraction of emission produced by HII regions and the DIG. As with the Hα surface brightness cut-off, we define a HII region to be a spaxel in which 90% of its emission originates from HII regions. A [SII]/Hα cut-off of 0.29 is determined at the native resolution of 41 pc. That is, a spaxel with [SII]/Hα < 0.29 is classified as a HII region. Since Equation 5.1 essentially maps the [SII]/Hα line ratio to Hα, classifying a spaxel as a HII region or DIG based on the Hα surface brightness or [SII]/Hα should be exactly the same. However, the differences between the two classification schemes exist because of the scatter around the line of best fit as shown in Figure 5.18.

Number of HII and DIG spaxels		
Classification Scheme	HII	DIG
[SII]/Hα	8823 (12%)	63288 (88%)
HIIPHOT	4215 (6%)	67896 (94%)
Hα SB	11280 (15%)	60831 (85%)

Table 5.2 The number of spaxels considered as HII regions or DIG regions within 1.5 R_e based on the different HII classification schemes.

HII Region Finding Algorithms

HII region finding algorithms provide a way to systematically define the boundaries of HII regions, removing the individual biases that may be present when defining by eye. HIIEXPLORER is one such algorithm, used widely in many CALIFA studies (Sánchez et al. 2012, 2014; Sánchez-Menguiano et al. 2016b). Thilker et al. (2000) presents HIIPHOT, a robust and systematic method of determining HII regions from the Hα emission line. HIIPHOT first finds 'seed' HII regions and then iteratively grows the seeds until the termination condition is reached. HIIPHOT uses the slope of the Hα surface brightness to determine whether it has reached the edge of a HII region. The seed threshold and termination conditions of HIIPHOT are user defined, meaning that some subjectivity is inevitably present. We adjust the settings of HIIPHOT to produce HII region maps which match our expectations and produce similar regions to the Hα surface brightness and [SII]/Hα cut-off. The difference between HIIPHOT and the other classification schemes lies within the ability of HIIPHOT to produce smoother boundaries rather than the sharp cut-offs present in the other two classifications.

HII Region and DIG Separated Cubes

Figure 5.3 shows the HII region maps for each classification scheme. The [SII]/Hα classification scheme produces HII regions which appear noisy due to its sharp cut-off. The spiral arm structure is easily extracted using the [SII]/Hα emission line ratio and identifies spaxels with low Hα surface brightness. The HIIPHOT classification schemes produces much smoother HII regions compared to [SII]/Hα, with HII regions appearing rounder with defined borders. A significant difference between regions defined by [SII]/Hα and HIIPHOT occurs in the central section of M83. The [SII]/Hα classification scheme has a smaller central HII region than HIIPHOT, signalling the presence of a high surface brightness region with an enhanced [SII]/Hα emission line ratio. Finally, the Hα surface brightness cut-off defines the most HII region spaxels and bridges all the HIIPHOT HII regions together due to its inability to distinguish the presence of high surface brightness DIG regions.

For each HII region classification scheme, we create two additional datacubes: one that contains only emission from HII regions and one that contains only emission from the rest of the original data cube, which we classify to be DIG. We then rebin the original and each of these new data cubes to lower resolution scales.

The rebinned HII region data cubes are used to simulate how pure spatial smoothing affects observations in the absence of DIG. However the rebinned cubes containing emission outside of the HII regions not only contains the DIG emission, but also includes low surface

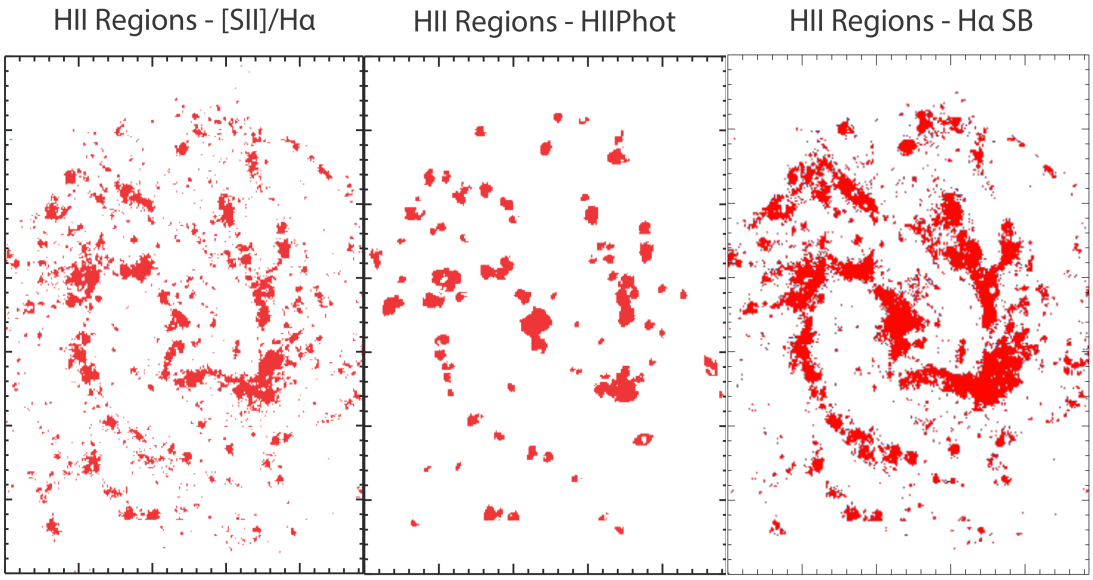

Figure 5.3 Maps of the three DIG classification schemes used in this paper. *Left*: HII region classification using the [SII]/Hα emission line ratio. [SII]/Hα < 0.29 is defined as HII regions and [SII]/Hα > 0.29 is defined as DIG. *Middle*: HII regions defined using a modified version of HIIPHOT (Thilker et al. 2000). HIIPHOT determines HII regions based on local Hα surface brightness profiles. *Right*: HII regions determined by a Hα surface brightness cut-off. Σ(Hα)> 1.86×10^{-15} erg s^{-1} cm^{-2} arcsec^{-2} is defined as HII regions with anything less being classified as DIG.

brightness (LSB) regions that fall below the S/N cut at the native resolution. As we rebin to lower resolutions, the LSB regions either merge together with other LSB regions until they have a significant enough S/N or contribute to DIG emission.

Each rebinned data cube is processed by LZIFU (Ho et al. 2016). LZIFU extracts total line fluxes for the dominant emission lines by fitting and subtracting the underlying stellar continuum using PPXF (Cappellari & Emsellem 2004; Cappellari 2017) and the MIUSCAT simple stellar population models (Vazdekis et al. 2012). The dominant emission lines are then fit using up to 3 Gaussian profiles with the Levenberg-Marquardt least-squares method (Markwardt 2009). For this paper, we use the 1-component fits from LZIFU for our analysis as including extra Gaussian components does not significantly improve the emission line fits due to relatively low spectral resolution. LZIFU returns maps of the flux and flux errors for each emission line, as well as maps of the ionized gas velocity and velocity dispersion and their associated errors (see Ho et al. (2016) for a detailed explanation of the routine).

5.3.2. Metallicity Diagnostics

Extinction Correction

Before being used in diagnostic ratios, emission lines must be first corrected for attenuation by dust in the interstellar medium (ISM). The attenuation of emission lines is wavelength dependent, meaning that emission line diagnostics that use emission lines with wide

wavelength differences are most heavily affected such as N2O2, R_{23} and O32. To correct the emission lines, we apply a S/N cut of 3 and create maps of the observed Balmer ratio, $(H\alpha/H\beta)_{obs}$, and solve for E(B-V) by using the relation:

$$E(B-V) = \log_{10}(\frac{(H\alpha/H\beta)_{obs}}{(H\alpha/H\beta)_{int}})/(0.4(k(H\beta) - (k(H\alpha)))) \quad (5.2)$$

where $(H\alpha/H\beta)_{int}$ is the intrinsic ratio of 2.86 for case B recombination (Osterbrock 1989). We use the Cardelli et al. (1989) extinction curve and assume a typical R(V) value of 3.1 to determine k values for Hα and Hβ. We then use the calculated E(B-V) to determine A(λ), the absolute extinction as a function of wavelength, at our emission line wavelengths to de-redden the emission line fluxes. We apply the extinction correction to the N2O2, $R_{23}$and O32 emission line ratios.

We find an average E(B-V) of 0.61 for HII regions and 0.80 for DIG regions, corresponding to an A_v of 1.89 and 2.48 respectively assuming R(V)=3.1. This agrees with Tomičić et al. (2017), who found an increase in the [SII]/Hα with A_v for resolved spectra in M31. However, a large scatter exists between [SII]/Hα and A_v, leading to the trend being relatively weak. The trend is largely driven by the physical characteristics of the ISM such as gas-phase metallicity and ionization parameter which may vary across a galaxy (e.g. Tomičić et al. 2017).

N2O2

A popular metallicity diagnostic uses the ratio between nitrogen and oxygen emission lines, [NII]λ6583/[OII]λ3726, λ3729 (N2O2 Kewley & Dopita 2002, hereafter KD02). The main advantage to the N2O2 diagnostic is that because of the similar ionizing potentials of the nitrogen and oxygen species, the diagnostic has very little dependence on the ionization parameter, especially at high metallicity values. Another benefit of the N2O2 diagnostic is that it appears to be one of the metallicity diagnostics least affected by DIG contamination (Zhang et al. 2017), making it ideal for low resolution data where HII regions can not be separated reliably from the DIG.

R_{23}

The ([OII]$\lambda\lambda$3726, 3729 + [OIII]$\lambda\lambda$4959, 5007)/Hβ (R_{23}) emission line ratio is one of the most widely used metallicity diagnostics due to its direct use of the oxygen emission lines with a large amount of calibrations using this particular emission line ratio (Pagel et al. 1979, 1980; Edmunds & Pagel 1984; McCall et al. 1985; Dopita & Evans 1986; Torres-Peimbert et al. 1989; McGaugh 1991; Zaritsky et al. 1994; Pilyugin 2000; Charlot & Longhetti 2001; Kewley & Dopita 2002; Kobulnicky & Kewley 2004). A more complex method of determining the metallicity is by using an iterative method presented in Kobulnicky & Kewley (2004, hereafter KK04). The KK04 metallicity diagnostic uses the R_{23}line ratio together with the [OIII]$\lambda\lambda$4959, 5007/[OII]$\lambda\lambda$3726, 3729 O32 emission line ratio to simultaneously determine the metallicity and ionization parameter. The R_{23}metallicity diagnostic has a strong dependence on the ionization parameter, making it an ideal diagnostic when determining the metallicity distribution of a galaxy with large ionization parameter variations.

O3N2

([OIII]λ5007/Hβ)/([NII]λ6583/Hα) (O3N2 Pettini & Pagel 2004, hereafter PP04) is another very popular metallicity diagnostic. O3N2 uses the emission lines that are commonly used on the BPT diagram to determine the metallicity. The emission lines involved in the O3N2 metallicity diagnostic are close enough in wavelength that differential extinction (ie. reddening) is minimal. Metallicity varies linearly with the O3N2 emission line ratio, allowing for easy and fast calculations. The only drawback of the O3N2 metallicity diagnostic is that it appears to depend heavily on ionization parameter (Kewley et al. 2019), which is not taken into account by PP04. This could lead to potential systematic errors in the metallicity calculations if there is a large variation in ionization parameter throughout the galaxy.

N2Hα

[NII]λ6583/Hα (N2Hα Storchi-Bergmann et al. 1994; Raimann et al. 2000; Denicoló et al. 2002; Pettini & Pagel 2004) is another common metallicity diagnostic. Like O3N2, N2Hα utilizes emission lines that are close in wavelength to minimise extinction correction, allowing for metallicity measurements where the Balmer ratio can not be reliably determined. Because of the simplicity of only needing two relatively strong emission lines, N2Hα is the most popular high redshift metallicity diagnostic. We use the N2Hα calibration by PP04 for this paper. However, the N2Hα metallicity diagnostic also appears to have a strong dependence on ionization parameter (Kewley et al. 2019), resulting in possible systematic errors when using the metallicity diagnostic in its current form.

N2S2

The newest metallicity emission line diagnostic that will be used in our analysis involves the Hα, [NII]λ6583 and [SII]$\lambda\lambda$6717, 6731 emission lines (N2S2 Dopita et al. 2016). The N2S2 diagnostic uses a combination of the [NII]/Hα and [NII]/[SII] emission line ratios in the following sum log([NII]/[SII])+0.264 $\times$ log([NII]/Hα). N2S2 provides the best of both worlds as the wavelength gap between Hα, [NII] and [SII] is small enough to ignore for the purposes of extinction correction and is insensitive to changes in the ionization parameter due to the inclusion of the [NII]/[SII] emission line ratio.

5.3.3. Error Propagation

To propagate line flux errors produced by LZIFU through to the metallicity calculations, we simulate 1000 maps for all emission lines used in the calculation. The maps are created such that the fluxes are Gaussian distributed within the LZIFU standard deviation for that emission line.

Using the simulated line maps, metallicity maps are created for each metallicity diagnostic. The non-linearity of some of the metallicity diagnostics means that the metallicity distributions are not necessarily Gaussian. To represent the spread of metallicity, we determine the distance from the true value to the 16^{th} and 84^{th} percentiles and calculate the average. This

provides us with a measure of the error of the metallicity maps which are then propagated to the gradient errors.

5.4. Results

Using the [SII]/Hα HII classification scheme, we analyze the basic properties of the DIG regions. Figure 5.4 shows the Hα surface brightness radial profiles of HII regions and DIG regions for spaxels where S/N(Hα)> 3 and S/N(Hβ)> 3 at the native resolution. We note that the surface brightness profile shapes of the two regions are extremely similar, with

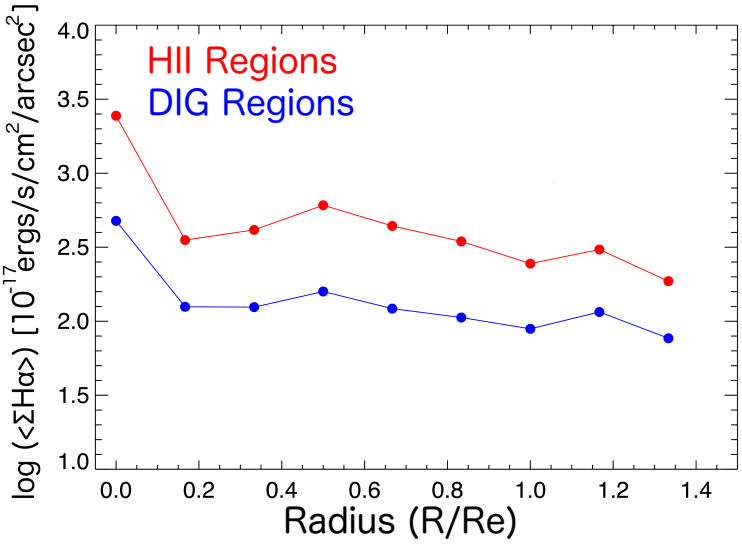

Figure 5.4 Radial Hα surface brightness profiles for HII regions and DIG regions using the [SII]/Hα HII classification scheme. The shape of the radial profiles look almost identical with the HII regions being significantly brighter than the DIG regions.

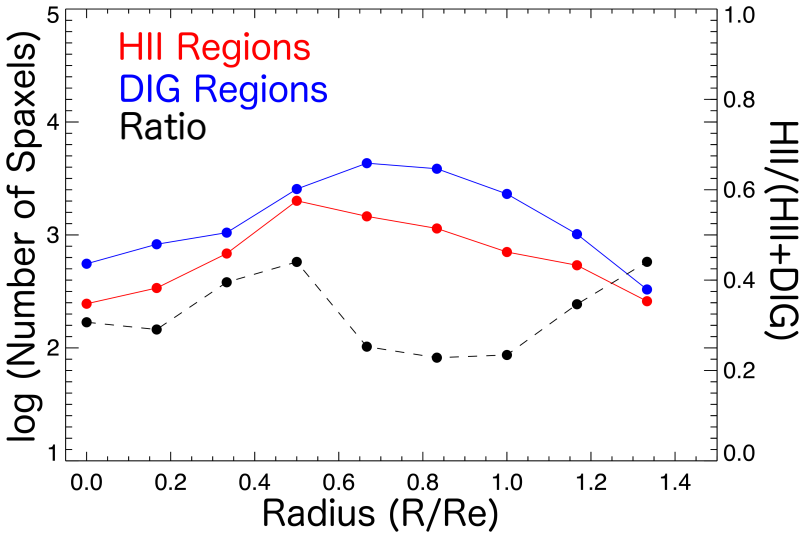

Figure 5.5 The number of spaxels classified as HII and DIG using the [SII]/Hα HII classification scheme. There are vastly more DIG spaxels than HII spaxels at all radii. The number of HII region spaxels peaks at R/R$_e$ = 0.6, corresponding to the location of the spiral arms. The number of DIG spaxels steadily increases at larger radii due to the increase in area but flattens as detection of faint regions becomes difficult.

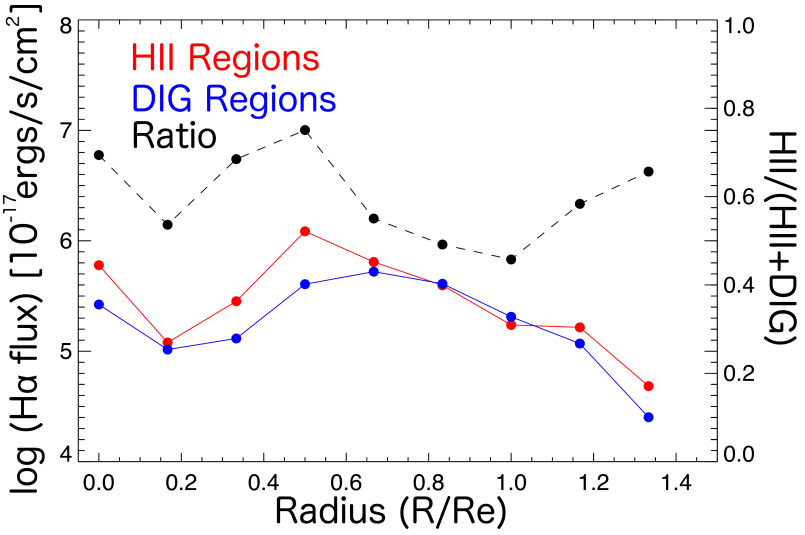

Figure 5.6 The Hα luminosity radial profile of M83. The luminosity profiles of HII and DIG regions are almost identical meaning that the total Hα luminosity is almost evenly contributed by HII regions and DIG regions. Even though HII regions are significantly brighter (Figure 5.4), there are far more DIG regions (Figure 5.5) to contribute to the luminosity.

the HII regions being consistently brighter than the DIG regions by about 0.6 dex. As expected, the peak of the Hα surface brightness occurs at the centre. However, an increase in surface brightness of about 0.2 dex from the previous radial bin happens at $R/R_e = 0.6$ corresponding to the location of the spiral arms.

Figure 5.5 shows that there are more DIG spaxels than HII region spaxels at each radial bin, with the HII regions peaking at 45% of the total spaxels at the location of the spiral arms. For the [SII]/Hα classification scheme, just 12% of spaxels are classified as HII regions (Table 5.3). The number of spaxels for both HII and DIG regions steadily increase until we reach the spiral arms ($R/R_e = 0.6$). Beyond this radii, the number of detected spaxels begins to drop due to surface brightness limits.

The combination of Figure 5.4 and Figure 5.5 gives the Hα luminosity profile. Figure 5.6 presents the Hα luminosity profile for HII and DIG regions. The shape of these two profiles are very similar with only slight variations. Up to the spiral arms ($R/R_e = 0.6$), the total Hα luminosity is slightly dominated by the HII regions. Beyond the spiral arms, the DIG regions contribute approximately half of the overall Hα luminosity in radial annuli.

For each resolution scale, we create spatially resolved metallicity maps and their associated error maps using the metallicity diagnostics described in Section 5.3. Some of these metallicity diagnostics rely on the detection of emission lines that are relatively weaker than others. For example, $R_{23}$and N2O2 rely on the accurate detection of the [OII] emission doublet which drastically reduces the amount of usable spaxels in their metallicity maps. Only 2674 (3%) spaxels out of the total 72111 spaxels within 1.5 R_e have [OII] emission with a $S/N > 3$. Metallicity diagnostics which use stronger emissions lines and do not require extinction correction such as N2S2 and N2HA have metallicity maps which cover a larger fraction of the galaxy, even in the areas dominated by DIG where the [OII] emission flux typically has $S/N < 3$. The [NII], [SII] and Hα emission lines all have over 57000 (79%) spaxels within $1.5R_e$ with a $S/N > 3$.

When determining the radial metallicity gradients at each resolution, we first correct for the observed ellipticity of the galaxy using the ellipticity and PA listed in Table 5.1. We then use the robust line fitting program LTS_LINEFIT (Cappellari et al. 2013) to fit a linear trend to the metallicity gradient at each resolution, propagating the uncertainty in metallicity through. The gradients are then normalised by the effective radius (R_e) of the galaxy to remove the size dependence of metallicity gradients (Sánchez et al. 2014; Ho et al. 2015; Sánchez-Menguiano et al. 2016b). Sánchez-Menguiano et al. (2018) found wide-spread deviations from single linear metallicity gradients and instead uses multiple linear gradients to more accurately fit the radial metallicity distribution. For this study we adopt a single linear fit to our metallicity gradients.

Figure 5.7 shows the measured metallicity gradients of M83 for the five chosen metallicity diagnostics at the five different spatial resolutions using the [SII]/Hα DIG classification scheme. We show the same plots for the HIIphot and Hα surface brightness (SB) HII classification schemes in the supplementary material. In each panel we show the metallicity as a function of radius and fit the metallicity gradient using only HII regions (red), DIG regions (blue) and the full set (black) of spaxels. The median error of each panel is shown as black bars in the bottom left corner. Throughout this work we consider the radial metallicity gradient of the HII regions at the 41 pc to be the true metallicity gradient of M83. It is also important to note that the measured metallicity gradients of the DIG regions is non-physical and does not represent the true metallicity of the DIG. To measure the metallicity of the DIG, you need to apply a metallicity diagnostic which was specifically calibrated for DIG ionisation mechanisms (e.g. Kumari et al. 2019). We simply apply the HII region calibrated diagnostics to the DIG regions to show how the emission line ratios of the DIG are handled by current emission line diagnostics.

We summarise Figure 5.7 in Figure 5.8 by plotting the metallicity gradient as a function of spatial resolution. The dashed red line represents the observed metallicity gradient when applying DIG corrections at the given resolution after contamination has already occurred. For example, the dashed red line in the [SII]/Hα classification column at 502 pc represents the observed metallicity gradient when using combined emission spaxels at 502 pc and applying HII and DIG separation methods outlined in Section 3.1.1 and Section 3.1.2. At the native resolution of 41pc, the dashed red line is exactly the same as the red solid line. The original method outlined by Kaplan et al. (2016) requires a minimum of 200 spaxels in order to determine the characteristic HII and DIG [SII]/Hα emission line ratio. When applying this method to the lower resolution scales with an insufficient spaxel count, we instead use brightest and dimmest 5% of spaxels. We do not attempt to use HIIphot at coarse resolution scales as it is optimised for high spatial resolution data and will likely fail at kiloparsec resolutions.

The red line representing the change in HII region metallicity gradient with resolution demonstrates the effects of pure spatial smoothing. The black line demonstrates the effects of both spatial smoothing and DIG contamination. Figure 5.8 shows that for the R_{23}, N2O2 and O3N2 metallicity diagnostics, M83 possesses a negative metallicity gradient. However, for the N2Hα and N2S2 metallicity diagnostics, M83 has a positive metallicity gradient. This highlights the significant differences in metallicity gradient calculations between different metallicity diagnostics.

In general we see very similar trends from all the classification schemes across all metallicity diagnostics. The only outstanding difference occurs when applying a Hα surface brightness cut to the N2Hα metallicity diagnostic at 1005 pc.

5.4.1. The Impact of Different Metallicity Diagnostics

Figure 5.8 show 3 different types of patterns. The metallicity gradient from both the DIG regions and full set of spaxels of the $R_{23}$and N2O2 metallicity diagnostics tend to diverge away from the metallicity gradient of the HII regions, becoming shallower with coarser resolution. We expect spatial smoothing to flatten steeper gradients at a quicker rate. However, since the metallicity gradients of the combined spaxels and DIG regions appear to be flattening quicker than the steeper HII region metallicity gradients, another effect aside from DIG contamination must be present.

For the O3N2 metallicity diagnostic, the metallicity gradient of the full set of spaxels converge to the metallicity gradient of the HII regions as we move to coarser resolution scales, with agreement between the two at the 1005 pc scale. The metallicity gradient of the DIG regions tends to remain a relatively fixed offset (~0.075 dex/R_e) from that of the HII regions.

The N2Hα and N2S2 metallicity diagnostics appear to be the most impacted by DIG contamination. Except for the N2Hα metallicity diagnostic with the Hα DIG classification scheme, the metallicity gradient of the full sample appears to be tied to the DIG metallicity gradient. The N2S2 metallicity gradients produce significantly steeper metallicity gradients in the DIG regions compared to HII regions as opposed to shallower metallicity gradients in the other 3 metallicity diagnostics. The N2Hα metallicity DIG gradients appear to be flat at all resolution scales.

Although the systematic differences between the various metallicity diagnostics will not be discussed in detail in this paper, it is important to note that between different metallicity diagnostics, the metallicity gradient of HII regions do not agree with each other. Part of the differences seen between the HII metallicity gradients seen in Figure 5.8 is caused by the different set of spaxels available to each diagnostic. Figure 5.9 shows the metallicity gradients of HII regions where the same set of spaxels are used for all metallicity diagnostics. Figure 5.9 clearly demonstrates the lingering issues that exist between the different metallicity diagnostics. Using the Sloan Digital Sky Survey (SDSS), Kewley & Ellison (2008) provides empirical conversions for a suite of metallicity diagnostics and calibrations for aperture metallicities. Until a similar study has been done for metallicity gradients, metallicity gradients determined from different metallicity diagnostics should not be compared to one another.

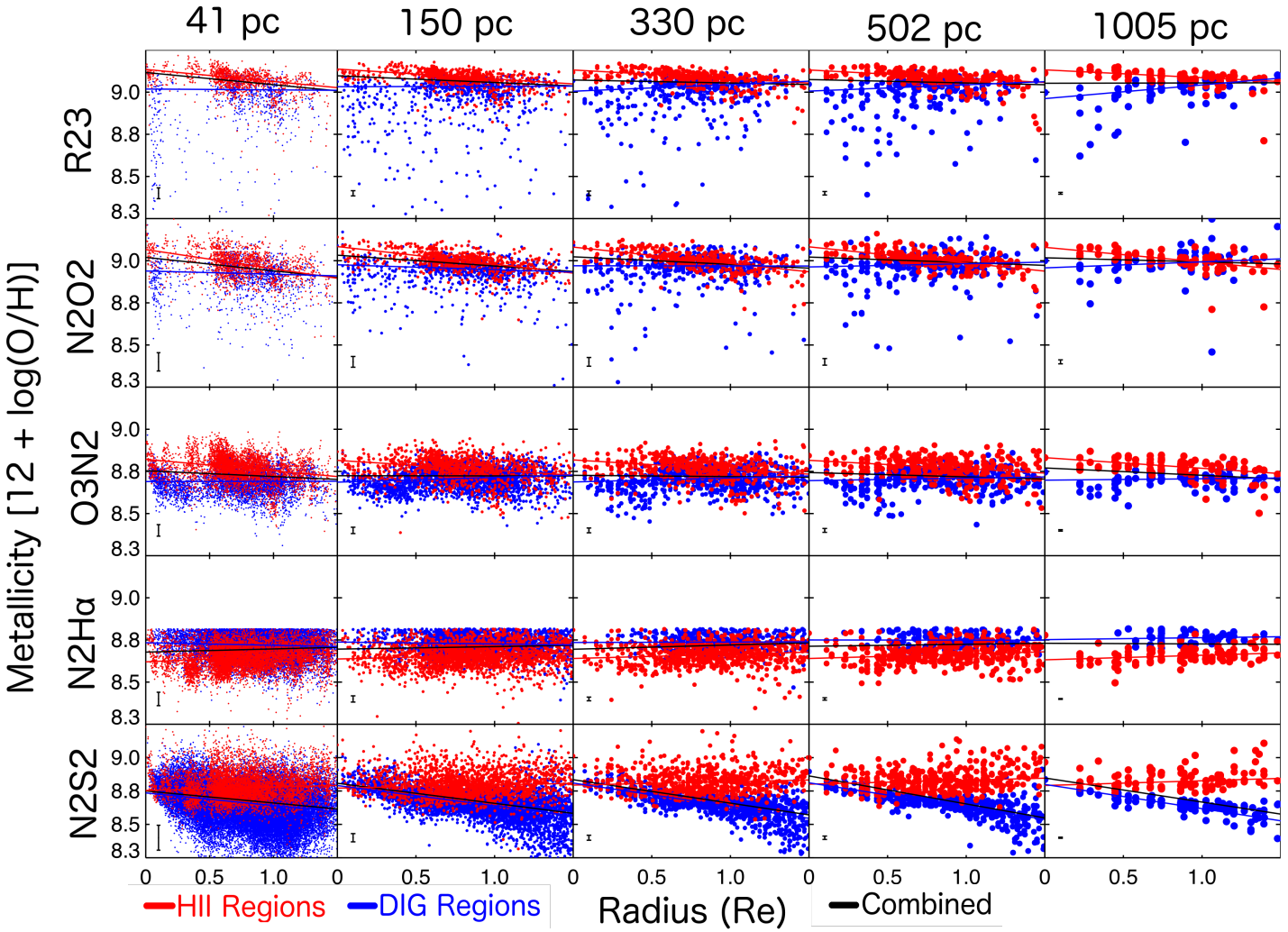

Figure 5.7 Metallicity gradient linear fits for each metallicity diagnostic at each resolution scale. Red points represent HII regions and blue points represent the DIG regions. The black line shows the combined, non-separated metallicity gradients. We provide the median error of each panel in the bottom left corner. HII and DIG regions are separated using the [SII]/Hα classification scheme.

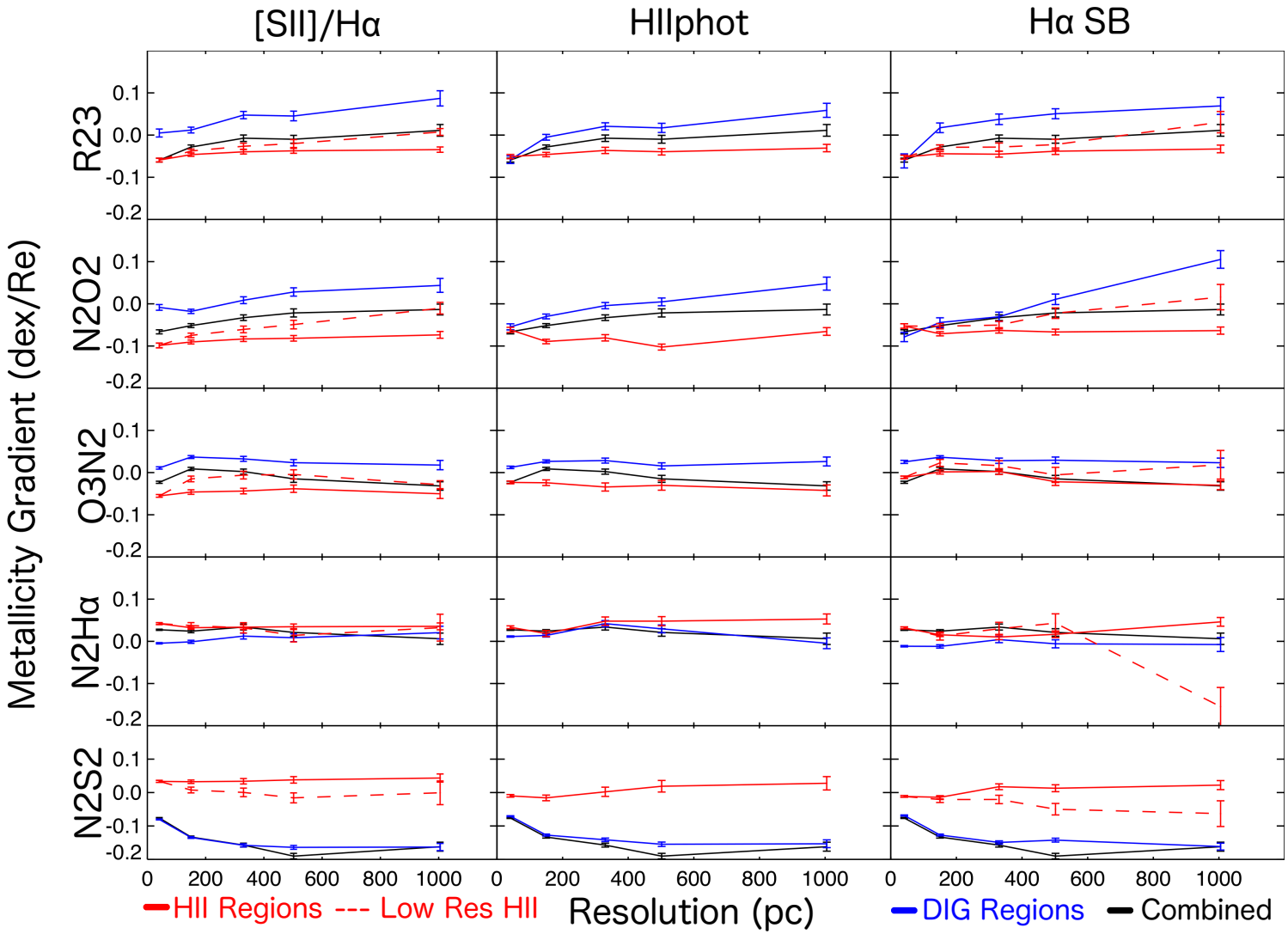

Figure 5.8 We summarise the results of Figure 5.7 by plotting the metallicity gradients of each DIG classification scheme as a function of resolution scale. The red dashed line represents the metallicity gradient when the DIG classification scheme is applied after DIG contamination has occurred. Further detail is given in Section 5.4. We provide all values for metallicity gradient fits in Appendix 5.7.

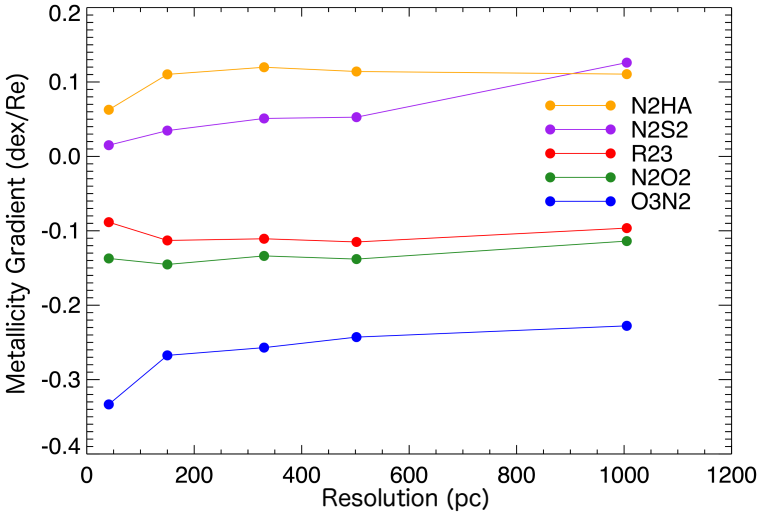

Figure 5.9 Metallicity gradients of HII regions where each diagnostic is restricted to using the same set of spaxels at each resolution scale. This highlights the significant systematic differences between the different metallicity diagnostics even when the same HII region spaxels are used.

5.5. Discussion

5.5.1. Low Surface Brightness Regions

Spatial smoothing and diffuse ionized gas (DIG) contamination are not the only factors which affect the metallicity gradient when using coarser resolutions. Metallicity diagnostics that use weak or low S/N emission lines have fewer spaxels with which to determine the metallicity gradients. As the data is smoothed, the S/N increases, meaning spaxels containing lower surface brightness emission are now included in the gradient determination.

In our data, metallicity diagnostics that use [OII] such as $R_{23}$and N2O2 are more impacted by low surface brightness (LSB) regions than other diagnostics. Furthermore, as each diagnostic uses different sets of emission lines, they will also have different sets of LSB spaxels and will be affected differently by their inclusion. Different HII region classification schemes also contribute to differences in the set of spaxels used. Figure 5.8 demonstrates that the general trends are preserved regardless of which classification is used, so we therefore select the [SII]/Hα classification scheme as our fiducial model for the following discussion.

In this paper, we do not separate the effects of spatial smoothing and the inclusion of LSB HII region spaxels. We briefly discuss the effects of LSB regions in Section 5.5.2.

5.5.2. Spatial Smoothing

Several factors are believed to be contributing to metallicity gradient flattening, including the effect of spatial smoothing. Spatial smoothing is the effect of averaging regions of high and low metallicity together when using larger spaxel sizes. The effect of spatial smoothing is most prominent with steep gradients and obviously does not affect galaxies that possess flat gradients (e.g. NGC 5474 Mast et al. 2014).

	HII spaxels		
Diagnostic	[SII]/Hα	HIIPhot	Hα SB
R_{23}	0.14	0.25	0.15
N2O2	0.17	0.28	0.18
O3N2	0.48	0.74	0.56
N2Hα	0.86	0.93	0.90
N2S2	0.86	1.00	1.00

Table 5.3 Fraction of HII region spaxels with metallicity estimates at 41 pc. As the metallicity diagnostics require less emission lines or use stronger detected emission lines, the fraction increases. These fractions are relative to the numbers presented in Table 5.2.

The change in metallicity gradient with resolution in the pure HII region data demonstrates this effect of spatial smoothing. Overall in Figure 5.8 we can see that HII region metallicity gradients generally remain constant, with all the HII metallicity gradients remaining within ±0.01 dex for the [SII]/Hα classification scheme and within ±0.02 dex for HIIPHOT and the Hα classification scheme.

As mentioned in Section 5.5.1, LSB HII regions (where e.g. [OII] is not of sufficient S/N), are also impacting the change in the HII region metallicity gradient with resolution. Table 5.3 and 5.4 reveal that the $R_{23}$and N2O2 metallicity diagnostics are only possible in a very small fraction of spaxels. This is mostly driven by the lower S/N of [OII], which is due to the higher noise in the blue part of the TYPHOON spectra. We therefore expect $R_{23}$and N2O2 to be the most heavily affected by the effects of the inclusion of LSB regions as we decrease the resolution. The $R_{23}$and N2O2 HII region metallicity gradients are flattened relatively more compared to those calculated using the N2Hα and N2S2 metallicity diagnostics. However, this is also consistent with the fact that $R_{23}$and N2O2 have steeper gradients to begin with and are therefore naturally more affected by pure spatial smoothing.

For the following sections, we emphasise once again that these metallicity diagnostics can not be applied to emission originating from the DIG. However, we apply them to the DIG regions in order to assist the reader in understanding the effects of DIG contamination and refer to them as "DIG metallicity gradients" for simplicity. The DIG metallicity gradients are clearly affected by more than just spatial smoothing. The DIG metallicity gradients from the N2S2 metallicity diagnostic become steeper (-0.095 dex/R_e at 41 pc to -0.181 dex/R_e at 1005 pc with the [SII]/Hα classification scheme) as we decrease the resolution. Whereas the DIG metallicity gradients from the $R_{23}$and N2O2 metallicity diagnostics start off with a negative gradient (-0.005 and -0.019 dex/R_e respectively with the [SII]/Hα classification scheme) and are positive at the 1005 pc resolution (0.081 and 0.036 dex/R_e respectively with the [SII]/Hα classification scheme). The O3N2 and N2Hα DIG metallicity gradients appear to remain fairly constant and relatively unaffected (within ±0.02 dex/R_e) by the decreasing resolution. The steepening of the negative DIG metallicity gradient of N2S2 and transition from negative to positive metallicity gradient of the R23 and N2O2 diagnostics can not be explained by spatial smoothing alone.

Table 5.4 shows the ratio of DIG spaxels with metallicity measurements. The $R_{23}$and N2O2 metallicity diagnostics at a resolution scale of 41 pc are measuring the metallicity gradient of the DIG using only 1% and 2% of the total amount of DIG spaxels respectively. As we

	DIG spaxels		
Diagnostic	[SII]/Hα	HIIPhot	Hα SB
R_{23}	0.01	0.01	0.01
N2O2	0.02	0.02	0.01
O3N2	0.07	0.09	0.04
N2Hα	0.29	0.32	0.26
N2S2	0.68	0.68	0.65

Table 5.4 Same as Table 5.3 for DIG spaxels.

increase the spaxel size, we gradually include more LSB DIG regions which causes the DIG metallicity gradient to steepen towards the positive direction. As we are only starting with 1% and 2% of DIG spaxels, the DIG metallicity gradient continues to steepen all the way to the coarsest resolution.

For the N2S2 metallicity diagnostic, we are measuring the DIG metallicity gradient with 68% of DIG spaxels at a resolution scale of 41 pc. Since most of the DIG spaxels are already included at the finest resolution, less binning is needed to include all the emission from the LSB DIG regions. At a resolution of about 330 pc, the N2S2 DIG metallicity gradients stop steepening and remain constant within the uncertainties for coarser resolution scales. This is likely due to all the LSB DIG spaxels being included at the 330 pc scale and pure spatial smoothing happening as we continue to degrade the resolution. Although the O3N2 metallicity diagnostic only uses 7% of DIG spaxels at a resolution scale of 41 pc, the DIG metallicity gradients remain within ±0.02 dex/R_e at all resolution scales. This suggests that the ([OIII]/Hβ)/([NII]/Hα) emission line ratio is relatively independent of Hα surface brightness, and hence the inclusion of low surface brightness DIG spaxels has no effect on the emission line ratio radial profile.

It is difficult to assess how the N2Hα DIG metallicity diagnostic evolves with varying spatial resolution. We expect the [NII]/Hα ratio to increase in DIG regions, and hence the N2Hα metallicity. However, the PP04 N2Hα metallicity diagnostic imposes an upper and lower limit on the [NII]/Hα line ratio. Most of the DIG spaxels lie above this upper limit, meaning that most of the DIG is removed from the metallictity gradient measurements. This upper limit can be seen clearly in Figure 5.7. Table 5.4 shows that only ~29% of DIG spaxels lie within the limits of this diagnostic.

5.5.3. DIG Contamination of HII Regions

At increasingly coarse resolution scales, the boundary between HII regions and the DIG becomes unclear, leading to an increasing DIG contamination in the HII region emission line spectrum. DIG dominated regions have different ionization mechanisms and tend to have increased line ratios ([SII]/Hα, [NII]/Hα) compared to HII regions (Blanc et al. 2009; Zhang et al. 2017). The inclusion of DIG therefore systematically alters the line ratios of affected spaxels, leading to changes in their metallicity measurements.

As discussed in Section 5.4.1, Figure 5.8 shows that the $R_{23}$and N2O2 metallicity diagnostic gradients of the full set of spaxels diverges away from those determined using only pure HII region spaxels. If metallicity gradient flattening for the full set of spaxels was solely due

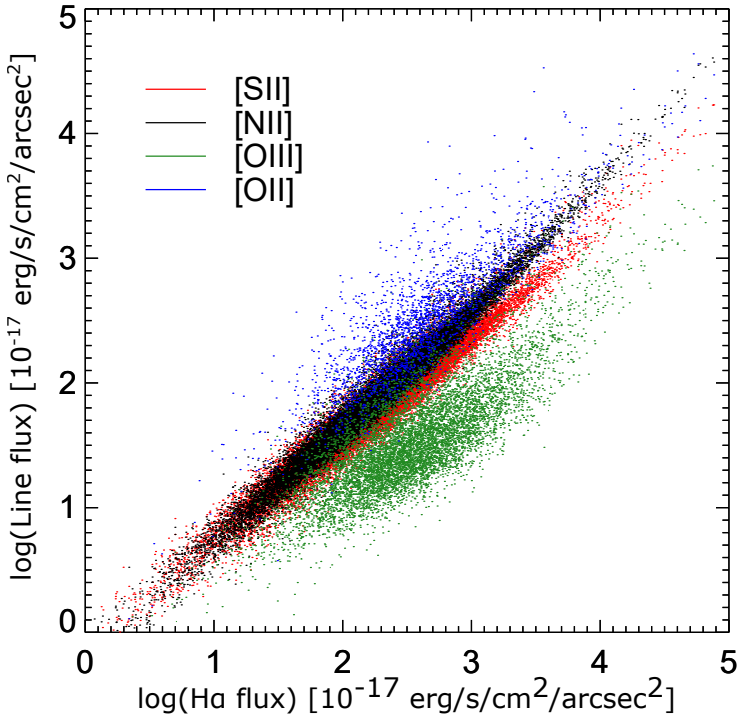

Figure 5.10 An almost linear relationship is seen between the Hα flux and all other strong emission line fluxes. This means that Hα can be used as a proxy for the strength of all other strong emission lines. [OII] and [OIII] have the greatest scatter from a linear relationship but can still be sufficiently described by the Hα flux.

to spatial smoothing, we would be expecting these two quantities to converge since spatial smoothing has a bigger effect on steeper gradients.

Figure 5.10 shows the relationship between the flux of various strong emission lines and Hα. An almost linear relationship is seen amongst all the strong emission lines. This means that when spaxels are merged together at coarser resolution scales, the resulting emission line ratio is a luminosity weighting of the line ratios of the individual spaxels. We can therefore determine how much of an impact DIG contamination has on emission line ratios by looking at the amount of Hα flux contributed by the DIG. We determine the HII dominance in each coarse-resolution spaxel by taking the ratio of the Hα surface brightness of the HII region datacube relative to that in the combined emission datacube. We then take the median of each radial bin to create a radial profile of the HII dominance. As each metallicity gradient is measured using a different set of spaxels, we create a HII region dominance profile for each metallicity diagnostic at every resolution scale above native (41 pc). This shows how each metallicity diagnostic is affected differently by DIG contamination.

From Figure 5.11, we can see that DIG contamination affects each diagnostic differently and the HII dominance profile is constantly changing at each resolution. As the resolution is decreased, the differences between the HII dominance profiles begin to disappear since at the coarsest resolution, the set of spaxels used for each metallicity diagnostic are essentially the same.

The HII dominance profiles of $R_{23}$and N2O2 are the same to within 10% of each other. This is expected as both diagnostics are both limited by the [OII] emission line. At a resolution scale

of 150 pc, the HII dominance profile has a spike at approximately $R/R_e = 0.6$ corresponding with the location of the spiral arms. At the resolution scales of 330 and 502 pc, the HII dominance profile consistently stays within 30% - 50%.

The inner-most radial bin ($0 < R/R_e < 0.25$) for $R_{23}$and N2O2 demonstrates the transition from being dominated by sheer number of DIG spaxels to luminosity weighting at 1005 pc. When fitting the metallicity gradients, HII region and DIG region spaxels are numerically weighted rather than luminosity weighted, meaning that a large number of DIG spaxels is able to overcome a small number of higher luminosity HII region spaxels. However, the merging of spaxels is a luminosity weighted action. As there are a relatively small number of DIG spaxels compared to their surface brightness in the inner radii, the higher surface brightness HII regions dominate in this process. However, in the outer regions, the HII dominance remains stable within 30% - 50% . This is because in the outer regions, there exists sufficient DIG spaxels to overcome the higher surface brightness HII regions.

The O3N2 and N2S2 HII dominance profiles demonstrates the transition from numeric weighting to luminosity weighting at all radii rather than just the inner radii as seen in $R_{23}$and N2O2. Since the O3N2 and N2S2 diagnostics use very strong emitting lines (no [OII] dependence), at fine resolution scales, the large number of DIG spaxels numerically dominate metallicity gradient determinations over the fewer more luminous HII regions. As we move to coarser resolution scales, luminous HII regions dominate the emission in increasingly more spaxels until the final HII dominance profile at 1005 pc resembles the other diagnostics.

While the DIG remains within the calibration limits of the R_{23}, N2O2, O3N2 and N2S2 diagnostics, the same is not true for the N2Hα diagnostic. Since the DIG has a significantly enhanced [NII]/Hα ratio, the upper limit removes most of these spaxels from the metallicity gradient calculation. Due to the inherent nature of the [NII]/Hα calibration, the weighting effect caused by the sheer number of DIG spaxels is severely reduced. A negative gradient HII dominance profile is persistent throughout every resolution scale.

Figure 5.12 shows the changes in the emission line ratio profiles of M83 at the coarse resolution scales. As expected, the emission line ratio profiles of HII regions are relatively unchanged as we decrease the resolution across all diagnostics. The emission line profiles of the DIG regions change significantly with decreasing resolution in the ([OII]+[OIII])/Hβ and [NII]/[OII] emission line ratios. This is a result of the inclusion of emission from LSB regions at coarser resolution scales. However, from Table 5.4 we see that the ([OIII]/Hβ)/([NII]/Hα) emission line ratio should also be significantly affected by the inclusion of LSB regions as very few DIG spaxels are present at the native resolution. The ([OIII]/Hβ)/([NII]/Hα) emission line ratio profile remains relatively unchanged across all resolution scales despite the inclusion of LSB regions. This suggests that LSB DIG regions have similar ([OIII]/Hβ)/([NII]/Hα) emission line ratios to the high surface brightness (HSB) DIG regions, while being significantly different for the ([OII]+[OIII])/Hβ and [NII]/[OII] emission line ratios.

For the ([OII]+[OIII])/Hβ and [NII]/[OII] emission line ratio profile, we can see a clear difference between the profiles of the HII and DIG regions. For both of these emission line ratios, the HII regions and DIG regions exhibit opposite radial gradients at the coarsest resolution scale. The upper-branch (12+log(O/H)>8.5) of the R_{23}metallicity diagnostic is approximately a one-to-one anti-correlated function of the ([OII]+[OIII])/Hβ emission line

ratio. From Figure 5.12 we can easily see that the HII regions have a positive radial gradient in the ([OII]+[OIII])/Hβ emission line ratio, leading to a negative metallicity gradient, while the DIG has a negative radial gradient in the ([OII]+[OIII])/Hβ emission line ratio, causing the observed positive metallicity gradient in the DIG regions. Conversely, the N2O2 metallicity diagnostics is a one-to-one positively correlated function of the [NII]/[OII] emission line ratio. We see that for HII regions, the [NII]/[OII] emission line ratio has a negative radial gradient, which produces the negative metallicity gradient. The DIG regions have a positive radial gradient for the [NII]/[OII] emission line ratio, leading to the positive metallicity gradient in the DIG regions.

By combining Figure 5.11 and Figure 5.12, we can get an understanding of how the DIG can severely affect the measured metallicity gradient at low resolution scales where HII and DIG emission can not be separated. The dominance profiles for $R_{23}$and N2O2 are approximately constant at around 0.4 and show a negative radial gradient at the coarsest resolution scale. If we combine the HII region and DIG region emission line ratio profiles together using Figure 5.11 as weights, we can see that the metallicity gradient would be flattened as a result. With HII regions and DIG regions having opposite emission line ratio gradients and the constant HII dominance profile at 0.4, the HII region and DIG regions cancel each other out, leaving a flat emission line ratio profile and hence no metallicity gradients when combined.

Applying this same process to the other metallicity diagnostics explains most of the behavior that we see in Figure 5.8. The O3N2 metallicity diagnostic is a negative linear fit to the ([OIII]/Hβ)/([NII]/Hα) emission line ratio. The O3N2 HII dominance profile shows us that the metallicity gradient fit is initially dominated by DIG, with the HII regions slowly taking over in the inner-sections of the galaxy as we decrease the resolution. Neither the HII region or DIG region emission line ratio profiles change significantly as a function of resolution. This means that as the inner-sections of the galaxy tend towards the HII regions while the outer regions remain the same, we end up with a steepening of the metallicity gradient as we decrease the resolution scale.

The [NII]/Hα emission line ratio profiles for HII regions and DIG regions undergo no changes as we decrease the resolution. This is due to the upper limit of the N2Hα metallicity diagnostic which places boundaries on [NII]/Hα for which the diagnostic can be used. The N2Hα metallicity diagnostic is a one-to-one positively correlated function with the [NII]/Hα emission line ratio. There is a very small positive gradient in the HII region [NII]/Hα emission line ratio profile which causes the positive metallicity gradient. The [NII]/Hα emission line profile for the DIG regions shows that its lowest emission line ratio occurs at [NII]/Hα = -0.3. This coincidentally corresponds to the upper limit of the N2Hα metallicity diagnostic which can only be used for -2.5 <[NII]/Hα < -0.3. This explains why the DIG metallicity gradients are flat for the N2Hα metallicity diagnostic at all resolution scales. As the resolution is decreased, the [NII]/Hα ratio can only increase from its lowest point of [NII]/Hα = -0.3. Since anything above [NII]/Hα > -0.3 is simply cut by the boundaries of the calibration, nothing but a flat gradient can exist.

Since the HII regions are also positioned quite close to the upper limit ([NII]/Hα = -0.4), as the resolution is decreased, the combined emission also exceeds this upper limit, causing the flat metallicity gradients. Based off of the HII region dominance profiles of the other 4 metallicity diagnostics and the emission line ratio radial profile of [NII]/Hα, we would

expect to see a positive metallicity gradient at low resolution scales for lower metallicity galaxies where we do not exceed the upper limit. The high HII region dominance in the inner-region combined with the increased DIG dominance and increasing [NII]/$H\alpha$ ratio in the outer regions lead to an overall positive [NII]/Hα emission line ratio radial profile.

Much like the [NII]/Hα emission line ratio, the log([NII]/[SII]) + 0.264× log([NII]/Hα) emission line ratio also does not change significantly as we decrease the resolution scale. This is expected since the majority of spaxels already have a metallicity estimate and thus the impact of including emission from LSB regions is minimal. The N2S2 metallicity diagnostic is very closely approximated by a linear fit with a gradient of 1. The HII dominance profile of the N2S2 metallicity diagnostic makes it very clear why the combined metallicity gradient is almost perfectly tied with the DIG metallicity gradient. Similar to the O3N2 metallicity diagnostic, the HII dominance profile of N2S2 starts off with a very low HII dominance at all radii with the inner-section becoming more HII dominated relative to the outer radii as we decrease the resolution. We can clearly see that the HII regions have a higher log([NII]/[SII]) + 0.264× log([NII]/Hα) emission line ratio at all radii compared to the DIG, meaning a higher absolute metallicity overall. The flat radial distribution of the HII regions means that it does not compensate for the DIG emission like the $R_{23}$and N2O2 metallicity diagnostics, meaning the combined emission metallicity gradients are dictated by the DIG emission.

5.5.4. Implications for Low Resolution Observations

As we have thoroughly demonstrated, measurements of the radial metallicity gradient deviate significantly from the true metallicity gradient as we decrease the spatial resolution. We have shown that contamination by the DIG and LSB regions have a far greater effect on the metallicity gradient than spatial smoothing. This means that the removal of DIG is an extremely important step in determining accurate radial metallicity gradients.

Ideally, the best method of obtaining the true metallicity gradient is to isolate the pure HII regions, however this is not always possible at higher redshift due to the limits of angular resolution. Therefore, we require either a metallicity diagnostic that is less sensitive to the DIG or some way to estimate and correct for the DIG contamination at the resolution of our observations.

The dashed red lines in Figure 5.8 show how each HII classification scheme performs at coarser resolution scales. In most cases, attempting to correct for DIG after contamination has occurred, results in metallicity gradients closer to their true value, with benefits diminishing as the resolution is decreased. For the [SII]/Hα HII classification scheme, applying the DIG correction either improves metallicity gradient measurements or has no effect for all metallicity diagnostics and resolution scales used. For the N2O2, N2HA and O3N2 metallicity diagnostic using the Hα surface brightness HII classification scheme, applying a DIG correction at 1005 pc results in a worse measurement of the metallicity gradient.

Figure 5.12 shows that the radial emission line ratio profiles of the DIG is often in the opposite direction to the HII region profiles. Any amount of DIG contamination would lead to shallower metallicity gradients. Applying the HII classification scheme to contaminated data removes all of the 'pure' DIG spaxels, but is unable to remove spaxels that contain a mixture of HII and DIG regions. By removing the 'pure' DIG spaxels, we are improving

the measurement of the metallicity gradient but are unable to remove the effects of DIG completely.

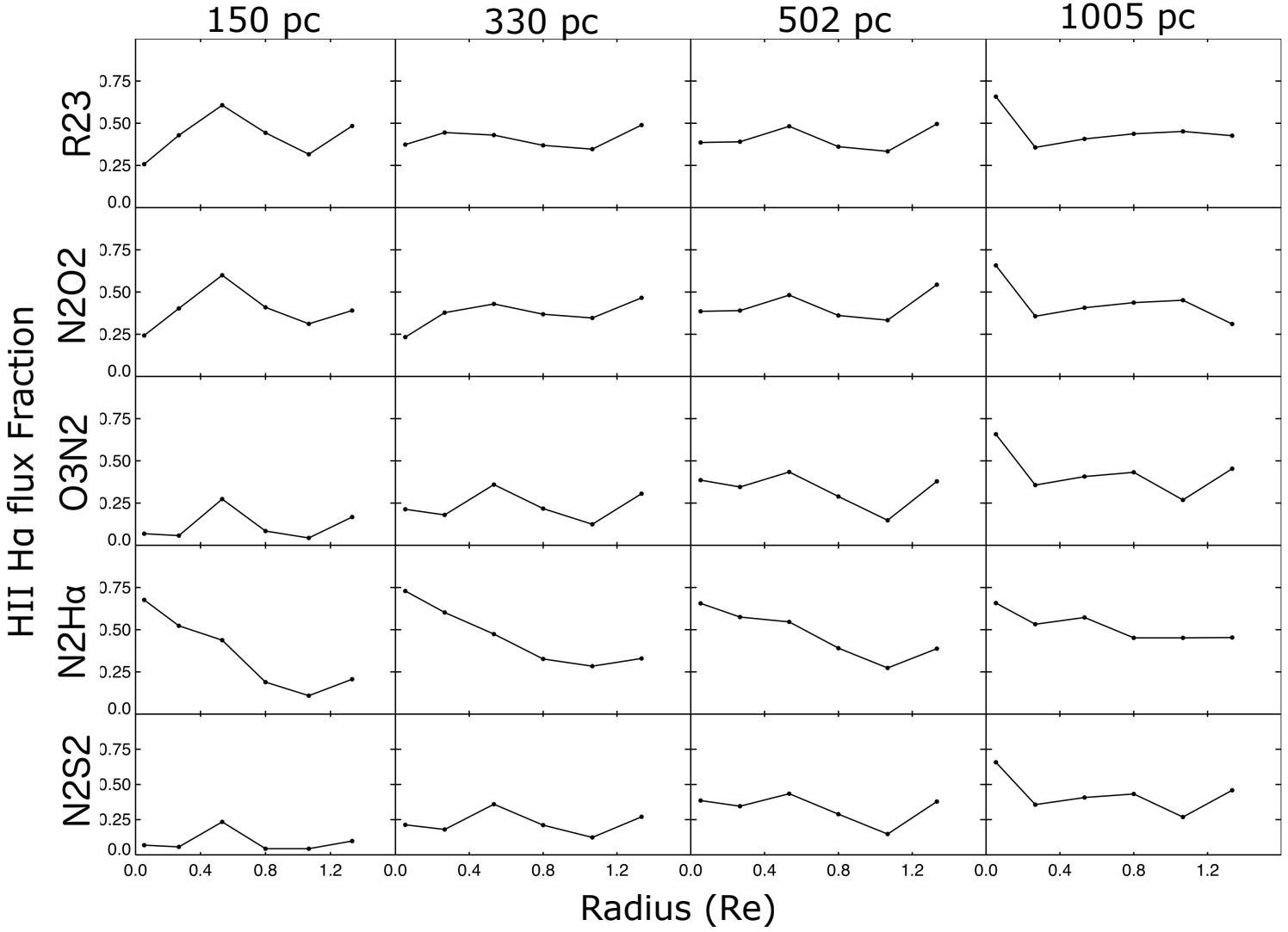

Figure 5.11 Here we show the median fraction of flux originating from HII regions in radial bins of $0.25R_e$ for each metallicity diagnostic at each binned resolution based on the spaxels used in each metallicity gradient fit. Since each metallicity gradient fit uses a different set of spaxels, the HII dominance profiles are different for each metallicity diagnostic. The difference in HII dominance profiles is dictated by which emission lines are used in the metallicity diagnostics. $R_{23}$and N2O2 have essentially identical profiles due to the limitations imposed by the [OII] emission line. At a resolution of 1005 pc, all metallicity diagnostics are basically using the same spaxels, hence the HII dominance profiles are very similar.

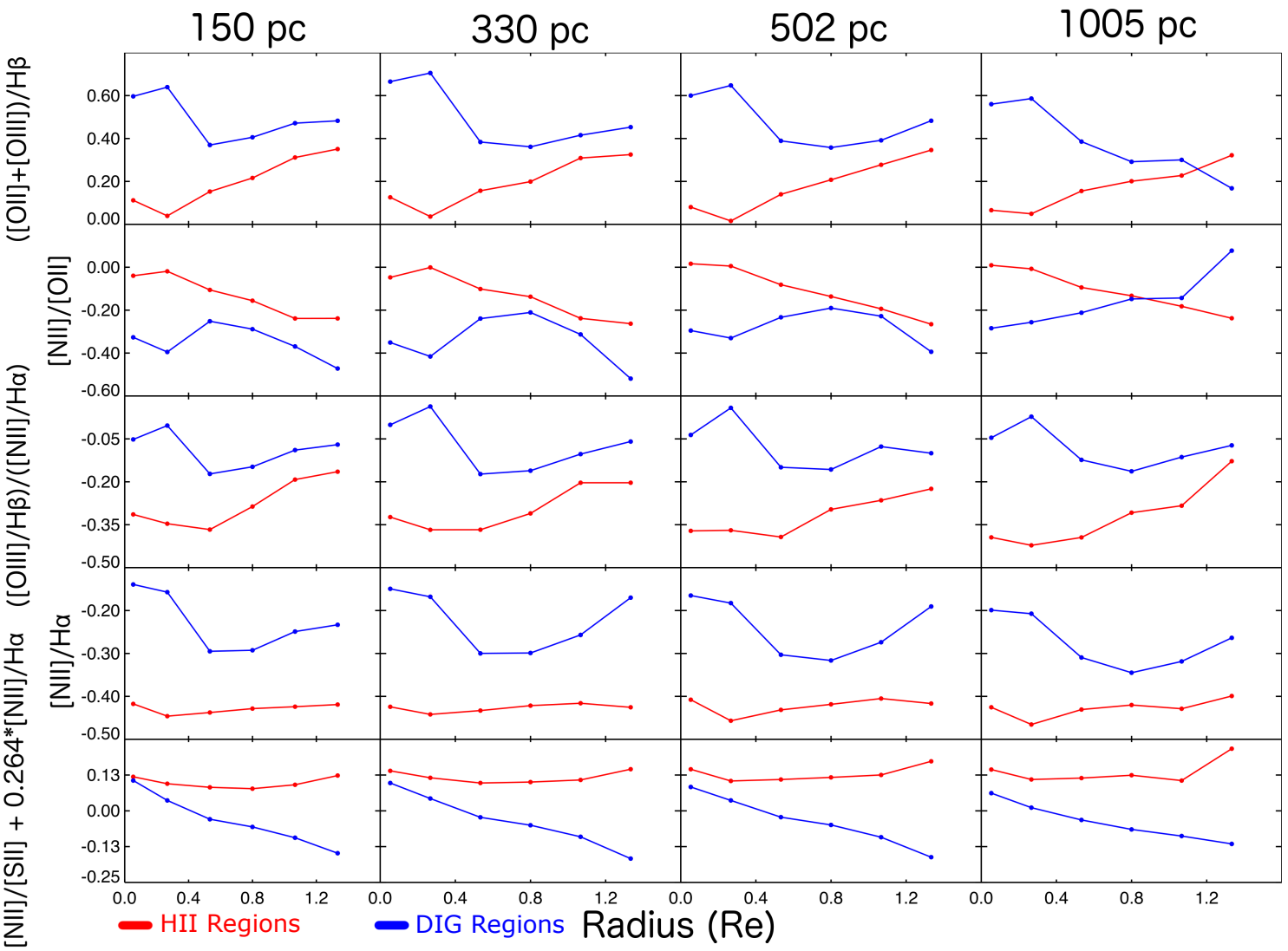

Figure 5.12 The emission line ratio profiles of each metallicity diagnostic at each binned resolutions in radial bins of $0.25R_e$. The HII region emission line ratios are largely unaffected by decreasing the resolution scales. However, the DIG emission line ratios are significantly different depending on how coarse the resolution scale is. The change in the DIG emission line profiles are caused by the inclusion of LSB regions as the data is binned.

5.6. Summary

We have presented a systematic study of how the diffuse ionized gas (DIG) affects the metallicity gradient determined from a range of metallicity diagnostics using high spatial resolution (41 pc) IFS data on the face-on spiral M83. We separate the HII and DIG regions using three different HII region classification schemes: the [SII]/Hα ratio, HIIPHOT (Thilker et al. 2000) and the Hα surface brightness. Once the regions have been separated, we rebin the datacubes to 150, 330, 502 and 1005 pc to simulate low resolution observations.

We find that the average Hα surface brightness of the HII regions is about 0.6 dex greater than the DIG regions at a given radii for R/R$_e$ < 1.5. However, depending on which HII classification scheme is used, DIG and low surface brightness spaxels comprise between 85% - 94% of spaxels within R/R$_e$ < 1.5. Although HII regions are significantly brighter than the DIG regions, DIG region spaxels are vastly more numerous. These two effects mean that the total Hα luminosity is approximately contributed by 70% HII region emission and 30% DIG emission for R/R$_e$ < 1.5 in M83. The spiral arms of M83 extend to about R/R$_e$ = 0.6, where the Hα luminosity is 75% contributed from HII regions. Beyond this (0.6 < R/R$_e$ < 1.5), HII regions contribute only 60% of the total Hα luminosity.

Using five different metallicity diagnostics we calculate the radial metallicity gradients as a function of resolution and HII region classification scheme. We find that the inclusion of DIG significantly affects the measured metallicity gradient by more than we would expect from pure spatial smoothing. Using a [SII]/Hα DIG classification scheme, the R$_{23}$(Kobulnicky & Kewley 2004) and N2O2 (Kewley & Dopita 2002) metallicity gradients are significantly flattened by the DIG by up to 0.048 dex/Re and 0.063 dex/Re respectively. The O3N2 (Pettini & Pagel 2004) metallicity gradients are initially flattened by the DIG by 0.057 dex/Re at 150 pc, with the metallicity gradients steepening and converging to within 0.02 dex/Re of the true metallicity gradient as the resolution is further lowered. The true metallicity gradient of the N2S2 (Dopita et al. 2016) metallicity diagnostic is positive and relatively flat at 0.025 dex/Re. The DIG induces a strong negative metallicity gradient of up to -0.21 dex/Re, a deviation of 0.24 dex/Re from the HII region metallicity gradient.

Like the N2S2 metallicity gradient, the N2Hα (Pettini & Pagel 2004) metallicity gradient is positive and relatively flat at 0.034 dex/Re. The [NII]/Hα emission line ratio is significantly enhanced in the DIG and exceeds the upper limit of the metallicity calibration. Due to the high metallicity and flat gradient of the HII regions, any spaxels which are significantly affected by DIG will exceed the upper limit and be removed from the metallicity gradient calculation. For M83, the N2Hα metallicity gradient is unaffected by the DIG because of its proximity to the upper limit of the Pettini & Pagel (2004) calibration.

As the spatial resolution is decreased from the native 41 pc to 1005 pc, the emission line ratios of the larger region are a luminosity weighted average of the smaller regions within it. To help untangle the evolution of the metallicity gradients with resolution, we present the HII dominance profile of M83. The HII dominance profile shows the percentage of Hα luminosity contributed by HII regions as a function of radius. The HII dominance profile clearly shows the transition from a numerical weighted average at 41 pc to a luminosity weighted average at 1005 pc.

Luminosity weighted averaging affects the emission line ratios rather than the metallicities

directly. We show the emission line ratio profiles of the HII and DIG regions as a function of radius and resolution for each emission line ratio. For all resolution scales, the emission line ratio radial profiles of HII regions remains relatively unchanged. However there appears to be significant changes to the DIG emission line ratio profiles for ([OII]+[OIII])/Hβ and [NII]/[OII]. The change in the emission line ratio profiles indicate the significance of low surface brightness regions. As resolution is decreased, more low surface brightness emission is included in the spectrum, leading to significant changes in the emission line ratio profiles of DIG regions. The origin of the low surface brightness DIG emission is still uncertain, but is likely due to a combination of photon leakage from HII regions as well as ionization from low-mass evolved stars. The different ionizing mechanisms of the DIG cause the emission line ratios to vary from what we would expect from HII regions.

We find that the ([OIII]/Hβ)/([NII]/Hα) emission line ratio radial profile is similar for both high surface brightness DIG and low surface brightness DIG, meaning that decreasing the resolution to kiloparsec resolution scales does not change the overall DIG emission line ratio profile. ([OII]+[OIII])/Hβ and [NII]/[OII] have different emission line ratio radial profiles for the high and low surface brightness DIG, leading to changes in the overall DIG emission line ratio profiles as we decrease the resolution scales. Overall this means that the O3N2 emission line diagnostic will provide the closest metallicity gradient to the pure HII region metallicity gradient at a resolution of 1005 pc, the resolution scales of large galaxy surveys.

Finally we discuss the implications this study has for low resolution observations where the DIG is difficult to remove due to the mixing of HII and DIG regions. Based on the DIG characteristics of M83, the emission line radial profiles of DIG tend to possess an opposite gradient to the HII regions to varying degrees at a resolution of 1005 pc, the resolution scales of large galaxy surveys.

Applying the [SII]/Hα classification scheme at any resolution for all metallicity diagnostics used in this study will yield a metallicity gradient closer to the metallicity gradient of pure HII regions, but is unable to fully produce it. The DIG contamination associated with coarser resolution elements is unavoidable, but we are able to remove spaxels which are almost completely comprised of DIG by applying the [SII]/Hα cut.

It is not yet possible to correct for the DIG in large galaxy surveys or high redshift observations without analysing the DIG fractions and DIG emission line properties of multiple galaxies. We therefore recommend that when measuring metallicity gradients at low spatial resolutions, that a [SII]/Hα cut is used at resolution scales between 150 - 1005 pc to remove spaxels which are almost completely comprised of DIG. When measuring metallicity gradients at low resolution scales, it will inevitably be affected by DIG and should be used with extreme caution.

Acknowledgements

This paper includes data obtained with the du Pont Telescope at the Las Campanas Observatory, Chile as part of the TYPHOON Program, which has been obtaining optical data cubes for the largest angular-sized galaxies in the southern hemisphere. We thank past and present Directors of The Observatories and the numerous time assignment committees for

their generous and unfailing support of this long-term program.
Parts of this research were conducted by the Australian Research Council Centre of Excellence for All Sky Astrophysics in 3 Dimensions (ASTRO 3D), through project number CE170100013.
BG gratefully acknowledges the support of the Australian Research Council as the recipient of a Future Fellowship (FT140101202).
This research has made use of the NASA/IPAC Extragalactic Database (NED), which is operated by the Jet Propulsion Laboratory, California Institute of Technology, under contract with the National Aeronautics and Space Administration.

5.7. Appendix: Metallicity Gradient Fits

[SII]/Hα Cut

Diagnostic	41pc	150pc	330pc	502pc	1005pc
R23					
HII	-0.072±0.005	-0.059±0.004	-0.052±0.006	-0.049±0.006	-0.046±0.007
HII Low Res	-	-0.050±0.005	-0.038±0.008	-0.031±0.010	-0.002±0.008
Full	-0.072±0.005	-0.040±0.005	-0.018±0.008	-0.020±0.010	0.002±0.015
DIG	-0.005±0.010	0.002±0.007	0.040±0.009	0.037±0.012	0.081±0.019
N2O2					
HII	-0.114±0.006	-0.105±0.005	-0.097±0.006	-0.096±0.007	-0.087±0.008
HII Low Res	-	-0.089±0.006	-0.074±0.008	-0.062±0.011	-0.021±0.014
Full	-0.080±0.005	-0.064±0.005	-0.044±0.007	-0.033±0.010	-0.024±0.013
DIG	-0.019±0.007	-0.029±0.005	-0.001±0.009	0.019±0.010	0.036±0.017
O3N2					
HII	-0.068±0.003	-0.058±0.006	-0.056±0.007	-0.050±0.009	-0.063±0.012
HII Low Res	-	-0.026±0.007	-0.016±0.010	-0.015±0.012	-0.040±0.010
Full	-0.034±0.003	-0.001±0.004	-0.008±0.006	-0.026±0.009	-0.043±0.010
DIG	0.002±0.003	0.029±0.004	0.024±0.006	0.015±0.008	0.009±0.012
N2Hα					
HII	0.034±0.002	0.024±0.004	0.025±0.006	0.026±0.007	0.027±0.009
HII Low Res	-	0.029±0.007	0.024±0.013	0.005±0.016	0.024±0.033
Full	0.019±0.001	0.015±0.004	0.026±0.007	0.012±0.009	-0.004±0.014
DIG	-0.015±0.002	-0.011±0.004	0.003±0.007	-0.001±0.010	0.012±0.016
N2S2					
HII	0.025±0.003	0.024±0.005	0.026±0.009	0.030±0.010	0.036±0.013
HII Low Res	-	-0.002±0.009	-0.009±0.013	-0.027±0.016	-0.011±0.037
Full	-0.090±0.001	-0.150±0.003	-0.175±0.006	-0.210±0.009	-0.180±0.014
DIG	-0.095±0.001	-0.151±0.003	-0.176±0.005	-0.182±0.006	-0.181±0.011

Figure 5.13 Metallicity gradient fits for Figure 5.7

	Hα Cut				
Diagnostic	41pc	150pc	330pc	502pc	1005pc
R23					
HII	-0.065±0.005	-0.056±0.006	-0.058±0.007	-0.050±0.008	-0.044±0.009
HII Low Res	-	-0.040±0.006	-0.040±0.010	-0.034±0.013	0.022±0.027
Full	-0.072±0.005	-0.040±0.005	-0.018±0.008	-0.020±0.010	0.002±0.015
DIG	-0.074±0.018	0.008±0.012	0.029±0.013	0.043±0.012	0.063±0.021
N2O2					
HII	-0.065±0.006	-0.085±0.005	-0.076±0.007	-0.080±0.007	-0.077±0.009
HII Low Res	-	-0.066±0.007	-0.063±0.009	-0.033±0.013	0.007±0.032
Full	-0.080±0.005	-0.064±0.005	-0.044±0.007	-0.033±0.010	-0.024±0.013
DIG	-0.092±0.012	-0.057±0.012	-0.042±0.012	0.001±0.013	0.100±0.022
O3N2					
HII	-0.022±0.003	-0.008±0.005	-0.007±0.007	-0.033±0.009	-0.042±0.011
HII Low Res	-	0.014±0.009	0.007±0.012	-0.016±0.019	0.009±0.036
Full	-0.034±0.003	-0.001±0.004	-0.008±0.006	-0.026±0.009	-0.043±0.010
DIG	0.017±0.004	0.028±0.004	0.020±0.007	0.021±0.008	0.014±0.012
N2Hα					
HII	0.023±0.002	0.006±0.004	0.001±0.006	0.008±0.008	0.038±0.011
HII Low Res	-	0.003±0.010	0.021±0.016	0.035±0.023	-0.173±0.048
Full	0.019±0.001	0.015±0.004	0.026±0.007	0.012±0.009	-0.004±0.014
DIG	-0.022±0.002	-0.023±0.004	-0.006±0.008	-0.016±0.010	-0.018±0.017
N2S2					
HII	-0.022±0.003	-0.025±0.005	0.008±0.009	0.004±0.011	0.013±0.014
HII Low Res	-	-0.032±0.009	-0.032±0.013	-0.062±0.018	-0.076±0.040
Full	-0.090±0.001	-0.150±0.003	-0.175±0.006	-0.210±0.009	-0.180±0.014
DIG	-0.082±0.002	-0.143±0.003	-0.167±0.005	-0.159±0.006	-0.180±0.011

Figure 5.14 Same as Figure 5.13 for the Hα cut.

HIIphot

Diagnostic	41pc	150pc	330pc	502pc	1005pc
R23					
HII	-0.064±0.005	-0.058±0.006	-0.048±0.008	-0.052±0.008	-0.042±0.009
HII Low Res	-	-	-	-	-
Full	-0.072±0.005	-0.040±0.005	-0.018±0.008	-0.020±0.010	0.002±0.015
DIG	-0.071±0.009	-0.016±0.007	0.012±0.009	0.008±0.011	0.052±0.018
N2O2					
HII	-0.075±0.006	-0.104±0.006	-0.095±0.008	-0.118±0.007	-0.079±0.010
HII Low Res	-	-	-	-	-
Full	-0.080±0.005	-0.064±0.005	-0.044±0.007	-0.033±0.010	-0.024±0.013
DIG	-0.067±0.008	-0.041±0.006	-0.014±0.008	-0.005±0.010	0.040±0.016
O3N2					
HII	-0.034±0.004	-0.035±0.007	-0.046±0.010	-0.042±0.012	-0.054±0.014
HII Low Res	-	-	-	-	-
Full	-0.034±0.003	-0.001±0.004	-0.008±0.006	-0.026±0.009	-0.043±0.010
DIG	0.003±0.003	0.018±0.004	0.020±0.006	0.007±0.008	0.018±0.011
N2Hα					
HII	0.025±0.004	0.009±0.007	0.040±0.010	0.040±0.011	0.046±0.013
HII Low Res	-	-	-	-	-
Full	0.019±0.001	0.015±0.004	0.026±0.007	0.012±0.009	-0.004±0.014
DIG	0.002±0.002	0.005±0.004	0.034±0.008	0.021±0.010	-0.015±0.013
N2S2					
HII	-0.020±0.004	-0.027±0.009	-0.008±0.014	0.010±0.018	0.019±0.021
HII Low Res	-	-	-	-	-
Full	-0.090±0.001	-0.150±0.003	-0.175±0.006	-0.210±0.009	-0.180±0.014
DIG	-0.084±0.002	-0.144±0.003	-0.158±0.005	-0.172±0.007	-0.171±0.012

Figure 5.15 Same as Figure 5.13 for HIIphot.

5.8. Appendix: Metallicity Gradient as a Function of Resolution

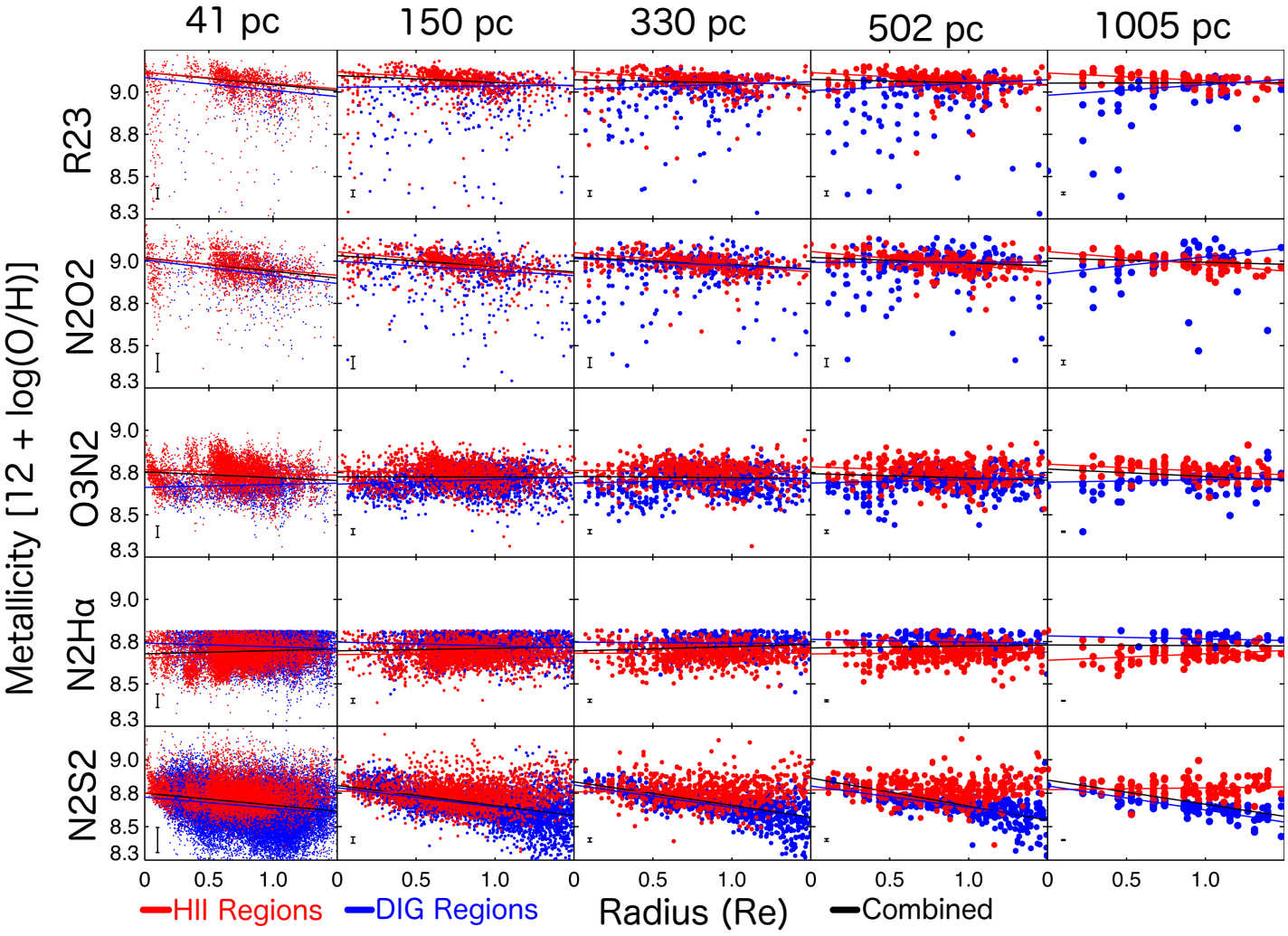

Figure 5.16 Same as Figure 5.7 for the Hα cut.

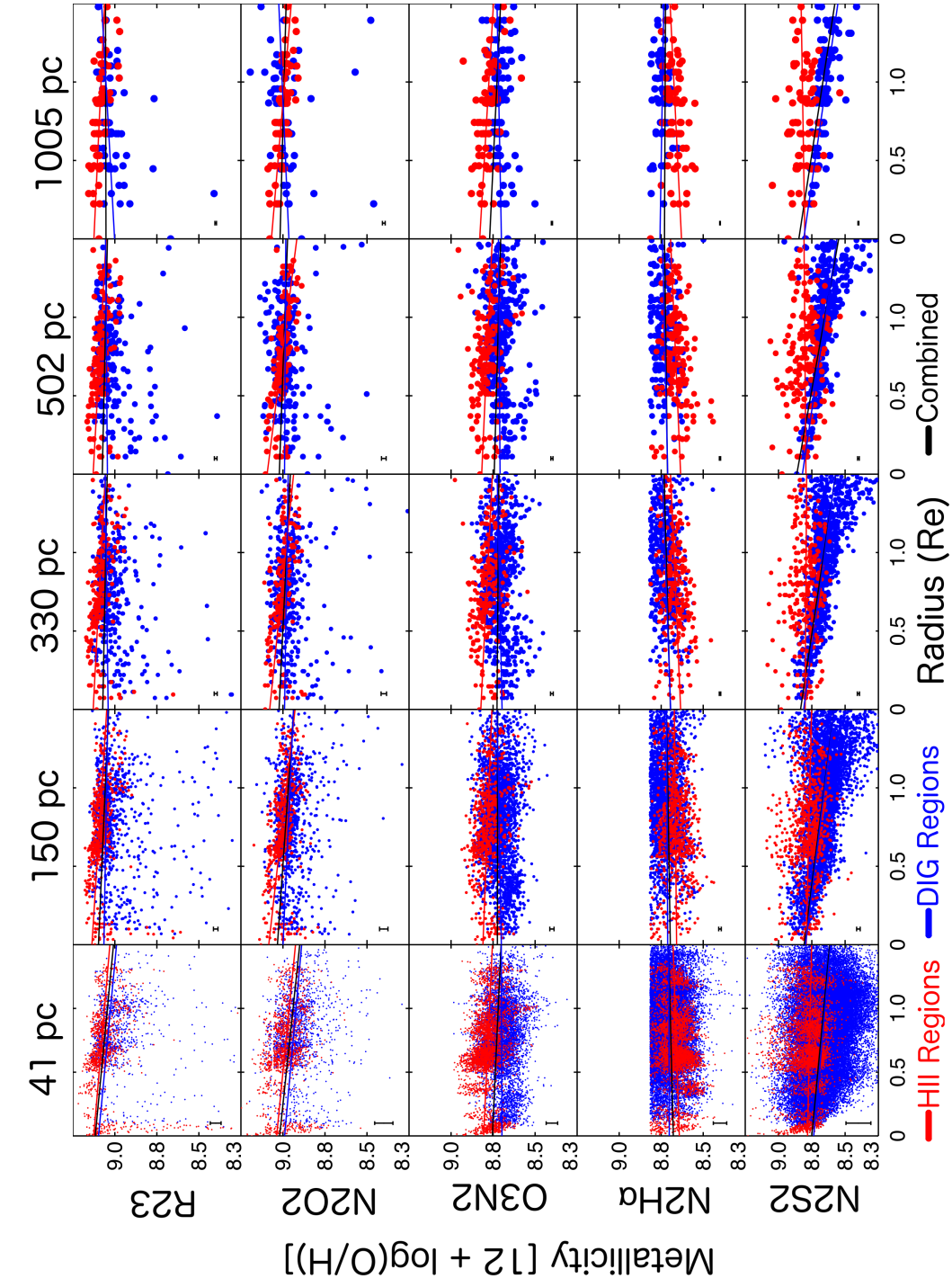

Figure 5.17 Same as Figure 5.7 for the HIIPHOT regions.

5.9. Appendix: Defining HII Regions Based on Kaplan et al. 2016

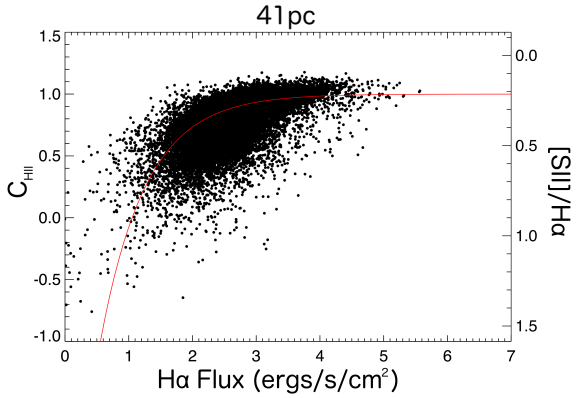

Figure 5.18 The relationship between [SII]/Hα and the extinction corrected Hα surface brightness. We use the method by Kaplan et al. (2016) to determine the amount of flux originating from HII regions and DIG regions at the native resolution.

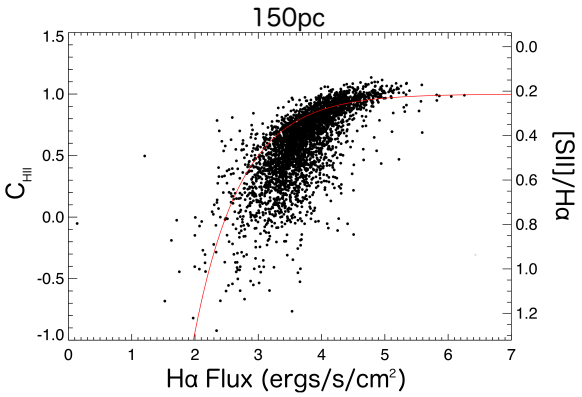

Figure 5.19 Same as Figure 5.18 at 150pc

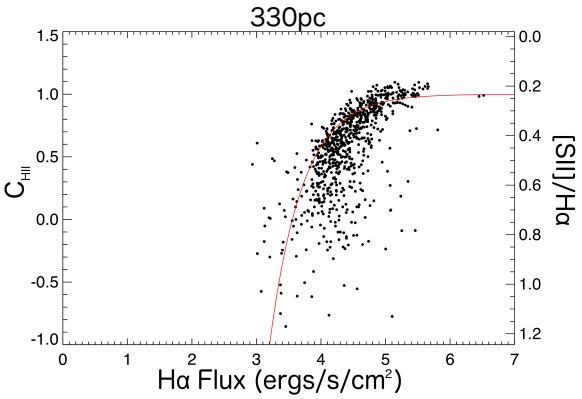

Figure 5.20 Same as Figure 5.18 at 330pc

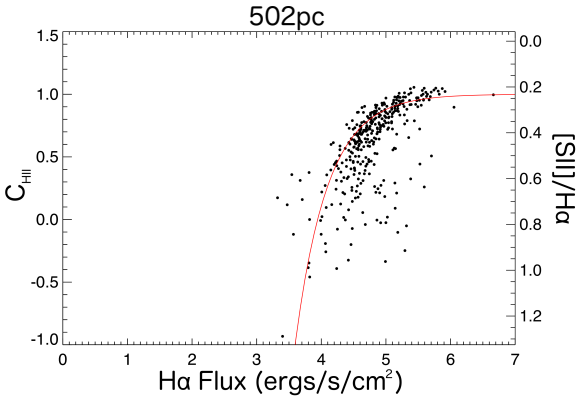

Figure 5.21 Same as Figure 5.18 at 502pc

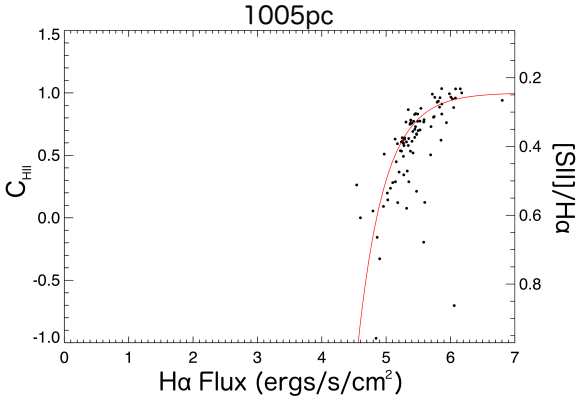

Figure 5.22 Same as Figure 5.18 at 1005pc

DIG Fraction Parameters		
Resolution	$\log(f_0)$	β
41 pc, Figure 5.18	1.05	0.61
150 pc	2.49	0.59
330 pc	3.56	0.85
502 pc	3.94	0.87
1005 pc	4.85	1.05

Figure 5.23 Fit parameters for Equation 1 at each resolution

CHAPTER 6

Summary

With the emergence of integral field spectroscopy surveys, the measurement of gas-phase radial metallicity gradients can be done with relative ease in high volumes. However at the typical kiloparsec spatial resolution of these galaxy surveys, there are many caveats that need to be understood and corrected for to obtain the intrinsic metallicity gradient. In this thesis, we have explored some of the main sources of uncertainty when measuring metallicity gradients such as: the effect of ionization parameter, the choice of metallicity diagnostic, and the contamination by the diffuse ionized gas. We also provide a brief analysis into how the metallicity gradient changes with environmental density. A brief summary of each of the topics covered is provided below.

6.1. Spatially Resolved Metallicity and Ionization Parameter in SAMI

In Chapter 2 (published as Poetrodjojo et al. 2018), we present the first spatially resolved maps of the gas-phase metallicity and ionization parameter for 25 galaxies in the SAMI galaxy survey. The metallicity and ionization parameter distributions are compared to important galactic properties such as stellar mass, star-formation rate and specific star-formation rate.

We measure the radial metallicity gradients of each galaxy and find an average metallicity gradient of -0.12 ± 0.05 dex/R_e using the R_{23}metallicity diagnostic calibrated by Kobulnicky & Kewley (2004). Metallicity gradients were also calculated using the O3N2 diagnostic calibrated by Pettini & Pagel (2004) and the N2O2 diagnostic calibrated by Kewley & Dopita (2002) and found consistent results with similar studies (Ho et al. 2014; Sánchez et al. 2012, 2014; Sánchez-Menguiano et al. 2016b).

We find that the ionization parameter maps lack coherent structure, making their effect on metallicity diagnostics unpredictable. Unlike Dopita et al. (2014) and Kaplan et al. (2016), we find no significant radial ionization parameter gradients, likely due to differences in sample selection or spatial resolution limitations. The ionization parameter range of our

galaxy sample ranges between $7.0 < \log(q[cm/s]) < 7.8$, leading to potential deviations of 0.3 dex when using the O3N2 metallicity diagnostic.

6.2. Metallicity Gradients as a Function of Environment

The motivation for Chapter 3 was to form a continous link between the negative metallicity gradients of isolated galaxies to the flattened metallicity gradients of merging galaxies. It is known that merging galaxies have significantly flatter metallicity gradients. Here we analyse how the metallicity gradients of SAMI DR2 vary with environmental density.

Using the Scal metallicity diagnostic, the metallicity gradients of 248 galaxies from SAMI DR2 are measured. Dependencies on disk scale length and stellar mass are removed from the metallicity gradients to allow small variations to be compared to differences in environmental density.

We find no dependence of the metallicity gradients on any of the three environmental density parameters. We suggest that the absence of a relationship between metallicity gradients and environmental density is likely due to underlying secondary effects which are not being corrected for. The fundamental metallicity relation Mannucci et al. (2010) shows evidence for the dependence of gas-phase metallicity on the star-formation rate. It is therefore possible that the star-formation rate may have a larger effect on the metallicity gradients than the environmental density, eclipsing any influence the environmental density may have.

6.3. Reconciling Metallicity Diagnostics

Chapter 4 marks the beginning of our investigation into the major problems regarding the measurement of gas-phase metallicity. In this chapter (Accepted by Monthly Notices of the Royal Astronomical Society), we investigate the significant discrepancies present between the many strong emission line metallicity diagnostics available.

We measure the metallicity gradients of 248 galaxies from the SAMI galaxy survey using 13 popular metallicity diagnostics and techniques. Metallicity gradients calculated from different diagnostics suffer from systematic offsets similar to aperture metallicities (Kewley & Ellison 2008), however, we find that the metallicity gradients calculated from different diagnostics can be easily converted using a linear transformation with a non-unity gradient. We find the zero-point offset of the linear transformations remains close to 0 for all diagnostic conversions, meaning flat metallicity gradients are consistent regardless of diagnostic.

As expected, metallicity gradients calculated from diagnostics which share emission line ratios tend to agree better than diagnostics using different sets of emission lines. Diagnostics calibrated through the direct temperature method have tighter correlations with other diagnostics calibrated through the direct temperature method. This is likely due to the significant overlap in calibrating data for direct temperature metallicities. Conversely, diagnostics calibrated through photoionization models are less consistent with other diagnostics also calibrated through photoionization models. Due to the large customisable

parameter space present in photoionization models, this allows for a wider variation in calibrating data and hence room for discrepancies between different calibrations.

With the impending release of JWST and future instruments which probe deeper into the universe, it will be valuable to compare the metallicity gradients of high redshift galaxies to those of local galaxies. Due to the nature of high redshift observations, only the strongest emission lines will be observable, limiting the selection of metallicity diagnostics and calibrations that can be used. It is therefore valuable to be reminded of the systematic differences present when comparing different metallicity diagnostics and calibrations if high redshift surveys are limited to certain emission line diagnostics.

6.4. Effects of DIG and Spatial Resolution on Metallicity Gradients

In addition to the major inconsistencies between strong emission line metallicity diagnostics, contamination by foreign ionizing sources can significantly influence the measured metallicity gradients of galaxies. In Chapter 5 (published as Poetrodjojo et al. 2019), we provide a systematic investigation into how the diffuse ionized gas affects the measurements of metallicity gradients at low spatial resolution scales. We use highly spatially resolved spectra of M83 from the TYPHOON survey to identify HII regions and the diffuse ionized gas using HIIPHOT, the Hα surface brightness and the [SII]/Hα emission line ratio. The native 41pc resolution data is then artificially rebinned to simulate observations at resolutions scales of 150pc, 330pc, 502pc and 1005pc.

For M83, the DIG regions contribute 30% of the total Hα luminosity within 1.5R_e. This amount of DIG flattens the metallicity gradient of M83 by up to 0.048 dex/R_e and 0.063 dex/R_e at the coarse resolution scales for the R_{23}(Kobulnicky & Kewley 2004) and N2O2 (Kewley & Dopita 2002) metallicity diagnostics respectively. The O3N2 metallicity diagnostic by Pettini & Pagel (2004) appears to be relatively unaffected by the presence of DIG with the metallicity gradient remaining within 0.02 dex/R_e at the 1005pc resolution.

Applying any of the HII region finding algorithms at the kiloparsec resolution has little to no effect on bringing the measured metallicity gradient to its true value. This is because the coarse resolution inevitibly includes a significant amount of DIG emission in each individual spaxel, which can not be removed via these methods. Without knowing how the distribution of the DIG varies from galaxy to galaxy, we are unable to provide a robust method for completely removing the effects of DIG on metallicity gradients.

6.5. Future work

While this thesis has focussed on gaining a better understanding of metallicity gradients and how we measure them, Chapter 3 and Chapter 5 in particular, have left lingering questions which could not be answered at the time due to insufficient data. Here we will outline the steps required in order to further expand the work done in Chapter 3 and Chapter 5.

In Chapter 3, we try to expand on the works of Kewley et al. (2010); Rich et al. (2012); Sánchez et al. (2014) which showed flatter metallicity gradients in galaxies with merger signatures.

Using the 3 environmental measurements provided by the GAMA survey, we were unable to find a continuous relationship between the environmental density and metallicity gradient.

As discussed in Chapter 3, one reason a smooth transition to flattened metallicity gradients might not have been observed, could be that the flattening of the metallicity gradient does not occur until a galaxy engages in a merger process. The environmental measures used in Chapter 3, fifth nearest neighbour, number of galaxies within a cylindrical volume and density of galaxies within an adaptive Gaussian ellipsoid, all focus on counting the number of galaxies within a certain volume. While these environmental measures may tell us how likely a merger is to occur, it does not accurately measure if a merger has actually happened. If a more specific parameter which can objectively determine the extent a merger pair has interacted is invented, then this will likely produce a much better correlation with the metallicity gradient of the galaxy.

In Chapter 5, we expose the risks of using strong emission line metallicity diagnostics at low resolution scales. With large galaxy surveys such as SAMI, MaNGA and HECTOR having average spatial resolutions on the kiloparsec scales, is it possible to correct for the effects of DIG and accurately measure metallicity gradients at these resolution scales?

The main limitation of the research completed in Chapter 5 is clearly that only one galaxy was analysed. Before developing a method to remove the emission contributed by the DIG, two outstanding questions must first be answered: How does the distribution and spectral properties of DIG vary from galaxy to galaxy? To answer these questions, a large high spatial resolution dataset consisting of galaxies spanning a wide range of stellar mass, star-formation rate and metallicities needs to be constructed. This will allow us to characterise the properties of DIG as a function of global properties which can then be used as assumptions at lower resolution scales. Such a dataset will soon be available with the TYPHOON survey which is currently undergoing an intensive data reduction process.

Bibliography

Allen, J. T., et al. 2015, MNRAS, 446, 1567 (ADS entry)

Alloin, D., Collin-Souffrin, S., Joly, M., & Vigroux, L. 1979, A&A, 78, 200 (ADS entry)

Azimlu, M., Marciniak, R., & Barmby, P. 2011, AJ, 142, 139 (ADS entry)

Baldwin, J. A., Phillips, M. M., & Terlevich, R. 1981, PASP, 93, 5 (ADS entry)

Barrera-Ballesteros, J. K., Sánchez, S. F., Heckman, T., Blanc, G. A., & MaNGA Team. 2017, ApJ, 844, 80 (ADS entry)

Belfiore, F., et al. 2017, MNRAS, 469, 151 (ADS entry)

Blanc, G. A., Heiderman, A., Gebhardt, K., Evans, II, N. J., & Adams, J. 2009, ApJ, 704, 842 (ADS entry)

Blanc, G. A., Kewley, L., Vogt, F. P. A., & Dopita, M. A. 2015, ApJ, 798, 99 (ADS entry)

Blanc, G. A., et al. 2013, AJ, 145, 138 (ADS entry)

Bland-Hawthorn, J. 2015, in IAU Symposium, Vol. 309, Galaxies in 3D across the Universe, ed. B. L. Ziegler, F. Combes, H. Dannerbauer, & M. Verdugo, 21–28 (ADS entry)

Bland-Hawthorn, J., et al. 2011, Optics Express, 19, 2649 (ADS entry)

Boettcher, E., Gallagher, III, J. S., & Zweibel, E. G. 2017, ApJ, 845, 155 (ADS entry)

Boissier, S., & Prantzos, N. 1999, MNRAS, 307, 857 (ADS entry)

Bresolin, F., Kennicutt, R. C., & Ryan-Weber, E. 2012, ApJ, 750, 122 (ADS entry)

Bresolin, F., & Kennicutt, Jr., R. C. 2002, ApJ, 572, 838 (ADS entry)

Bresolin, F., Kudritzki, R.-P., Urbaneja, M. A., Gieren, W., Ho, I.-T., & Pietrzyński, G. 2016, ApJ, 830, 64 (ADS entry)

Bresolin, F., Ryan-Weber, E., Kennicutt, R. C., & Goddard, Q. 2009, ApJ, 695, 580 (ADS entry)

Bresolin, F., Schaerer, D., González Delgado, R. M., & Stasińska, G. 2005, A&A, 441, 981 (ADS entry)

Bruzual, G., & Charlot, S. 2003, MNRAS, 344, 1000 (ADS entry)

Bryant, J. J., Bland-Hawthorn, J., Fogarty, L. M. R., Lawrence, J. S., & Croom, S. M. 2014, MNRAS, 438, 869 (ADS entry)

Bryant, J. J., et al. 2015, MNRAS, 447, 2857 (ADS entry)

Bundy, K., et al. 2015, ApJ, 798, 7 (ADS entry)

Burbidge, E. M., Burbidge, G. R., Fowler, W. A., & Hoyle, F. 1957, Reviews of Modern Physics, 29, 547 (ADS entry)

Cappellari, M. 2017, MNRAS, 466, 798 (ADS entry)

Cappellari, M., & Emsellem, E. 2004, PASP, 116, 138 (ADS entry)

Cappellari, M., et al. 2011, MNRAS, 413, 813 (ADS entry)

—. 2013, MNRAS, 432, 1709 (ADS entry)

Cardelli, J. A., Clayton, G. C., & Mathis, J. S. 1989, ApJ, 345, 245 (ADS entry)

Castellanos, M., Díaz, A. I., & Terlevich, E. 2002a, MNRAS, 329, 315 (ADS entry)

—. 2002b, MNRAS, 337, 540 (ADS entry)

Charlot, S., & Longhetti, M. 2001, MNRAS, 323, 887 (ADS entry)

Croom, S. M., Allen, J. T., Cortese, L., Fogarty, L., & Ho, I.-T. 2015, in IAU Symposium, Vol. 311, Galaxy Masses as Constraints of Formation Models, ed. M. Cappellari & S. Courteau, 104–109 (ADS entry)

Croom, S. M., et al. 2012, MNRAS, 421, 872 (ADS entry)

Curti, M., Cresci, G., Mannucci, F., Marconi, A., Maiolino, R., & Esposito, S. 2017, MNRAS, 465, 1384 (ADS entry)

D'Agostino, J. J., Kewley, L. J., Groves, B. A., Medling, A., Dopita, M. A., & Thomas, A. D. 2019a, MNRAS, 485, L38 (ADS entry)

D'Agostino, J. J., Poetrodjojo, H., Ho, I.-T., Groves, B., Kewley, L., Madore, B. F., Rich, J., & Seibert, M. 2018, MNRAS(ADS entry)

D'Agostino, J. J., et al. 2019b, MNRAS, 487, 4153 (ADS entry)

Davies, R. L., Rich, J. A., Kewley, L. J., & Dopita, M. A. 2014, MNRAS, 439, 3835 (ADS entry)

Davies, R. L., et al. 2016, MNRAS, 462, 1616 (ADS entry)

—. 2017, MNRAS, 470, 4974 (ADS entry)

De Vis, P., et al. 2019, A&A, 623, A5 (ADS entry)

de Zeeuw, P. T., et al. 2002, MNRAS, 329, 513 (ADS entry)

Denicoló, G., Terlevich, R., & Terlevich, E. 2002, MNRAS, 330, 69 (ADS entry)

Diaz, A. I., Terlevich, E., Vilchez, J. M., Pagel, B. E. J., & Edmunds, M. G. 1991, MNRAS, 253, 245 (ADS entry)

Díaz, R. J., Dottori, H., Aguero, M. P., Mediavilla, E., Rodrigues, I., & Mast, D. 2006, ApJ, 652, 1122 (ADS entry)

Dopita, M. A., & Evans, I. N. 1986, ApJ, 307, 431 (ADS entry)

Dopita, M. A., Kewley, L. J., Sutherland, R. S., & Nicholls, D. C. 2016, Ap&SS, 361, 61 (ADS entry)

Dopita, M. A., Rich, J., Vogt, F. P. A., Kewley, L. J., Ho, I.-T., Basurah, H. M., Ali, A., & Amer, M. A. 2014, Ap&SS, 350, 741 (ADS entry)

Dopita, M. A., & Sutherland, R. S. 2003, Astrophysics of the diffuse universe (ADS entry)

Dopita, M. A., Sutherland, R. S., Nicholls, D. C., Kewley, L. J., & Vogt, F. P. A. 2013, ApJS, 208, 10 (ADS entry)

Dopita, M. A., et al. 2006, ApJ, 647, 244 (ADS entry)

Draine, B. T. 2011, Physics of the Interstellar and Intergalactic Medium (ADS entry)

Driver, S. P., et al. 2011, MNRAS, 413, 971 (ADS entry)

Drory, N., et al. 2015, AJ, 149, 77 (ADS entry)

Dufour, R. J., Talbot, Jr., R. J., Jensen, E. B., & Shields, G. A. 1980, ApJ, 236, 119 (ADS entry)

Edmunds, M. G., & Pagel, B. E. J. 1984, MNRAS, 211, 507 (ADS entry)

Erroz-Ferrer, S., et al. 2019, MNRAS, 484, 5009 (ADS entry)

Ferguson, A. M. N., Wyse, R. F. G., & Gallagher, J. S. 1996, AJ, 112, 2567 (ADS entry)

Ferland, G. J., et al. 2017, , 53, 385 (ADS entry)

Gallazzi, A., Charlot, S., Brinchmann, J., White, S. D. M., & Tremonti, C. A. 2005, MNRAS, 362, 41 (ADS entry)

Garnett, D. R., & Shields, G. A. 1987, ApJ, 317, 82 (ADS entry)

Green, A. W., et al. 2018, MNRAS, 475, 716 (ADS entry)

Greenawalt, B., Walterbos, R. A. M., Thilker, D., & Hoopes, C. G. 1998, ApJ, 506, 135 (ADS entry)

Groves, B. A., Dopita, M. A., & Sutherland, R. S. 2004, ApJS, 153, 75 (ADS entry)

Gutiérrez, L., Beckman, J. E., & Buenrostro, V. 2011, AJ, 141, 113 (ADS entry)

Haffner, L. M., et al. 2009, Reviews of Modern Physics, 81, 969 (ADS entry)

Heiderman, A. L., Evans, II, N. J., Gebhardt, K., Blanc, G., Davis, T. A., Papovich, C., Iono, D., & Yun, M. S. 2011, in New Horizons in Astronomy, Proceedings of the Frank N. Bash Symposium 2011, held October 9-11, 2011. Austin, Texas, USA. Edited by S. Salviander, J. Green, and A. Pawlik. Published online at <A href="http://pos.sissa.it/cgi-bin/reader/conf.cgi?confid=149">http://pos.sissa.it/cgi-bin/reader/conf.cgi?confid=149</A>., id.29, 29 (ADS entry)

Hinshaw, G., et al. 2009, ApJS, 180, 225 (ADS entry)

Ho, I.-T. 2019, MNRAS(ADS entry)

Ho, I.-T., Kudritzki, R.-P., Kewley, L. J., Zahid, H. J., Dopita, M. A., Bresolin, F., & Rupke, D. S. N. 2015, MNRAS, 448, 2030 (ADS entry)

Ho, I. T., et al. 2014, MNRAS, 444, 3894 (ADS entry)

Ho, I.-T., et al. 2016, Ap&SS, 361, 280 (ADS entry)

—. 2017, ApJ, 846, 39 (ADS entry)

Ho, L. C., Filippenko, A. V., & Sargent, W. L. W. 1993, ApJ, 417, 63 (ADS entry)

Hoopes, C. G., & Walterbos, R. A. M. 2003, ApJ, 586, 902 (ADS entry)

Hoopes, C. G., Walterbos, R. A. M., & Greenwalt, B. E. 1996, AJ, 112, 1429 (ADS entry)

Hoopes, C. G., Walterbos, R. A. M., & Rand, R. J. 1999, ApJ, 522, 669 (ADS entry)

Hoyle, F. 1954, ApJS, 1, 121 (ADS entry)

Hubble, E. P. 1926, ApJ, 64, 321 (ADS entry)

Kaplan, K. F., et al. 2016, MNRAS, 462, 1642 (ADS entry)

Karim, A., et al. 2011, ApJ, 730, 61 (ADS entry)

Kelvin, L. S., et al. 2012, MNRAS, 421, 1007 (ADS entry)

Kewley, L. J., & Dopita, M. A. 2002, ApJS, 142, 35 (ADS entry)

Kewley, L. J., & Ellison, S. L. 2008, ApJ, 681, 1183 (ADS entry)

Kewley, L. J., Groves, B., Kauffmann, G., & Heckman, T. 2006, MNRAS, 372, 961 (ADS entry)

Kewley, L. J., Jansen, R. A., & Geller, M. J. 2005, PASP, 117, 227 (ADS entry)

Kewley, L. J., Nicholls, D. C., Sutherland, R., Rigby, J. R., Acharya, A., Dopita, M. A., & Bayliss, M. B. 2019, ApJ, 880, 16 (ADS entry)

Kewley, L. J., Rupke, D., Zahid, H. J., Geller, M. J., & Barton, E. J. 2010, ApJ, 721, L48 (ADS entry)

Kobulnicky, H. A., Kennicutt, Jr., R. C., & Pizagno, J. L. 1999, ApJ, 514, 544 (ADS entry)

Kobulnicky, H. A., & Kewley, L. J. 2004, ApJ, 617, 240 (ADS entry)

Kobulnicky, H. A., & Skillman, E. D. 1997, ApJ, 489, 636 (ADS entry)

Kudritzki, R.-P., Urbaneja, M. A., Bresolin, F., Hosek, Jr., M. W., & Przybilla, N. 2014, ApJ, 788, 56 (ADS entry)

Kumari, N., Maiolino, R., Belfiore, F., & Curti, M. 2019, MNRAS, 485, 367 (ADS entry)

Lacerda, E. A. D., et al. 2018, MNRAS, 474, 3727 (ADS entry)

Lauberts, A., & Valentijn, E. A. 1989, The Messenger, 56, 31 (ADS entry)

Lee, H., & Skillman, E. D. 2004, ApJ, 614, 698 (ADS entry)

Lequeux, J., Peimbert, M., Rayo, J. F., Serrano, A., & Torres-Peimbert, S. 1979, A&A, 80, 155 (ADS entry)

Leroy, A. M., & Rousseeuw, P. J. 1987, Robust regression and outlier detection (ADS entry)

Liske, J., et al. 2015, MNRAS, 452, 2087 (ADS entry)

López-Sánchez, Á. R., Dopita, M. A., Kewley, L. J., Zahid, H. J., Nicholls, D. C., & Scharwächter, J. 2012, MNRAS, 426, 2630 (ADS entry)

López-Sánchez, Á. R., & Esteban, C. 2010, A&A, 517, A85 (ADS entry)

López-Sánchez, Á. R., Mesa-Delgado, A., López-Martín, L., & Esteban, C. 2011, MNRAS, 411, 2076 (ADS entry)

López-Sánchez, Á. R., Westmeier, T., Esteban, C., & Koribalski, B. S. 2015, MNRAS, 450, 3381 (ADS entry)

Madsen, G. J., Reynolds, R. J., & Haffner, L. M. 2006, ApJ, 652, 401 (ADS entry)

Maiolino, R., et al. 2008, A&A, 488, 463 (ADS entry)

Makarov, D., Prugniel, P., Terekhova, N., Courtois, H., & Vauglin, I. 2014, A&A, 570, A13 (ADS entry)

Mannucci, F., Cresci, G., Maiolino, R., Marconi, A., & Gnerucci, A. 2010, MNRAS, 408, 2115 (ADS entry)

Marino, R. A., et al. 2012, ApJ, 754, 61 (ADS entry)

—. 2013, A&A, 559, A114 (ADS entry)

Markwardt, C. B. 2009, in Astronomical Society of the Pacific Conference Series, Vol. 411, Astronomical Data Analysis Software and Systems XVIII, ed. D. A. Bohlender, D. Durand, & P. Dowler, 251 (ADS entry)

Martin, P., & Roy, J.-R. 1994, ApJ, 424, 599 (ADS entry)

Mast, D., et al. 2014, A&A, 561, A129 (ADS entry)

Matteucci, F., & Francois, P. 1989, MNRAS, 239, 885 (ADS entry)

McCall, M. L., Rybski, P. M., & Shields, G. A. 1985, ApJS, 57, 1 (ADS entry)

McGaugh, S. S. 1991, ApJ, 380, 140 (ADS entry)

Medling, A. M., et al. 2018, MNRAS, 475, 5194 (ADS entry)

Meurer, G. R., et al. 2006, ApJS, 165, 307 (ADS entry)

Moustakas, J., Kennicutt, Jr., R. C., Tremonti, C. A., Dale, D. A., Smith, J.-D. T., & Calzetti, D. 2010, ApJS, 190, 233 (ADS entry)

Nicholls, D. C., Sutherland, R. S., Dopita, M. A., Kewley, L. J., & Groves, B. A. 2017, MNRAS, 466, 4403 (ADS entry)

Oberhummer, H., Csótó, A., & Schlattl, H. 2000, Science, 289, 88 (ADS entry)

Oey, M. S., et al. 2007, ApJ, 661, 801 (ADS entry)

Osterbrock, D. E. 1989, Astrophysics of gaseous nebulae and active galactic nuclei (ADS entry)

Owers, M. S., et al. 2017, MNRAS, 468, 1824 (ADS entry)

Pagel, B. E. J., & Edmunds, M. G. 1981, ARA&A, 19, 77 (ADS entry)

Pagel, B. E. J., Edmunds, M. G., Blackwell, D. E., Chun, M. S., & Smith, G. 1979, MNRAS, 189, 95 (ADS entry)

Pagel, B. E. J., Edmunds, M. G., & Smith, G. 1980, MNRAS, 193, 219 (ADS entry)

Peng, C. Y., Ho, L. C., Impey, C. D., & Rix, H.-W. 2002, AJ, 124, 266 (ADS entry)

Peng, Y.-j., et al. 2010, ApJ, 721, 193 (ADS entry)

Pérez-Montero, E. 2014, MNRAS, 441, 2663 (ADS entry)

Pettini, M., & Pagel, B. E. J. 2004, MNRAS, 348, L59 (ADS entry)

Pilkington, K., et al. 2012, A&A, 540, A56 (ADS entry)

Pilyugin, L. S. 2000, A&A, 362, 325 (ADS entry)

—. 2001, A&A, 374, 412 (ADS entry)

Pilyugin, L. S., & Grebel, E. K. 2016, MNRAS, 457, 3678 (ADS entry)

Pilyugin, L. S., Grebel, E. K., & Mattsson, L. 2012, MNRAS, 424, 2316 (ADS entry)

Pilyugin, L. S., & Thuan, T. X. 2005, ApJ, 631, 231 (ADS entry)

Pilyugin, L. S., Vílchez, J. M., & Thuan, T. X. 2010, ApJ, 720, 1738 (ADS entry)

Poetrodjojo, H., D'Agostino, J. J., Groves, B., Kewley, L., Ho, I. T., Rich, J., Madore, B. F., & Seibert, M. 2019, MNRAS, 487, 79 (ADS entry)

Poetrodjojo, H., et al. 2018, MNRAS, 479, 5235 (ADS entry)

Press, W. H., Teukolsky, S. A., Vetterling, W. T., & Flannery, B. P. 1992, Numerical recipes in FORTRAN. The art of scientific computing (ADS entry)

Raimann, D., Storchi-Bergmann, T., Bica, E., Melnick, J., & Schmitt, H. 2000, MNRAS, 316, 559 (ADS entry)

Reynolds, R. J. 1984, ApJ, 282, 191 (ADS entry)

Rich, J. A., Torrey, P., Kewley, L. J., Dopita, M. A., & Rupke, D. S. N. 2012, ApJ, 753, 5 (ADS entry)

Richards, S. N., et al. 2014, MNRAS, 445, 1104 (ADS entry)

Rosales-Ortega, F. F., Díaz, A. I., Kennicutt, R. C., & Sánchez, S. F. 2011, MNRAS, 415, 2439 (ADS entry)

Rosales-Ortega, F. F., Kennicutt, R. C., Sánchez, S. F., Díaz, A. I., Pasquali, A., Johnson, B. D., & Hao, C. N. 2010, MNRAS, 405, 735 (ADS entry)

Rossa, J., & Dettmar, R.-J. 2003, A&A, 406, 493 (ADS entry)

Rupke, D. S. N., Kewley, L. J., & Chien, L.-H. 2010, ApJ, 723, 1255 (ADS entry)

Salpeter, E. E. 1952, Physical Review, 88, 547 (ADS entry)

—. 1955, ApJ, 121, 161 (ADS entry)

Sánchez, S. F., et al. 2012, A&A, 546, A2 (ADS entry)

—. 2014, A&A, 563, A49 (ADS entry)

—. 2017, MNRAS, 469, 2121 (ADS entry)

—. 2019, MNRAS, 484, 3042 (ADS entry)

Sánchez-Menguiano, L., et al. 2016a, ApJ, 830, L40 (ADS entry)

—. 2016b, A&A, 587, A70 (ADS entry)

—. 2018, A&A, 609, A119 (ADS entry)

Schaefer, A. L., et al. 2017, MNRAS, 464, 121 (ADS entry)

—. 2019, ApJ, 884, 156 (ADS entry)

Schweizer, F. 1982, ApJ, 252, 455 (ADS entry)

Scott, N., et al. 2018, MNRAS, 481, 2299 (ADS entry)

Sharp, R., et al. 2006, in Proc. SPIE, Vol. 6269, Society of Photo-Optical Instrumentation Engineers (SPIE) Conference Series, 62690G (ADS entry)

Storchi-Bergmann, T., Calzetti, D., & Kinney, A. L. 1994, ApJ, 429, 572 (ADS entry)

Sutherland, R., Dopita, M., Binette, L., & Groves, B. 2013, MAPPINGS III: Modelling And Prediction in PhotoIonized Nebulae and Gasdynamical Shocks (ADS entry)

—. 2018, MAPPINGS V: Astrophysical plasma modeling code (ADS entry)

Sweet, S. M., Drinkwater, M. J., Meurer, G., Bekki, K., Dopita, M. A., Kilborn, V., & Nicholls, D. C. 2014, ApJ, 782, 35 (ADS entry)

Taylor, E. N., et al. 2011, MNRAS, 418, 1587 (ADS entry)

Thilker, D. A., Braun, R., & Walterbos, R. A. M. 2000, AJ, 120, 3070 (ADS entry)

Thomas, A. D., Kewley, L. J., Dopita, M. A., Groves, B. A., Hopkins, A. M., & Sutherland, R. S. 2018, ApJ, 861, L2 (ADS entry)

Tomičić, N., Kreckel, K., Groves, B., Schinnerer, E., Sandstrom, K., Kapala, M., Blanc, G. A., & Leroy, A. 2017, ApJ, 844, 155 (ADS entry)

Toomre, A., & Toomre, J. 1972, ApJ, 178, 623 (ADS entry)

Torres-Peimbert, S., Peimbert, M., & Fierro, J. 1989, ApJ, 345, 186 (ADS entry)

Torrey, P., Cox, T. J., Kewley, L., & Hernquist, L. 2012, ApJ, 746, 108 (ADS entry)

Tremonti, C. A., et al. 2004, ApJ, 613, 898 (ADS entry)

Tully, R. B., Shaya, E. J., Karachentsev, I. D., Courtois, H. M., Kocevski, D. D., Rizzi, L., & Peel, A. 2008, ApJ, 676, 184 (ADS entry)

Vale Asari, N., Couto, G. S., Cid Fernandes, R., Stasińska, G., de Amorim, A. L., Ruschel-Dutra, D., Werle, A., & Florido, T. Z. 2019, arXiv e-prints, arXiv:1907.08635 (ADS entry)

van de Sande, J., et al. 2017, ApJ, 835, 104 (ADS entry)

Vazdekis, A., Ricciardelli, E., Cenarro, A. J., Rivero-González, J. G., Díaz-García, L. A., & Falcón-Barroso, J. 2012, MNRAS, 424, 157 (ADS entry)

Vila-Costas, M. B., & Edmunds, M. G. 1992, MNRAS, 259, 121 (ADS entry)

Vilchez, J. M., Pagel, B. E. J., Diaz, A. I., Terlevich, E., & Edmunds, M. G. 1988, MNRAS, 235, 633 (ADS entry)

Voges, E. S., & Walterbos, R. A. M. 2006, ApJ, 644, L29 (ADS entry)

Walterbos, R. A. M., & Braun, R. 1994, ApJ, 431, 156 (ADS entry)

Webster, B. L., & Smith, M. G. 1983, MNRAS, 204, 743 (ADS entry)

Whitmore, B. C., et al. 2011, ApJ, 729, 78 (ADS entry)

Williams, M. J., Bureau, M., & Cappellari, M. 2009, MNRAS, 400, 1665 (ADS entry)

Wu, J. F., & Boada, S. 2019, MNRAS, 484, 4683 (ADS entry)

Yin, S. Y., Liang, Y. C., Hammer, F., Brinchmann, J., Zhang, B., Deng, L. C., & Flores, H. 2007, A&A, 462, 535 (ADS entry)

York, D. G., et al. 2000, AJ, 120, 1579 (ADS entry)

Yuan, T.-T., Kewley, L. J., & Rich, J. 2013, ApJ, 767, 106 (ADS entry)

Zaritsky, D., Kennicutt, Jr., R. C., & Huchra, J. P. 1994, ApJ, 420, 87 (ADS entry)

Zhang, K., et al. 2017, MNRAS, 466, 3217 (ADS entry)

Special People

Caroline Chan
Andy Chen
Kevin Coelho
Ashwant Gobinathan
Jabbok Lam
Andy Li
Eu-Kin Lim
Emma Liyanarachchi
Chris Manchester
GyuChul Myeong
Namgyal Wangchuk
Danny Parker
Max Poetrodjojo
Odie Poetrodjojo
Sonia Poetrodjojo
Sujono Poetrodjojo
Eugenia Quach
Diane Salim
Rocky Sim
Tanya Sim
James Stuart-Smith
Benjamin Teo
Matt Theophile
Justine Wong
Eileen Xie
Joy Zeng